

UC Santa Barbara

UC Santa Barbara Electronic Theses and Dissertations

Title

Search for supersymmetry in the final state containing two hadronically decaying taus and missing transverse momentum with 77.2 fb⁻¹ of data collected by the CMS Detector from 13 TeV proton-proton collisions

Permalink

<https://escholarship.org/uc/item/6t8035nh>

Author

Colegrove, Owen R

Publication Date

2019

Peer reviewed|Thesis/dissertation

University of California
Santa Barbara

**Search for supersymmetry in the final state
containing two hadronically decaying taus and
missing transverse momentum with 77.2 fb^{-1} of data
collected by the CMS Detector from 13 TeV
proton-proton collisions**

A dissertation submitted in partial satisfaction
of the requirements for the degree

Doctor of Philosophy
in
Physics

by

Owen Robert Colegrove

Committee in charge:

Professor Joseph Incandela, Chair
Professor Jeffory Richman
Professor David Berenstein

June 2019

The Dissertation of Owen Robert Colegrove is approved.

Professor Jeffory Richman

Professor David Berenstein

Professor Joseph Incandela, Committee Chair

May 2019

Search for supersymmetry in the final state containing two hadronically decaying taus
and missing transverse momentum with 77.2 fb^{-1} of data collected by the CMS
Detector from 13 TeV proton-proton collisions

Copyright © 2019

by

Owen Robert Colegrove

To my father, Robert Colegrove.

Acknowledgements

Foremost, I would like to express my sincerest gratitude to my advisor, Prof. Joseph Incandela, for his guidance, support and for all the knowledge he has shared. The intellectual freedom and direction provided by him offered me the unique opportunity to pursue interesting research avenues while also producing valuable results.

Next, I would like to thank Jeff Richman and David Berenstein for agreeing to sit on my thesis committee.

As well, I would like to acknowledge support and guidance I have had through my advisors immediate research group – Valentina Dutta, Nick McColl, Sam Mullin, Loukas Gouskos and Huilin Qu. Along the way, these individuals have shown me tolerance and generously shared their time.

Our collaborators at SLAC also deserve special mention: Omar Moreno, Tim Nelson, Philip Schuster, Natalia Toro. As well as the many professors at UCSB who helped me to further my growth as a student and researchers.

Lastly, I would also like to thank researchers on CMS who have further helped my continued growth – Anadi Canepa and Jan Steggeman who both generously shared their time, as well as fellow collaborators Isabell Melzer-Pellmann, Alexis Kalogeropoulos and Basil Schnieder, among many others.

Beyond our immediate group and senior colleagues, I would like to thank the physics department at UCSB, and several of my friends and classmates, Nick Amin, John McCann, Michael Rosenthal, Milind Shyani, Chaitanya Murthy and Wade Bloomquist, to name a few.

As well I would like to thank a few of my excellent friends who have supported me during my time at CERN: William Holmkvist, Fer JUSDADO, Daniel Björkman, Arthur Charléty-Meano, Dani Blasco-Serrano, Sara Benítez, Francisco Javier, Danielle Hodgkinson, Alex Sherman, Laura Green, Fran Rupérez-Yuste, Illia Babounikau, Dwayne Spiteri and Ranveig Strøm.

Lastly, I would like to acknowledge the support that my sister Katie provided.

Curriculum Vitæ

Owen Robert Colegrove

EDUCATION

2019	Ph.D. in Physics, University of California, Santa Barbara.
2017	M.S. in Physics, University of California, Santa Barbara.
2014	B.S. in Physics, University of Rochester.

PUBLICATIONS & PREPRINTS

- **Rejection of multi-GeV photon background for a light dark matter experiment using an electron beam and missing-momentum techniques**, LDMX Collaboration, in preparation.
- **Search for direct stau production in the all-hadronic final state at 13 TeV (77.5/fb)**, CMS Collaboration, SUS-18-006, in preparation.
Search for supersymmetry with direct stau production at the HL-LHC with the CMS Phase-2 detector, CMS Collaboration, FTR-18-010, public CMS note anticipating publication in CERN Yellow Report.
- **Search for supersymmetry in events with a τ lepton pair and missing transverse momentum in proton-proton collisions at $\sqrt{s} = 13$ TeV**, CMS Collaboration, SUS-17-003, arXiv:1807.02048, JHEP 11 (2018) 151
- **Light Dark Matter eXperiment (LDMX)**, LDMX Collaboration, arXiv:1808.05219, pending journal submission.
- **US Cosmic Visions: New Ideas in Dark Matter 2017: Community Report**, M. Battaglieri *et al.*, arXiv:1707.0459.
- ***Search for direct production of supersymmetric partners of the top quark in the all-jets final state in proton-proton collisions at $\sqrt{s} = 13$ TeV**, CMS Collaboration, SUS-16-049, arXiv:1707.03316, JHEP 10 (2017) 005, *Note – not listed as official CMS author at time of publication.
- **Giant Convection Cells Found on the Sun**, Hathaway, Upton, Colegrove, Science, 342, 1217.

Abstract

Search for supersymmetry in the final state containing two hadronically decaying taus and missing transverse momentum with 77.2 fb^{-1} of data collected by the CMS Detector from 13 TeV proton-proton collisions

by

Owen Robert Colegrove

The dissertation herein presents the latest public search for direct tau slepton ($\tilde{\tau}$) production at the Large Hadron Collider (LHC). The search is performed using data collected from the Compact Muon Solenoid (CMS) experiment. A total of 77.2 fb^{-1} of data from proton-proton collisions at 13 TeV are recorded and analyzed. The analysis probes the final state with $\tilde{\tau}$ decay branching ratio, that of two hadronic taus.

No significant deviation from Standard Model expectations are observed in the data a 95% confidence level upper limit on the direct stau pair production cross section is set accordingly. Mass degenerate stau pair production is excluded for minimally supersymmetric models with $m(\tilde{\tau}) \in 90\text{-}150 \text{ GeV}$. Similarly, exclusion is expected for left-handed only pair production with $m(\tilde{\tau}_L)=125 \text{ GeV}$. However, no such exclusion is observed in the data.

These results motivate an additional study carried out in a simulation of the High-Luminosity LHC environment with the CMS Phase-2 detector. This scenario corresponds to 3000 fb^{-1} of data taken at a center-of-mass energy of 14 TeV. The study shows sufficient sensitivity to formally expect the discovery of mass degenerate direct stau pair production for $m(\tilde{\tau}) \in [100, 650 \text{ GeV}]$.

Contents

Curriculum Vitae	vii
Abstract	viii
1 The Standard Model of Particle Physics	1
1.1 Introduction and History	2
1.2 Introduction to Quantum Field Theory	5
1.3 Fundamental Forces Explained	8
1.4 Particle Mass and the Higgs Boson	14
1.5 The Neutrino Sector	19
1.6 Shortcomings of the Standard Model	20
2 Supersymmetry	23
2.1 Supersymmetry	24
2.2 SUSY Phenomenology	25
2.3 Searching for Staus	28
3 The LHC and the CMS Experiment	32
3.1 The Large Hadron Collider	33
3.2 The Compact Muon Solenoid Experiment	42
4 Event Reconstruction	55
4.1 Object Reconstruction	56
4.2 Identifying Jets Associated with b -quark Decay	65
4.3 Tau Identification	66
4.4 Missing Transverse Momentum and Scalar Transverse Momenta Sum Re- construction	68
5 Event Simulation	71
5.1 Overview of Event Simulation at CMS	72
5.2 Event Generation Packages Used by CMS	76

6	Deep Neural Networks for Hadronic Tau Identification	78
6.1	Introduction to Artificial Neural Networks	79
6.2	Training Neural Networks	81
6.3	Convolutional Neural Networks	83
6.4	DeepPF Isolation	85
7	CMS Stau Search Using 2016+2017 Data : Introduction	90
7.1	Simplified Models at the LHC	91
7.2	CMS Stau Search Using 2016+2017 Data : Introduction	92
7.3	Triggers and Datasets	93
7.4	Object Selection	93
7.5	Event Selection	100
8	CMS Stau Search Using 2016+2017 Data : Analysis	105
8.1	Background Estimation Techniques	106
8.2	Validation regions of the analysis	113
8.3	Systematic Uncertainties	114
8.4	Results	118
9	CMS Stau Search Using 2016+2017 Data : Interpretation	122
9.1	Limits on Direct Stau Production	122
10	CMS Future New Physics Search : Staus at the HL-LHC	125
10.1	The High-Luminosity LHC	126
10.2	Searching for Staus at the HL-LHC	127
10.3	Adjusting Delphes Simulation	132
10.4	Systematic Uncertainties	136
10.5	Results	136
10.6	Interpretation	136
11	Summary	139
11.1	Summary and Conclusions	140
A	Appendix B	142
B	Appendix A	157
B.1	The di- τ_h Trigger	157
B.2	p_T^{miss} Trigger	158
B.3	Datasets Used	159
B.4	Simulation Corrections and Their Uncertainties	163
B.5	Statistical Methods at the LHC	164
B.6	Additional Validation Regions	164
	Bibliography	168

Abbreviations

Abbreviation	Full Expression
LHC	L arge H adron C ollider
CMS	C ompact M uon S olenoid
ATLAS	A Toroidal LHC Apparatu S
ALICE	A Large I on C ollider E xperiment
SM	S tandard M odel
BSM	B eyond the S tandard M odel
LHCb	LHC -beauty
SUSY	S upersymmetry
MSSM	M inimal S upersymmetry M odel
MET	M issing T ransverse E nergy
QED	Q uantum E lectro D ynamics
QCD	Q uantum C hromo D ynamics
PU	P ile- U p
ECAL	E lectromagnetic CAL orimeter
HCAL	H adronic CAL orimeter
L1T	L evel- 1 T rigger
HLT	H igh L evel T rigger
PF	P article F low
EWK	E lectro W ea K
PDF	P arton D istribution F unction
ML	M achine L earning
MVA	M ulti V ariate A lgorithm
BDT	B oosted D ecision T ree
ANN,NN	A rtificial N eural N etwork
ReLU	R ectified L inear U nit
SGD	S tochastic G radient D escent
ADAM	A Daptive M oment G eneration
DeepPF	D eep P article F low T au I solation
SMP	S imple M odel P arameterization
POG	P hysics O bject G roup
SF	S cale F actor
LO	L eading O der
NLO	N ext to L eading O der
NLL	N ext to L eading L ogarithm
NNLO	N ext to N ext to L eading O der
PS	P arton S hower
SR	S earch R egion
CR	C ontrol R egion
VR	V alidation R egion

Physical Constants

Physical Constant	Symbol	Value
Speed of Light	c_0	2.99792458e8 (exact)
Photon Mass	m_A	0 GeV
Electron mass	m_e	511 KeV
W Boson Mass	m_W	80.4 GeV
Z Boson Mass	m_Z	90.2 GeV
Higgs boson vacuum expectation	v	246 GeV
Electromagnetic coupling constant	α	$\approx 1/137.$
Weak coupling constant	α_W	10^{-6}
Weak coupling constant	α_S	1
Weak Mixing Angle	$\theta_W = \arccos(M_W/M_Z) / \frac{\alpha}{\alpha_W}$	$.0.2223 \pm .0021$

Symbols

Constant Name	Symbol
Lagrangian	\mathcal{L}
Lagrangian Density	\mathcal{L}
γ Boson Field	A^μ
W Boson Fields	W^\pm
Z Boson Field	Z^0
gluon Field	\mathcal{A}^μ
Gauge covariant derivative	D_μ
Electromagnetic Field Strength Tensor	$F^{\mu\nu} = \partial_\mu A_\nu - \partial_\nu A_\mu$
QCD Field Strength Tensor	$G_{\mu\nu}^a = \partial_\mu \mathcal{A}_\nu^a - \partial_\nu \mathcal{A}_\mu^a + gf^{abc} \mathcal{A}_\mu^b \mathcal{A}_\nu^c$
lepton (any generation)	ℓ
neutrino (any generation)	ν_ℓ
electron, muon, tau	e, μ, τ
electron, muon, tau neutrino	ν_e, ν_μ, ν_τ
up, charm, top quarks	u, c, t
down, strange, bottom quarks	d, s, b
Electromagnetic Charge Sign	Q
Field Spinor	ψ
Gel-Mann Matrices	X^μ
Dirac Matrices	γ^μ
Field Spinor Adjoint	$\bar{\psi} = \gamma^0 \psi^\dagger$
Pauli Spin Matrices	τ^a
Unitary Group N	$U(N)$
Special Unitary Group N	$SU(N)$
Ultraviolet Cutoff	Λ_{UV}
Stau	$\tilde{\tau}$
Lightest Supersymmetric Particle	$\tilde{\chi}_1^0$
Missing Transverse Momentum	p_T^{miss}
ϵ	Efficiency

Chapter 1

The Standard Model of Particle Physics

1.1 Introduction and History

Today, science is a multi-discipline area of study that spans an almost unfathomably deep knowledge base – many attribute the success of modern science to a style of critical thought dubbed the *scientific method*. Since introducing the scientific method in the 17th century, scientists have iteratively used rigorous thinking to develop and, subsequently, to validate or falsify new scientific theories. A more careful historian may even trace the birth of modern science back further, e.g., to the work of ancient Greek philosophers, such as Democritus who was one of many great philosophers of the antiquities. Democritus theorized that the universe is made up of indivisible and indestructible building blocks called atoms.

In the years since Democritus, our understanding of the universe has grown and been refined in many domains. Modern physics first demonstrated all solid matter in the cosmos to be composed of vast swaths of molecules which are in turn composed of atoms, named for their similarity to Democritus’s theory. However, later results showed that atoms are not fundamental, but instead they are in turn composed of more basic building blocks called neutrons and protons, which are themselves composite objects of primary particles called quarks and gluons. Perhaps Democritus had the correct model, and these are just additional layers of abstraction being peeled away.

The *Standard Model* (SM) of particle physics is a comprehensive modern theory which attempts to build an accurate model of all particles and interactions. The Standard Model accomplishes this by introducing three fundamental forces (Weak, Strong, and Electromagnetic), and a slew of particles – leptons, quarks, neutrinos, and last but not least, the Higgs boson [Fig. 1.1]. The force carriers mediate interactions between all particles with characteristics that can be determined by an associated gauge symmetry.

The Standard Model was built and confirmed through numerous experiments of ever-

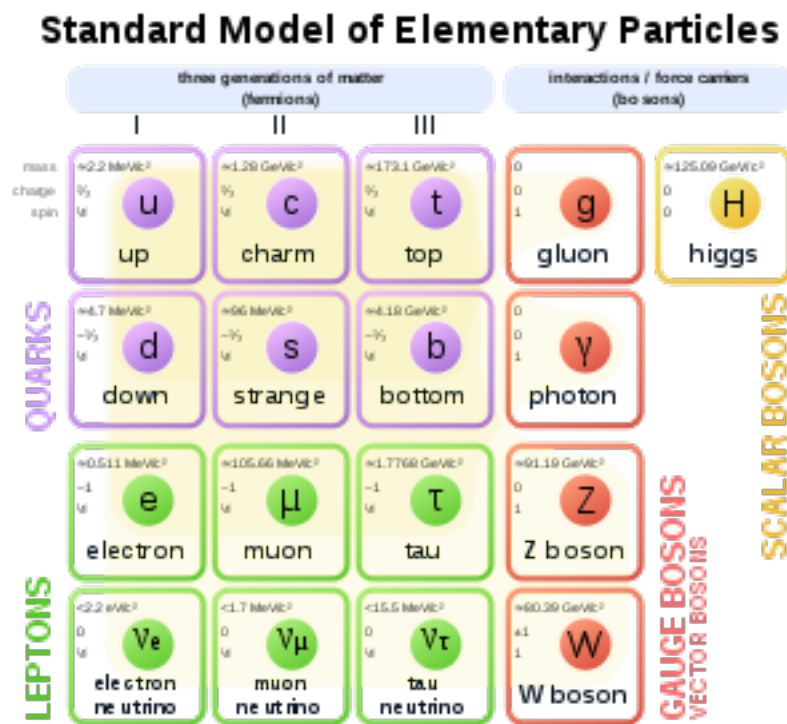


Figure 1.1: The Standard Model of particle physics

increasing sophistication. One of the first modern experiments along this path was conducted by Ernest Rutherford who invalidated J.J. Thomson's *plum-pudding* model of the atom and replaced it with a model that included a dense core called the nucleus [1, 2]. The experiment devised by Rutherford et al. found *new physics*, physics that was beyond that which was previously known, by measuring an anomalous rate of wide-angle alpha particle scatter in nuclear collisions. The results roughly coincided with the first emergence of modern quantum theory and marked the beginning of a century of significant discoveries which created the Standard Model as it is known today [3]. Ultimately, it is the goal of every particle physics experiment to either find such deviations, called *Beyond the Standard Model* (BSM) physics, or to provide a more precise measurement of known Standard Model processes.

1.1.1 Fermions

The Standard Model is composed of two types of elementary particles referred to as *bosons*, spin 1 or 0 particles, and *fermions*, spin 1/2 particles [4]. The fermions can be separated into three distinct sub-classes called *quarks*, *leptons* and *neutrinos*. Quarks are the only fermions to have color charge and to therefore participate in strong interactions [5], non-neutrino leptons participate in electromagnetic and weak interactions, and neutrinos interact only weakly. The leptons come in three generations which follow a mass hierarchical structure [Tab. 1.1]. The understanding of the properties of quarks and leptons greatly exceeds that of the neutrino sector. Known characteristics of neutrinos has grown slowly because of the relatively small cross section for weak interactions which makes neutrino detection exceedingly difficult.

Table 1.1: List of all fermions.			
Particles	Names	Masses	Mediated By
Neutrinos	ν_e, ν_μ, ν_τ	$< 1 \text{ eV}$	Weak
Leptons	e, μ, τ	511 KeV, 105 MeV, 1776 MeV	E&M, Weak
Quarks	u, d, c, s, t, b	$\approx 1 \text{ MeV} - 200 \text{ GeV}$	Strong, E&M, Weak

1.1.2 Bosons

The vector bosons of the Standard Model are responsible for mediating interactions between all particles with a strength proportional to the interactions *coupling constant*. Bosons are separated into vector (spin 1) and scalar (spin 0) categories and are often referred to as "fields" in recognition of their unique ability to cause action at a distance. Among the vector bosons, the *photon* is a single massless particle responsible for mediating electromagnetic forces, the *gluons* are eight massless particles responsible for mediating the strong forces, and the *W and Z bosons* are three massive particles responsible for weak interactions. Lastly, the *Higgs boson* a massive scalar particle which is responsible for generating the mass of the other particles in the Standard Model. The Higgs boson is known to "give mass" to other particles through electroweak symmetry breaking [Sec. 1.4]. The Higgs boson is produced with the smallest frequency of all Standard Model particles and was, therefore, the last building block of the Standard Model to be experimentally verified.

1.2 Introduction to Quantum Field Theory

The interactions within the Standard Model can all be explained through a self-consistent formalism known as *Quantum Field Theory* (QFT). Within QFT, field equations and particle kinematics are derived by varying the action, S , which can be written as a time integral over the Lagrangian, L , and a space-time integral over the corresponding

Lagrangian density, \mathcal{L} :

$$S = \int L \, dt = \int \mathcal{L}(\phi, \partial\phi) \, d^4x \quad (1.1)$$

The action is composed of Lorentz invariant terms that couple together mathematical representations of the particles and fields of the Standard Model. All interactions of the Standard Model can be derived directly from the Lagrangian, but exact calculations are as of yet too complicated to perform, and so such calculations are made by approximate techniques. The most standard approach for such calculations is a graphical perturbation schema referred to as *Feynman Diagrams* [6]. Each Feynman diagram is built from basic pieces associated with allowable interactions of the Standard Model that are contained in \mathcal{L} [Fig. 1.2, Fig. 1.6] and are used to approximate the full path integral as described below. Every additional interaction added to a diagram constitutes a higher order term of the perturbation expansion, written in terms of the associated coupling constants, except for low energy strong interactions where the coupling is non-perturbative. In this regime other methods such as lattice QCD must be employed [Sec. 1.3.3].

1.2.1 Classical field theory – symmetry and conservation laws

The *principle of least action* dictates that any variation of the action, δS , of any classically described system must vanish as deviations are made from the extremal path – the path selected by nature. Mathematically, this statement indicates that the system is tracing out a stationary path, and an example of the physical consequence of this law in classical mechanics is the apple falling deterministically from a tree to the ground underneath it. Application of this mathematical principle yields the *Euler-Lagrange equations of motion* [7] :

$$\partial_\mu \left(\frac{\partial \mathcal{L}}{\partial(\partial_\mu \phi)} \right) - \frac{\partial \mathcal{L}}{\partial \phi} = 0 \quad (1.2)$$

A symmetry is any variation of the fields, $\phi \rightarrow \phi' = \phi + \alpha \Delta \phi$ for which the equations of motion remain unchanged. This can only be achieved if the Lagrangian is invariant up to a 4-divergence, that is $\mathcal{L} \rightarrow \mathcal{L}' = \mathcal{L} + \alpha \partial_\mu \mathcal{J}^\mu$.

From *Noether's theorem* this then leads to a conserved current j^μ :

$$j^\mu = \frac{\partial \mathcal{L}}{\partial(\partial_\mu \phi)} \Delta \phi - \mathcal{J}^\mu \quad (1.3)$$

Applying Noether's theorem to the QFT of the Standard Model allows for natural physical interpretations, such as the conservation of charge and energy.

1.2.2 Quantum field theory – path integral formulation

Phenomena in the quantum mechanical world can only be described probabilistically. This in turn creates a more complicated description of nature than that which is observed in the classical world. The double-slit experiment provided an early demonstration of this challenge by showing that light incident on a boundary wall with two open slits created an interference pattern on an opposite screen consistent with a wave-like source [8]. Moreover, the probability amplitude in this experiment, as could be inferred by the observed intensity on the screen, was shown to be a sum over the amplitude of the two paths allowed by the two slits. Free space can be thought of as the limiting case of an infinite number of boundary walls, each with infinite slits, which, in light of the previously described double-slit experiment, illustrates the point that all paths must be considered in a quantum system [9]. Therefore, the probability amplitude in free space, $A_{if}(T)$, for a single particle to traverse from point q_i to point q_f over a time

interval T is given by the sum over all allowable paths, the *path integral*,

$$\mathcal{A}_{if}(T) = \langle q_i | e^{-iHT} | q_f \rangle = \int \mathcal{D}q(t) \exp \left[-i \int_0^T L(q, \dot{q}) dt \right], \quad (1.4)$$

where H is the Hamiltonian of the system, so that e^{-iHT} is the time evolution operator, and where

$$\int \mathcal{D}q(t) = \lim_{N \rightarrow \infty} \left(\frac{im}{2\pi\delta t} \right)^{N/2} \prod_{i=0}^{N-1} \int dq_i. \quad (1.5)$$

Assuming a polynomial representation of the potential, $V(\phi) = \sum_i a_i \phi^i$, in the Lagrangian above, it becomes clear that the path integral may be expanded in powers of a_i . The constant a_i is the previously described coupling constant because it specifies the strength of interactions with the potential. Each term in this expansion of the path integral can then be represented by a single Feynman Diagram which simplifies the computation and implies a physical interpretation of the expansion term.

1.3 Fundamental Forces Explained

The Standard Model is an experimentally driven theory wherein the majority of introduced particles did not have any theoretical motivation, save for the fact that at various points in time new particles were predicted for the internal coherence of the model. However, all observed particles and forces now fit neatly into a formalized QFT, with an associated Lagrangian which accurately describes almost all observed phenomena.

The Standard Model vector bosons have underlying *gauge symmetries* built into the Lagrangian. The gauge symmetry of the Standard Model corresponds to the product of these symmetries, $U(1)_Y \times SU(2)_L \times SU(3)_C$ [10].

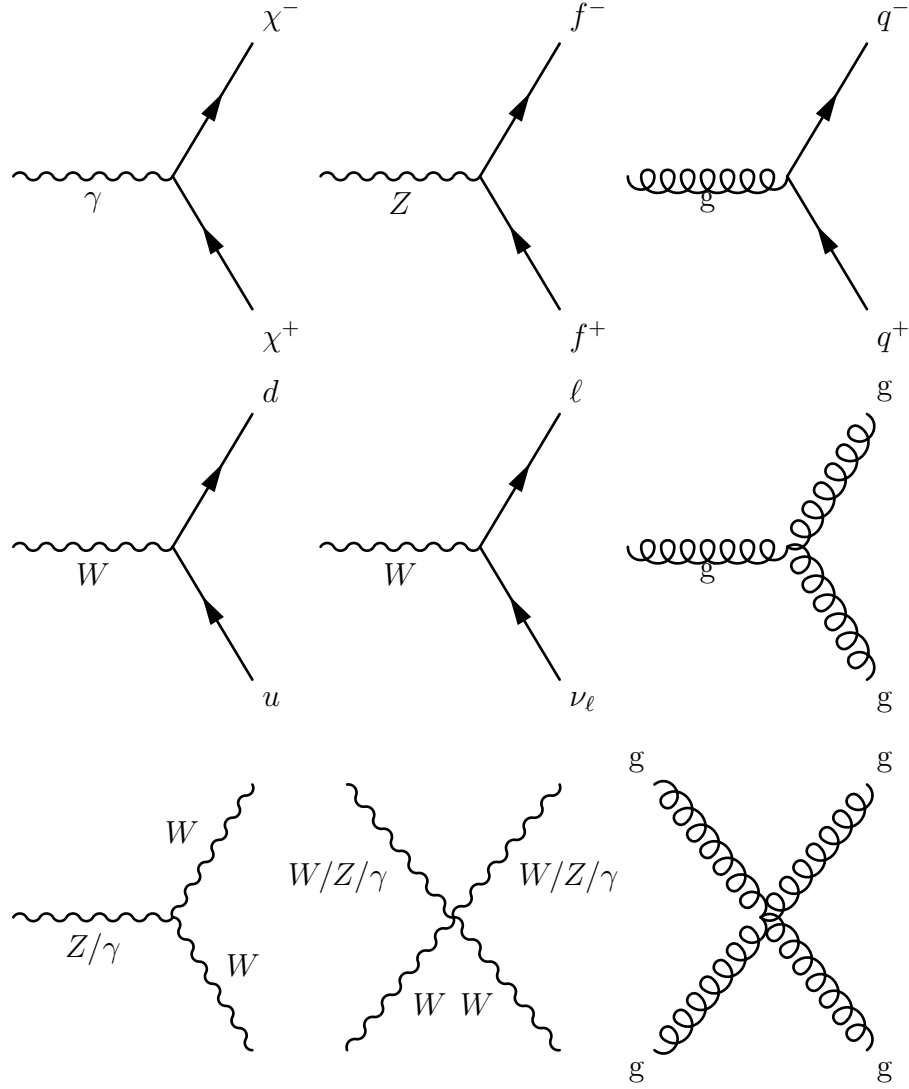


Figure 1.2: The gauge boson mediated interactions of the Standard Model. Above, f is any fermion, u/d are interchangeable with c/s and t/b , and χ^\pm is any particle with electromagnetic charge. The notation X/Y indicates that either particle X or Y can be used freely as long as the diagram conserves charge.

1.3.1 Quantum electrodynamics and the electromagnetic force

Quantum electrodynamics (QED) is the simplest sector of the Standard Model, and any particle charged under it participates in the interactions it describes [11].

The Lagrangian density describing QED is given by

$$\mathcal{L}_{QED} = \bar{\psi}(i\gamma^\mu D_\mu - m)\psi - \frac{1}{4}F^{\mu\nu}F_{\mu\nu}. \quad (1.6)$$

Coupling between the Dirac spinor, ψ , its adjoint, $\bar{\psi} = \psi^\dagger \gamma^0$, and the photon field A^μ are determined by the covariant derivative $D_\mu = \partial_\mu - iQeA_\mu(x)$.

The QED Lagrangian is invariant under the simultaneous transformation of the photon field, $A(x)^\mu \rightarrow A'(x)^\mu = A(x)^\mu - \partial^\mu \alpha$, and the spinor $\psi \rightarrow e^{i\alpha(x)}\psi$. This is classified as a $U(1)$ Abelian (commutative) local symmetry. One way that this symmetry can be thought of is as a redundancy in physical systems that yield a given equation of motion. I.e., it is the potential difference across space, and not the potential values, that dictate the motion of a charged particle. Moreover, this gauge invariance can be physically interpreted as conservation of electromagnetic charge through Noether's theorem.

One can obtain the *Dirac Equation* by varying this Lagrangian with respect to the spinor ψ . This equation governs the motion for any charged particle subject to any given electromagnetic field configuration A^μ :

$$\partial_\mu \left(\frac{\partial \mathcal{L}}{\partial(\partial_\mu \psi)} \right) - \frac{\partial \mathcal{L}}{\partial \psi} = 0 \longrightarrow i\gamma^\mu \partial_\mu \psi - m\psi = eQ\gamma_\mu A^\mu. \quad (1.7)$$

Alternatively, one may vary the Lagrangian with respect to the field A^μ in order to find an equation for the field in terms of the spinor ψ

$$\partial_\nu \left(\frac{\partial \mathcal{L}}{\partial(\partial_\nu A_\mu)} \right) - \frac{\partial \mathcal{L}}{\partial A_\mu} = 0 \longrightarrow \partial_\nu F^{\nu\mu} = eQ\bar{\psi}\gamma^\mu\psi. \quad (1.8)$$

The gauge invariance of A_μ can be used to select $\partial_\mu A^\mu = 0$. This selection is known as the *Lorenz gauge* and reduces to the equation governing A_μ to:

$$\partial^\nu \partial_\nu A^\mu = eQ\bar{\psi}\gamma^\mu\psi. \quad (1.9)$$

1.3.2 Weak isospin/hypercharge and the electroweak force

Glashow, Salam, and Weinberg showed that unification of the weak and electromagnetic forces provides a more accurate description of nature [12]. The Lagrangian of the weak isospin sector obeys a $SU(2)$ gauge symmetry and admits three bosons (W_1, W_2, W_3). The W^\pm , Z and γ bosons observed in nature are composed as a superposition over the three weak eigenstates and a $U(1)$ invariant boson B , from the QED sector, according to:

$$\begin{bmatrix} A \\ Z^0 \end{bmatrix} = \begin{bmatrix} \cos \theta_W & \sin \theta_W \\ -\sin \theta_W & \cos \theta_W \end{bmatrix} \begin{bmatrix} B \\ W_3 \end{bmatrix}, \quad (1.10)$$

and,

$$W^\pm = \frac{1}{\sqrt{2}}(W_1 \mp iW_2). \quad (1.11)$$

Latest measurements show the electroweak mixing angle satisfies $\sin^2 \theta_W = 0.23146 \pm 0.00012$, consistent with theoretical predictions [13]. The W boson couples to particles according to weak isospin, T_W , which is determined in part for fermions by the given particles *chirality*. Chirality is a somewhat nebulous quantum property of fundamental particles that can be described as an intrinsic *handedness*, with values ± 1 , which maps onto helicity in the massless particle limit. The field of the W boson, W^\pm , has weak isospin values $I_W = \pm 1$ and acts according to a $SU(2)$ symmetry to mediate transitions between isospin doublet states, e.g. $\left(\frac{e}{\nu_e}\right)_{L/R}$, of T_W . The subscript "L/R" corresponds

Table 1.2: Electroweak coupling constants

Fermion	Q	I_W	Y_L (left-handed)	Y_R (right-handed)
ℓ^\pm	± 1	$\pm 1/2$	± 1	± 2
ν_ℓ	0	$1/2$	-1	0
u,c,t	$2/3$	$1/2$	$1/3$	$4/3$
d,s,b	$-1/3$	$-1/2$	$1/3$	$-2/3$

to left/right-handed chiral states.

Because the weak hypercharge is a linear combination of two operators, it is computationally efficient to decompose the interactions it mediates into axial and vector components with coefficients $c_V = T_W - 2Q \sin^2 \theta$, and $c_A = T_W$, respectively. Lastly, all particles participate in interactions with the γ boson with strength determined by their coupling $e = g_W \sin \theta_W$.

The portion of the electroweak Lagrangian responsible for governing the interaction between fermions and the fields, \mathcal{L}_{EWK}^{int} , can be written as the sum over three terms describing the interactions mediated by these four bosons, \mathcal{L}_A^{int} , \mathcal{L}_W^{int} , \mathcal{L}_Z^{int} , where [14]:

$$\mathcal{L}_A^{int} = -eQ A_\mu (\bar{\psi} \gamma^\mu \psi), \quad (1.12)$$

$$\mathcal{L}_W^{int} = \frac{g_W}{2\sqrt{2}} [W_\mu^- (\bar{u} \gamma^\mu (1 - \gamma^5) d) + W_\mu^+ (\bar{d} \gamma^\mu (1 - \gamma^5) u)], \quad (1.13)$$

$$\mathcal{L}_Z^{int} = \frac{g_W}{2 \cos \theta_W} Z_\mu^0 [\bar{\psi} \gamma^\mu (c_V - c_A \gamma^5)] \psi. \quad (1.14)$$

In an analogous manner to section 1.3.1 one may obtain the equations that govern the fields and particles therein varying the Lagrangian.

1.3.3 Quantum chromodynamic and the strong force

Chromodynamics (QCD) is a non-Abelian theory that follows a relatively complicated $SU(3)$ gauge symmetry [15]. The discovery of the gluon, the strong force mediator, came in 1979 after evidence for QCD was provided in three-jet events at the PETRA experiment [16]. The governing Lagrangian of QCD, \mathcal{L}_{QCD} , is given as

$$\mathcal{L}_{\text{QCD}} = \bar{\psi}_i (i(\gamma^\mu D_\mu)_{ij} - m \delta_{ij}) \psi_j - \frac{1}{4} G_{\mu\nu}^a G_a^{\mu\nu}, \quad (1.15)$$

where index a on the field tensor runs over the three conserved color charges of QCD. The Lagrangian, \mathcal{L}_{QCD} , admits a gauge symmetry similar to that of QED with the slightly more complicated transformation, $U(x) = \exp i \Sigma_a \alpha_a(x) X_a$ which is called *non-Abelian* as $U(x)U(y) \neq U(y)U(x)$.

The coupling constant of the strong force is different from that of the electroweak sector, in that it decreases at higher energy scales. This phenomenon, dubbed asymptotic freedom, was first proposed by David Gross, Frank Wilczek, and independently David Politzer, who all shared the 2004 Nobel prize in physics for this work [17]. Asymptotic freedom implies a point-like nature of quarks in bound states and also a strong force which grows with separation. Moreover, asymptotic freedom implies *color confinement*, i.e., quarks cannot exist individually in nature. Instead, quarks form composite mesons, diquark states, baryons, triquark states, and perhaps more exotic states such as pentaquarks. The coupling constant, $\alpha_s(Q^2)$, scales logarithmically with the resolution, Q^2 , in respect to a known reference scale $\alpha_s(\mu^2)$,

$$\alpha_s(Q^2) = \frac{\alpha_s(\mu^2)}{1 + B\alpha_s(\mu^2) \ln\left(\frac{Q^2}{\mu^2}\right)}, \quad (1.16)$$

where $B = (11N_C - 2N_f)/12\pi$, given N_C number of colors and N_f number of quark

flavors. In the Standard Model experiments have verified $N_C = 3$ and $N_f = 3$ and so indeed the coupling constant α_s does decrease with increasing energy.

The non-perturbative nature of QCD at low energies makes it difficult to perform accurate calculations. Challenging to compute quantities include interaction cross sections as well as more fundamental quantities such as meson/baryon masses. Such estimates are an ongoing area of active research called *Lattice QCD* [18]. However, at higher energies, such as those seen at typical accelerator experiments today, it is possible to obtain very accurate predictions of QCD related quantities. These predictions, such as the differential dijet production cross section [Fig. 1.3], have been confirmed by many distinct measurements. However, despite accurate cross section predictions, QCD events can remain hard to model at collider experiments due to high production rates and hard to simulate rare detector effects.

1.4 Particle Mass and the Higgs Boson

In order for all previously described gauge symmetries to hold the Standard Model requires all elementary particles to be massless. Beyond the problem of particle mass, there are also some processes such as $e^+e^- \rightarrow W^+W^-$ which violate unitarity with the existence of only electroweak and strong forces [20]. Introducing the Higgs boson through a mechanism called electroweak symmetry breaking solves these problems [21, 22]. Within the standard model, the Higgs boson is a superposition over two complex scalar fields that make up a weak isospin doublet

$$\phi = \frac{1}{\sqrt{2}} \begin{pmatrix} \phi^1 + i\phi^2 \\ \phi^0 + i\phi^3 \end{pmatrix}. \quad (1.17)$$

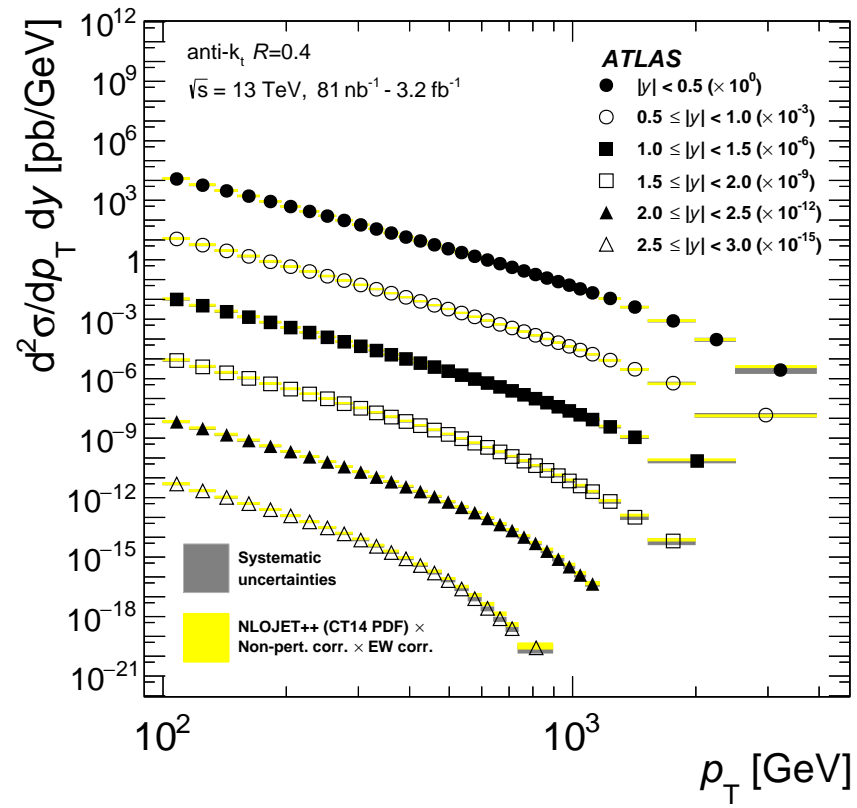


Figure 1.3: The differential production cross section for dijet QCD [19].

The Higgs boson field interacts with the Standard Model through the Lagrangian

$$\mathcal{L}_H = |D_\mu \phi|^2 + \mu^2 \phi^\dagger \phi - \lambda (\phi^\dagger \phi)^2. \quad (1.18)$$

The potential in the Lagrangian, $V(\phi) = \mu^2 \phi^\dagger \phi - \lambda (\phi^\dagger \phi)^2$, breaks the $U(1)$ global symmetry of the Lagrangian when $\mu^2 < 0$. This results in a non-zero vacuum expectation value $\langle \phi \rangle = \frac{|\mu|}{\sqrt{2\lambda}} = v$. For a Higgs with an observable mass of roughly 125 GeV the constant v is approximately 246 GeV [Fig. 1.4]. Subsequently, the Higgs boson can give mass to other particles via coupling mechanisms. For vector bosons, this coupling to the Higgs boson is achieved through the gauge covariant derivative, D_μ :

$$D_\mu = \left(\partial_\mu - igW_\mu^a \tau^a - i\frac{1}{2}g'B_\mu \right), \quad (1.19)$$

where g_W and g' are the coupling constants of the previously introduced eigenstate W_μ^a and B_μ gauge bosons, and τ^a are the Pauli spin matrices. The mass of the massive gauge bosons can then be calculated theoretically

$$m_W = \frac{1}{2}v |g_W|, \quad m_Z = \frac{1}{2}v \sqrt{g_W^2 + g'^2}, \quad m_H = \sqrt{2\mu^2} \equiv \sqrt{2\lambda v^2}, \quad (1.20)$$

whereas for fermions the mass is generated through a direct *Yukawa coupling* to the Higgs boson field,

$$\mathcal{L}_{\text{Yukawa}} = -\lambda_f \bar{\psi} \phi \psi. \quad (1.21)$$

The neutrino is suspected of only existing in a right-handed state and of being a Majorana particle, which in turn implies that the neutrino cannot obtain a mass through this interaction. Experimental evidence shows that the neutrinos are not massless and so uncovering the source of neutrino mass is an ongoing effort [Sec. 1.5].

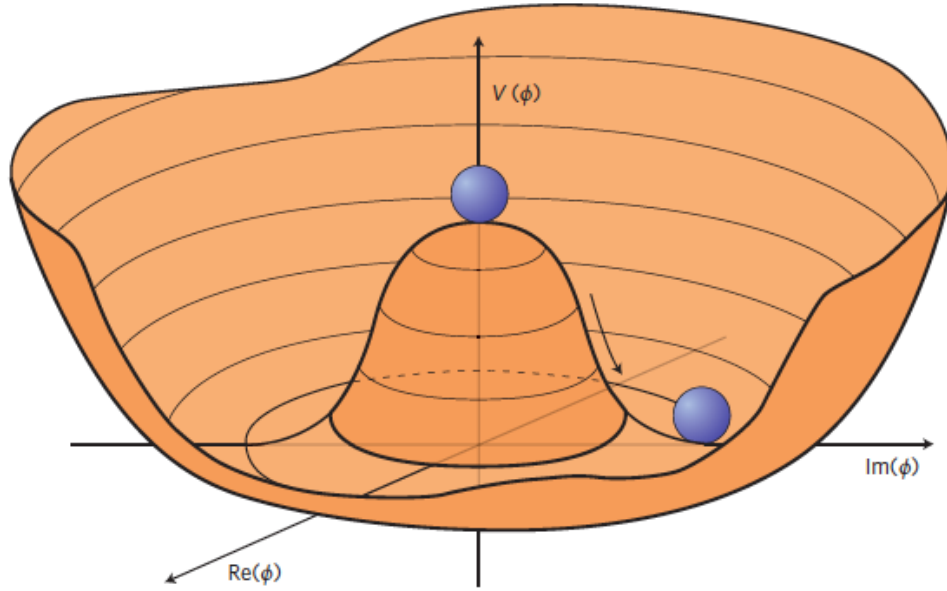


Figure 1.4: The potential term in the Lagrangian of the Higgs field has a minimum value that is centered v , a phenomenon which is often referred to as symmetry breaking because it breaks the $U(1)$ global symmetry inherent in the Higgs Lagrangian. The physical significance of this point is that it corresponds to a non-zero vacuum expectation value.

There are five basic Feynman diagrams for interactions associated with the Higgs [Fig. 1.6]. Two of these diagrams correspond to the Higgs self-interactions, one diagram corresponds to the previously mentioned Yukawa couplings, and two diagrams describe the Higgs coupling to W/Z bosons that are responsible for restoring unitarity to WW scattering.

Because of the Higgs bosons mass-proportional coupling, the leading production mechanism of the Higgs boson at the LHC is gluon-gluon fusion through a top quark loop. Careful examination of the di-photon and 4-lepton mass spectrums led to the observation of the Higgs boson in 2012. A bump can be seen clearly around the measured mass of the Higgs boson at approximately 125 GeV [Fig. 1.5].

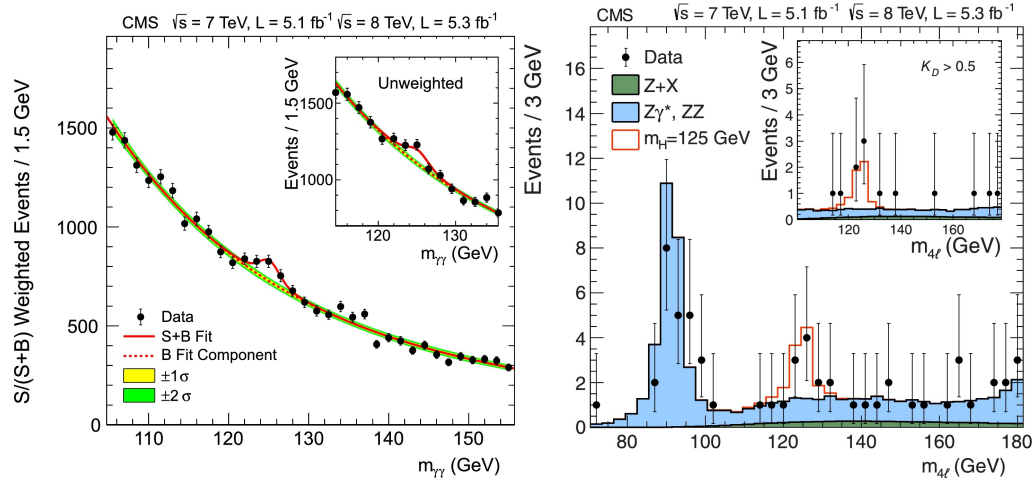


Figure 1.5: Invariant mass distributions from the Higgs boson discovery [23]

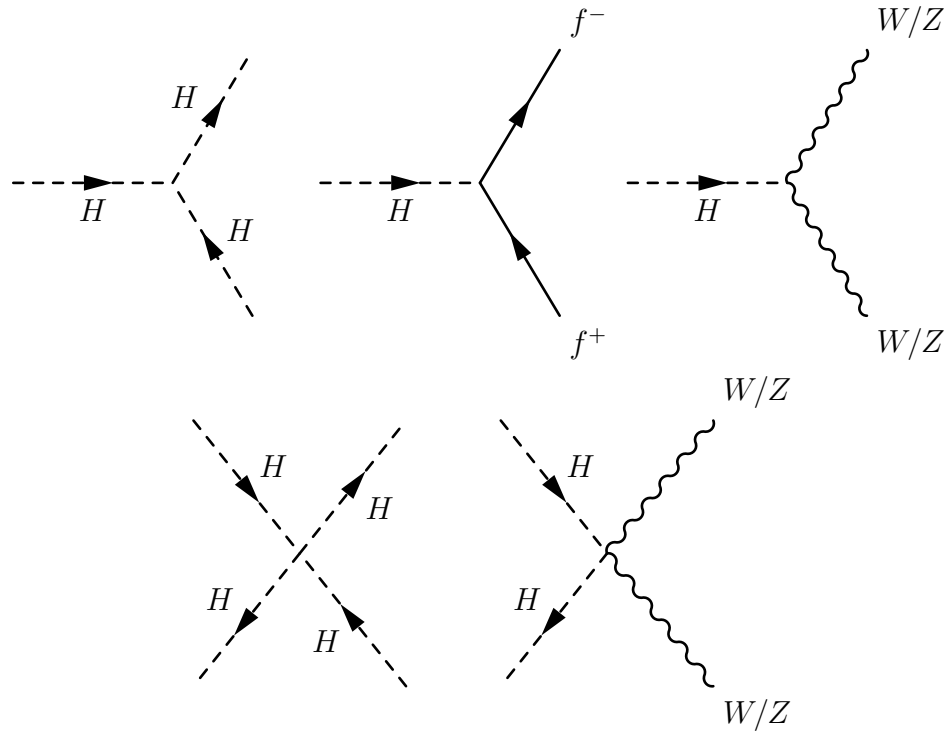


Figure 1.6: The Higgs boson mediated interactions of the Standard Model.

1.5 The Neutrino Sector

The "electron neutrino", ν_e , is called such because it is produced in charged-current weak interactions involving an electron. The muon and tau neutrinos, ν_μ and ν_τ , respectively, are named similarly for their interactions involving muons and taus, respectively. Early neutrino experiments sought to gain understanding of the sector by probing high energy neutrinos produced from rare solar fusion events, such as ${}^8_5\text{B} \rightarrow {}^8_4\text{B} \ e^- + e^+ + \nu_e$. These initial experiments reported less interactions than theoretical calculations predicted and the best explanation was provided through Bruno Pontecorvo's theory of *neutrino oscillation* [24]. This theory postulated that the electron, muon, and tau neutrinos are composites of mass eigenstates ν_1, ν_2, ν_3 and therefore oscillate between different neutrino flavors as they propagate through space. The electron, muon, and tau neutrinos can be composed as a product of the Pontecorvo–Maki–Nakagawa–Sakata (PMNS) matrix with the true mass eigenstates [25]:

$$\begin{bmatrix} \nu_e \\ \nu_\mu \\ \nu_\tau \end{bmatrix} = \begin{bmatrix} U_{e1} & U_{e2} & U_{e3} \\ U_{\mu 1} & U_{\mu 2} & U_{\mu 3} \\ U_{\tau 1} & U_{\tau 2} & U_{\tau 3} \end{bmatrix} \begin{bmatrix} \nu_1 \\ \nu_2 \\ \nu_3 \end{bmatrix}. \quad (1.22)$$

Evidence from experiments and cosmological data constrain the sum of the neutrino masses to be less than 1 eV, however, such oscillations imply that no neutrino is entirely massless. In practice the mixing of neutrinos 1 and 3 is small, and so the oscillations between neutrinos 1 and 2 can be approximated by a simpler pair-wise mixing [26]:

$$\begin{bmatrix} \nu_\alpha \\ \nu_\beta \end{bmatrix} = \begin{bmatrix} \cos \theta & \sin \theta \\ -\sin \theta & \cos \theta \end{bmatrix} \begin{bmatrix} \nu_i \\ \nu_j \end{bmatrix}, \quad (1.23)$$

which gives the probability $P_{\alpha \rightarrow \beta}$ of a neutrino ν_α with energy E to oscillate into a

neutrino ν_β ($\beta \neq \alpha$) after traversing a distance of L

$$P_{\alpha \rightarrow \beta, \beta \neq \alpha} = \sin^2(2\theta) \sin^2\left(\frac{\Delta m_{i,j}^2 L}{4E}\right). \quad (1.24)$$

Because oscillation only depends on the absolute value of the squared mass splittings, it is difficult to realize the entire picture of neutrino oscillations. Still, recent experimental results have reliably determined the following relations [27, 28]

$$m_2^2 - m_1^2 \approx 7.6 \times 10^{-5} \text{ eV}^2 \quad |m_3^2 - m_2^2| \approx 2.3 \times 10^{-3} \text{ eV}^2. \quad (1.25)$$

Lastly, oscillation experiments have measured the mixing angles of the PMNS matrix to be [29, 30]

$$\theta_{1,2} \approx 35^\circ, \theta_{2,3} \approx 45^\circ, \theta_{1,3} \approx 10^\circ. \quad (1.26)$$

1.6 Shortcomings of the Standard Model

The Standard Model is an undeniably successful theory that has been able to accurately describe almost all the critical particle interactions observed in every recorded collider experiment. With the discovery of the Higgs boson in 2012 a steady march towards understanding our known universe was completed, in some sense, as this was the last missing piece of the Standard Model. Moreover, along the way the Standard Model has shown that it is capable of making predictions that are accurate to over ten decimal places and has been verified countless times [31, 32]. A model that successfully unifies the observed effects of the strong, weak, and electromagnetic forces is one of the crowning achievements of human intellect. However, there are some fundamental limitations in terms of what the Standard Model can describe.

1.6.1 Missing/unexplained phenomena

As of yet, the Standard Model is incomplete. Empirically, missing parts include the total omission of the gravitational force and other known phenomena, and theoretically, there are many parts of the model with no explanation. The quantum numbers associated with the fundamental particles, such as the electromagnetic and weak hypercharges, the weak isospin, and the strong color charge do not come from first principles.

Depending on how the accounting is done, up to 25 parameters of the Standard Model are not fixed by any theoretical means [33]. Beyond straightforward questions about quantum numbers, one can also begin to ask more profound questions for which there is no answer – e.g., why are there three generations of leptons? A complete theory of nature would successfully resolve all such tensions.

Moreover, there are additional puzzles for which there is no explanation. The most important among these is the apparent cosmological abundance of *dark matter* and *dark energy* [34]. Strong observational evidence exists for the as of yet undiscovered dark matter/energy that comes from galactic rotation curves, cosmological structure formation, the cosmic microwave background, and gravitational lensing [35]. These are not trivial omissions given that it has been estimated that only 23% of the known universe is composed of the "ordinary" matter in the Standard Model [36].

1.6.2 The hierarchy problem

In addition to the incomplete nature of the Standard Model there is a very puzzling self-inconsistency called *the hierarchy problem* [37]. As was discussed previously, each fermion couples directly to the Higgs boson and obtains a mass through the Yukawa term. According to the formalism of QFT, interactions of this type will yield corrections

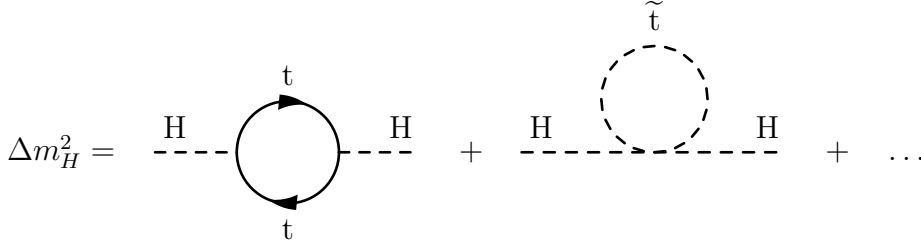


Figure 1.7: The Feynman diagrams Standard Model (left) and SUSY (right) responsible for the largest corrections to the Higgs mass.

to the Higgs mass of the form

$$\Delta m_H^2 = -\frac{|\lambda_f|^2}{8\pi^2} [\Lambda_{UV}^2 + \dots]. \quad (1.27)$$

The larger the particle mass, the larger the coupling λ_f and therefore the larger the term in this correction above. Calculations show that the terms in the summation above require fine-tuning at an order of 38 decimal places to cancel each other out [38]. Thus, unless such a cancellation exists the Higgs mass is expected to diverge, with the greatest contribution coming from the coupling to the top quark. However, observation of the Higgs boson at a mass of roughly 125 GeV contradicts this. One possible explanation for stabilizing of the Higgs boson mass comes from a theory called *Supersymmetry* [Sec. 2.1], which, among other things, introduces a complex scalar for every chiral state of the fermionic particles. Supposing that these additional scalars have a coupling to the Higgs given by λ_S , additional corrections to the Higgs boson are given by [39]

$$\Delta m_H^2 = 2 \times \frac{\lambda_S}{16\pi^2} [\Lambda_{UV}^2 + \dots] \quad (1.28)$$

Therefore, $\Delta m_H^2 \rightarrow 0$ as $\lambda_S \rightarrow |\lambda_f|^2$. Broken symmetries in many models of supersymmetry can result in only a partial cancellation of these masses. Among these scenarios, those limiting the amount of fine-tuning required to stabilize the Higgs are referred to as *natural* [40].

Chapter 2

Supersymmetry

2.1 Supersymmetry

SUSY introduces an exchange operator which maps bosons and the chiral states of fermions in the Standard Model onto fermionic and bosonic superpartners, respectively. In addition to helping alleviate the hierarchy problem, as previously shown, in many SUSY scenarios the lightest SUSY particle (LSP) cannot decay and is, therefore, a natural candidate for dark matter. Formally, the symmetry of SUSY introduces the operation shown below [41]

$$Q|\text{Boson}\rangle = |\text{Fermion}\rangle, \quad Q|\text{Fermion}\rangle = |\text{Boson}\rangle. \quad (2.1)$$

The generators of the SUSY algebra, Q , and its conjugate \bar{Q} are nominally given an explicit representation through *Weyl spinors* [42]. The corresponding algebra is given by

$$\{Q_\alpha, Q_\beta\} = \{\bar{Q}_{\dot{\alpha}}, \bar{Q}_{\dot{\beta}}\} = 0, \quad (2.2)$$

$$\{Q_\alpha, \bar{Q}_{\dot{\beta}}\} = 2\sigma_{\alpha\dot{\beta}}^\mu P_\mu, \quad (2.3)$$

$$[Q_\alpha, P_\beta] = 0, \quad (2.4)$$

where $P^\mu = i\partial^\mu$ is the usual momentum generator.

Accordingly, an explicit representation of the generators can be selected, much like the Gell-Mann matrix representation of the QCD transformation generators:

$$Q_\alpha = \frac{\partial}{\partial\theta^\alpha} - i\sigma_{\alpha\dot{\beta}}^\mu \bar{\theta}^{\dot{\beta}} \partial_\mu, \quad (2.5)$$

$$\bar{Q}_\alpha = \frac{\partial}{\partial \bar{\theta}^{\dot{\alpha}}} - i\theta^\beta \sigma_{\beta\dot{\alpha}}^\mu \partial_\mu, \quad (2.6)$$

where θ and $\bar{\theta}$ are anti-commuting "Grassman" variables that satisfy $\{\theta, \theta\} = 0$, $\{\bar{\theta}, \bar{\theta}\} = 0$.

A finite SUSY transformation operator, $U(x)$, follows the form

$$U(x) = \exp \left[i \left(\theta Q + \bar{Q} \bar{\theta} - x_\mu P^\mu \right) \right]. \quad (2.7)$$

2.2 SUSY Phenomenology

The minimal supersymmetric model (MSSM) is a SUSY theory that introduces the smallest number of parameters required to be consistent with all experimental observations of the Standard Model [43, 44, 45]. In the MSSM SUSY particles take on a value of +1, and Standard Model particles take on a value of -1 under the R-parity operator:

$$P_R = (-1)^{3B+L+2s}, \quad (2.8)$$

where s is spin, B is baryon number, and L is lepton number. The MSSM is an R-parity conserving theory which stabilizes the LSP against decay and thereby provides a candidate for dark matter. In addition, the MSSM can potentially solve the hierarchy problem, as described previously, and also provides a schema that unifies the strong, weak, and electromagnetic forces at high energy, a *Grand Unified Theory* (GUT) [46]. The Standard Model by itself is not a GUT as there is no known energy scale where the coupling constants merge to a single value [Fig. 2.1].

SUSY particles such as the stop and gluino can be pair produced in pp collisions, $pp \rightarrow \tilde{g}\tilde{g}/\tilde{t}\tilde{t}$, through strong interactions and are expected to have large production

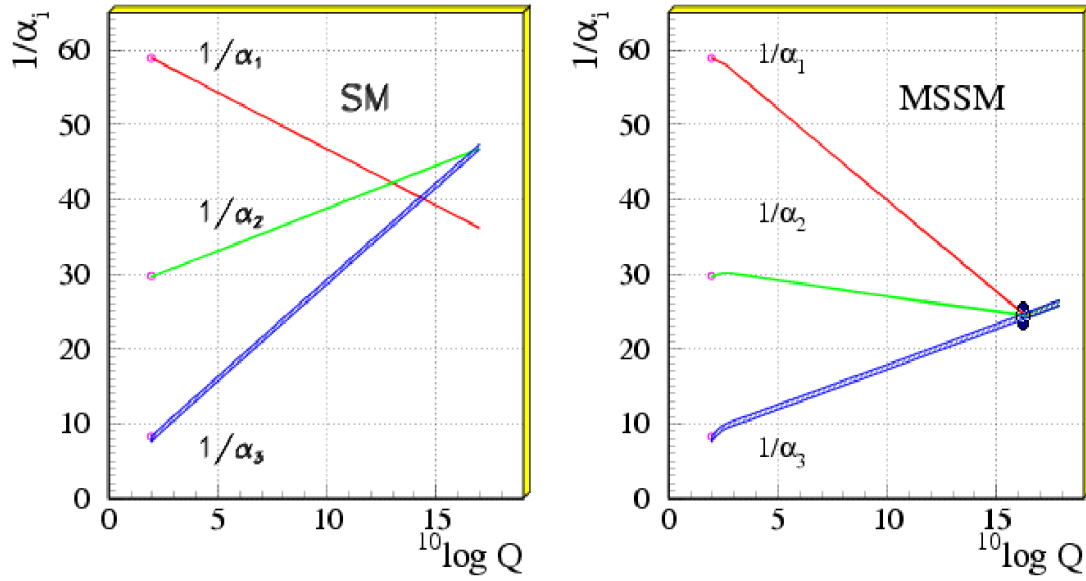


Figure 2.1: Within the SM there is no scale for which all coupling constants converge, however in MSSM such a point can exist [47].

Table 2.1: Particles and superpartners in the MSSM

SM Particle Type	Corresponding SUSY Particle	Symbol	Spin
Quark	Squark	\tilde{q}	0
Lepton	Slepton	$\tilde{\ell}$	0
Neutrino	Sneutrino	$\tilde{\nu}$	1/2
Gluon	Gluino	\tilde{g}	1/2
γ, Z, H	Neutralino	$\tilde{\chi}_1^{[0-4]}$	1/2
Higgs/W	Chargino	$\tilde{\chi}_{[1-2]}^{\pm}$	1/2

cross sections, relative to their weakly produced counterparts. Still, the production cross section for most SUSY processes remains quite small in comparison to typical processes of the Standard Model [Fig. 2.3, Fig. 3.10]. In most allowable phase space within the MSSM or other R-parity conserving SUSY, gluinos typically decay to a stop and a top, $\tilde{g} \rightarrow t\tilde{t}$ and stops in turn often decay to a top and LSP, $\tilde{t} \rightarrow t\tilde{\chi}_1^0$ [48, 49].

The LSPs from the stop decay chain do not interact with ordinary matter and therefore escape detection, which results in a final state of two or four top quarks and significant missing energy. To this date, no experiment has found evidence for deviations from Standard Model expectations in the multi-top plus missing energy final states. Other more exotic R-parity conserving variants of stop and gluino pair production have also been probed by considering additional gluino ($\tilde{g} \rightarrow qq\tilde{\chi}_1^0, \dots$) or stop ($\tilde{t} \rightarrow qW\tilde{\chi}_1^0, \dots$) decay chains [50].

Null results for strongly produced SUSY have motivated more difficult searches for SUSY particles such as charginos, neutralinos, and sleptons. Chargino and neutralinos are weakly pair produced at the LHC via $pp \rightarrow \tilde{\chi}_1^\pm \tilde{\chi}_2^0 / \tilde{\chi}_1^\pm \tilde{\chi}_1^\pm$. The chargino then decays through $\tilde{\chi}_1^\pm \rightarrow \tilde{\ell}^\pm \nu / \ell \tilde{\nu}$ or $\tilde{\chi}_1^\pm \rightarrow W^\pm \tilde{\chi}_1^0$, whereas neutralinos decay through $\tilde{\chi}_2^0 \rightarrow \tilde{\ell}^\pm \tilde{\ell}^\mp$ or $\tilde{\chi}_2^0 \rightarrow H/Z + \tilde{\chi}_1^0$ [51, 52]. The neutralino/chargino decay branching ratios vary as a function of the mother mass and the daughter slepton mass.

All chargino and neutralino decay topologies can result in multi-lepton final states with additional missing energy. Note, in some SUSY phase space the intermediate boson can be off-shell which results in soft-lepton(s) in the final state. As of yet there has also been no experimental excess for significant deviation from Standard Model expectations in these final states [53].

Direct slepton pair production is another SUSY topology that has garnered attention from accelerator experiments. Searches for pair production of sleptons carried out by the LHC found no excess and yielded the most sensitive limits for pair production of the

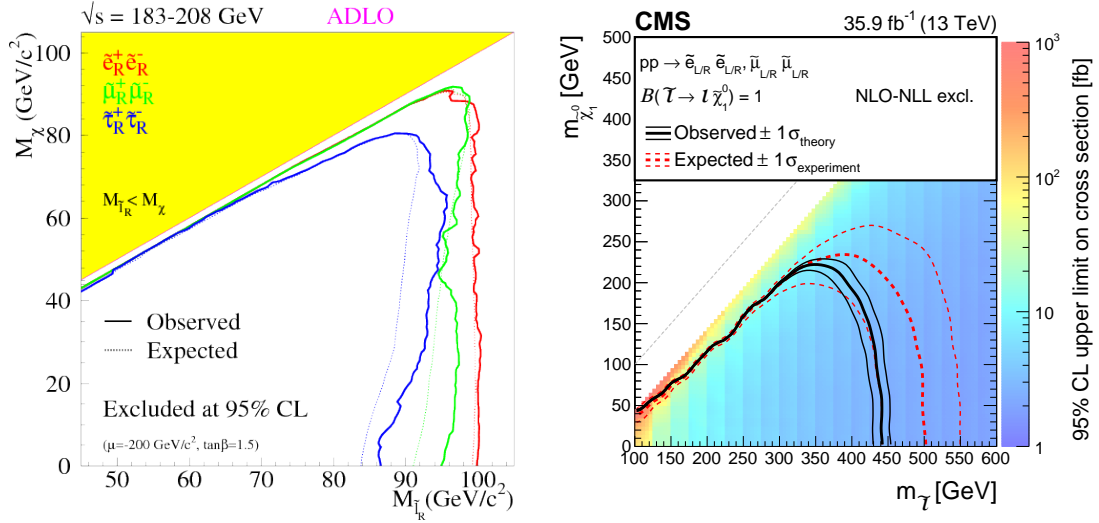


Figure 2.2: Left Panel: Final 95 % confidence level exclusion limits for slepton production by the LEP experiment [56]. Right Panel: Latest results from the CMS experiment for smuon and selectron production which supersede those produced by LEP [54]. The LEP experiment yielded very sensitive results for stau for production which excluded the difficult right-handed scenario up to $m(\tilde{\tau}_R) = 90 \text{ GeV}$.

superpartners of the electron and muon, the selectron and smuon, respectively, to date [54, 55][Fig. 2.2]. Searches for the superpartner of the tau lepton, the stau, have a more complicated history.

2.3 Searching for Staus

The stau is expected to be the lightest slepton in many MSSM models [57]. Moreover, there exist supersymmetric models with early universe neutralino coannihilation capable of explaining the observed DM relic density with a next-to-lightest supersymmetric stau [58, 59]. In these scenarios, the stau is relatively light and therefore has a greater likelihood to be accessible at the LHC. Moreover, the stau can have a small mass splitting with the LSP which would result in the stau having a finite lifetime.

To date the most sensitive search for direct stau pair production comes from the Large

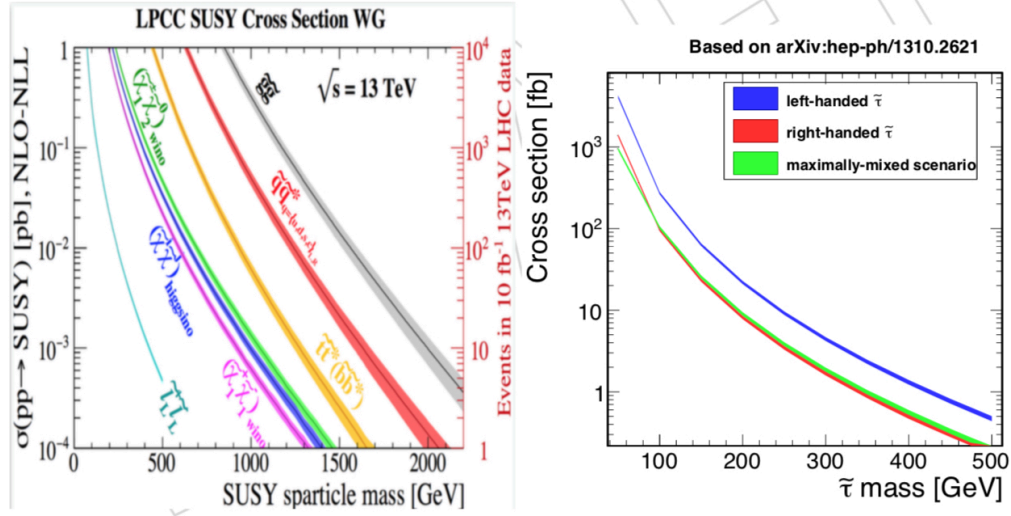


Figure 2.3: On the left: For pp collisions at $\sqrt{s} = 13$ TeV the NLO-NLL cross sections for every commonly searched for SUSY particle is displayed. Note the diminished size of direct slepton production with respect to all other processes. On the right: The stau production cross section is shown for three pair production scenarios in $\sqrt{s} = 13$ TeV pp collisions, exclusive left-handed, exclusive right-handed, and maximally mixed left/right-hand production.

Electron-Positron (LEP) Collider which was able to exclude the difficult right handed stau production scenario up to a mass of $m(\tilde{\tau}_R) = 90$ GeV. Both ATLAS and CMS have been unable to exclude a single point in phase space for this scenario [60, 61].

LEP was the most powerful lepton accelerator ever built and reached center-of-mass collision energies of up to approximately 209 GeV. Because of the cleaner electron-positron collision environment, LEP achieved higher signal efficiencies than the LHC while maintaining an acceptable background yield. At these low masses the analyses at the LHC struggle to separate signal because of insufficient genuine missing transverse momentum. However, the LHC can probe higher stau masses than were accessible at LEP, but the steeply falling cross section limits the sensitivity of such searches [Fig. 2.3].

This thesis presents an analysis ("The analysis", "The Run-II analysis") which builds upon the first CMS search for stau pair production by including the data collected in 2017 by the CMS detector and by improving upon the previous analysis design. The first

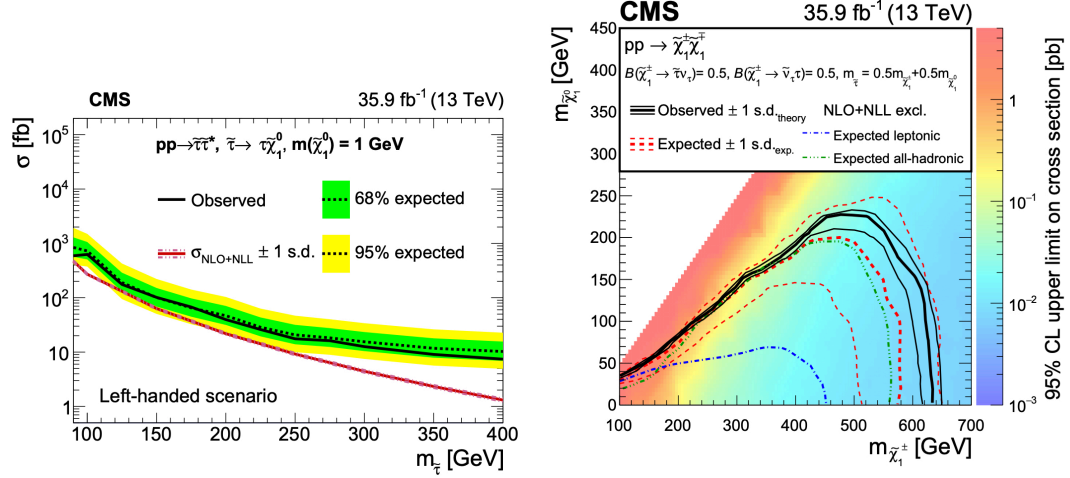


Figure 2.4: The first experimental results searching for SUSY in the ditau plus missing transverse energy final state with the CMS detector. The analysis considered approximately 36 fb^{-1} of collected data [61]. This analysis can be compared to the 8 TeV result produced by ATLAS [60]. On the left: expected and observed 95 % upper exclusion limit on the direct stau production cross section. Note that the shown limits are for the more favorable left-handed production scenario. On the right: Similar results from the same analysis for direct chargino production. From side-by-side comparison one may draw the conclusion that direct stau production is significantly harder to detect than chargino production at the LHC.

analysis carried out at the LHC had limited sensitivity to direct stau production and motivated this the timely completion of this work [Fig. 2.4].

The analysis sensitivity depends on how the observed stau states $(\tilde{\tau}_1, \tilde{\tau}_2)$ are composed from the underlying chiral eigenstates $(\tilde{\tau}_L, \tilde{\tau}_R)$. The cross section for pair production and the decay kinematics are both a function of the mixing between these chiral states. The analysis makes a simplifying assumption by only considering independent and mass degenerate pure left and right-handed production.

The handedness of the scenarios results in polarization being transferred to the tau. When the tau decays the polarization produces differences in acceptance, as right-handed taus transfer more momentum to the visible leg of the decay. In either case, the full stau decay chain often results in noticeable energy transfer to invisible particles.

Due to these missing particles the reconstructed events will have a substantial trans-

verse momentum imbalance. Direct computation of the total missing energy in the underlying event is impossible because the momentum distributed to the interacting partons is unknown in the lab frame [Sec. 3.1.2]. Note, however, that the total transverse momentum is always equal to zero at the collision point in all frames of reference. Thus, this explains why the most critical variable in this search for new physics at the LHC is the missing transverse momentum (p_T^{miss}) [Sec. 4.4].

Chapter 3

The LHC and the CMS Experiment

3.1 The Large Hadron Collider

The Large Hadron Collider is the largest machine built in human history [62]. The particle accelerator consists of a 27 km ring containing 1232 sequentially placed 15-meter-long superconducting magnets capable of operating at up to 8.36 Tesla [Fig. 3.1]. More than 10,000 scientists collaborated in the construction of the apparatus and in running the primary experiments located thereupon – ALICE, ATLAS, CMS and LHCb [63, 64, 65, 66]. The headquarters of the entire operation is the main campus of the European Organization for Nuclear Research (CERN). Since the beginning of LHC operation in 2008, the accelerator has steadily increased its performance and capabilities. Now, the LHC successfully produces proton-proton collisions at a previously unprecedented center-of-mass energy of 13 TeV while maintaining instantaneous luminosities of $10^{34} \text{ cm}^{-2} \text{ s}^{-1}$ which corresponds to about one billion collisions per second.

Both ATLAS and CMS are general purpose experiments that have made outstanding contributions to science through the discovery of the Higgs boson [Sec. 1.4]. In addition to finding the Higgs boson and searching for SUSY, these experiments also test the validity of exotic new theories, such as extra-dimensions. Also, there is an ongoing campaign to make extremely precise measurements of Standard Model quantities. Moreover, the accelerator also collides heavy-ions, which ALICE specializes in investigating, allowing these experiments to study quark-gluon plasma and other exotic matter states. Experiments at the LHC have also made the first observation of jet quenching [67]. Lastly, LHCb is a specialized experiment which makes precision measurements of b and c -hadron properties. Together, the four major collaborations have produced thousands of publications investigating the nature of physics across the TeV energy scale.

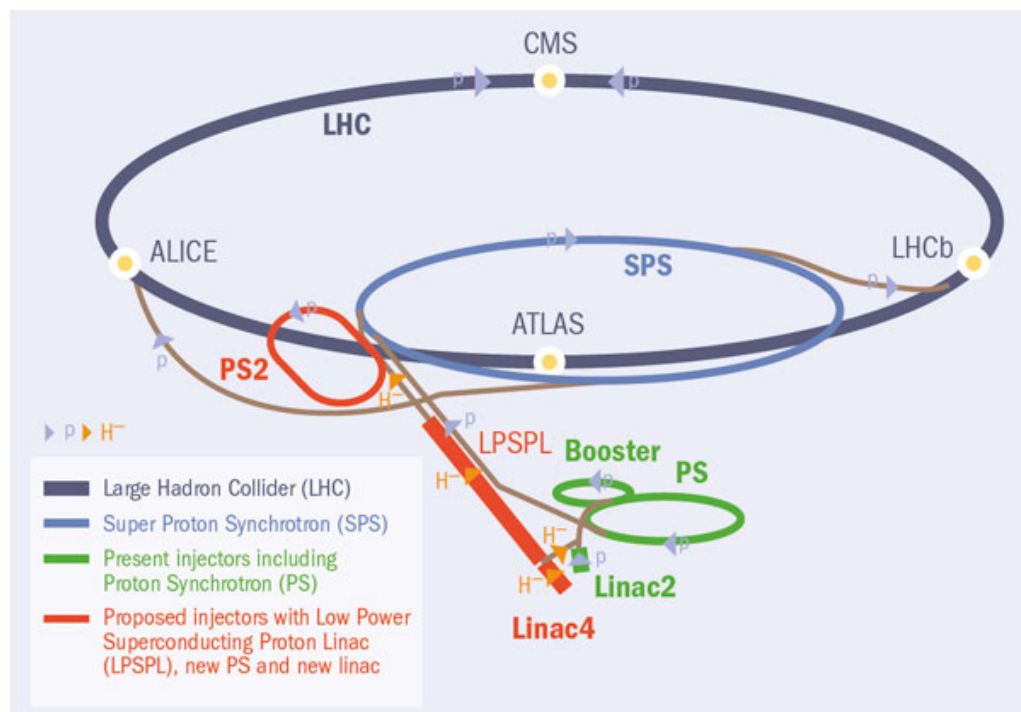


Figure 3.1: A graphical schematic of the CERN accelerator complex. Multiple small accelerator rings such as the booster and Proton Synchrotron (PS) and Super Proton Synchrotron (SPS) progressively increase the proton bunch energy until the bunches are fed into the primary LHC tunnel.

3.1.1 Proton-proton physics

The instantaneous luminosity, \mathcal{L} , is the expected number of detected events per unit time and cross section [68, 69]. Integrating the luminosity over time gives the number of expected inelastic collisions, or *events*

$$N_{evt}^{inel} = \sigma_{inel} \int \mathcal{L} dt, \quad (3.1)$$

where σ_{inel} is the inelastic pp cross section.

When colliding protons at the LHC the instantaneous luminosity is given by [70, 71]:

$$\mathcal{L} = \frac{\gamma f k_B N_p^2}{4\pi\epsilon_n\beta^*} F, \quad (3.2)$$

where γ is the Lorentz factor, f is the revolution frequency (11.245 kHz at the LHC), k_B is the number of bunches, N_p is the number of protons/bunch, ϵ_n is the normalized transverse emittance (with a design value of 3.75 μm), β^* is the betatron function on impact, and F is the reduction factor due to the crossing angle.

The number of expected interactions per bunch-crossing, N_{PU} , is an important quantity that is a function of the luminosity, pp cross section, revolution frequency and number of bunches [72] :

$$N_{PU} = \frac{\sigma_{inel}\mathcal{L}}{fk_B} \quad (3.3)$$

The equation for N_{PU} illustrates that increasing the rate of data collection is challenging, because most parameters related to luminosity are fixed by experimental design. Therefore, the LHC may only increase luminosity by increasing the number of protons in a given bunch, decreasing the width of the bunch crossing, or increasing the number of bunches in the LHC at any given time. The first two create more unwanted *pile-up*

(PU) interactions associated with hard scattering events, whereas the second increases detector noise called *out-of-time* pile-up [73].

As the LHC experiments have matured over time, both the rate of bunch crossing and the size of bunches delivered by the LHC have steadily increased [Fig. 3.2].

The majority of collisions at the LHC are uninteresting, a typical event of interest, or a *selected event*, at the LHC consists of one relatively rare hard pp interaction and an average of N_{PU} additional soft pile-up interactions. Understanding and mitigating pile-up effects within the CMS detector has received a great deal of attention throughout the lifetime of the experiment. With the beam-line parameters selected for the LHC's current 13 TeV operation, the LHC averaged roughly 50 pile-up interactions per event in data collected from 2016-18.

3.1.2 Parton distribution functions

There is another challenge beyond the major difficulties introduced by pile-up effects and QCD interactions at pp accelerators. The bound state of a proton consists three *valance quarks* (uud) and complicated QCD binding effects that distributes energy to *sea quarks* and gluons [74].

Modeling the proton as an effective sea of strongly interacting parts, *partons*, with their momenta distributed according to *parton distribution functions* produces a description consistent with observation. The PDFs have been measured empirically by electron-proton colliding experiments such as HERA and ZEUS [75], [76] as well as by CMS and ATLAS [77]. The measurements are made by experiments after decomposing the differential cross section into *structure functions* that allow for accurate parameterization of the parton distribution functions from data [Fig. 3.3].

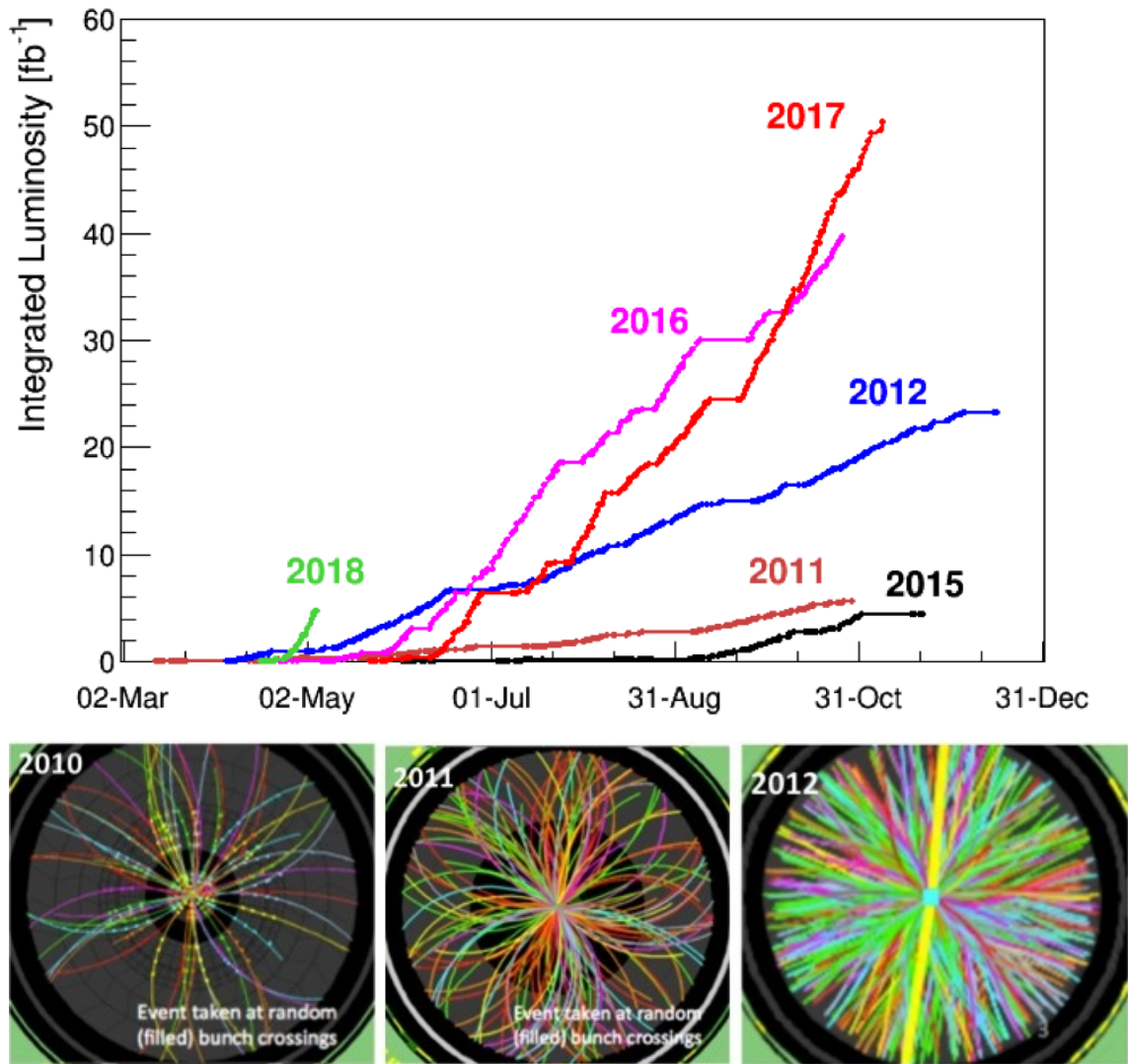


Figure 3.2: Upper Panel: Luminosity collected as a function of time by CMS, up until May 2018. Lower Panel: Transverse slice of single collision events sampled by the CMS detector between 2010-2012. One can see that the increased luminosity results in a significantly more active environment.

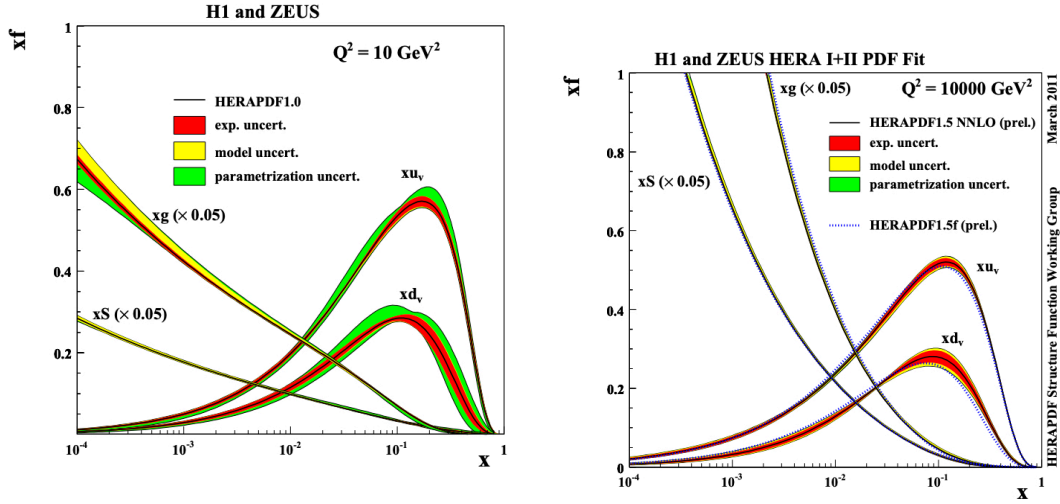
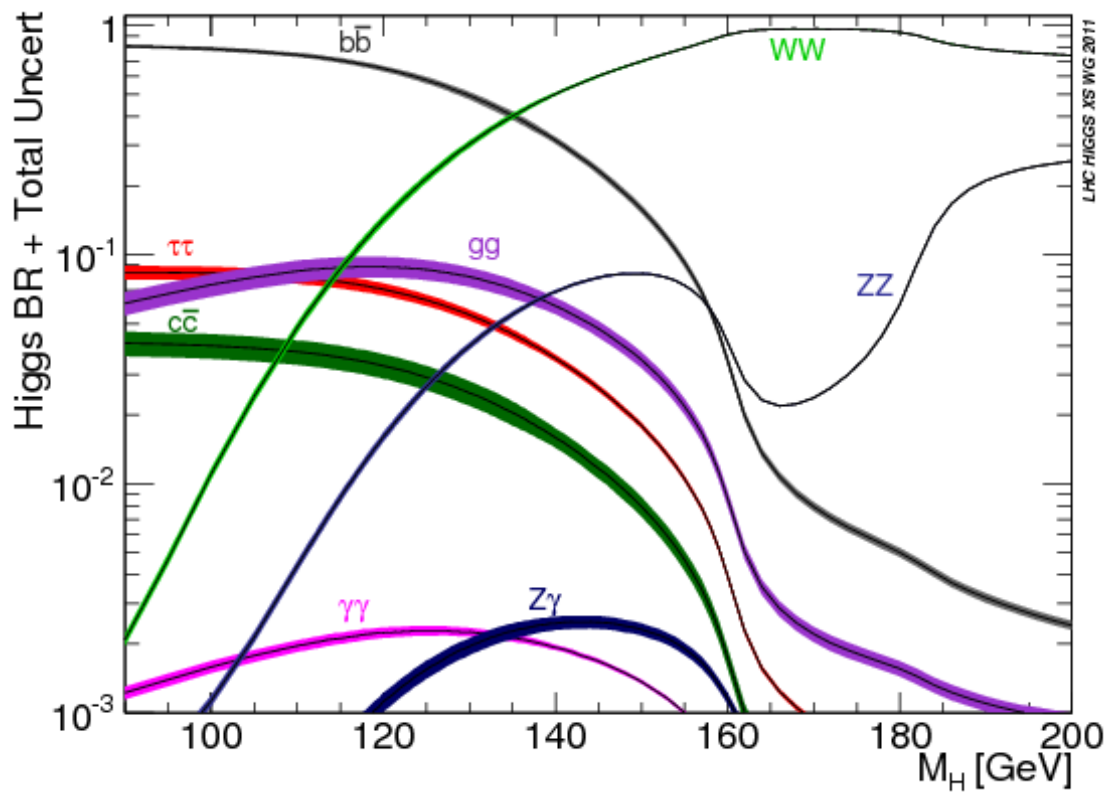


Figure 3.3: The parton distribution functions as measured for a resolution scale $Q^2 = 10, 10000 \text{ GeV}^2$ respectively. The parton distributions are plotted as a longitudinal momentum fraction x versus the parton distribution function value f times the fractional value x . Note, at higher momenta the total fraction of the proton energy distributed to gluon and strange quark states increases. [78]

3.1.3 LHC experimental goals : before operation

Before operation the principal experimental goal of the LHC was to discover or exclude the Higgs boson across as wide a mass range as possible, with searches for physics beyond the Standard Model (BSM) being the next highest priority. Before LHC operation the LEP accelerator excluded the existence of the Higgs boson up to a mass of approximately 115 GeV, which subsequently had a substantial impact on the allowable phase space for Higgs boson decay and the optimal detector design. The general purpose detectors at the LHC, ATLAS and CMS, were optimized with this viewpoint. All optimizations were made with careful consideration of the strong dependence of the hypothetical Higgs boson decay topology versus mass [Fig. 3.4].

For a Higgs boson with mass $M_H \in [115-130] \text{ GeV}$ the leading discovery sensitivity was expected to come from the $\gamma\gamma$ channel. The most substantial Higgs boson decay branching fraction in this mass window belongs $H \rightarrow b\bar{b}$, but observation $b\bar{b}$ is more



H

Figure 3.4: The Higgs boson decay branching ratios plotted versus the mass of the Higgs boson, M_H [79].

difficult because of large QCD to b -quark jet backgrounds. The QCD background consists of b -quarks and light quarks misidentified as jets coming from the genuine decay of a b -quark. Moreover, the QCD background consists of two such jets that have been identified as b -quarks with an invariant mass near that of the hypothetical Higgs boson under consideration.

By similar arguments, the gg and $\tau\tau$ decay channels are also quite difficult to observe, and so the relatively clean decay $H \rightarrow \gamma\gamma$ yields the largest sensitivity. This channel is not without backgrounds and so sensitivity is driven largely by how accurately the mass of the decaying Higgs boson can be reconstructed from the two photons. The next most sensitive decay mode is $H \rightarrow ZZ \rightarrow 4\ell$ which has a slightly smaller effective branching ratio in this mass range but offers an exceedingly clean event topology.

These considerations in the design phase emphasized the importance of di-photon mass resolution, which in turn elevated the importance energy resolution of the electromagnetic calorimeter for the ATLAS and CMS experiments.

The branching ratio for $H \rightarrow ZZ \rightarrow 4\ell$ grows relative to $H \rightarrow \gamma\gamma$ as a function of the mass and begins to drive sensitivity for $M_H \in [130-150]$ GeV. Few Standard Model processes can produce four genuine leptons and so $Z^*\gamma/ZZ$ constitute the dominant backgrounds. The decay $ZZ \rightarrow 4\ell$ yields a distinct mass-peak in the four lepton mass distribution which provides natural discrimination from backgrounds.

Highly efficient muon detection and reconstruction became an important property for both experiments. These general considerations all proved correct as the di-photon and 4-lepton final states played the most substantial roles in the discovery of the Higgs [Fig 1.5].

Lastly, it should be mentioned that in the higher mass regime $m_H > 150$ GeV the decay mode $H \rightarrow WW$ becomes dominant. In this case, the leptonic decay modes of the W are used to probe for the Higgs boson. This final state is be more complicated

because it contains hard neutrino(s) which pass through the detector without detection [Sec. 3.1.1]. In this case the relevant quantity under consideration is the missing transverse momentum, p_T^{miss} , defined as :

$$\vec{p}_T^{miss} = -\sum_{particles,i} \vec{p}_{T,i}, \quad (3.4)$$

where the sum is over the transverse momentum, $p_{Ti} = \sqrt{p_x^2 + p_y^2}$, associated with the i th detected particle. In this Higgs boson mass scenario, it is the p_T^{miss} resolution that becomes the dominant detector consideration. Moreover, p_T^{miss} resolution is a significant quantity in many searches for new physics. Optimizing p_T^{miss} resolution is non-trivial as it depends on every reconstruction effect of the detector. For these reasons p_T^{miss} has been the focus of many studies by the CMS experiment dating back to the experiments inception [80].

3.1.4 LHC future goals

Moving into the future, with the discovery of the Higgs in hand, the objective of the primary detectors at the LHC are:

- 1) Further study of the Higgs boson (self and second generation couplings).
- 2) Continue searches for SUSY, extra dimensions, and other exotic new physics.
- 3) Contribute to understanding heavy-ion collisions.
- 4) Better the general understanding of TeV-scale hadron physics.

3.2 The Compact Muon Solenoid Experiment

The CMS experiment is a cylindrical apparatus with length 21.6 m and radius 15 m² and a total weight of over 14,000 tonnes. The CMS coordinate system is constructed with the x-axis pointing inwards towards the centroid, a y-axis points vertically upwards, and the z-axis pointing along the beam-line [81]. It can be valuable to work in azimuthal and polar angular variables, ϕ, θ , respectively. Often the polar coordinate is replaced with an approximately Lorentz invariant function of θ called pseudo-rapidity:

$$\eta = -\ln \left[\tan \frac{\theta}{2} \right]. \quad (3.5)$$

One last important quantity relating to angular distributions is the angular separation, $\Delta R = \sqrt{(\Delta\phi)^2 + (\Delta\eta)^2}$.

Selecting $z=0$ to be at the center of the CMS detector, the central detection region ($|\eta| \leq 1.44$) is cylindrical along the beam-axis, whereas the forward regions ($|\eta| > 1.44$) are composed of disc-shaped "end-caps" oriented perpendicular to the beam-line [Fig. 3.5]. The main components of the central detector region are a pair of silicon trackers, a lead tungstate electromagnetic calorimeter, a brass-scintillator hadronic calorimeter, a steel-scintillator hadronic calorimeter, muon chambers, and a 3.8 Tesla superconducting magnet that encloses the tracker and calorimeters [65]. In the forward detector regions, the detector also includes a silicon pre-shower layer.

3.2.1 The tracking system

The CMS tracker lies in the innermost region of the detector and is responsible for reconstructing the trajectories of charged particles resulting from the underlying pp collisions. When operating at a pile-up rate of approximately 50 interactions per bunch crossing

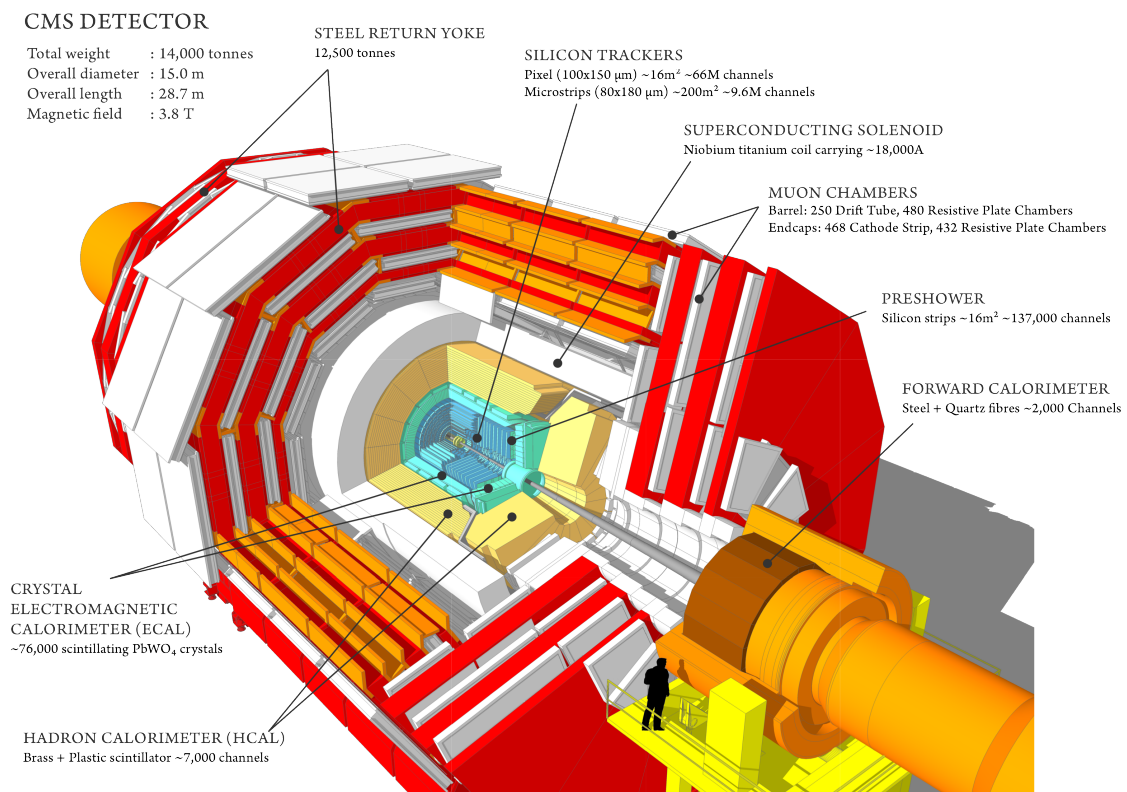


Figure 3.5: Cutaway view of the CMS detector. Labels point to the primary systems of the detector.

an average of approximately 2000 charged particles created from inelastic collisions are expected to traverse through the CMS detector at any given time, as well as a significant number of neutral particles [82]. As a result, after a collision the detector is subject to intense radiation that increases as one moves towards the beam-line center, and so the innermost tracker must be made radiation hard. These considerations led the CMS experiment to adopt a pioneering silicon inner tracking device [83].

This innermost sub-detector of the experiment is the pixel detector, which is responsible for seeding reconstructed tracks and giving accurate track vertexing. The pixel detector is a modular device, composed of many sub-modules read out sections of 100 by 150 μm^2 Si pixels. The original pixel detector used in the 2016 data collection and consisted of three layers at radii of $r=4.4$, 7.3 and 10.2 cm from the beamline center [Fig. 3.6] [84]. The pixel detector has since been upgraded to a four layer device that begins at a radius of 2.9 cm, to further enhance the vertex resolution and implement improved readout chips. New readout chips were necessary to maintain performance in an environment with larger pile-up. The relatively small pixels sizes of the detector were selected for their enhanced radiation hardness and to keep the silicon occupancy rate below one in 500.

In total, the pixel detector is constructed from roughly 1200 modules in the central region and 700 in the forward region. Each module has 16 readout chips that are each responsible for registering hit information recorded in 4,160 pixels that are arranged into a 80 x 26 x 2 structure. Summing these components one may see that the pixel detector consists of over roughly 120 million channels.

Moving further outwards radially the next sub-detector is the silicon strip tracker. Since particle flux falls off as radius squared, from the interaction point, the radiation hardness considerations are relaxed in this detector. At a distance of $20 < r < 55$ cm from the beam-line the tracker consists of modules with a strip length of 10 cm. At

greater radial distances a strip length of 25 cm is selected. Increasing strip length also increases strip capacitance, so that thicker silicon is required to maintain a high signal to noise ratio. Integrating over the ten layers of the silicon strip tracker results in a total of over 15,000 modules.

The effect of silicon radiation damage is also minimized by increasing the potential across the silicon to maintain full depletion or by cooling the modules to a low temperature. To maintain necessary performance all silicon modules inside of the tracker are cooled to as low as -20 C. The mechanical structure necessary to meet these demands results in the distribution of a significant amount of material across the tracker. The standard unit of measurement for the total material in a given space is the radiation length, X_0 , which corresponds to the expected distance through a given material that an electron must traverse to radiate all but $1/e$ of its initial energy. An empirically derived formula for the inverse this quantity is given below for any solid material with an atomic number of Z and a nuclear mass of A [13]

$$X_0 = 716.4 \text{ g cm}^{-2} \frac{A}{Z(Z+1) \ln \frac{287}{\sqrt{Z}}} = 1433 \text{ g cm}^{-2} \frac{A}{Z(Z+1)(11.319 - \ln Z)}. \quad (3.6)$$

The tracker material budget is maximized around $|\eta| \approx 1.8$, where a charged particle may pass through up to $1.8 X_0$ of material when traversing the entirety of a tracker [Fig. 3.7]. Overall, the tracker averages energy resolution below $1 - 2\%$ for centrally produced muons between 10-200 GeV. In the higher momentum range, $p_T(\mu) \gtrsim 200 \text{ GeV}$, the muon chamber resolution is the dominant uncertainty, whereas at lower momentum multiple scattering dominates. In some regions of phase-space, such as the very forward region, the expected energy resolution is degraded and reaches values as high as 10%.

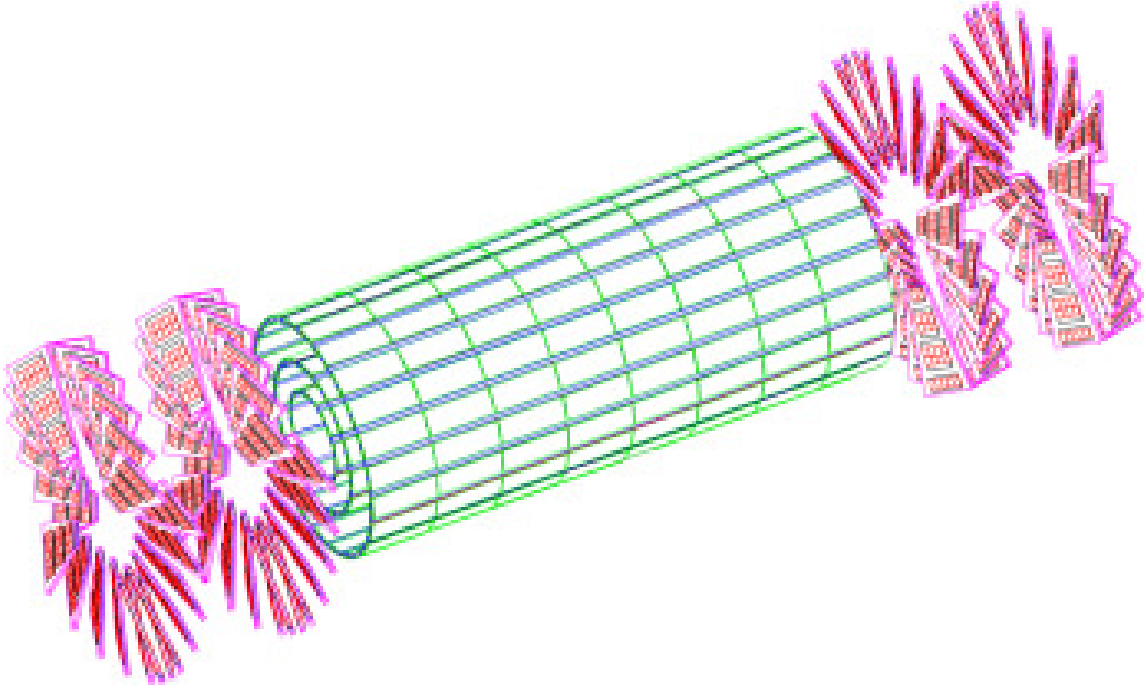


Figure 3.6: Schematic of the CMS pixel detector [84].

3.2.2 The electromagnetic calorimeter

The calorimetric system of the CMS detector consists of a *hadronic calorimeter* (HCAL) and a *electromagnetic calorimeter* (ECAL). The ECAL follows the design structure of the tracker, wherein the central component is cylindrical with disc-shaped endcaps [Fig. 3.8]. The ECAL construction aims for radiation hardness, readout speed and hermeticity and therefore the chosen construction material is a lead tungstate (PbWO_4). This dense scintillating material has a short radiation length, $X_0 = .89$ cm, and a small Moliere radius, $r_0 = 2.2$ cm. The low gain of the lead tungstate requires readout by avalanche photodiodes attached to the ends of the crystals. In the forward region, a thin layer of *preshower* silicon strips precedes the calorimetry.

The primary downside of the ECAL construction lies in the difficulty of crystal procurement and a lack of granularity along the crystals longitudinal axis, as each crystal in the central (forward) ECAL has dimensions of 22×22 (28×28) $\times 230$ mm³. However,

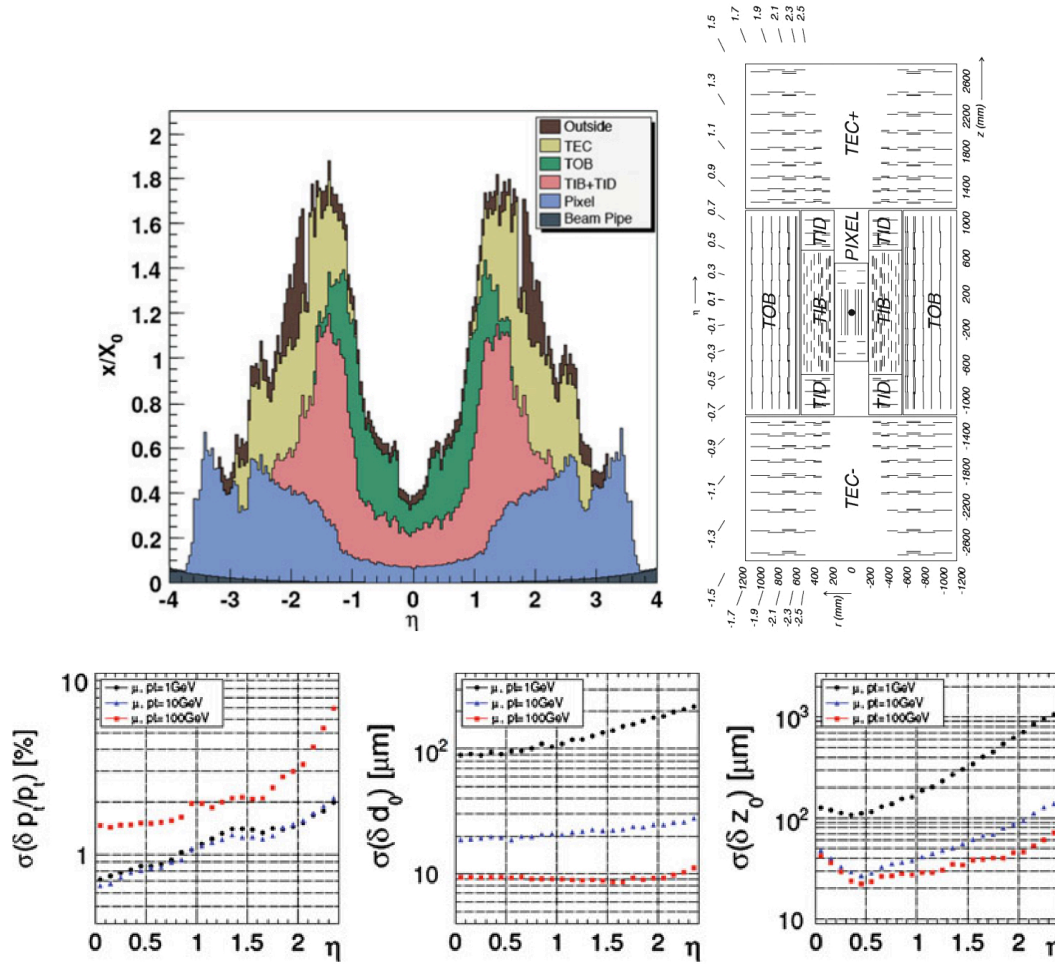


Figure 3.7: The barrel region tracker is divided into two parts: a TIB (Tracker Inner Barrel) and a TOB (Tracker Outer Barrel). The endcaps are then divided into the TEC (Tracker End Cap) and TID (Tracker Inner Disks). Upper Panel: The material budget and tracker schematic. Lower Panel: The tracker resolution, transverse, and longitudinal impact parameter are shown left to right for simulated muons of 1, 10 and 100 GeV. [85].

this design is hermetic and in total corresponds to an integrated radiation length of approximately $25.8X_0$ for the ECAL. Additionally, the granularity along the beam axis is quite high, as the angular coverage per crystal in the barrel is approximately 0.0178 by 0.0178 in $\Delta\phi$ by $\Delta\eta$. Finally, the detector offers excellent energy resolution, due to the entire volume of the calorimeter being active material.

The stochastic effect in the relative resolution of an electromagnetic shower is proportional to $1/\sqrt{E}$, whereas readout noise is typically proportional to the total amount of energy deposited. This motivates a functional fit to the resolution in E

$$\left(\frac{\sigma(E)}{E}\right)^2 = \left(\frac{S}{\sqrt{E}}\right)^2 + \left(\frac{N}{E}\right)^2 + C, \quad (3.7)$$

where test beams showed the best fit values for these constants to be $S = 3.63 \pm 0.1$, $N = 124$ MeV, $C = 0.26$. At high energies, the constant term dominates, whereas at low energies the stochastic and noise effects are of increasing import. With resolution at this level of precision, one can naively anticipate that error on the mass measurement for a 125 GeV Higgs decaying to di-photons must at an order of a GeV. The actual measured value in the discovery corresponded to an experimental width of approximately 3 GeV.

3.2.3 The hadronic calorimeter

The HCAL follows after the ECAL and surrounds the ECAL in its entirety. The central physics goal of the HCAL is to resolve energy carried by charged and neutral hadrons as accurately as possible. This resolution is crucial for accurately measuring the energy of each hadronic jet. Designing the HCAL was complicated by the physical constraint that it must fit inside of the solenoid magnet and operate inside the resulting 3.8 T magnetic field.

To have a high likelihood of nuclear interactions the total material budget of the

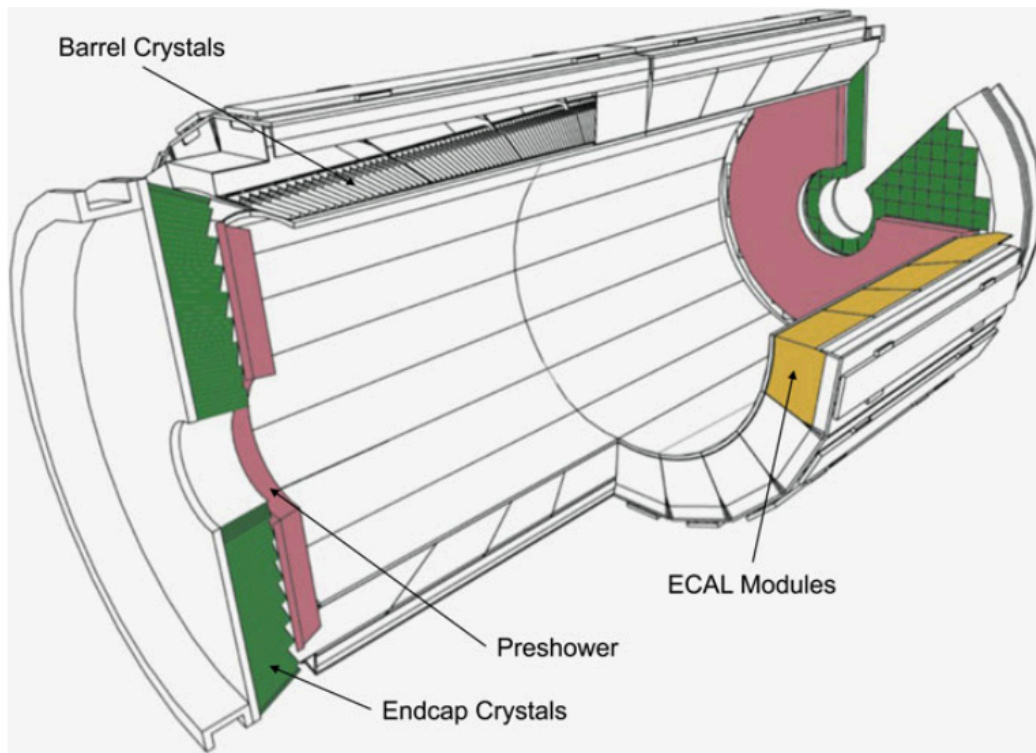


Figure 3.8: Schematic of the electromagnetic calorimeter [85]

HCAL is much higher than that of the ECAL, while the transverse granularity of the barrel is reduced to sectors of $\Delta\phi \times \Delta\eta = 0.087 \times 0.087$. The HCAL is a sampling calorimeter, rather than being fully active as is the ECAL, with scintillators layered between thick brass absorbers. The forward absorbers, $3 < |\eta| < 5$, are made of steel rather than brass.

The *Hadron Barrel* (HB) is situated between $0 < |\eta| < 1.3$ and is comprised of 15 5 cm brass absorbers with interleaved scintillating material, resulting in an active length of over eight nuclear interaction lengths. The nuclear interaction length is the mean distance travelled by a hadronic particle before undergoing an inelastic nuclear collision, which is typically approximated as

$$\lambda_I = 35\text{cm} \frac{A^{1/3}}{\rho}, \quad (3.8)$$

where A is the atomic number of the material and ρ is the density. Wavelength shifting fibers read the scintillators out. The *Hadron Outer* (HO) is a hadronic shower tail-catcher consisting of scintillators interleaved in the muon system comes after the brass absorber section, and solenoid magnet comes. The HO adds over one nuclear interaction length to the design and results in a total of 11 interaction lengths when combined with the HB and ECAL.

The *Hadron Endcap* (HE) region is situated between $1.3 < |\eta| < 3$ and follows a design very similar to that of the HB. The major difference between the HE and the HB is that no HO system follows the HE system.

The *Hadron Forward* (HF) system lies between $3 < |\eta| < 5$ where there is much greater radiation anticipated. This sampling calorimeter is constructed from steel absorbers and quartz readout fibers to handle the tougher environment. The primary goal of this system is to ensure an accurate global description of the event by measuring

energetic forward jets.

Because of the highly varied response across various nuclear reactions the best metric of performance for the HCAL is jet and p_T^{miss} resolution. Still, there does exist a parameterized resolutions, which take the form below in the central region

$$\left(\frac{\sigma(E)}{E}\right)^2 = \left(\frac{.9}{\sqrt{E}}\right)^2 + 0.048^2, \quad (3.9)$$

and in the forward region, where the resolution is worsened,

$$\left(\frac{\sigma(E)}{E}\right)^2 = \left(\frac{1.98}{\sqrt{E}}\right)^2 + 0.09^2. \quad (3.10)$$

3.2.4 The muon system

The muon system is the final major component of the CMS detector. The system encloses the 12,000-ton superconducting solenoid which in turn wraps around the tracker, ECAL, and most of the HCAL. Interleaved inside of the iron return yoke of the superconducting magnet are four muon stations. The system spans a radial distance of roughly 4 meters and remains at a constant 2 Tesla magnetic field [86].

In the barrel region, $|\eta| < 1.4$, the muon system is comprised of *drift tubes* (DTs), whereas in the endcap region it is made up of *cathode strip chambers* (CSCs). There exists a dead space the two systems that are filled in with *resistive plate chambers* (RPCs) [Fig. 3.9]. The muon system reaches coverage out to $|\eta| < 2.4$ and can efficiently reconstruct muons in roughly 98 % of this region.

DTs are gas chambers with an ionizing wire running along the centroid and therefore readout at slower readout times than CSCs. A slower readout time is acceptable in the central region where fewer muons are anticipated. The RPCs are included for a fast response time that allows muons incident on the system to be unambiguously associated

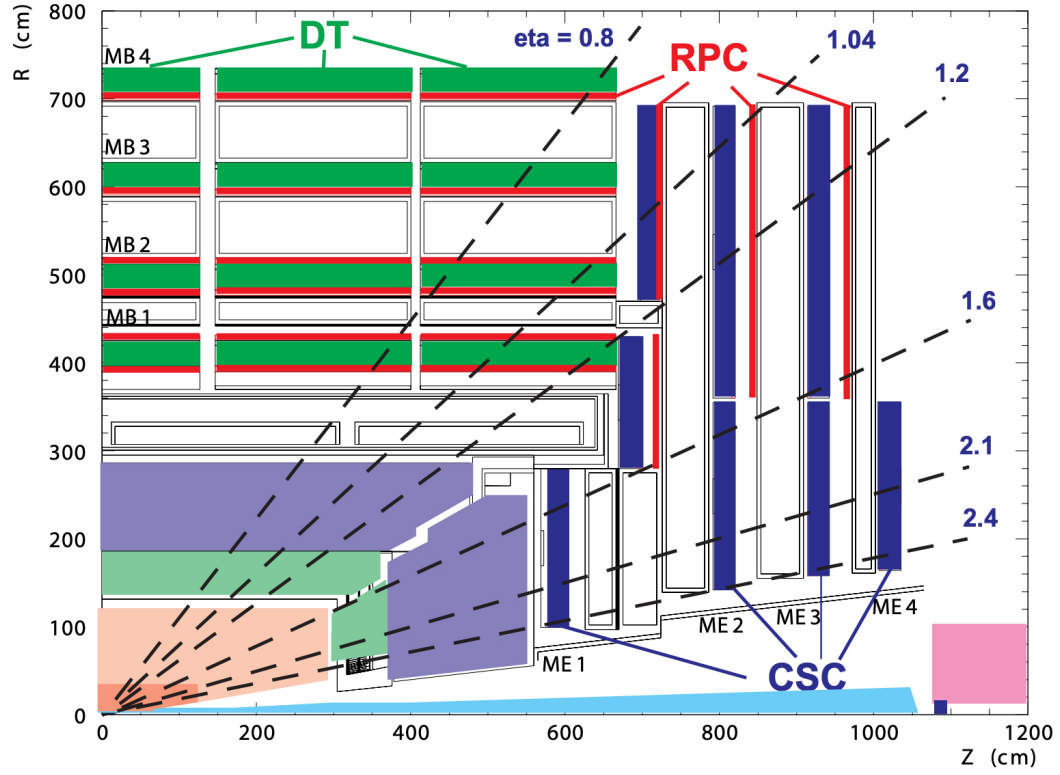


Figure 3.9: Graphical r-z slice of the muon system. Note that the CSCs fill the deadspace between the endcap and barrel regions.

with a single bunch-crossing.

3.2.5 Trigger and data acquisition

The LHC crosses bunches of protons at a rate of 40 MHz. The majority of bunch crossings do not contain relevant physics, and so they may be disregarded. The single event size is of order 1 Mb, and thus it is beyond current compute and electronic capabilities to readout, store, and process all the information produced by the LHC. Therefore, it is the responsibility of the trigger and data acquisition to select the events containing relevant physical processes [87].

Events are readout in stages; the first stage of readout is hardware driven and is called the *level one trigger* (L1T). The L1T uses *Field Programming Gate Arrays* and *Appli-*

cation Specific Circuits to select events that are deemed relevant based on primitives received from the calorimeter and muon systems. The rate of the L1T is of order 10-100 kHz. At this stage, in roughly $3.2 \mu\text{s}$ of real-time a crude event reconstruction is performed. This reconstruction uses localized subdetector measurements from the E/HCAL and the muon system to approximate jets, missing energy, photons, electrons, etc.

When an event passes the L1T a more refined selection is made by the *high level trigger* (HLT). The HLT choose events with software-based algorithms computed across a farm of servers. The extra computing power of the HLT combines tracking information with calorimeter and muon system information to perform a crude particle-flow (PF) reconstruction [Sec. 4.1.3]. This much more selective trigger system brings the frequency of selected events down to roughly 100 Hz, for a total of 5-6 orders of magnitude reduction in event rate when combined with the L1T. Together, the L1T and HLT reduce the data and computing budget down to a scale where it is possible to do physics analyses. Note, the different orders of magnitude over which processes occur at the LHC implies that such reduction rates can be obtained without losing the important physics processes [Fig 3.10].

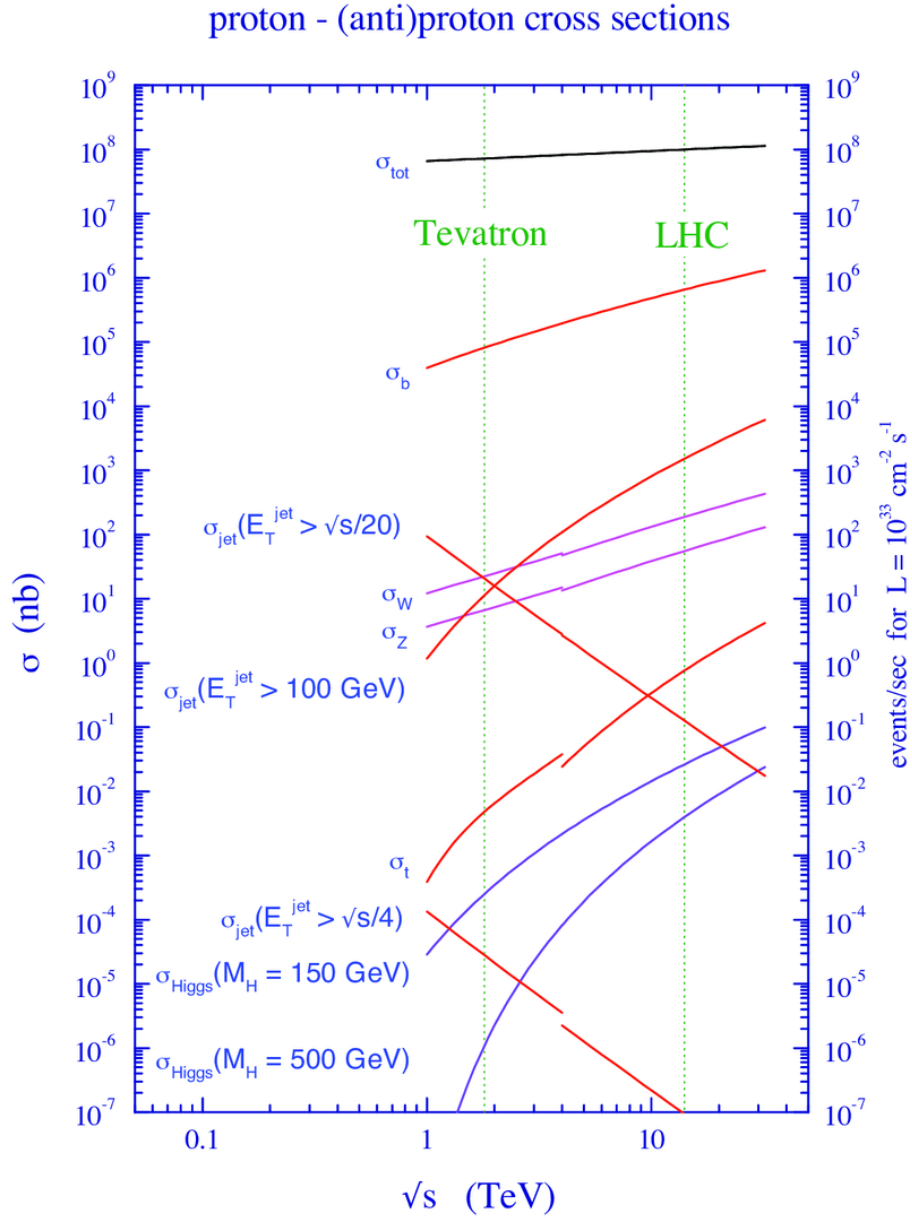


Figure 3.10: Shown above are the cross sections of relevant processes at the LHC. Note that even fairly common electroweak production such as W or Z occurs at roughly 10^{-5} the rate of the soft inelastic scattering that dominates σ_{tot} [88].

Chapter 4

Event Reconstruction

4.1 Object Reconstruction

The most important step in object reconstruction for the CMS experiment is a technique known as particle-flow (PF) [89]. PF leverages underlying physics knowledge to infer the most likely particle type associated with a given sequence of energy deposits. The PF technique is made possible by CMS's strong magnetic field, hermetic and granular calorimetry, and accurate tracking system. PF begins by using information from the silicon tracker to identify the distinct tracks associated with charged particles. Next, information contained in the measured energy deposits readout from the calorimeter systems and muon spectrometers allows for classification into neutral and charged hadrons, electrons, muons, and photons.

At this point, localized views of particle trajectories, energy, and type have been developed. Next, the high-level detector objects used to calculate relevant kinematic quantities are built from *PF candidates* (PFCands) through an iterative process called jet clustering. A properly calibrated particle flow can significantly help in reducing the uncertainties in jet energy measurements when compared to jets constructed from raw energy deposits.

The high-level view of reconstruction is simple in practice, but the complications rest in the details of PF implementation.

4.1.1 Track reconstruction

The entire PF algorithm hinges on proper track reconstruction. Moreover, proper track reconstruction is necessary for identification of hard electrons and muons that play a central role in many analyses at the LHC, and on average 60 % of the energy from hadronization flows through charged hadrons which can be better measured when matched to a reconstructed track. The tracking process begins locally with the cluster-

izing of seed strip/pixel hits to nearby neighbors above a specified signal to noise ratio [90]. Application of an iterative track fit to the centroid of local clusters then proceeds. The next step in the process of track reconstruction is seed generation where triplets of hits in the pixel tracker and some special pairs of hits in the pixel/tracker seed full track reconstruction.

At each subsequent tracking layer, the previous seed trajectory is combined with valid candidate hits or a "fake hit" if no such hit exists. A Kalman filter probabilistically updates the predicted trajectory. If no attempts are made to clean the track collection, this approach will grow the number of tracks exponentially, and so pruning is applied in each step as a function of each track candidates normalized χ^2 , missing hits, and valid hits. In the event that two tracks are sufficiently overlapping, i.e., $f_{shared} = N_{shared}^{hits} / \min(N_1^{hits}, N_2^{hits}) > 0.5$, disambiguation is performed by selecting the tracks with the lesser χ^2 value. Final track candidates are fitted, smoothed and reduced in quantity via quality checks.

Simulation verifies that the seeding process is nearly 100% efficient for valid tracks and that final track reconstruction efficiencies for valid muons exceeds 95% efficiency at all energies and coverage.

4.1.2 Primary vertex reconstruction

The primary collision combined with the additional pile-up collisions will typically result in a multitude of charged and neutral particles propagating throughout the detector. Properly reconstructing the charged particle tracks allows for the fitting of the vertices associated with these different interaction points, which can in turn help to reduce the impact of pile-up interactions. Tracks are initially clustered along the beam-line such that each vertex candidate is separated by at least 1 cm from the nearest neighbor. After

finding a first iteration of vertex candidates, the adaptive vertex fitter is applied to locate the final vertex position [91]. The algorithm by calculating a weight for each associate track, w_i , based on the tracks compatibility with the given common vertex. The best fit vertex is then found sequentially by stepping towards the vertex fit which minimizes a χ^2 error estimate over the the weighted tracks.

After reconstructing all vertices, the primary vertex of the event is selected to be the vertex with the largest sum of squared transverse momenta over all associated tracks [92].

4.1.3 Particle-flow reconstruction

Attempts are made to match all significant energy deposits in the CMS detector to an associated particle construct. The particles of the detector are divided into five types depending on energy deposit characterization [Fig. 4.1]:

- Photons: Shower in the ECAL with no associated tracks.
- Electrons: Shower in the ECAL with an associated track.
- Neutral Hadrons: Shower in the HCAL with no associated tracks.
- Charged Hadrons: Shower in the HCAL with associated track and no shower in ECAL.
- Muons: Hits in the muon spectrometer with associated track and no significant E/HCAL showers.

It is shown later that these simplified particle types lead to simplified identification b-quarks and hadronic tau decays. Also, PF results in improved jet energy resolution, pile-up rejection, and lepton isolation calculations.

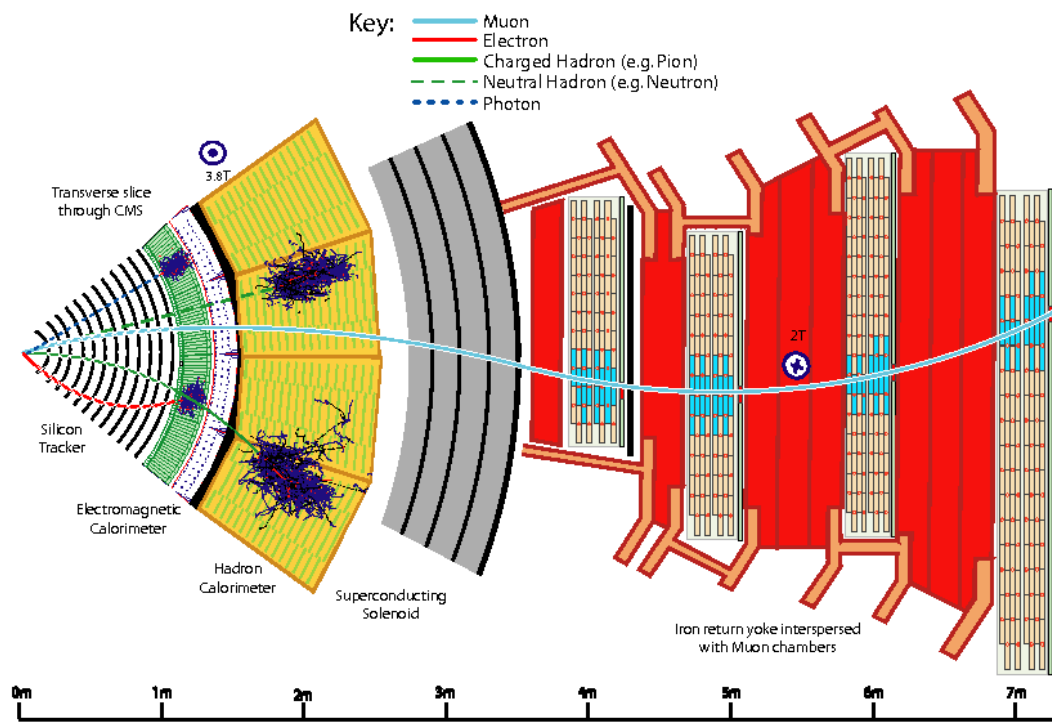


Figure 4.1: The longitudinal slice of the CMS detector shown above highlights how the CMS detector design allows for Particle-Flow identification

PF Reconstruction proceeds first by performing local reconstruction in each subdetector. Track reconstruction is carried out in the tracker, clusters are formed by grouping energy deposits in the calorimeter, and calculation of track segments is performed in the muon chambers.

The individual subdetector energy deposits are connected by a linking algorithm that attempts to form coherent particle trajectories. The nearest neighbors in the (η, ϕ) -plane are linked to keep computation linear. Because of this algorithmic design, the performance of particle disambiguation is driven in most part by transverse granularity. Please refer to the specific sections for a detailed description of muon and electron reconstruction [Sec. 4.1.4, 4.1.5].

The first reconstructed particles are muons and electrons, and next charged hadrons are located by linking reconstructed tracks with HCAL deposits.

Neutral particle reconstruction follows after charged particle reconstruction. Significant ECAL clusters that do not link to an upstream track or downstream HCAL deposit are reconstructed into photons. The measured energy of these candidates is calculated according to calibrations measured in the simulation. Lastly, significant unmatched deposits in the HCAL are reconstructed as neutral hadrons.

4.1.4 Muon reconstruction

Muon reconstruction by the CMS experiment is pivotal, but in many ways, the muon is the easiest particle to identify unambiguously. Muons behave as minimum ionizing particle (MIP) as they traverse through the detector and so muons are the only charged particle which consistently reach the muon chambers. Muons are selected with over 99% efficiency based on a simple selection of cuts related to the global track χ^2 , CSC and DT track segment compatibility and kink finding [93].

In addition to the cuts above, it is required that the relative isolation, $I_{\delta\beta}$, be less than 0.3 for selected muons veto objects within this thesis. $I_{\delta\beta}$ is calculated as a scalar sum over the momenta of all particle flow candidates in a cone of radius $\Delta R = 0.4$ centered around the muon [89, 94]:

$$I_{\delta\beta} = [\Sigma p_{T,\text{charged}} + \text{Max}(0, \Sigma p_{T,\text{neutral}} - \delta\beta \Sigma p_{T,\text{pile-up}})] / p_T \quad (4.1)$$

The multiplier $\delta\beta$ is typically set near 0.5 on the CMS experiment and is used to scale a sum over the anticipated pile-up contribution inside of the muon cone. The $\delta\beta$ subtraction removes the expected energy deposition from neutral pile-up particles inside of the muons cone. Charged pile-up needs no such correction since vertex fitting naturally rejects the majority of this contribution. After applying all the muon selections the misidentification rate of non-muons is less than one in a million [86].

4.1.5 Electron reconstruction

Electron identification connects a reconstructed track with a shower in the electromagnetic calorimeter. This unique signature of the electron differs from that of charged hadrons and muons which typically behave as MIPs in the electromagnetic calorimeter.

Electron reconstruction is made complicated by the significant material budget in the tracker which results in substantial downstream bremsstrahlung. The bremsstrahlung acts to spread the electron's energy in a cone over the calorimeter. A significant portion of the tracker is in excess $.75 X_0$ [Sec. 3.2.1]. As a result, more than half of produced electrons will radiate away more than half of their production energy.

Radiated photons can become even more problematic if they undergo subsequent pair-conversion. The pair-produced electrons act to further spread and reduce the electron energy.

Electron reconstruction accounts for bremsstrahlung effects by selecting a *seed cluster* corresponding to the electron trajectory and then by clustering nearby energy deposits to form a *supercluster*. One measurement of the electron energy comes from summing over these cluster energies and using the known linear response of the electromagnetic calorimeter to calibrate. A second measurement comes directly from the reconstructed track p_T . Combination of the two measurements occurs with different weights according to the shower profile of the electron.

Electron selection in this thesis follows from a simple cut-based approach. These cuts include $|\eta|$ dependent quality cuts on the inverse difference of reconstructed energy in the tracker and ECAL, relative isolation, impact parameters, seed cluster and track angular separation, and some other relevant parameters. Using an optimized cut-flow on these variables one can obtain a misidentification rate of under 1% for fake electron candidates [95].

4.1.6 Jet reconstruction

Particle flow candidates are clustered into collimated objects referred to as jets, objects which result from the hadronization process [Sec. 5.1.2]. Clustering is performed by the anti- k_T algorithm. It begins by calculating the anti- k_T pair-wise distance, d_{ij} , across all particles in the current collection :

$$d_{ij} = \min(k_{T,i}^{-2}, k_{T,j}^{-2}) \frac{\Delta R_{ij}}{D^2}, \quad (4.2)$$

and the distance to the beamline of each particle, $d_{iB} = k_{T,i}^{-2}$. In the equation above the nominal distance scale used in the equation by the CMS experiment is $D=.4$, and $k_{T,i}$ is the transverse momenta of the i th particle.

Clustering is done in an iterative manner with FASTJET [96]. At each step, if the

smallest value lies amongst d_{ij} the two corresponding collections are merged into one single collection and the calculation repeats over all elements. Otherwise, if the smallest value is amongst d_{iB} then that particle collection is removed and the entirety constitutes a final clustered jet.

Looking at the equations used we see that the highest momentum particles are clustered first according to the specified distance scale. Moreover, all final jets must be separated by $\Delta R > D^2$, hence why D is referred to as a distance.

A highly efficient loose jet selection from derived by the JetMET Physics Object Group is then applied to reject pathological objects [97]:

- Neutral Hadron Fraction > 0.99
- Neutral EM Fraction > 0.99
- Number of Constituents < 1
- For jets with $\eta < 2.4$:
 - Charged Hadron Fraction < 0
 - Charged Multiplicity < 0
 - Charged EM Fraction > 0.99

Reconstructed jets have known calibration issues stemming from many effects, such as imperfect particle-flow calibration, pile-up, and simulation vs. data discrepancies. These corrections are applied in successive levels 1,2-3, and then as residual level-3 corrections. The first two corrections are measured in simulation, whereas the third correction corrects differences between simulation and data [98].

- Level 1 (L1) : Corrections are performed to subtract the estimated impact of pile-up. For this thesis the corrections are measured as function of p_T and η . This gives

a binned correction

$$C_{\text{offset}}(\eta, p_T^{\text{raw}}) = 1 - \left(\frac{(N_{pv} - 1)F(\eta)}{p_T^{\text{raw}}} \right), \quad (4.3)$$

where N_{pv} is the number of reconstructed primary vertices and p_T^{raw} is the uncorrected jet p_T [99, 100].

- Level 2-3 (L2) : After subtracting the contribution from pile-up the next step is to correct the calibration. The correction is parameterized as

$$C_{\text{calibration}}(\eta, p_T^{\text{L1}}) = p_T^{\text{L1}} / p_{T,\text{gen}}, \quad (4.4)$$

where $p_{T,\text{gen}}$ is the p_T of a generator-level jet matched to the corresponding reconstructed jet with L1 corrected response p_T^{L1} .

- Level-3 (L3) : This correction is implemented to remove residual differences between data and simulation. Residual discrepancies are measured using a well-calibrated process, such as $Z \rightarrow \mu\mu$, with exactly one additional jet. The excellent muon resolution of CMS allows for accurate reconstruction of the Z kinematics. The single jet must then be balanced against the Z and a fractional mismeasurement can be approximated by $\mathcal{R}_{\text{bal}} = \frac{p_T^{\text{L2}}(j)}{p_T(Z)}$, where $p_T^{\text{L2}}(j)$ is the L2 corrected jet p_T and $p_T(Z)$ is the reconstructed Z p_T . Then, by measuring this quantity in both data and simulation the L3 jet correction can be applied in simulation as

$$C_{\text{res}}(p_T^{\text{L2}}, \eta) = \frac{\mathcal{R}_{\text{bal}}(\text{DATA})}{\mathcal{R}_{\text{bal}}(\text{MC})} \quad (4.5)$$

.

A fully corrected reconstructed jet p_T is given by :

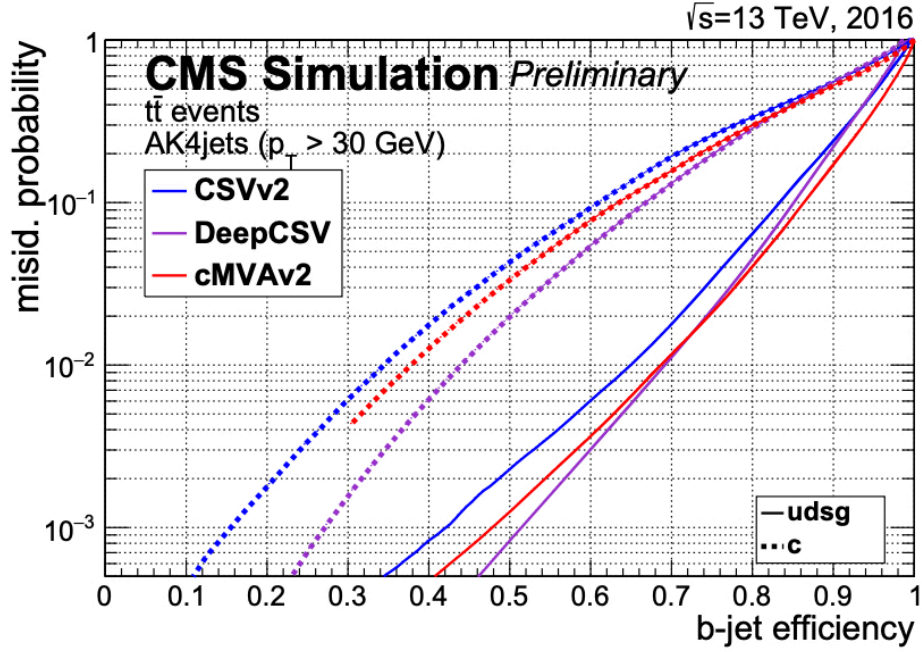
$$p_T^{\text{corr}} = C_{\text{res}}(p_T^{L2}, \eta) C_{\text{calibration}}(\eta, p_T^{L1}) C_{\text{offset}}(\eta, p_T^{\text{raw}}) p_T^{\text{raw}}. \quad (4.6)$$

Selected jets in the event are required to pass $p_T \geq 30$ GeV and $|\eta| < 2.4$. Note that in the p_T^{miss} calculation this requirement is reduced to 10 GeV.

4.2 Identifying Jets Associated with b -quark Decay

Production of bottom quarks occurs in many Standard Model processes of note, e.g., boson, $H/Z \rightarrow bb$, and top, $t \rightarrow bW$, decays. Correctly identifying events from such decay topologies is important to many analyses at the LHC and so significant effort has been invested into identifying reconstructed jets associated with a decaying b -quark (b-jets).

In most analyses carried out by the CMS experiment, a multivariate (MVA) approach called the Combined Secondary Vertex (CSV) b-tagging algorithm has been the default [101]. The main thrust of this technique is to identify displaced *secondary vertices* inside of clustered jets. These vertices arise naturally in b -quark decay because of the finite lifetime of the b . The natural correlation between b -lifetime and the secondary vertex displacement provide some of the motivation for a multivariate approach, but there are also additional variables that contribute to discrimination. These include, but are not limited to, the existence of a secondary vertex, impact parameter, and significance of secondary vertex, number of tracks in jet and number associated to secondary vertex, and kinematic variables relating the secondary vertex to the primary jet. However, despite the strength of this approach and its intuitive nature, further advances in machine learning resulted in a new approach to identifying b-jets.



This analysis adopts a *Deep-Learning* based approach to identifying b-jets dubbed *DeepCSV* [102]. The approach further extends the previous multivariate approaches to include more relevant track information for a slight improvement in performance [Fig. 4.2].

4.3 Tau Identification

Hadronic tau (τ_h) reconstruction performance is pivotal for the analysis that will be described later in this thesis. In this section, a multivariate approach employed by the CMS experiment is described, but in the following chapters a dedicated deep neural network approach will be presented.

Following jet clustering, the Hits Plus Strips (HPS) algorithm looks to identify jets which are consistent with hadronic tau decay [103]. The three primary hadronic decay modes the tau are a single charged hadron, a single charged hadron plus one or two

neutral pion(s), and three charged hadrons. Together these three decay modes account for 95% of the hadronic tau decays, which in turn account for roughly 61% of all tau decays. Neutral pions are reconstructed by finding pairs of reconstructed photons that are consistent with pion decay.

The single and three charged hadron final states of tau decay are straightforward to reconstruct, but neutral pion decay can be much harder to reconstruct. Neutral pions will decay promptly to two photons with relatively high probabilities of undergoing pair-conversion before reaching the ECAL. Because of this, HPS reconstruction proceeds by looking to cluster potential neutral pion candidates in *strips* of $\Delta\eta \times \Delta\phi$. The relevant strips are then combined with the charge hadron candidates to test the various decay mode hypotheses.

The HPS algorithm alone is not powerful enough to reject a sufficiently reject *misidentified* hadronic taus coming from muon, electron, quark and gluon jets. To reach desired performance, tau candidates passing the HPS algorithm are further differentiated according to the output of a boosted decision tree discriminator. Shower shape variables, electron and photon multiplicity, tau flight length, and relative isolation are among the roughly 20 variables that are fed into the boosted decision tree. Across all $p_T(\tau_h)$ the relative isolation of the tau is the most sensitive discriminator [Fig. 4.2].

Lastly, there is a high residual rate of electrons and muons passing the isolation MVA and are reconstructed as a fake hadronic τ_h . This additional source of fake taus is reduced using a dedicated multivariate (MVA) discriminator. Inputs to this MVA come from all subdetectors and are similar to the information that is used for the genuine tau MVA [105, 106].

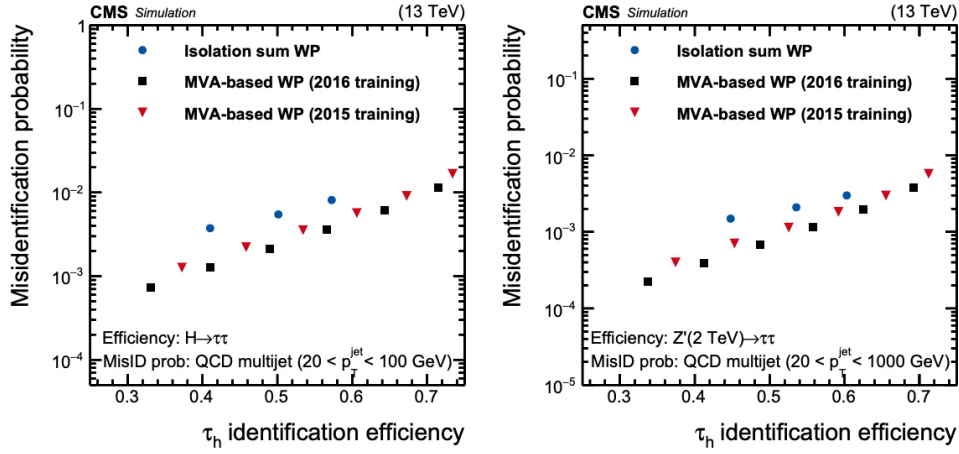


Figure 4.2: Receiver operator curves (misidentification rate vs. genuine τ_h efficiency) for hadronic tau decays coming from Standard Model $H \rightarrow \tau\tau$ (left) and BSM $Z'(2 \text{ TeV}) \rightarrow \tau\tau$ (right). On each plot "working points" (WP) calibrated by the CMS experiment are shown for a simple cut-based approach using only isolation and for a multivariate (MVA) approach [104].

4.4 Missing Transverse Momentum and Scalar Transverse Momenta Sum Reconstruction

The missing transverse momentum, p_T^{miss} , and the scalar transverse momenta sum, H_T , are two global event reconstruction variables which aim to capture the missing energy and total observed energy of an event, respectively. Significant measurements of p_T^{miss} at the CMS experiment result from the presence of weakly interacting particles, such as neutrinos, or large mismeasurements of objects in the underlying event. Precisely determining p_T^{miss} is important for many Standard Model analyses such as those involving the leptonic decays of W and Z bosons, $W \rightarrow \ell\nu$, $Z \rightarrow \nu\nu$, respectively. Moreover, p_T^{miss} is one of the strongest discriminating variables in many searches for new physics.

A formal definition of this quantity is given at CMS as a sum over all reconstructed

PFCands.

$$\vec{p}_T^{miss} = -\sum_{i \in \text{PFCands}} \vec{p}_{T,i}, \quad (4.7)$$

However, this fails to incorporate known issues with jet-by-jet calibration which can be corrected [Sec. 4.1.6]. Propagation of corrections is done by splitting p_T^{miss} into a source from jets and a source from unclustered particles :

$$\vec{p}_T^{miss} = -\sum_{i \in \text{jets}} \vec{p}_{T,i}^{\text{corr}} - \sum_{i \in \text{unclustered}} \vec{p}_{T,i}, \quad (4.8)$$

where $\vec{p}_{T,i}^{\text{corr}}$ is the corrected jet p_T . In general, leptons and photons are not likely to have a significant contribution to p_T^{miss} due to the superior resolution. Instead, the leading contribution to mismeasurements comes from hadronic activity which in turn results in a 5-20 % jet momentum resolution. The bulk of the p_T^{miss} distribution is well modeled in simulation, however tail effects often need special considerations [Fig. 4.3].

An additional global variable of important is defined as

$$H_T = \sum_{i \in \text{jets}} p_{T,i}, \quad (4.9)$$

where $p_{T,i}$ is the transverse momentum of the i th reconstructed jet in the event.

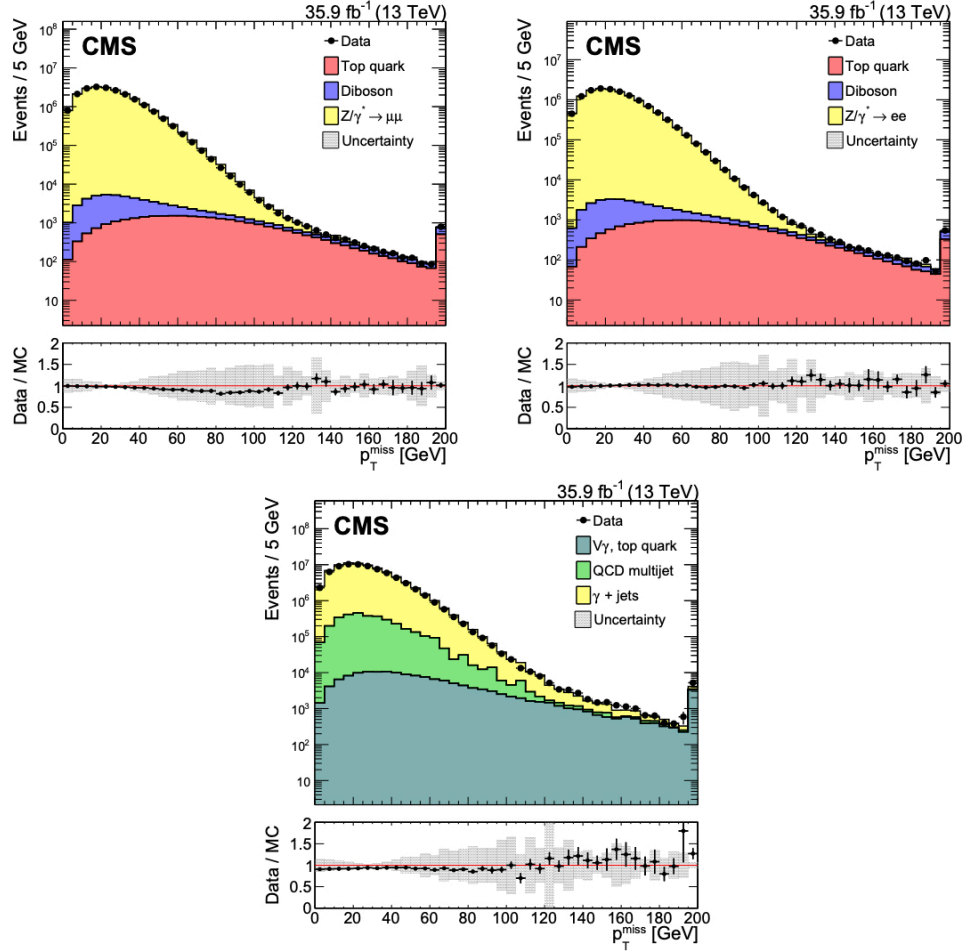


Figure 4.3: Upper panel : Distributions of p_T^{miss} in dimuon (left) and dielectron final states (right). Distribution for γ +jets shown in the bottom panel. The leading source of uncertainty comes from systematic effects on the jet energy corrections that relate to jet energy scale and resolution [107].

Chapter 5

Event Simulation

5.1 Overview of Event Simulation at CMS

Most successful analyses carried out at the LHC require accurate and precise modeling of the background and signal processes. Without such modeling, it is impossible to detect the signature of new physics or make a precision measurement of a known Standard Model process. Towards this end, Monte Carlo methods use pseudo-random numbers to approximate nature by probabilistically sampling from possible outcomes. Generation begins by sampling hard parton-parton scattering from a chosen final state X according to matrix-level calculations. Different matrix-element calculators are implemented depending on whether Leader Order (LO) or Next to Leading Order (NLO) precision is desired. Next, the strongly interacting particles in the final state X undergo a process called hadronization, as explained further below, wherein the partons of final state X produce a *parton shower* (PS), i.e., collimated jets of stable particles [Fig. 5.1]. Lastly, physics simulation software propagates final stable particles through the detector and emulates the subsequent detector readout.

Over the years the physics packages associated with these simulations have been iteratively tuned to match distributions seen in the data collected at the LHC. However, there is still many systematic uncertainties related to the use of simulation, and so analyses attempt to predict their backgrounds directly from data whenever possible. When this is not possible, techniques are employed to factorize and correct independent sources of mismodeling in simulation.

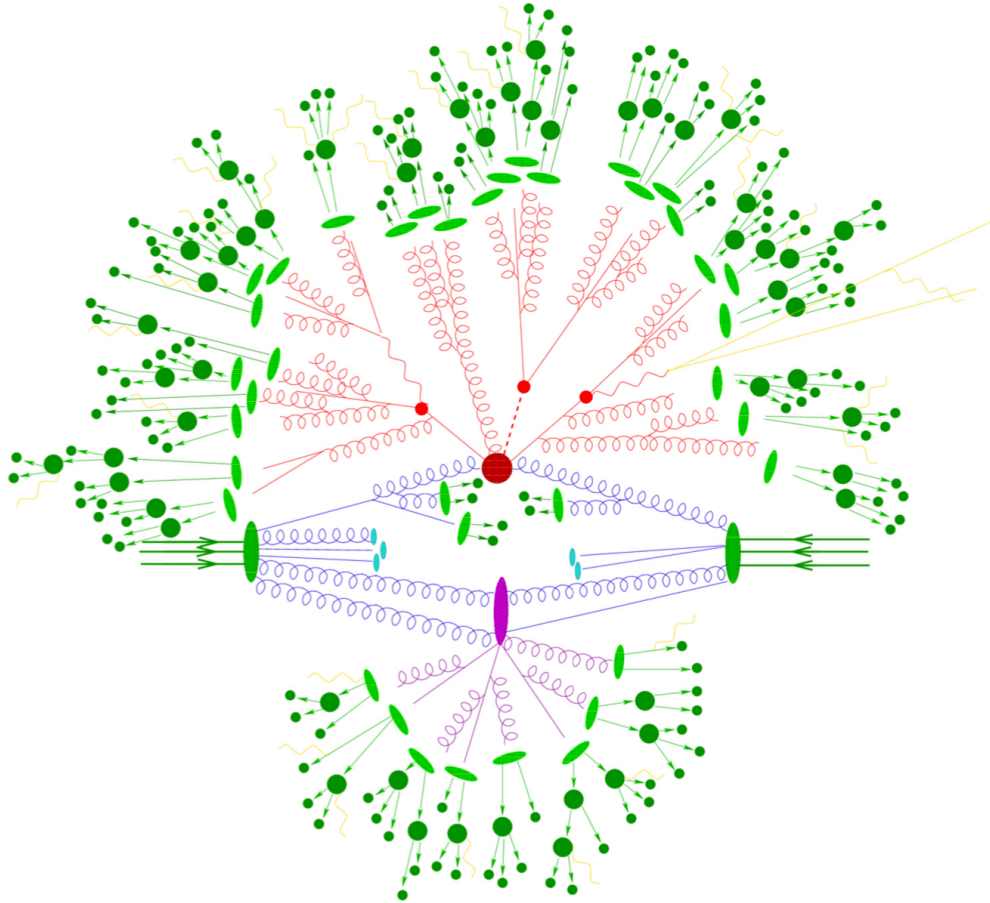


Figure 5.1: The image above shows a schematic of typical event at the LHC [108]. First, hard scattering (red circle) and remnant interactions (purple circle) are simulated. Next, parton showering (red lines) and hadronization and decay (green circles) occur. Lastly, not pictured are overlaid pile-up events from soft pp interactions.

5.1.1 Hard scattering processes

The cross section to produce a final state X in a hard proton-proton scattering process may be written as a sum over the available parton states and a corresponding integral over the parton momenta fractions x_1, x_2 , total proton-proton center of mass energy, \sqrt{s} , and the partonic scatter cross section $\hat{\sigma}$ as follows [44, 109]

$$\sigma(pp \rightarrow X) = \sum_{i,j} \int dx_1 dx_2 f_{i,p}(x_1, \mu_F^2) f_{j,p}(x_2, \mu_F^2) \hat{\sigma}_{ij \rightarrow X}(x_1 x_2 s, \mu_R^2, \mu_F^2), \quad (5.1)$$

where μ_R and μ_F are the renormalization and factorization scales, respectively. Thus, given a parton density function, it is possible to calculate the total cross section when provided with the individual partonic scatter cross sections $\hat{\sigma}$. This equation illustrates that computing the final states at LO or NLO matrix-elements is equivalent to approximating the partonic cross sections in the equation above to the same order.

Hard outgoing radiation is calculated explicitly down to a selected cut-off scale Q_{cut} during the matrix-element calculation of the final state. A cut off is implemented because of the significant complexity of soft radiation and because of associated theoretical problems such as infrared divergence.

5.1.2 Parton showering

Further gluon splitting and radiative effects are simulated downstream to a smaller cut-off scale, Q_0 , from empirical descriptions known as Sudakov Form Factors [110]. This simulation process can easily lead to erroneous behavior since initial partons with energy well above Q_{cut} can radiate hard and separated partons in the showering process. To prevent this a *MLM matching* criterion are applied for events generated at CMS which

requires each initial parton to match with a downstream jet of similar p_T . Events with additional jets are kept provided that the additional jets are softer than those matched to partons. In general, the value of the Q_{cut} must be selected carefully to ensure that the generator level jet p_T spectrum remain smooth.

The potential energy arising from the strong force between two quarks can be modeled empirically as a force which increases linearly with separation distance. Therefore, as two quarks propagate in space, their potential energy grows until it becomes energetically favorable to create a new quark anti-quark pair from the vacuum in order to reduce the total energy of the system. This process repeats ad infinitum until there is no longer sufficient energy to support additional splittings, i.e., until the partons are below the energy scale Q_0 . This described mechanism for hadronization is referred to as *string fragmentation* [111]. The time and length scales of hadronization are very short. After completing the hadronization step, an additional package can readily describe the propagation of all stable particles through the detector.

5.1.3 Pile-up

Recall that previously we discussed pile-up an effect where additional pp collisions occur in each bunch crossing. The impact of this effect can be probabilistically sampled, first note that the probability distribution for the number of pile-up collisions $P(N_{PU})$ follows a Poisson likelihood

$$P(N_{PU}) = \frac{(\mathcal{L}\sigma)^{N_{PU}}}{N_{PU}!} \exp^{-\mathcal{L}\sigma}. \quad (5.2)$$

After sampling the number of interactions, pile-up interactions from inclusive pp collisions are randomly selected. An event is created by overlaying these pile-up interactions with the hard-scattering.

5.2 Event Generation Packages Used by CMS

After completing the underlying event generation, event reconstruction proceeds in the same manner as was described for data in chapter four. The specific packages used by the CMS experiment for the various steps in the simulation process are listed below:

- PYTHIA 8.212 (8.230) for 2016 (2017) [112]
 - Parton Showering software to be interfaced with MADGRAPH5_AMC@NLO and POWHEGv2.
- MADGRAPH5_AMC@NLO 2.3.3 (2.4.2) for 2016 (2017) [113]
 - A LO/NLO+PS cross section calculator and event generator. Calculations are LO for any user defined Lagrangian and offers NLO QCD corrections. Moreover, tree and loop corrections can be included.
- POWHEGv2 Generator [114]
 - Positive Weight Hardest Emission (POWHEG) is an NLO+PS matrix event generator that is typically interfaced with PYTHIA. Since POWHEG is a full NLO generator it incorporates initial state and final state radiation of up to one additional parton.
- NNPDF3.0(3.1)LO/NLO for 2016 (2017) [115]
 - Experimentally measured PDFs.
- SYSCALC [116]
 - Renormalization and factorization scale and PDF uncertainties

- GEANT4 [117]
 - An extensively validated package which pseudo-randomly samples interactions from available physical processes as each simulated particle incrementally steps through detector material. This simulation typically includes, down to some cutoff scale, all processes ranging from those responsible for bulk energy loss, such as ionization, rare hard processes such as electro/photo-nuclear reactions, and radiative processes that introduce additional particles. To obtain an accurate simulation, it is essential that the material budget of the detector be accurately modeled, with sensing volumes in appropriate locations.
- Delphes [118]
 - A fast simulation that applies a parameterization of a detector according to the physics described by a more fundamental geometric simulator such as GEANT4.

Chapter 6

Deep Neural Networks for Hadronic Tau Identification

6.1 Introduction to Artificial Neural Networks

Machine learning (ML) is a technique which builds a predictive model from a specified *training set* of data. ML is a highly empirical approach where a specified algorithm *learns* from a set of examples to generalize to unseen cases. A *supervised* learning process is one where the input dataset has clearly labeled categories.

In this case, the training set consists of many examples, each with a feature vector \vec{X} and a corresponding *truth value*, y , which the model learns to predict. Depending on the nature of the problem, y could be a discrete or continuous variable. In this manner, the trained machine learning algorithm generates a function $f(\vec{X})$ that produces a prediction \hat{y} of the truth value.

In addition to supervised learning problems there are *unsupervised* algorithms, such as a k-means clustering, which attempt to categorize events without the use of event labels. Lastly, *reinforcement learning* is an ML technique where an algorithm learns to navigate a specified environment through positive and negative stimuli called rewards.

Artificial Neural Networks, or Neural Networks (NNs) for short, are a biologically motivated and once pioneering concept developed in the 1940s [119]. Early models of the brain described the brain as a composition of cells which receive and pass along electrical signals. The neuron is composed of dendrites and axons and is the basic building block of the brain [120, 121]. The neuron receives an input pulse in the dendrites that are passed along through the axon when the signal is of sufficient strength. Indeed, NNs are mathematical models developed to approximate this behavior by learning from an input data set.

The principal unit of computation in a NN is the *neuron* or *node*. A layer of input-nodes that each receives the initial feature set \vec{X} of an event are the first layer of the NN. Next, hidden-nodes that perform sequential operations until the final output layer

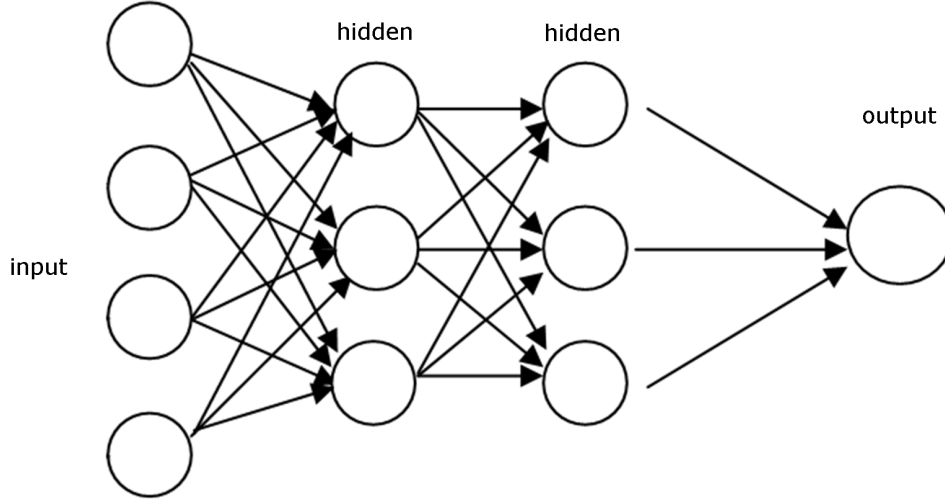


Figure 6.1: Above: A schematic of a multi-layer NN. The internal units are referred to as *hidden* because the user of the NN does not interact directly with them.

generates the final prediction [Fig. 6.1].

Each neuron computes a functional operation, f , after receiving a vector of input \vec{X} and produces a single output value. Along this design the entire output of a layer containing M neurons and receiving an input \vec{X} of length N may be written:

$$f(\vec{X}) = \sigma(w \cdot \vec{X} + \vec{b}), \quad (6.1)$$

where w is a M by N matrix of floats that is randomly initialized. The *activation function*, σ , is applied element-wise and introduces non-linearity into the layer. Typical activation functions include the sigmoid ($\sigma(x) = 1/(1 + e^{-x})$), tanh, and the rectified linear unit (ReLU, $R(x) = \max(0, x)$). The number of neurons in a given layer is a *hyperparameter*, i.e. a parameter of the model that may be tuned by the user.

Note that the weight matrix, w , is fit during the learning process so as to best discriminate signal from background. Learning is not well defined without an *objective function* that offers a reward or penalty for decisions made by the algorithm. For the

problems covered in this thesis the scope is restricted to that of *binary classification* where the data is labeled as background (0) or signal (1). The *log-loss* or *cross-entropy* is the selected objective function, \mathcal{L} , used to train the NN [122]:

$$\mathcal{L} = y \log(\hat{y}) + (1 - y) \log(1 - \hat{y}), \quad (6.2)$$

where \hat{y} is the prediction generated by the learner. For problems of this type the final output layer of the neural network is typically just a single sigmoid and the intermediate activations are usually ReLUs, and so for example the final output from a two-layer neural network can be written:

$$\hat{y} = \sigma(w_O \cdot R(w_2 \cdot R(w_1 \cdot \vec{X} + \vec{b}_1) + \vec{b}_2) + b_O) \quad (6.3)$$

Here, \vec{X} is an input of N predictive *features* used for prediction, w_1 (w_2) is an M by N (O by M) matrix, and w_O is a weight vector of length O . Note, dimensions M and O are user-specified and that the final sigmoid is not counted as layer in our terminology above.

6.2 Training Neural Networks

The process of fitting the weights of a NN on a training set is called *training* the NN. One of the greatest early challenges in NN research was developing a method to accurately and quickly fit the weights. Eventually, a successful approach was shown to be a variant of the old Gauss-Newton approach for functional minimization called *Stochastic Gradient Descent* (SGD). SGD incrementally adjusts the value of the weights of the NNs over a set of randomly sampled training samples, at step t , according to the gradient of the loss function, $\nabla_W \mathcal{L}$. A constant of proportionality λ called the learning

rate is introduced :

$$w^{(t+1)} \leftarrow w^{(t)} - \lambda \nabla_w L \quad (6.4)$$

Below is a variant of SGD named *ADaptive Moment Estimation* (ADAM) which has been shown empirically to far surpass the performance of simple SGD in most applications [123]. ADAM applies *momentum* to the gradient by replacing it by an exponential moving average with a diminishing return of β_1 . Also, the momentum is normalized by an exponentially moving root-mean-square with the rate of β_2 . The intent is to create an algorithm that takes equal size steps along a smooth gradient trajectory. Lastly, a constant ϵ is introduced to avoid potential infinities.

$$m_w^{(t+1)} \leftarrow \beta_1 m_w^{(t)} + (1 - \beta_1) \nabla_w \mathcal{L}^{(t)} \quad (6.5)$$

$$v_w^{(t+1)} \leftarrow \beta_2 v_w^{(t)} + (1 - \beta_2) (\nabla_w \mathcal{L}^{(t)})^2 \quad (6.6)$$

$$\hat{m}_w = \frac{m_w^{(t+1)}}{1 - (\beta_1)^{t+1}}, \quad \hat{v}_w = \frac{v_w^{(t+1)}}{1 - (\beta_2)^{t+1}} \quad (6.7)$$

$$w^{(t+1)} \leftarrow w^{(t)} - \lambda \frac{\hat{m}_w}{\sqrt{\hat{v}_w} + \epsilon} \quad (6.8)$$

Note that the use of ADAM introduces three new hyperparameters. Given that a NN is composed of many layers, each with a given set of individual weights, the application of this approach is non-trivial. The preferred method for such optimization is called *backpropagation*, and it relies on the chain rule of calculus [124].

Let the output before and after applying activation at the l th layer of a neural network

be given by $Z^{[l]}$ and $A^{[l]}$, respectively. Given the derivative $dZ^{[l]} = \frac{\partial \mathcal{L}}{\partial Z^{[l]}}$ it is then possible to use the chain rule to as follows compute $dw^{[l]} = \frac{\partial \mathcal{L}}{\partial w^{[l]}}$, $db^{[l]} = \frac{\partial \mathcal{L}}{\partial b^{[l]}}$, $dA^{[l-1]} = \frac{\partial \mathcal{L}}{\partial A^{[l-1]}}$:

$$dw^{[l]} = \frac{\partial \mathcal{L}}{\partial w^{[l]}} = \frac{1}{m} dZ^{[l]} A^{[l-1]T} \quad (8)$$

$$db^{[l]} = \frac{\partial \mathcal{L}}{\partial b^{[l]}} = \frac{1}{m} \sum_{i=1}^m dZ^{[l](i)} \quad (9)$$

$$dA^{[l-1]} = \frac{\partial \mathcal{L}}{\partial A^{[l-1]}} = w^{[l]T} dZ^{[l]} \quad (6.9)$$

Then, from the equations above it is shown that backpropagation can recursively derive the weight updates once given the exact form the loss function \mathcal{L} and the specifications of the NN.

6.3 Convolutional Neural Networks

Convolutional Neural Networks (CNNs) are another biologically inspired learning algorithm [125]. In this instance, the motivation for the design came from a deep understanding of the human vision system. CNN's replace the previously described hidden-neuron architecture with n_C channels of n_H by n_W weight matrices called *filters* at each layer. Each filter makes a unique convolutional calculation along a sliding window [Fig. 6.4].

Zero padding can be performed around the edges of the input at each layer in order preserve image dimensionality. Moreover, a stride may be introduced whereby the window spacing between steps is increased. After introducing these two concepts the formulas relating the output shape of the convolution to the input shape is given by the set of

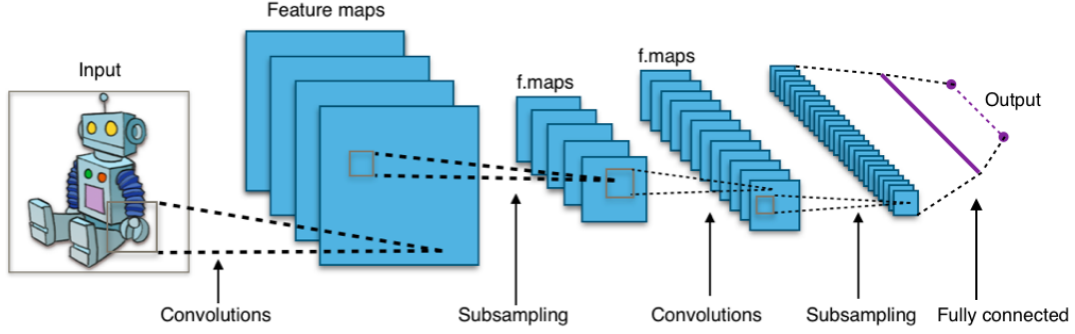


Figure 6.2: Schematic of a single layer CNN. In a typical application many layers of such convolution and pool operations are stacked upon each-other to form a DNN before flattening and feeding into a typical feed forward network. [126]

equations below :

$$n_H = \lfloor \frac{n_{H_{prev}} - f + 2 \times pad}{stride} \rfloor + 1 \quad (6.10)$$

$$n_W = \lfloor \frac{n_{W_{prev}} - f + 2 \times pad}{stride} \rfloor + 1 \quad (6.11)$$

$$n_C = \text{number of filters used in the convolution} \quad (6.12)$$

Forward pooling is an applied method to reduce the spatial dimensions of the resulting filters. Pooling takes the maximum or average over a sliding window of size f by f , which reduces the dimensions accordingly:

$$n_H = \lfloor \frac{n_{H_{prev}} - f}{stride} \rfloor + 1 \quad (6.13)$$

$$n_W = \lfloor \frac{n_{W_{prev}} - f}{stride} \rfloor + 1 \quad (6.14)$$

$$n_C = n_{C_{prev}} \quad (6.15)$$

Backpropagation proceeds through the pulling layer in a manner similar to that described in the previous section.

6.4 DeepPF Isolation

6.4.1 Input features

To further improve the suppression of the fake jet background while retaining high signal efficiency, we have pursued a new approach for improved τ_h isolation, based on the use of the CNNs previously described. Discriminating variables are calculated from PFCands within a cone of $\Delta R \leq 0.5$ centered on the τ_h candidate. This approach is called *Deep Particle Flow* (DeepPF) isolation.

The selected PFCands are formatted into a two-dimensional table with particles running down one axis and discriminating features such as $p_T(p)$, $\Delta R(p, \tau)$, 3-D impact parameter, particle type. A full list of input features is provided along with the pre-processing applied to help in NN training [Tab. 6.1]. On average, approximately 10 PFCands associated to a genuine tau are reconstructed, with the number resting between 2 and 30 for almost all cases. Charged candidates that are not associated with a primary vertex or candidates with $p_T \leq .5$ GeV inside of the cone are not considered.

Tracking related variables do not exist for neutral particles and so a value must be *imputed* without biasing the learning process. Moreover, the absolute value of some features is taken to preserve physical interpretation while satisfying the preference of NNs to have input in the range of 0-1. *One-hot-encoding* aids the NN evaluation by transforming a single N category feature into a vector of N booleans with the location of

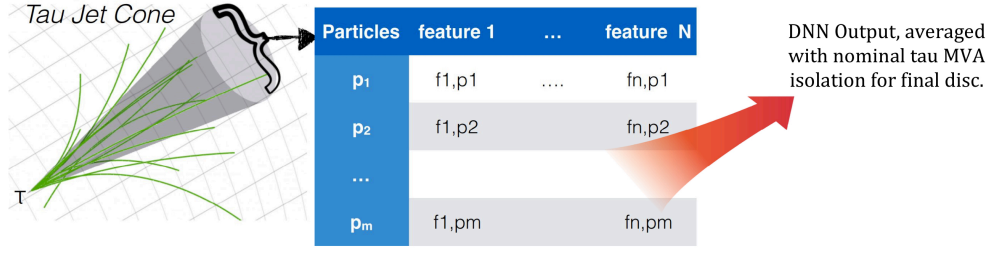


Figure 6.3: Schematic of the DeepPF implementation.

truth value corresponding to the selected category of a given example.

Some variables such as d_z and d_0 are prone to mis-modelling in the tails and so in these cases, a more aggressive pre-processing has been applied.

The selected PFCands are sorted according to particle p_T in ascending order. Up to 32 particles are fed in per a given tau candidate. The dimensionality of the table is 32 by 47, after accounting for the one-hot-encoding of the variable categorical variables listed below. Null vectors are appended to the end of the table when the τ_h candidate has less than 32 associated PFCands.

Training is then performed with KERAS and TENSORFLOW [127, 128]. Several architecture choices were tested, ranging from locally connected NNs to recurrent NNs. In the end, 1-D convolutions were selected for their acceptable performance and the low number of model parameters [Tab. 6.2]. The model was fitted on roughly 100M simulated tau candidates from all types of Standard Model processes. ADAM was the chosen optimization algorithm with $\beta_1 = .9, \beta_2 = .99, \epsilon = 1e^{-8}, \lambda = .0001$. The final results demonstrate a significant improvement in the ability to identify tau leptons at the CMS experiment. Validation of the results is shown in data follows in the analysis sections of the thesis that follows.

PFCand Variable	Pre-Processing (charged pf)	Imputed Value (neutral)	Figure
$p_T(\text{cand})$	$\min(1, \text{var}/500)$	-	A.4
$p_z(\text{cand})$	$\min(1, \text{var}/1000)$	-	A.6
$p_T(\text{cand})/p_T(\tau)$	$\min(1, \text{var})$	-	A.5
$p_z(\text{cand})/p_z(\tau)$	$\min(1, \text{var}/100)$	-	A.7
$\eta(\text{cand})$	$\text{var}/.5$	-	A.8
$\Delta R(\text{cand}, \tau)$	$\text{var}/.5$	-	A.11
$\Delta \phi(\text{cand}, \tau)$	$\text{var}/.5$	-	A.10
$\Delta \eta(\text{cand}, \tau)$	$\text{var}/.5$	-	A.9
$d_z(\text{cand})$	$\min(1, \text{var} /5) * \text{sign}(\text{var})$	(-1 or 1, by pseudo-random number)	A.16
$\sigma(d_z)(\text{cand})$	$\min(1, \text{var})$	1	A.14
$d_0(\text{cand})$	$\min(1, \text{var} /5) * \text{sign}(\text{var})$	(-1 or 1, by pseudo-random number)	A.17
$\sigma(d_0)(\text{cand})$	$\min(1, \text{var})$	1	A.15
$d_z/\sigma(d_z)(\text{cand})$	$\min(1, \text{var} /3) * \text{sign}(\text{var})$	(-1 or 1, by pseudo-random number)	A.12
$d_0/\sigma(d_0)(\text{cand})$	$\min(1, \text{var} /3) * \text{sign}(\text{var})$	(-1 or 1, by pseudo-random number)	A.12
$d_0 d_0(\text{cand})$	Pre-processed d_0	1	-
$d_0 d_z(\text{cand})$	Pre-processed d_0, d_z	(-1 or 1, by pseud-random number)	A.18
$d_0(\text{cand}) \Delta \phi(\text{cand}, \tau)$	Pre-processed $d_0 \Delta \phi$	(-1 or 1, by pseud-random number)	A.19
Charge	One-Hot-Encoded	-	-
PdgId	One-Hot-Encoded	-	-
$(p_T(\text{cand})/p_T(\tau))^2$	-	-	-
NPixHits	$\text{var}/30.$	0	A.22
NHits	$\text{var}/7.$	0	A.23
Lost Inner Hits	One-Hot-Encoded	-	A.21
pfCandPuppiWeight	-	-	A.20
Vertex Quality	One-Hot-Encoded	-	A.27
From PV	One-Hot-Encoded	-	A.24
In Barrel? ($ \eta < 1.4$)	-	-	A.26
High Purity track?	-	-	A.25
HPS Signal Candidate?	-	-	A

Table 6.1: Input variables for DeepPF algorithm. Data to simulation comparisons for every inclusive input distributions after applying a loose MVA isolation selection are checked and linked in the table below.

Internal Name	Keras Operation	Kernal Size	Output Shape	NParameters
input_1	(InputLayer)	-	(None, 47, 32)	0
conv1d_2	(Conv1D)	4	(None, 47, 1024)	132096
leaky_re_lu_2	(LeakyReLU)	-	(None, 32, 1024)	0
conv1d_3	(Conv1D)	4	(None, 47, 512)	2097664
leaky_re_lu_3	(LeakyReLU)	-	(None, 47, 512)	0
conv1d_4	(Conv1D)	4	(None, 47, 512)	1049088
max_pooling1d_1	(MaxPooling1)	-	(None, 23, 512)	0
leaky_re_lu_4	(LeakyReLU)	-	(None, 23, 512)	0
conv1d_5	(Conv1D)	4	(None, 23, 256)	393472
leaky_re_lu_5	(LeakyReLU)	-	(None, 23, 256)	0
conv1d_6	(Conv1D)	3	(None, 23, 256)	196864
max_pooling1d_2	(MaxPooling1)	-	(None, 23, 256)	0
leaky_re_lu_6	(LeakyReLU)	-	(None, 11, 256)	0
conv1d_7	(Conv1D)	3	(None, 11, 64)	49216
leaky_re_lu_7	(LeakyReLU)	-	(None, 11, 64)	0
conv1d_8	(Conv1D)	3	(None, 11, 64)	12352
max_pooling1d_3	(MaxPooling1)	-	(None, 5, 64)	0
leaky_re_lu_8	(LeakyReLU)	-	(None, 5, 64)	0
conv1d_9	(Conv1D)	3	(None, 5, 16)	2064
leaky_re_lu_9	(LeakyReLU)	-	(None, 5, 16)	0
conv1d_10	(Conv1D)	3	(None, 5, 16)	528
max_pooling1d_4	(MaxPooling1)	-	(None, 2, 16)	0
leaky_re_lu_10	(LeakyReLU)	-	(None, 2, 16)	0
flatten_1	(Flatten)	-	(None, 32)	0
dense_1	(Dense)	-	(None, 2048)	67584
leaky_re_lu_11	(LeakyReLU)	-	(None, 2048)	0
dense_2	(Dense)	-	(None, 256)	524544
leaky_re_lu_12	(LeakyReLU)	-	(None, 256)	0
dense_3	(Dense)	-	(None, 64)	16448
leaky_re_lu_13	(LeakyReLU)	-	(None, 64)	0
dense_4	(Dense)	-	(None, 1)	65

Table 6.2: Structure of the convolutional neural network used for DeepPF. From the output shape and operation type one can trivially determine the number of filters, n_C , used in the convolution operation. For the Leaky ReLU a leaking parameter $\alpha = .01$ was selected.

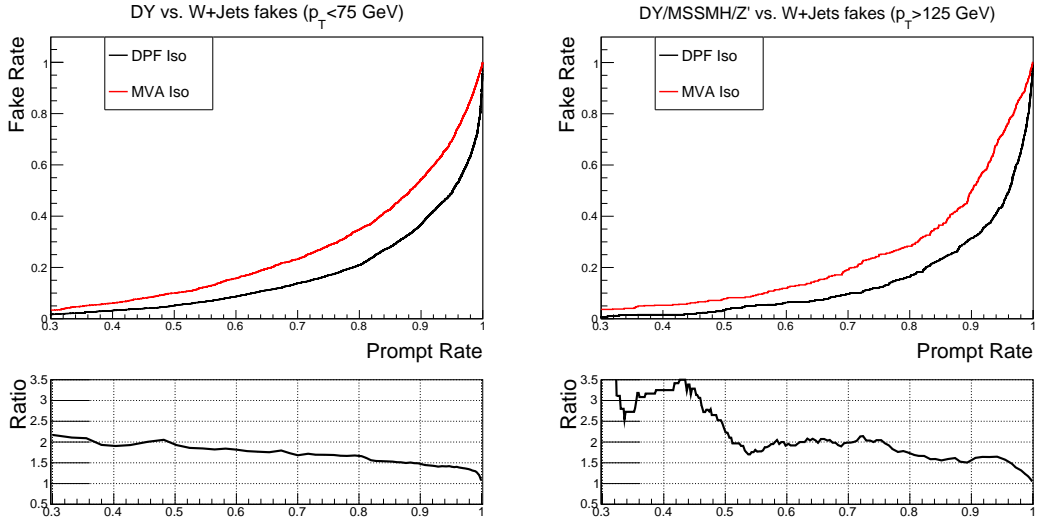


Figure 6.4: Above: Plots demonstrating the performance increase in moving from the previous multivariate approach used by the CMS experiment to the newly proposed DeepPF isolation. The genuine τ_h reconstruction efficiency is shown on the x-axis on the plots above whereas the fake rate is along the y-axis. Low $p_T(\tau_h)$ candidates are shown on the left whereas high $p_T(\tau_h)$ are shown on the right.

Chapter 7

CMS Stau Search Using 2016+2017

Data : Introduction

7.1 Simplified Models at the LHC

Even the MSSM contains far too many parameters for a full scan over parameter space to be performed by analyses at the LHC.

To reduce the complexity of SUSY searches at the LHC a *Simplified Model Parameterization* (SMP) is introduced which dramatically reduces the number of model parameters which must be considered [129, 130]. This simplification is achieved by assuming a 100% branching ratio and by limiting the spectrum of particles involved for the specific SUSY decay under consideration.

SMPs maintain all the relevant kinematic dependencies of the decay while reducing the parameters of the model to only those directly involved in the decay. The cost comes in terms of direct physical interpretability, as the model reduction may imply a nonphysical theory of SUSY. However, this is typically a non-issue as results from simplified models are intended to be reinterpreted by theorists into a physically realizable SUSY model.

This technique is particularly effective because it allows individual experimental results to later be combined. However, there is a pitfall in the implicit assumption that there is no impact on any given analysis from the additional SUSY decay modes removed by the simplification. For example, *control region* (CR) contamination from neglected SUSY process could have non-trivial impacts on background estimation technique employed by a given analysis. Therefore, inclusion of these neglected SUSY contributions could alter the *search region* (SR) predictions. Still, simplified models have seen widespread use at the LHC despite the potential drawbacks.

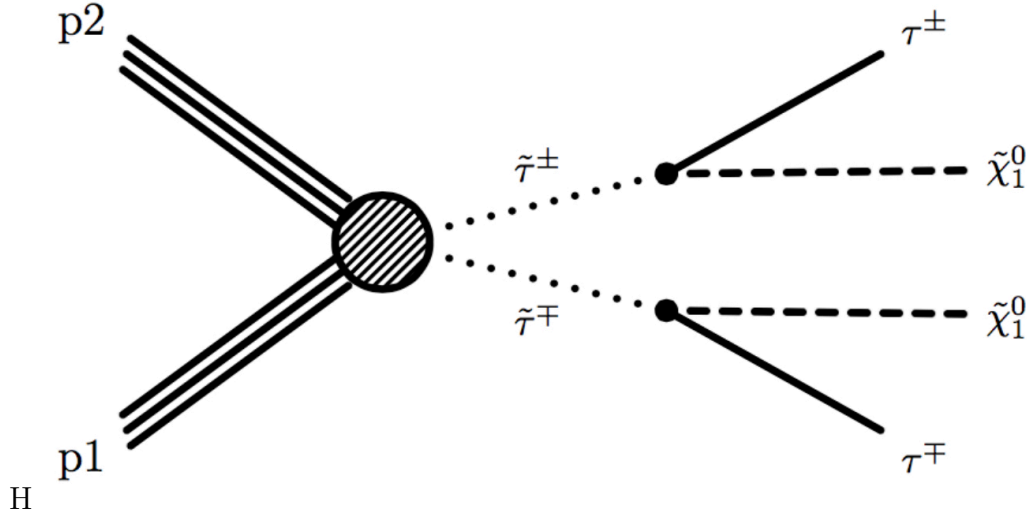


Figure 7.1: Simplified Feynman diagram for direct stau pair production.

7.2 CMS Stau Search Using 2016+2017 Data : Introduction

For the analysis a *Simplified Model Parameterization* (see Sec .7.1) is considered whereby produced staus decay promptly into a $\tilde{\chi}_1^0$ and a τ . The analysis considers the case where both taus decays hadronically, so that each stau decays follows the decay chain $\tilde{\tau} \rightarrow \tau \chi_1^0 \rightarrow \tau_h \nu_{\tau} \chi_1^0$. The resulting LSPs and neutrinos are not detected which yields an final state with two hadronic taus and missing energy. A simplified Feynman diagram for part of the decay chain in the scenario outlined above is pictured [Fig. 7.1].

Improvements to the analysis with respect to the previously mentioned stau search produced by CMS include a Deep Neural Network approach to identifying hadronically decaying tau leptons [Sec. 6.1] as well as additional validation regions (VRs) and enhanced search region binning. The case of left-handed and right-handed tau superpartner production are considered separately, and the case of mass degenerate production is also analyzed. The handedness distinction is important because, as described in further

detail in chapter two, the production cross section and experimental acceptance differs between left/right-handed production [Fig. 2.3].

Monte Carlo simulation generation of the signal processes is done at LO. As per CMS, "The production cross sections are computed at NLO plus next-to-leading-log (NLL) precision for any single generation of left- or right-handed sleptons, and with all the other sparticles assumed to be heavy and decoupled [131, 132]". Thus, the produced signal simulation is scaled to NLO/NLL precision according to latest theoretical calculations.

7.3 Triggers and Datasets

The recorded data for the SRs of this analysis comes from the di- τ_h and p_T^{miss} triggers. A single muon trigger is implemented to collect events for a dedicated τ_h CR [133, 134]. For a detailed description of the functionality of the di- τ_h and p_T^{miss} triggers and datasets used please refer to the appendix [App. B.1, B.2, B.3]. In total 77.2 fb⁻¹ of data collected by the CMS detector from pp collisions at an energy scale of $\sqrt{s} = 13$ TeV are analyzed by the analysis.

7.4 Object Selection

7.4.1 Vertex selection

Application of the following standard CMS selection criteria gives the interaction vertices reconstructed in an event:

- The vertices must come from fits to trajectories of reconstructed particle tracks with positive χ^2 values.
- There are at least 5 degrees of freedom in the vertex fit.

- The distance, absolute z , along the beam line from the nominal center of the detector is less than 24 cm.
- The transverse displacement, ρ , from the beam line is less than 2 cm.

At least one such vertex must exist in every selected event.

7.4.2 Tau candidate selection

The main Standard Model backgrounds after the baseline selection consist mainly of QCD multijet, W+jets, Z+jets, and top quark events. Separating the background into events where both reconstructed taus match to a generator τ_h , and misidentified events, where one or more non-generator matched jets passes the τ_h reconstruction, it is the misidentified background dominates the SRs. Stringent isolation requirements on the τ_h candidates are applied in order to reduce this background.

The selected τ_h candidates first pass HPS reconstruction, a very loose MVA isolation criterion, and electron and muon rejection discriminators [Sec. 4.3]. This *loose* working point corresponds to around 70% efficiency for genuine τ_h , with a p_T dependent misidentification rate of approximately 1-2% for light-quark or gluon jets.

In order to further improve the suppression of the fake jet background while retaining high signal efficiency an additional selection on the previously introduced DeepPF discriminator is included. The criteria used to select a *loose* τ_h candidate in the analysis are as follows [135]:

- $p_T(\tau_h) > 40(45)$ GeV for 2016 (2017)
- $|\eta(\tau_h)| < 2.1$
- trigger-matched to a distinct trigger object (for di- τ_h triggered events)

- HPS decay mode finding: 1-prong, 1-prong+ π_0 , or 3-prong decay
- very loose anti-electron discriminator (againstElectronVLooseMVA6)
- loose anti-muon discriminator (againstMuonLoose3)
- very loose MVA isolation

An additional selection on the DeepPF isolation is applied to select *tight* τ_h candidates. Including the DeepPF isolation reduces fakes by 75-80% which results in a 0.15-0.4% fake rate overall. The efficiency to pass the DeepPF is designed to be constant at 70-80% after applying the loose selection. An approximately linear trend in discriminator threshold vs. p_T is corrected to maintain these constant efficiencies [Fig. 7.2]. The results from the linear fit gives the working points for the DeepPF isolation [Tab. 7.1].

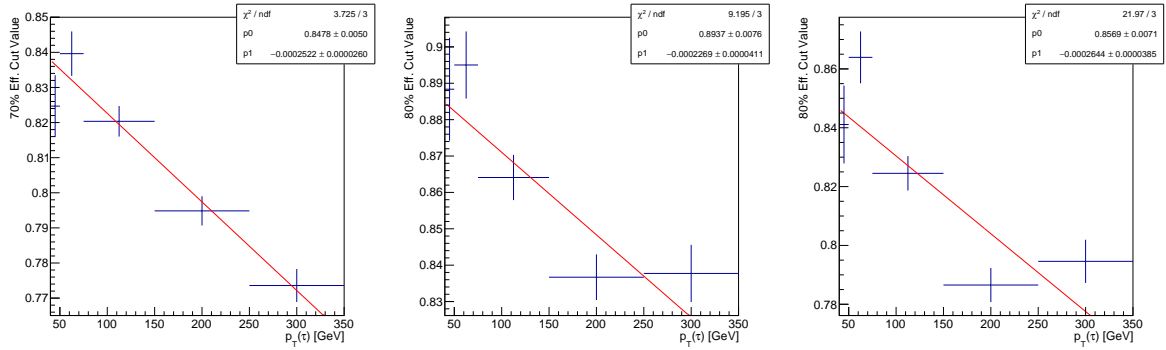


Figure 7.2: From left to right: DeepPF threshold required to maintain a constant 70, 80, and 80% efficiency for 1-prong, 1-prong+ π^0 , 3-prong, respectively, vs. $p_T(\tau_h)$ for a generator matched reconstructed τ_h passing the loose tau selections. A clear linear trend can be seen in these plots and the resulting fit, which is used to obtain the working points for this analysis.

7.4.3 Muon-hadronic tau Control Region

Measurement of the di- τ_h trigger efficiencies and the DeepPF isolation efficiency in data are made via the *tag-and-probe* method in the $\mu\tau_h$ channel. This method uses the a

Decay Mode	Working Point
1-Prong	$\text{DeepPF}(\tau_h) > 0.898328 - 0.000160992 * p_T(\tau_h) \text{ [GeV]}$
1-Prong+ π^0	$\text{DeepPF}(\tau_h) > 0.910138 - 0.000229923 * p_T(\tau_h) \text{ [GeV]}$
3-Prong	$\text{DeepPF}(\tau_h) > 0.873958 - 0.0002328 * p_T(\tau_h) \text{ [GeV]}$

Table 7.1: DeepPF Working Points used in the analysis. They correspond roughly to 70%, 80%, and 80% efficiency for 1-prong, 1-prong plus pion, and 3-prong decay, respectively.

”tag” object to select events enriched with a target ”probe” object. Selected events for the DeepPF scale factor ($\epsilon_{DATA}/\epsilon_{MC}$) measurement require an isolated muon passing a medium cut-based isolation selection [136, 137] with $p_T \geq 24(29)$ GeV in 2016 (2017). In addition the event requires a reconstructed τ_h passing the analyses loose tau requirement and with $p_T > 30$ GeV. Finally, the muon and tau must be of opposite charge.

Corrections are applied to the simulation to fix differences with respect to data in the pile-up distributions, Drell-Yan mass and p_T [Sec. 8.1.3], b-tagging efficiency, and muon isolation and trigger efficiencies. For a full description of the corrections please refer to the appendix [App. B.4].

An estimate of the contribution from QCD events is made in data by inverting the same-sign region after subtracting the expected non-QCD contamination and scaling the yields by 8% to account for the differences in same-sign and opposite-sign production.

A baseline selection is made on the $\mu\tau_h$ visible mass distribution of $M_{vis}(\mu, \tau_h) \geq 40$ GeV. The resulting visible mass distribution is mainly populated by events coming from W/Z +jets with at least one genuine tau. Background predictions are in agreement with data after scaling the τ_h reconstruction efficiency [Fig. 7.3]. A data-to-simulation efficiency scale factor of $0.93(0.96) \pm 0.05$ in 2016 (2017) is evaluated from this sample and is propagated throughout the analysis. Additional studies found no statistically significant evidence to necessitate residual corrections on reconstructed tau transverse momentum or decay mode.

Before the application of the measured isolation SFs to events passing the baseline $\mu\tau_h$ selection, plots are created to show the distribution of the two machine learning scores that are averaged to form the DeepPF isolation discriminator [Figs. A.2, A.3]. The DNN discriminator agrees with data in a manner comparable to the simple MVA discriminator. Moreover, all input variables are well modeled [Sec. A]. In conclusion, the studies conclusively demonstrate the performance improvement of DeepPF isolation.

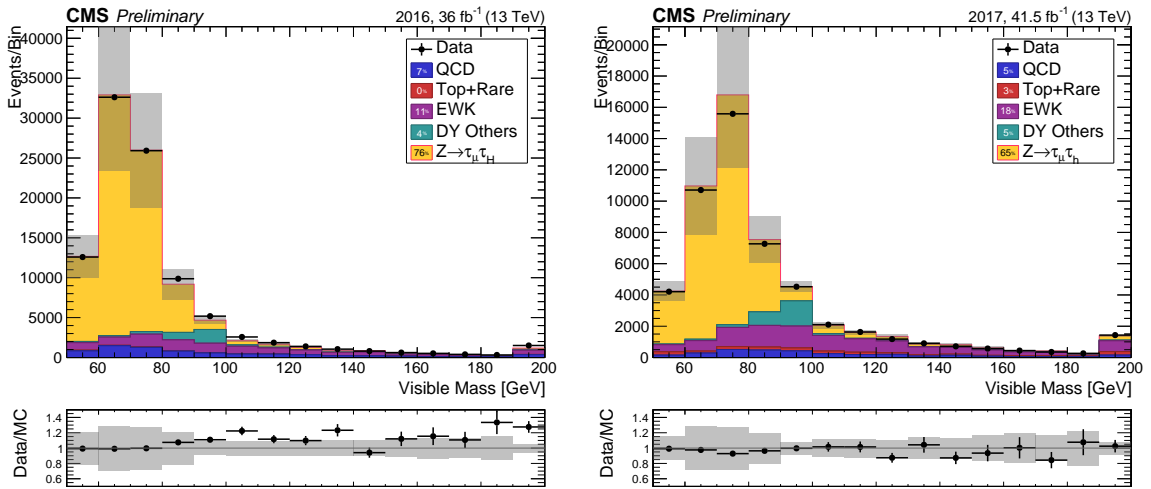


Figure 7.3: Visible mass spectrum for $\mu\tau_h$ events passing the VR selection [Sec. 7.4.3]. The probe τ_h in each plotted event passes the analyses tight isolation working point. On the left a scale factor of 0.93 has been applied whereas a scale factor of 0.96 has been applied on the right.

7.4.4 Lepton veto

To keep the analysis disjoint from the complementary analysis in the semi-leptonic decay channel and to reduce rare standard model backgrounds (dibosons, $t\bar{t}+V$), a veto is applied events containing muons (electrons) passing the selections :

- $p_T \not{e} > 20$ and $|\eta| > 2.4$ (2.5)
- $I_{\delta\beta} < .3$

- transverse impact parameter (d_0) $\leq .045$ cm
- longitudinal impact parameter (d_z) $\leq .2$ cm

In addition, several cuts are made on the particle-flow reconstruction quality of the lepton. It should be noted now that the complementary semi-leptonic analysis will be combined with the analysis in the final interpretation of results.

In addition, events containing a third τ_h candidate passing the loose selection with $p_T > 30$ GeV are vetoed.

7.4.5 Missing transverse momentum

The negative vector sum of all PFCands reconstructed in the event is computed to give the p_T^{miss} . This calculation is refined by including the jet energy corrections [Sec. 4.4]. Mass variables such as m_T and m_{T2} -like variables leverages the p_T^{miss} variable for maximum discrimination in this particular signal topology [Sec. 7.5.2].

A series of p_T^{miss} filters are designed to remove anomalous events occurring in data [Fig. 7.4] [138].

- Primary Vertex Filter – Filters events with no primary vertex.
- CSC Beam Halo Filter – Filters events consistent with particles produced upstream that traverse through the detector along the beam axis.
- HBHE Noise Filter – Filters events containing noise determined to be from HCAL instrumentation.
- HBHEiso Noise Filter – Filters events containing isolated noise in the HCAL.
- ee badSC Noise filter (2016 only) – Filters events containing noise from bad crystals in the ECAL endcap.

- ECAL TP Filter – Filters events containing significant energy deposited into 5 by 5 crystal cells with a dead readout in the ECAL.
- Bad PF Muon Filter – Filters events containing muons with anomalously large reconstructed p_T .
- Bad Charged Hadron Filter – Filters events containing muons reconstructed as hadrons with large p_T .
- ECAL Bad Calibration Filter (2017 only) – Filters events containing noise in the forward HCAL.

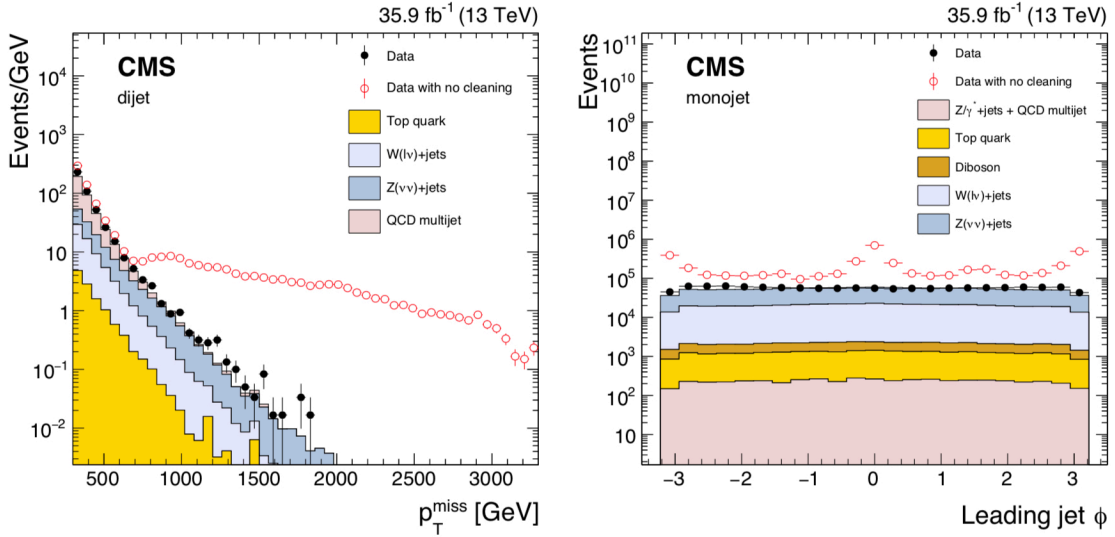


Figure 7.4: The p_T^{miss} (left) and jet ϕ (right) distributions for events passing dijet (left) and monojet (right) selections. The data to simulation agreement is shown with and without the application of the filters described above [107].

In 2017 an issue in the forward ECAL readout resulted in additional noise entering into events. This additional ECAL noise resulted in degraded performance and a significant discrepancy between data and simulation. A new p_T^{miss} calculation ($p_T^{\text{miss}} - V\cancel{2}$) introduced in 2017 replaces the previous definition for that year to mitigate the noise effects. When

calculating p_T^{miss} -V2 soft forward jets with uncorrected $p_T^{uncorr} < 50$ GeV and $2.65 < |\eta| < 3.139$ are neglected in both data and MC. This recipe improves agreement between simulation and data at the cost of degraded p_T^{miss} performance.

By definition the p_T^{miss} -V2 calculation excludes underlying soft activity that can take on substantial values in the tail distributions of background processes with large production cross sections, e.g., Z boson production and misidentified τ_h . A new variable selection, $H_T(\text{Soft, Forward}) \geq 50$ GeV, is introduced to mitigate the increased background coming from this redefinition of p_T^{miss} in the 2017 detector. This selection is also introduced to further protect the analysis from forward ECAL noise effects. Performing a sum over the scalar p_T of the jets neglected from the p_T^{miss} -V2 calculation gives $H_T(\text{Soft, Forward})$. Corrections for discrepancies introduced by selecting on the soft H_T between yields in data and simulation are derived from dedicated scale factors measured in the $\mu\tau_h$ control region [Sec. 7.4.3].

Lastly, one more selection is made to suppress events with fake p_T^{miss} coming from highly mismeasured jets. The selection requires each i th jet, j_i , to pass a minimum angular separation with respect to the p_T^{miss} of $|\Delta\phi(j_i, p_T^{miss})| > 0.25$. Included in this calculation are central jets with $p_T(j_i) > 30$ GeV and $|\eta(j_i)| < 2.4$ and forward jets with uncorrected $p_T^{uncorr}(j_i) > 50$ GeV in the region $2.4 < |\eta(j_i)| < 3.139$.

7.5 Event Selection

7.5.1 Baseline selection

Events passing the trigger selection with two opposite-sign tightly reconstructed τ_h candidates form the analysis baseline. An additional veto on events with electrons or muons and loosely b-tagged jets is applied to suppress Standard Model backgrounds.

7.5.2 Discriminating variables

The $\tilde{\tau} \rightarrow \tau \chi_1^0 \rightarrow \tau_h \nu_\tau \chi_1^0$ decay chain results in different correlation structure between p_T^{miss} and the reconstructed τ_h leptons than in typical Standard Model events. This difference still holds for background events containing true p_T^{miss} . As an example, take highly off-shell $Z \rightarrow \tau\tau \rightarrow \tau_h \tau_h \nu_\tau \nu_\tau$ events, in this case the taus from the decaying Z boson will be produced back-to-back with large momentum. Because the taus are aligned the p_T^{miss} vector will lie along the softer τ_h . However, in signal events the p_T^{miss} is not typically aligned with either τ_h . Variables are introduced to leverage these different correlation structures and to thereby garner heightened signal sensitivity.

Many kinematic discriminating variables were considered for this analysis and in the end only two were chosen, the first of which is the sum of the transverse mass between each τ_h and p_T^{miss} , $\Sigma m_T = m_T(\tau_1, p_T^{miss}) + m_T(\tau_2, p_T^{miss})$. The transverse mass, m_T , is calculated under the assumption that the p_T^{miss} corresponds to a massless particle from the corresponding decaying τ_h , q

$$m_T(q, p_T^{miss}) \equiv \sqrt{2p_{T,q}p_T^{miss}(1 - \cos \Delta\phi(\vec{p}_{T,q}, p_T^{miss}))}. \quad (7.1)$$

Note that the variable Σm_T fails to make use of the distinct decay topology resulting from stau production. Signal events of the analysis have a final state with four missing particles, two LSPs and two neutrinos. Another variable to help discriminate signal from background called the *stransverse mass* (m_{T2}) better utilizes this neglected information [139, 140]. That is to say, m_{T2} is an adaptation of m_T to the scenario with two invisible particles and two observed particles. Because of the similar decay chain, m_{T2} is correlated with the $m(\tilde{\tau})$ and is expected to take on larger values in the case of heavier stau production. Now, the calculation proceeds as a minimization procedure with both leptons and p_T^{miss} as input:

$$m_{T2} = \min_{\vec{p}_T^{X(1)} + \vec{p}_T^{X(2)} = \vec{p}_T^{miss}} \left[\max \left(m_T^{(1)}, m_T^{(2)} \right) \right], \quad (7.2)$$

where the vectors $\vec{p}_T^{X(i=1,2)}$ are the unknown transverse momenta of the two undetected particles that correspond, respectively, which combine with the respective detected hadronic taus ($q=1,2$) to yield transverse mass values $m_T^{(i=1,2)}$. The minimization is performed over all possible momenta of the invisible particles with the constraint that the vectorial sum must equal the \vec{p}_T^{miss} in the event. The m_{T2} distribution is bounded by the mass of the parent particle in the decay, up to detector resolution effects, and so natural kinematic endpoints occur for many Standard Model processes. It should be noted that investigations carried out showed that m_{T2} discrimination performance is significantly degraded by the presence of the two additional neutrinos in stau production – in future analyses it may be possible for a more effective discriminating variable to be constructed.

7.5.3 Cut-and-count selection

The SR selections for this analysis are based on a cut-and-count approach after applying the baseline selection, $p_T^{miss} \geq 50$ GeV, and $|\Delta\phi(\tau_{h,1}, \tau_{h,2})| > 1.5$ [Tab. 7.2]. These requirements suppress many backgrounds, such as boosted Z+jets and misidentified tau events, while retaining high signal efficiency. Selections define the regions on the following quantities: m_{T2} , Σm_T , and the number of reconstructed jets in an event (N_{jets}).

All SRs are required to pass an initial selection of $m_{T2} > 25$ GeV. After applying this minimum m_{T2} requirement, binning is performed along the remaining two kinematic distributions to gain sensitivity towards a large range of $m(\tilde{\tau})$. There are three bins in Σm_T , $\Sigma m_T \in [[200,250), [250,300), [300,\infty)]$ GeV. The events are then further subdivided into two m_{T2} regions: low m_{T2} (25–50 GeV) and high m_{T2} (> 50 GeV). Lastly, events

are split according to $N_{\text{jets}} = 0$, and $N_{\text{jets}} \geq 1$.

Binning on the number of jets is a surprisingly useful new addition to the analysis. This approach is powerful because often background events which pass the SR kinematic and isolation selections have a high jet multiplicity, while the majority of signal events do not have additional jets. In order to retain signal efficiency, all SRs are replicated with $N_{\text{jets}} \geq 1$. The m_{T2} and Σm_{T} distributions are plotted for $N_{\text{jets}} = 0$ [Fig. 7.5].

Ranges of m_{T2} , Σm_{T} , and N_{jets} used to define the SRs used in the $\tau_h \tau_h$ analysis are tabulated.

m_{T2} [GeV]	Σm_{T} [GeV]	N_{jets}
>50	>300	= 0
		≥ 1
	250–300	= 0
		≥ 1
	200–250	= 0
		≥ 1
25–50	>300	= 0
		≥ 1
	250–300	= 0
		≥ 1
	200–250	= 0
		≥ 1

Table 7.2: Definition of the six search regions used in the analysis.

In the final result a statistical combination is performed over all SR bins.

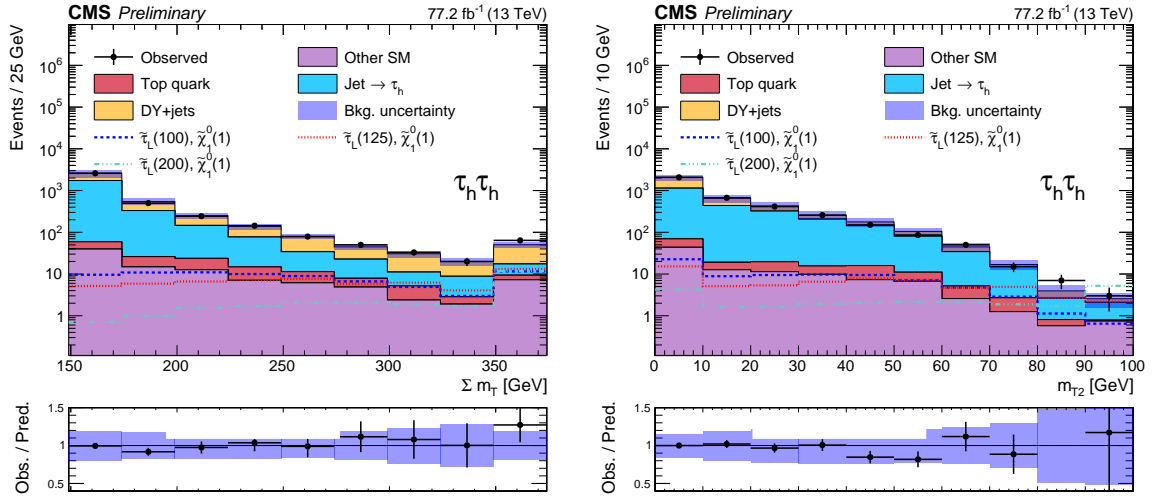


Figure 7.5: Predicted and observed distributions of Σm_T (left) and m_{T2} (right) for events in the combined 2016 and 2017 datasets passing the baseline selection. The expected distribution for three masses of left-handed stau production are also plotted. Shaded in purple is the combined systematic and statistical uncertainty. The methods used for predicting the background events follow in Chapter 8.

Chapter 8

CMS Stau Search Using 2016+2017

Data : Analysis

8.1 Background Estimation Techniques

The most substantial Standard Model background for this analysis originates from QCD multijet and W+jets processes. In these events, one or more of the τ_h candidates come from a hadronic jet and are misidentified as a genuine τ_h . Simulating the rare misidentification of jets is very difficult and error-prone. Thus, this background is estimated in a data-driven manner.

The remaining events consist of two genuine τ_h and the most substantial background among these comes from Drell-Yan+jets (DY+jets) events. Generation of DY+jets simulation proceeds at LO to reduce computation time and so the Z boson mass and p_T spectrum requires corrections using separately measured values from a $Z \rightarrow \mu\mu$ control region.

Finally, we have some other smaller contributions from SM backgrounds, e.g., Higgs boson, di-boson production, and top quark related processes that become more relevant in our exclusive search regions.

8.1.1 Non-prompt and misidentified tau leptons

A side-band of loose tau candidates coming from a mixture of genuine τ_h and hadronic jets ($\text{jet} \rightarrow \tau_h$) is used to extrapolate the expected number of tau candidates passing the full analysis selection. A fake enriched region must be constructed to accurately measure in data the parameterized *fake rate* that is necessary to calculate the prediction [Sec. 8.1.2]. The analysis readily yields such a region by inverting the opposite-sign baseline selection to require two same-charge τ_h leptons.

The jet to τ_h fake rate strongly depends on the mother parton flavor, generator p_T , and the reconstructed decay mode of the jet. Accordingly, the fake rates are measured in bins of p_T , decay mode, and the number of primary vertices (N_{PV}) to capture the effects

of the pileup on the fake rate. Since the underlying parton flavor cannot be determined in data a systematic uncertainty is applied to cover variations in the misidentification rate.

Processes with genuine hadronic taus may easily leak into the loosely isolated side-band because the DeepPF selection efficiency for such objects approximately 70-80%. A technique based in linear algebra called the *fake rate method* is utilized to correctly estimate the fake contribution in the corresponding search region [141].

Three categories are defined as follows: events with both τ_h candidates passing the tight isolation requirement (N_{tt}), events with one passing and one failing the tight isolation requirement (N_{tl}), and finally events with both τ_h candidates failing the tight isolation requirement (N_{ll}).

When provided with a *prompt rate*, $p = \epsilon(\text{genuine } \tau_h)$, measured in simulation and a measured fake rate, f , measured in data, the three observables listed above can be related to three separate categories which cannot be directly observed. These categories are the number of events with two genuine taus (N_{pp}), one genuine and one fake tau (N_{pf}), and the number events with two fake taus (N_{ff}).

Given below is the system of equations relating these quantities:

$$\begin{aligned}
 N &= N_{pp} + N_{pf} + N_{ff} = N_{tt} + N_{tl} + N_{ll}, \\
 N_{ll} &= (1-p)^2 N_{pp} + (1-p)(1-f)N_{pf} + (1-f)^2 N_{ff}, \\
 N_{tl} &= 2p(1-p)N_{pp} + [f(1-p) + p(1-f)]N_{pf} + 2f(1-f)N_{ff}, \\
 N_{tt} &= p^2 N_{pp} + pfN_{pf} + f^2 N_{ff}.
 \end{aligned} \tag{8.1}$$

The background contribution to the term $p^2 N_{pp}$ corresponds to events with two genuine taus and is taken from simulation with corrections applied. What remains to predict is N_{pf} and N_{ff} . These two background contributions are found by inverting the set of

equations above:

$$\begin{aligned} N_{pf} &= \frac{1}{(p-f)^2} [-2fpN_{ll} + [f(1-p) + p(1-f),] N_{tl} - 2(1-p)(1-f)N_{tt}] \\ N_{ff} &= \frac{1}{(p-f)^2} [p^2N_{ll} - p(1-p)N_{tl} + (1-p)^2N_{tt}.] \end{aligned} \quad (8.2)$$

The corresponding backgrounds surviving the tight selection cuts are read off from the equation for N_{tt} to be pfN_{pf} for single-fake events and f^2N_{ff} for double-fake events. In the analysis, the single-fake events are mostly W +jets events, while the double fakes come from QCD multijet processes.

8.1.2 Fake rate measurement in data

A control region to measure the $\text{jet} \rightarrow \tau_h$ fake rate is established by inverting the opposite sign requirement of the analysis baseline selection. A further requirement of $m_{T2} < 40$ GeV is introduced to reduce the contamination of genuine hadronic taus from W +jets in this control region. The remaining genuine hadronic tau contamination is then estimated in simulation and subtracted.

The numerator of the fake rate calculation is the analyses tight τ_h selection whereas the denominator is the loose τ_h selection. The fake rate measurement is binned in τ_h decay mode, p_T , and N_{PV} [Fig. 8.1]. Dedicated studies found a strong variance in fake rate as a function of N_{PV} and the absence of variation in fake rate as a function of m_{T2} .

The closure of the fake rate method is checked across m_{T2} in same-charge di- τ_h events after requiring $p_T(\tau_h, \tau_h) > 50$ GeV to obtain kinematics closer to those of the search region phase space. Excellent agreement is expected since this is the same region that the fake rates were measured. Note, however, that improper parameterization of the

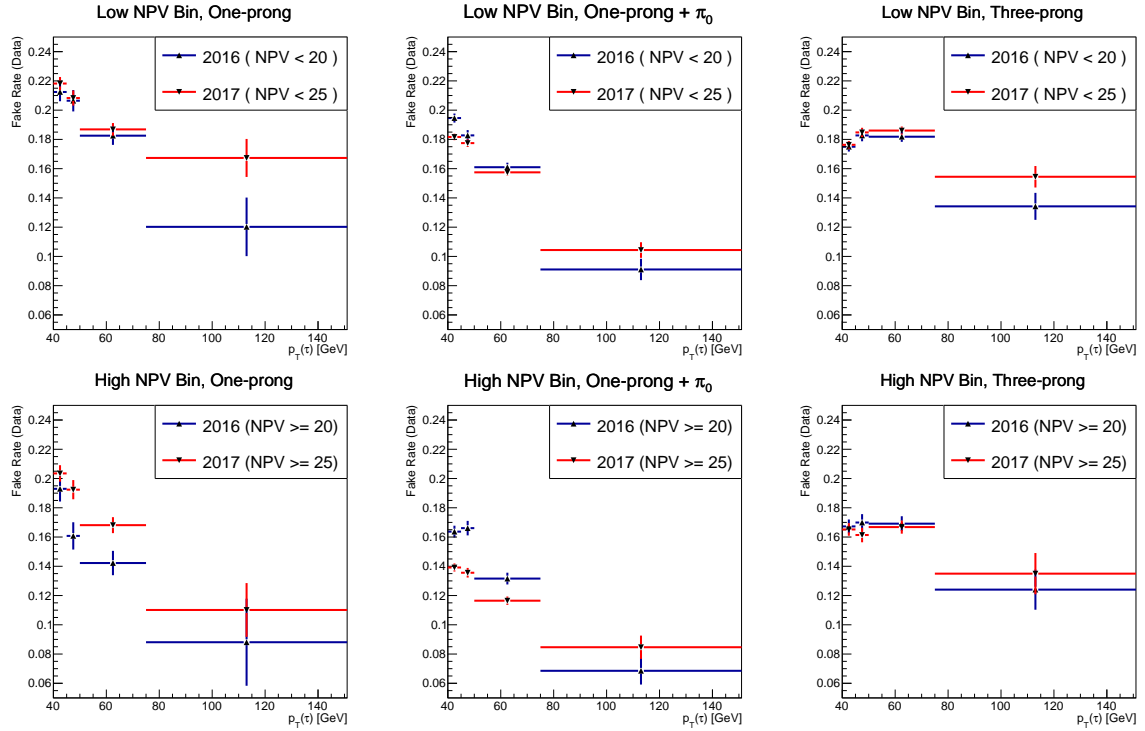


Figure 8.1: Fake rates measured in (2016, 2017) data for the different τ_h decay modes (left: one-prong, middle: one-prong+ π_0 , right: three-prong) as a function of $\tau_h p_T$, for $N_{PV} < (20, 25)$ (upper row) and $N_{PV} \geq (20, 25)$ (lower row). The error bands represent statistical uncertainties.

fake rate and/or genuine hadronic tau efficiency can cause discrepancies across the m_{T2} distribution. This follows because an incorrectly measured fake rate will change event yields according to the relative fraction of QCD and W +jets events, which is a changing quantity as a function of m_{T2} . No significant deviations from prediction are observed and so closure is verified [Fig. 8.2].

8.1.3 Drell-Yan background

Data-corrected simulation is used to produce an estimation of the Drell-Yan background. Disagreement in the tail-end of the distributions of the simulated shape or normalization of the Z boson mass or p_T can have a large impact on the resulting p_T^{miss} and m_{T2} distributions. As previously mentioned, the simulation is only to LO which results in noticeable discrepancies, and so corrections are measured in $Z \rightarrow \mu\mu$. After applying these corrections agreement is observed in the di- τ_h validation region after the baseline analysis selection [Fig. 8.3].

8.1.4 Top quark background

Predictions on top related backgrounds such as $t\bar{t}$, single-top, and $t\bar{t} + V$ with two genuine hadronic taus are estimated in simulation. The most relevant correction to the modelling of this process comes from the modeling of b -tagging. Thus, agreement between efficiency measured in data and simulation is checked by inverting the baseline b -jet veto and applying the measured scale factors. Studies of the tau and p_T^{miss} related kinematics in this region showed no significant evidence for the necessity of any top specific corrections to the simulation [Fig. 8.4].

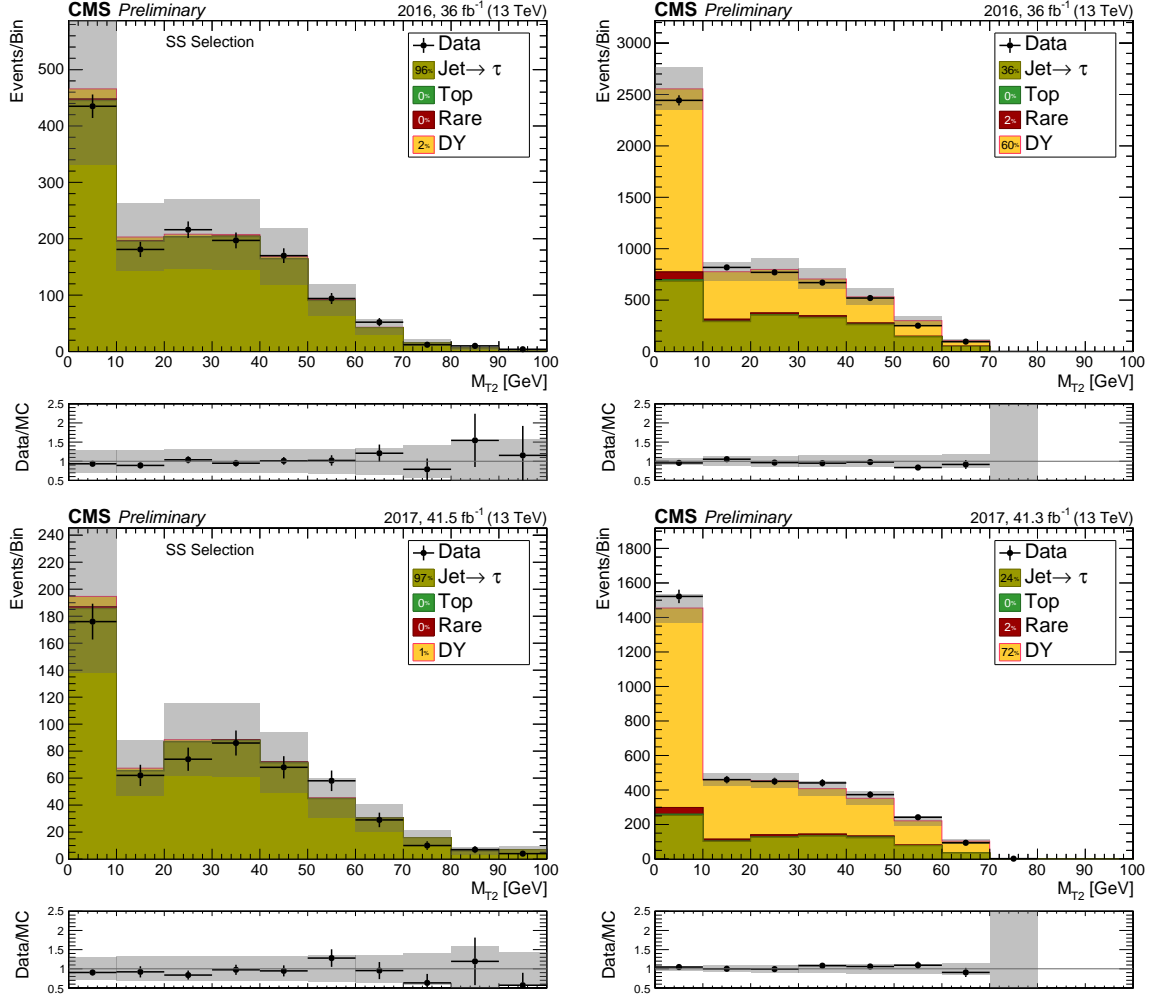


Figure 8.2: Closure test for the fake rate method in same-sign events (left) and validation of the background prediction in opposite-sign (right) events for 2016 (Upper Panel) and 2017 (Lower Panel). An additional requirement of $\Sigma m_T < 250$ GeV or $m_{T2} < 50$ GeV is required for same-sign events to prevent signal contamination. Agreement is observed for the entire m_{T2} spectrum in all cases. Statistical uncertainties along with a 10 % isolation and 30 % fake rate systematic are shaded in grey.

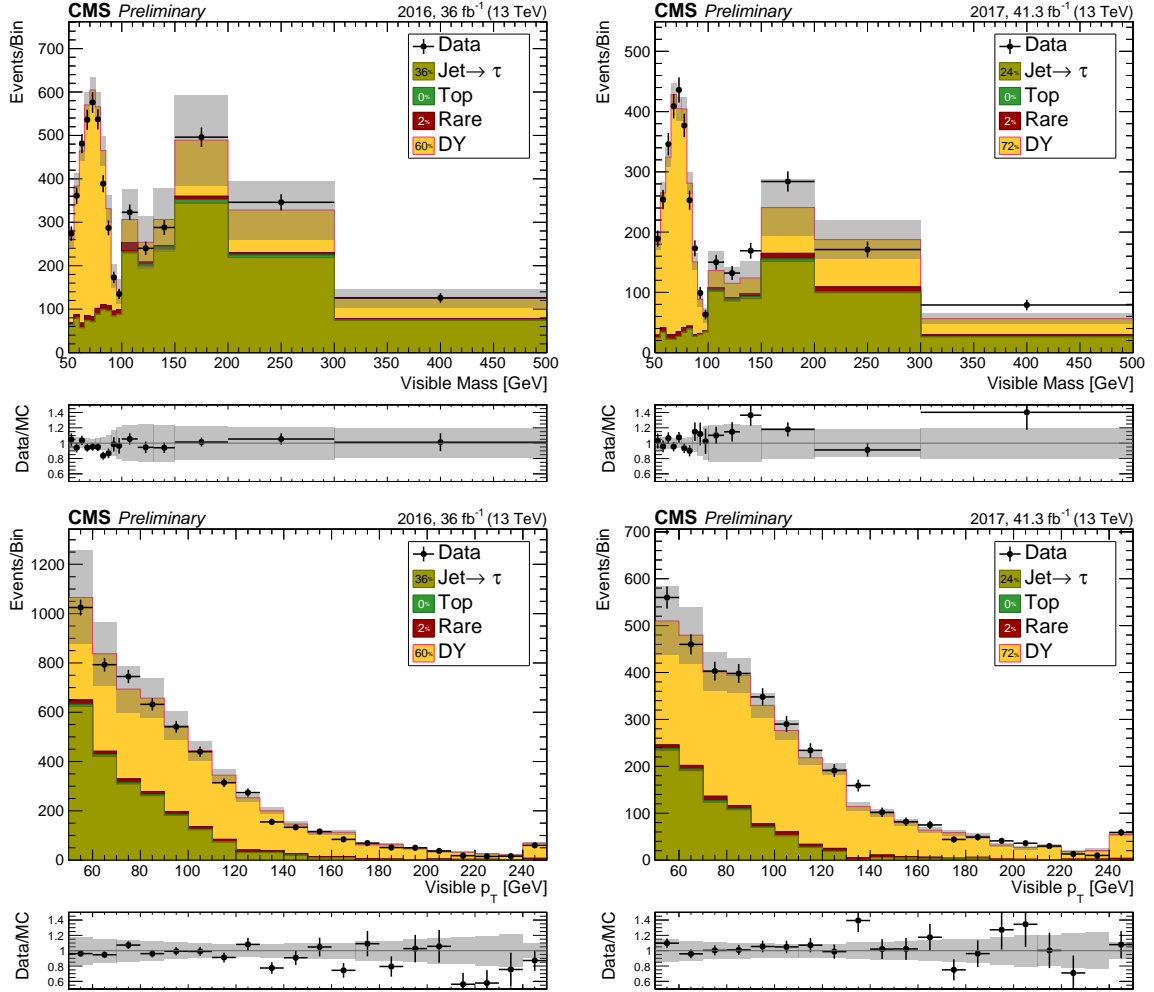


Figure 8.3: The visible mass and the visible $p_T(Z)$ spectrum for di- τ_h events in data and the corresponding prediction for the SM background for 2016 (left) and 2017 (right). The predicted event yields agrees within the experimental uncertainties. The events shown above pass the di- τ_h validation region selection described in 8.1.3. Statistical uncertainties along with a 10 % isolation and 30 % fake rate systematic are shaded in grey.

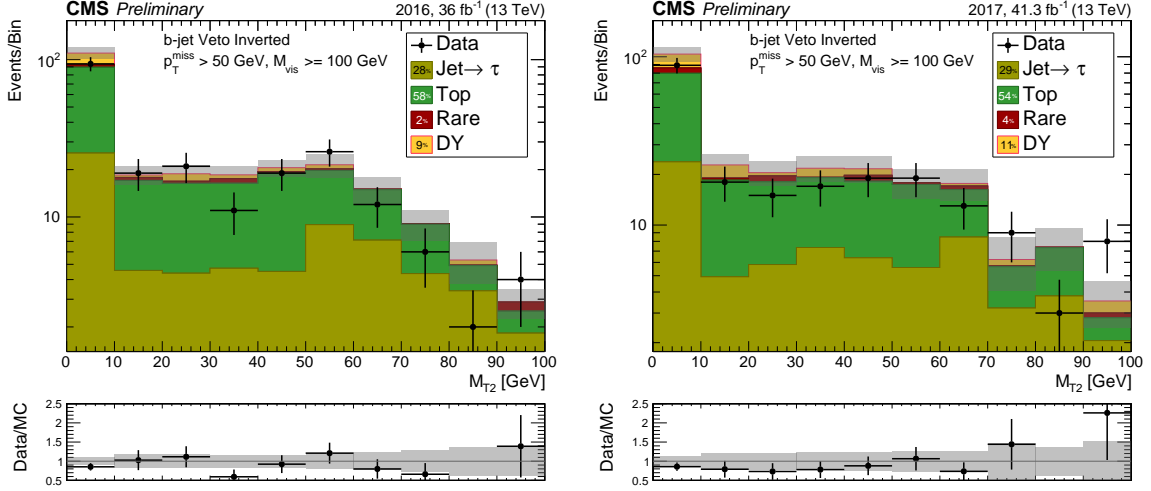


Figure 8.4: Validation of the top background is carried out in the m_{T2} spectrum after applying the baseline selection along with the requirement $p_T^{miss} > 50$ GeV and $M_{vis}(\tau_h, \tau_h) > 100$ GeV. Note that both regions yield a fairly pure selection of $t\bar{t}$ to di- τ_h – a topology which, to the authors knowledge, has not been studied extensively in many analyses at the LHC.

8.1.5 Other Standard Model backgrounds

The remaining Standard Model backgrounds largely consist of Higgs boson production, di/tri-boson production and have relatively small cross sections. Because of their rare production these backgrounds are very difficult to isolate in data; therefore we estimate them purely from the simulation and apply a normalization systematic to account for uncertainties in the rate of production.

8.2 Validation regions of the analysis

We also define several *validation regions* (VRs) with orthogonal selections to corresponding search regions in order to validate the background estimation methods in signal-depleted regions. These validation regions are chosen by variously inverting the *delta-phi* selection ($|\Delta\phi(\tau_{h,1}, \tau_{h,2})| > 1.5$), τ_h pair opposite sign requirement, or b-jet veto, in order to provide regions enriched in the different background processes [Tab 8.1].

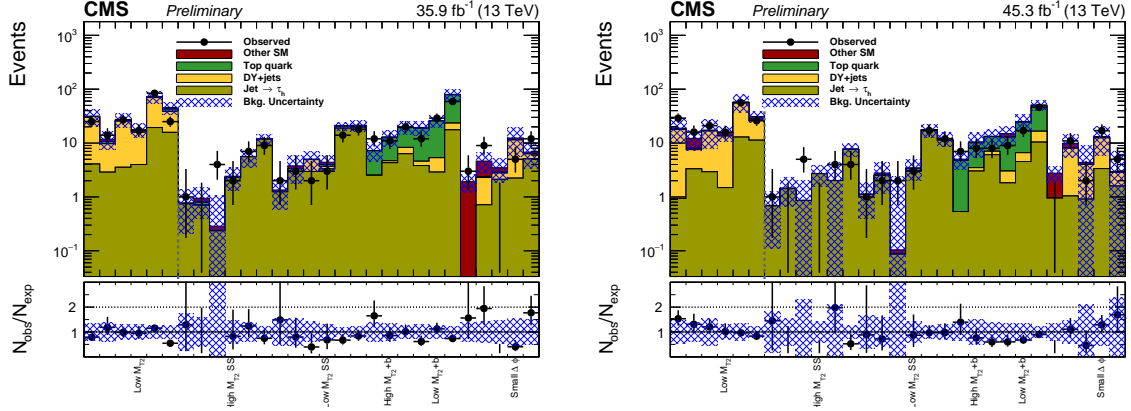


Figure 8.5: Observed and predicted event yields in the SR-specific validation regions for 2016 (left) and 2017 (right). Binning proceeds from low to high Σm_T along the x-axis in the above plots. Bin-by-bin kinematic definitions and printed yields are in the appendix [App. B.6]

Good agreement is seen between validation predictions and data in all search regions [Tab 8.5, App. B.6]

VR Selection Menu	Note : Each region is binned in Σm_T and N_{jets} where applicable
Very Low m_{T2} VR	Inverted Selection $m_{T2} < 25$ GeV
High m_{T2} Same-Sign VR	Inverted sign selection
Low m_{T2} Same-Sign VR	Inverted sign and m_{T2} selection
High m_{T2} b-Enriched VR	Inverted b-jet selections
Low m_{T2} b-Enriched VR	Inverted b-jet and m_{T2} selections
High m_{T2} , Small $\Delta\phi$ VR	Inverted separation selection, $.5 < \Delta\phi(\tau_h, \tau_h) < 1.5$

Table 8.1: Definition of the validation regions used in this analysis.

8.3 Systematic Uncertainties

Statistical errors from limited simulation and parton flavor systematic uncertainties related to misidentified taus are the dominant *pre-fit* uncertainties for the analysis. However, many additional smaller systematic effects must also be taken into account. The numerical value range of these additional systematics are tabulated below [Tab. 8.2]. Raw systematic uncertainties, i.e. pre-fit uncertainties, are pulled and constrained to

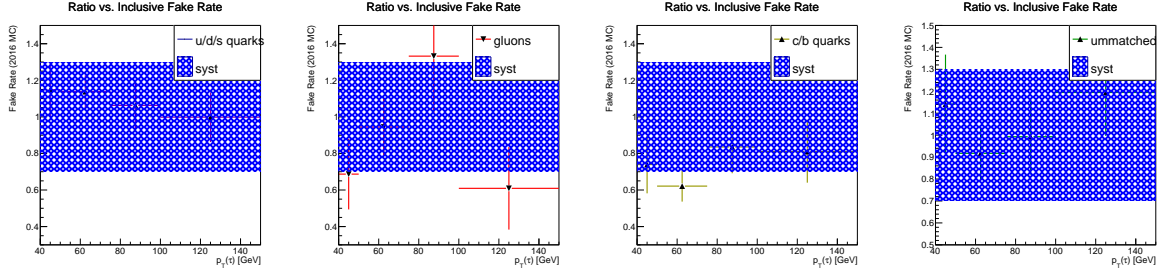


Figure 8.6: The p_T dependence of the fake rate on the parton flavor. A systematic uncertainty of 30% is assigned to cover the dependence of the fake rate on jet parton flavor. This effect is summed in quadrature with the per-bin statistical uncertainty on the fake rate to get the full systematic.

form *post-fit* uncertainties when fitting to the observed data. The fit to data is performed as a likelihood maximization with the systematic and statistical errors treated as nuisance parameters, please refer to the appendix for a full description of the statistical approach [App. B.5].

The fit can cause considerable changes in the magnitude of each nuisance parameter and the overly conservative fake rate estimate is found to be significantly constrained [Fig. 8.6].

Tau isolation uncertainties in simulation are propagated as a constant 5 % uncertainty per τ_h -leg plus an additional factor of $(+.05/- .35) \times p_T(\tau_h)[\text{GeV}]/1 [\text{TeV}]$ for highly energetic taus satisfying $p_T(\tau_h) > 150 \text{ GeV}$. Isolation uncertainty impacts the analysis most greatly after fitting to the data. Uncertainty in the hadronic tau energy scale is also taken into account by shifting the measured $p_T(\tau_h)$ up and down by 1.2 % and propagating the resulting yield variation.

In this same manner the binned jet energy scale and resolution correction uncertainties are propagated through to the final result. Additionally, the impact of unclustered particles on the p_T^{miss} is calculated by varying the unclustered energy across allowable uncertainties and propagating the result.

Also, uncertainties in total luminosity and simulation corrections to b-tagging, pileup,

Drell-Yan mass and p_T propagated through to the final yields. Lastly, additional uncertainties on predicted background rate from the PDFs, differential cross sections, and integrated luminosity are considered. These errors in the measured PDF are propagated along with a 15% normalization uncertainty and a 2.3-2.5 % luminosity systematic.

The signal simulation has two additional uncertainties stemming from factorization and renormalization scale and initial state radiation (ISR). Because the signal is produced at LO it is necessary to apply ISR corrections. After calculating the generator level p_T of the stau pair, p_T^{ISR} , the measured corrections from the $Z \rightarrow \mu\mu$ channel are applied as a shape correction, assuming an on-shell Z decay. Therefore, a systematic uncertainty corresponding to these ISR corrections introduced.

When performing the final fit to the background all statistical effects are treated as uncorrelated whereas all systematic effects per background are correlated across all SRs.

Uncertainty (%)	Signal	Misidentified τ_h	DY+jets	Top quark	Other SM
τ_h efficiency	5–13	-	5–15	1–14	10–51
τ_h energy scale	0.5–12	-	2.6–27	1.2–11	4.1–13
Jet energy scale	0.5–38	-	1.1–19	0.6–13	2.4–14
Jet energy resolution	0.3–22	-	1.9–10	0.7–22	0.2–11
Unclustered energy	0.3–21	-	2.6–30	0.2–6.4	1.7–14
B-tagging	0.2–0.9	-	0.2–23	1.7–25	0.2–1.2
Pileup	0.9–9.1	-	2–22	0.1–24	0.3–25
Integrated luminosity	2.3–2.5	-	2.3	2.3	2.3–2.5
Background normalization	-	-	5–15	2.5–15	15–25
Drell–Yan mass and p_T	-	-	0.2–11	-	-
τ_h misidentification rate	-	4.6–51	-	-	-
Signal ISR	0.2–8.2	-	-	-	-
Renormalization/factorization scale	1.6–7	-	0.7–14	0.7–30	6.7–16
PDF	-	-	0.1–1.2	0.1–0.4	0.1–0.6

Table 8.2: A range is given above for each systematic uncertainty considered in this analysis. A representative signal model of left-handed direct stau production with $m(\tilde{\tau}) = 100$ GeV, $m(\tilde{\chi}_1^0) = 1$ GeV was chosen for the table above. The uncertainty values are listed as a percentage of the predicted event yield.

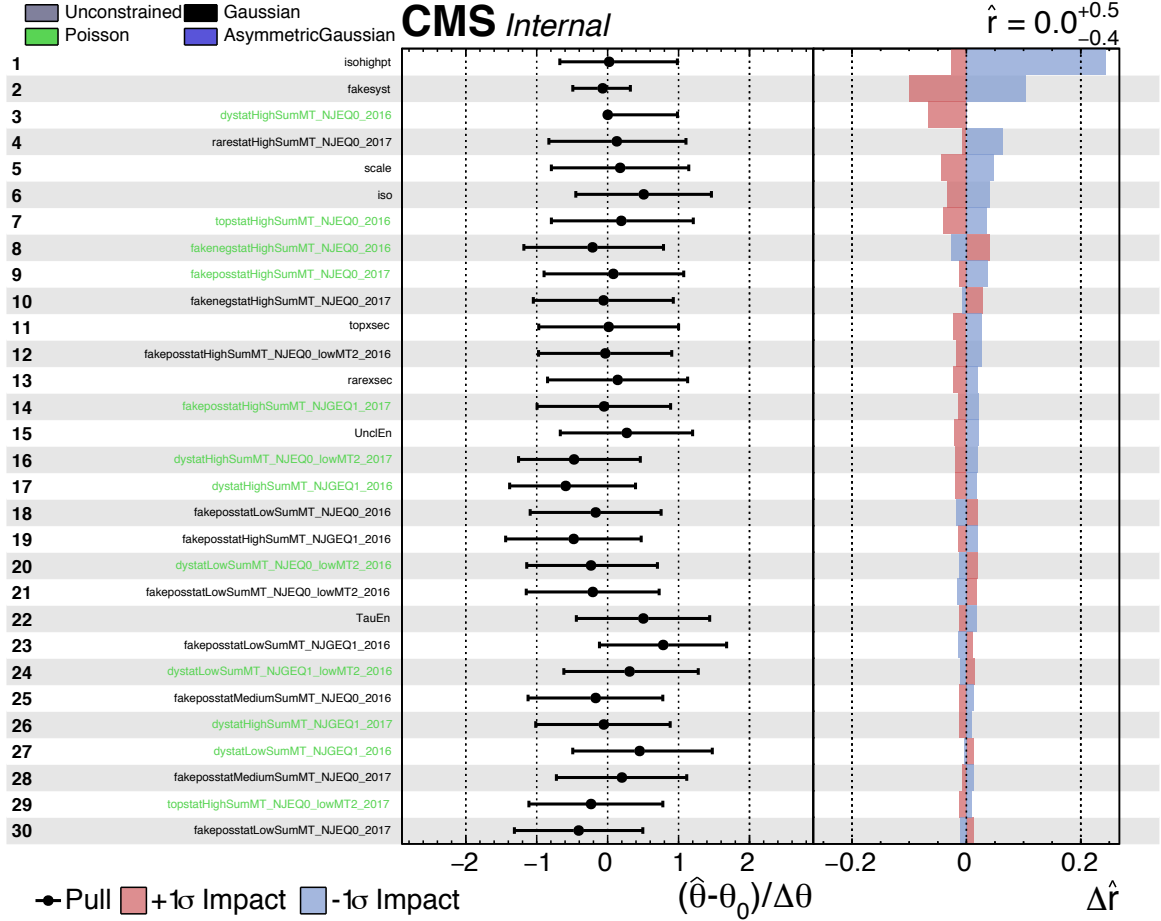


Figure 8.7: The impact ($I(\theta_i) = \delta\mu(\theta_i|\hat{\theta}_{i \neq j} \in \Theta)$) of a nuisance parameter θ_i is the variation it causes in the signal strength multiplier after first fitting all other nuisances with θ_i fixed and then subsequently performing a fit on only θ_i . The pull is how far the central value of the nuisance is skewed by the fit $((\hat{\theta} - \theta_0)/\sigma_\theta)$ [142]. The impact and pull of the top thirty nuisance parameters, rated by post-fit impact, are shown after performing a background-only fit. The largest pre-fit systematic effect is "fakesyst" which corresponds to the fake tau background, whereas after fitting the largest systematic is related to p_T dependent uncertainty of genuine tau isolation, "isohightpt". Additional systematics among the top thirty include Monte Carlo scale, energy scale, process cross-section.

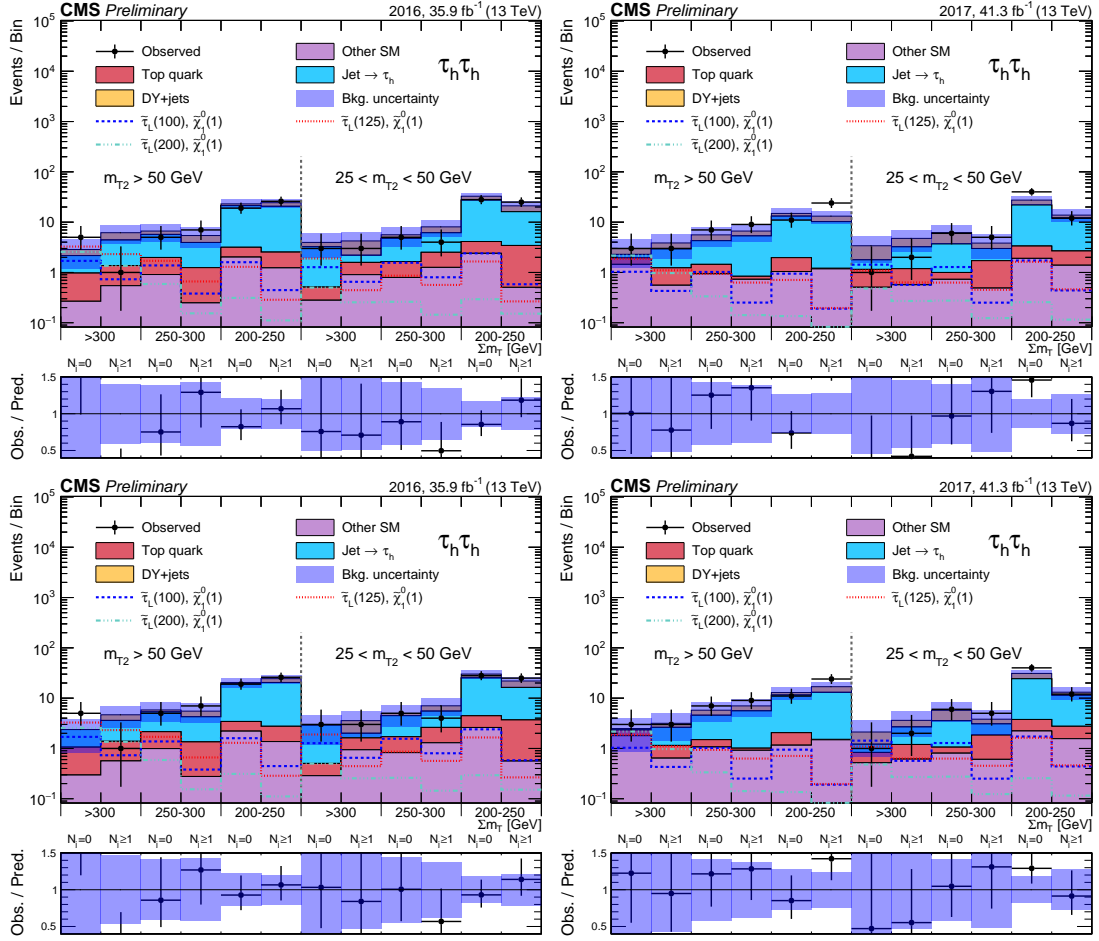


Figure 8.8: Observed and predicted event yields in each SR for 2016 (left) and 2017 (right) before and after fitting to background (top, bottom, respectively). Signal yields are shown for three benchmark left-handed stau production scenarios. The shaded background accounts for the total statistical and systematic uncertainty.

8.4 Results

The observed and predicted event yields are plotted for each SR before and after fitting to the observed data [Fig. 8.8]. These yields are best compared with the combined 2016 and 2017 expected bin-by-bin signal yields [8.7, 8.8]. To help clarify the final signal yields cutflows for left/right-handed $\tilde{\tau}$ pair production across multiple $\tilde{\tau}$ masses for a nearly massless $\tilde{\chi}_1^0$ were produced [Tab. 8.5, 8.6].

Table 8.3: Predicted background yields and observed event counts in all SRs for the 35.9 fb^{-1} of data collected in 2016. The uncertainties listed in quadrature are statistical and pre-fit systematics, respectively. For process with zero predicted background a 68% statistical upper limit is listed. Signal yields for a left-handed $m(\tilde{\tau}_L) = 100 \text{ GeV}$ and a $m(\tilde{\chi}_1^0) = 1 \text{ GeV}$ are listed at the end of the table for comparison.

$m_{T2} [\text{GeV}]$	> 50					
$\Sigma m_T [\text{GeV}]$	> 300		$250 - 300$		$200 - 250$	
N_{jets}	0	≥ 1	0	≥ 1	0	≥ 1
Misidentified τ_h	$1.1 \pm 0.6 \pm 0.6$	$2.9 \pm 0.8 \pm 1.6$	$3.7 \pm 1.0 \pm 2.2$	$2.7 \pm 1.1 \pm 0.5$	$18.2 \pm 2.8 \pm 9.5$	$18.1 \pm 2.9 \pm 6.0$
DY+jets	< 0.7	$1.3 \pm 0.8 \pm 0.5$	$0.5 \pm 0.5 \pm 0.1$	$1.0 \pm 0.7 \pm 0.1$	$1.1 \pm 0.8 \pm 0.2$	$3.3 \pm 1.3 \pm 0.7$
Top quark	$0.7 \pm 0.2 \pm 0.1$	$0.8 \pm 0.2 \pm 0.1$	$1.1 \pm 0.2 \pm 0.2$	$1.0 \pm 0.2 \pm 0.1$	$1.1 \pm 0.3 \pm 0.1$	$1.3 \pm 0.2 \pm 0.3$
Other SM	$0.3 \pm 0.1 \pm 0.1$	$0.5 \pm 0.2 \pm 0.2$	$0.9 \pm 0.4 \pm 0.1$	$0.2 \pm 0.1 \pm 0.1$	$2.0 \pm 0.6 \pm 0.3$	$1.2 \pm 0.4 \pm 0.2$
Total prediction	$2.1 \pm 0.6 \pm 0.6$	$5.5 \pm 1.2 \pm 1.7$	$6.2 \pm 1.2 \pm 2.2$	$4.9 \pm 1.3 \pm 0.5$	$22.5 \pm 3.0 \pm 9.5$	$23.9 \pm 3.3 \pm 6.0$
Observed	5	1	5	7	19	26
$m(\tilde{\tau}_L)=100 \text{ GeV}$	$1.7 \pm 0.2 \pm 0.4$	$0.7 \pm 0.2 \pm 0.2$	$1.4 \pm 0.2 \pm 0.2$	$0.4 \pm 0.1 \pm 0.1$	$1.6 \pm 0.2 \pm 0.3$	$0.4 \pm 0.1 \pm 0.1$
$m_{T2} [\text{GeV}]$	$25 - 50$					
$\Sigma m_T [\text{GeV}]$	> 300		$250 - 300$		$200 - 250$	
N_{jets}	0	≥ 1	0	≥ 1	0	≥ 1
Misidentified τ_h	$2.8 \pm 0.8 \pm 1.8$	$0.5 \pm 0.5 \pm 0.2$	$3.1 \pm 1.0 \pm 1.7$	$3.6 \pm 1.1 \pm 2.0$	$23.5 \pm 2.9 \pm 9.8$	$12.7 \pm 2.4 \pm 4.2$
DY+jets	< 0.7	$1.5 \pm 0.9 \pm 0.5$	$0.4 \pm 0.4 \pm 0.1$	$1.6 \pm 0.9 \pm 0.3$	$4.3 \pm 2.1 \pm 0.7$	$4.5 \pm 1.5 \pm 0.9$
Top quark	$0.2 \pm 0.1 \pm 0.1$	$0.6 \pm 0.2 \pm 0.2$	$0.8 \pm 0.2 \pm 0.1$	$1.3 \pm 0.2 \pm 0.2$	$1.7 \pm 0.3 \pm 0.3$	$2.9 \pm 0.4 \pm 0.3$
Other SM	$0.3 \pm 0.2 \pm 0.1$	$0.9 \pm 0.4 \pm 0.2$	$0.7 \pm 0.4 \pm 0.1$	$1.2 \pm 0.5 \pm 0.3$	$2.4 \pm 0.7 \pm 0.4$	$0.5 \pm 0.2 \pm 0.1$
Total prediction	$3.2 \pm 0.9 \pm 1.8$	$3.5 \pm 1.1 \pm 0.6$	$5.1 \pm 1.2 \pm 1.7$	$7.7 \pm 1.5 \pm 2.1$	$31.9 \pm 3.7 \pm 9.8$	$20.6 \pm 2.9 \pm 4.3$
Observed	3	3	5	4	28	25
$m(\tilde{\tau}_L)=100 \text{ GeV}$	$1.3 \pm 0.2 \pm 0.4$	$0.7 \pm 0.2 \pm 0.2$	$1.6 \pm 0.2 \pm 0.2$	$0.8 \pm 0.2 \pm 0.1$	$2.4 \pm 0.3 \pm 0.4$	$0.6 \pm 0.2 \pm 0.1$

Table 8.4: Predicted background yields and observed event counts in all SRs for the 41.3 fb^{-1} of data collected in 2017. The uncertainties listed in quadrature are statistical and pre-fit systematics, respectively. For process with zero predicted background a 68% statistical upper limit is listed. Signal yields for a left-handed $m(\tilde{\tau}_L) = 100 \text{ GeV}$ and a $m(\tilde{\chi}_1^0) = 1 \text{ GeV}$ are listed at the end of the table for comparison.

$m_{T2} [\text{GeV}]$	> 50					
$\Sigma m_T [\text{GeV}]$	> 300		$250 - 300$		$200 - 250$	
N_{jets}	0	≥ 1	0	≥ 1	0	≥ 1
Misidentified τ_h	$0.2 \pm 0.7 \pm 0.5$	$1.6 \pm 0.8 \pm 0.2$	$2.8 \pm 1.3 \pm 0.3$	$4.5 \pm 1.4 \pm 1.8$	$11.2 \pm 2.3 \pm 4.7$	$9.0 \pm 2.6 \pm 1.1$
DY+jets	< 0.7	$0.5 \pm 0.5 \pm 0.1$	$1.0 \pm 0.6 \pm 0.1$	$1.0 \pm 0.6 \pm 0.1$	$1.3 \pm 0.8 \pm 0.2$	$2.6 \pm 1.0 \pm 0.4$
Top quark	$0.4 \pm 0.3 \pm 0.1$	$0.6 \pm 0.5 \pm 0.2$	$0.3 \pm 0.3 \pm 0.1$	$0.1 \pm 0.1 \pm 0.1$	$0.8 \pm 0.4 \pm 0.1$	< 0.2
Other SM	$1.4 \pm 0.7 \pm 0.3$	$0.6 \pm 0.4 \pm 0.2$	$0.9 \pm 0.5 \pm 0.1$	$0.7 \pm 0.5 \pm 0.1$	$1.0 \pm 0.4 \pm 0.2$	$1.2 \pm 0.6 \pm 0.2$
Total prediction	$2.0 \pm 1.0 \pm 0.6$	$3.2 \pm 1.1 \pm 0.4$	$5.1 \pm 1.5 \pm 0.3$	$6.3 \pm 1.6 \pm 1.8$	$14.3 \pm 2.5 \pm 4.7$	$12.8 \pm 2.8 \pm 1.2$
Observed	3	3	7	9	11	24
$m(\tilde{\tau}_L)=100 \text{ GeV}$	$1.0 \pm 0.2 \pm 0.2$	$0.4 \pm 0.1 \pm 0.1$	$1.0 \pm 0.2 \pm 0.2$	$0.3 \pm 0.1 \pm 0.1$	$0.9 \pm 0.2 \pm 0.1$	$0.2 \pm 0.1 \pm 0.1$
$m_{T2} [\text{GeV}]$	$25 - 50$					
$\Sigma m_T [\text{GeV}]$	> 300		$250 - 300$		$200 - 250$	
N_{jets}	0	≥ 1	0	≥ 1	0	≥ 1
Misidentified τ_h	$0.5 \pm 0.5 \pm 0.1$	$1.9 \pm 0.8 \pm 1.3$	$2.7 \pm 0.9 \pm 1.0$	$1.1 \pm 0.8 \pm 0.3$	$18.6 \pm 3.1 \pm 3.6$	$9.4 \pm 2.1 \pm 1.7$
DY+jets	$1.1 \pm 0.8 \pm 0.3$	$1.0 \pm 0.8 \pm 0.1$	$1.9 \pm 1.4 \pm 0.5$	$0.6 \pm 0.4 \pm 0.2$	$5.0 \pm 2.0 \pm 0.7$	$1.5 \pm 0.7 \pm 0.2$
Top quark	$0.3 \pm 0.3 \pm 0.1$	$0.5 \pm 0.2 \pm 0.1$	$0.2 \pm 0.1 \pm 0.1$	$1.0 \pm 0.6 \pm 0.1$	$1.2 \pm 0.6 \pm 0.2$	$1.1 \pm 0.5 \pm 0.2$
Other SM	$0.5 \pm 0.3 \pm 0.1$	$0.6 \pm 0.4 \pm 0.3$	$0.7 \pm 0.5 \pm 0.1$	$0.5 \pm 0.5 \pm 0.1$	$1.9 \pm 0.7 \pm 0.4$	$1.4 \pm 0.6 \pm 0.4$
Total prediction	$2.4 \pm 1.0 \pm 0.4$	$4.0 \pm 1.2 \pm 1.4$	$5.5 \pm 1.8 \pm 1.1$	$3.2 \pm 1.2 \pm 0.4$	$26.7 \pm 3.8 \pm 3.7$	$13.3 \pm 2.3 \pm 1.8$
Observed	1	2	6	5	40	12
$m(\tilde{\tau}_L)=100 \text{ GeV}$	$1.4 \pm 0.2 \pm 0.4$	$0.6 \pm 0.1 \pm 0.2$	$1.3 \pm 0.2 \pm 0.2$	$0.3 \pm 0.1 \pm 0.1$	$1.7 \pm 0.2 \pm 0.2$	$0.4 \pm 0.1 \pm 0.1$

Table 8.5: Expected number of signal events passing sequential selections after collecting 77.2 fb^{-1} of data. Di- τ_h trigger, reconstruction, isolation, and $p_T(\tau_h)$ requirements create the largest source of signal inefficiency. Note that the scenario under consideration is left-handed production with $m(\tilde{\chi}_1^0) = 1 \text{ GeV}$.

Selection	$m(\tilde{\tau}_L)=100$	$m(\tilde{\tau}_L)=125$	$m(\tilde{\tau}_L)=200$
Loose Isolation Baseline	131.1	105.9	39.5
+ Tight Isolation	67.0	55.6	20.8
+ $p_T^{miss} \geq 50 \text{ GeV}$ and $ \Delta\phi(\tau_h, \tau_h) > 1.5$	55.3	46.8	17.6
+ $m_{T2} \geq 25 \text{ GeV}$	29.1	28.7	12.8
+ $\Sigma m_T \geq 200 \text{ GeV}$	23.8	25.8	12.4
+ $N_j=0$	17.9	17.6	8.3

Table 8.6: Expected number of signal events passing sequential selections after collecting 77.2 fb^{-1} of data. Di- τ_h trigger, reconstruction, isolation, and $p_T(\tau_h)$ requirements create the largest source of signal inefficiency. Note that the scenario under consideration is right-handed production with $m(\tilde{\chi}_1^0) = 1 \text{ GeV}$.

Selection	$m(\tilde{\tau}_R)=100$	$m(\tilde{\tau}_R)=125$	$m(\tilde{\tau}_R)=200$
Loose Isolation Baseline	58.2	41.1	17.1
+ Tight Isolation	30.1	21.5	8.8
+ $p_T^{miss} \geq 50 \text{ GeV}$ and $ \Delta\phi(\tau_h, \tau_h) > 1.5$	25.0	17.9	7.4
+ $m_{T2} \geq 25 \text{ GeV}$	13.7	11.8	5.5
+ $\Sigma m_T \geq 200 \text{ GeV}$	11.3	10.9	5.3
+ $N_j=0$	8.3	7.9	3.5

Table 8.7: Predicted signal yields followed by quadrature listed statistical and systematic uncertainties, respectively, for all SRs. The expected yields are for 77.2fb^{-1} in 2017 simulation and the selected signal points are $m(\tilde{\tau}_L)$ in $[100,125,200]$ GeV and $m(\tilde{\chi}_1^0)=1$ GeV.

Search Region	$m(\tilde{\tau})=100$	$m(\tilde{\tau})=125$	$m(\tilde{\tau})=200$
	$m_{T2} \lesssim 50$ GeV		
$300 < \Sigma M_T, N_J = 0$	$2.7 \pm 0.3 \pm 0.4$	$5.1 \pm 0.7 \pm 1.0$	$4.7 \pm 0.1 \pm 0.8$
$300 < \Sigma M_T, N_J \geq 1$	$1.2 \pm 0.2 \pm 0.3$	$3.4 \pm 0.6 \pm 0.7$	$2.3 \pm 0.1 \pm 0.4$
$250 < \Sigma M_T < 300, N_J = 0$	$2.4 \pm 0.3 \pm 0.3$	$2.6 \pm 0.5 \pm 0.3$	$0.9 \pm 0.1 \pm 0.1$
$250 < \Sigma M_T < 300, N_J \geq 1$	$0.6 \pm 0.1 \pm 0.1$	$1.3 \pm 0.4 \pm 0.2$	$0.3 \pm 0.0 \pm 0.0$
$200 < \Sigma M_T < 250, N_J = 0$	$2.5 \pm 0.3 \pm 0.3$	$2.0 \pm 0.4 \pm 0.3$	$0.4 \pm 0.0 \pm 0.0$
$200 < \Sigma M_T < 250, N_J \geq 1$	$0.6 \pm 0.1 \pm 0.1$	$0.5 \pm 0.2 \pm 0.1$	$0.2 \pm 0.0 \pm 0.0$
$25 \geq m_{T2} \leq 50$ GeV			
$300 < \Sigma M_T, N_J = 0$	$2.7 \pm 0.3 \pm 0.6$	$3.0 \pm 0.5 \pm 0.7$	$1.0 \pm 0.1 \pm 0.2$
$300 < \Sigma M_T, N_J \geq 1$	$1.2 \pm 0.2 \pm 0.3$	$1.1 \pm 0.3 \pm 0.2$	$0.5 \pm 0.0 \pm 0.1$
$250 < \Sigma M_T < 300, N_J = 0$	$2.8 \pm 0.3 \pm 0.3$	$1.5 \pm 0.4 \pm 0.2$	$0.5 \pm 0.0 \pm 0.1$
$250 < \Sigma M_T < 300, N_J \geq 1$	$1.1 \pm 0.2 \pm 0.1$	$1.0 \pm 0.3 \pm 0.1$	$0.3 \pm 0.0 \pm 0.0$
$200 < \Sigma M_T < 250, N_J = 0$	$4.1 \pm 0.4 \pm 0.5$	$3.3 \pm 0.5 \pm 0.4$	$0.5 \pm 0.0 \pm 0.1$
$200 < \Sigma M_T < 250, N_J \geq 1$	$1.0 \pm 0.2 \pm 0.1$	$0.7 \pm 0.3 \pm 0.1$	$0.3 \pm 0.0 \pm 0.0$

Table 8.8: Predicted signal yields followed by quadrature listed statistical and systematic uncertainties, respectively, for all SRs. The expected yields are for 77.2fb^{-1} in 2017 simulation and the selected signal points are $m(\tilde{\tau}_R)$ in $[100,125,200]$ GeV and $m(\tilde{\chi}_1^0)=1$ GeV.

Search Region	$m(\tilde{\tau}_R)=100$	$m(\tilde{\tau}_R)=125$	$m(\tilde{\tau}_R)=200$
	$m_{T2} \lesssim 50$ GeV		
$300 < \Sigma M_T, N_J = 0$	$1.7 \pm 0.1 \pm 0.3$	$2.7 \pm 0.3 \pm 0.5$	$2.1 \pm 0.0 \pm 0.4$
$300 < \Sigma M_T, N_J \geq 1$	$0.7 \pm 0.1 \pm 0.1$	$1.5 \pm 0.2 \pm 0.3$	$1.1 \pm 0.0 \pm 0.2$
$250 < \Sigma M_T < 300, N_J = 0$	$1.2 \pm 0.1 \pm 0.1$	$1.2 \pm 0.2 \pm 0.1$	$0.4 \pm 0.0 \pm 0.0$
$250 < \Sigma M_T < 300, N_J \geq 1$	$0.4 \pm 0.1 \pm 0.0$	$0.4 \pm 0.1 \pm 0.1$	$0.1 \pm 0.0 \pm 0.0$
$200 < \Sigma M_T < 250, N_J = 0$	$1.2 \pm 0.1 \pm 0.1$	$0.8 \pm 0.2 \pm 0.1$	$0.2 \pm 0.0 \pm 0.0$
$200 < \Sigma M_T < 250, N_J \geq 1$	$0.3 \pm 0.1 \pm 0.0$	$0.3 \pm 0.1 \pm 0.0$	$0.1 \pm 0.0 \pm 0.0$
$25 \geq m_{T2} \leq 50$ GeV			
$300 < \Sigma M_T, N_J = 0$	$1.1 \pm 0.1 \pm 0.2$	$1.2 \pm 0.2 \pm 0.3$	$0.4 \pm 0.0 \pm 0.1$
$300 < \Sigma M_T, N_J \geq 1$	$0.5 \pm 0.1 \pm 0.1$	$0.4 \pm 0.1 \pm 0.1$	$0.2 \pm 0.0 \pm 0.0$
$250 < \Sigma M_T < 300, N_J = 0$	$1.1 \pm 0.1 \pm 0.1$	$0.7 \pm 0.1 \pm 0.1$	$0.2 \pm 0.0 \pm 0.0$
$250 < \Sigma M_T < 300, N_J \geq 1$	$0.5 \pm 0.1 \pm 0.1$	$0.3 \pm 0.1 \pm 0.0$	$0.1 \pm 0.0 \pm 0.0$
$200 < \Sigma M_T < 250, N_J = 0$	$1.7 \pm 0.1 \pm 0.2$	$1.0 \pm 0.2 \pm 0.1$	$0.2 \pm 0.0 \pm 0.0$
$200 < \Sigma M_T < 250, N_J \geq 1$	$0.5 \pm 0.1 \pm 0.1$	$0.4 \pm 0.1 \pm 0.1$	$0.1 \pm 0.0 \pm 0.0$

Chapter 9

CMS Stau Search Using 2016+2017 Data : Interpretation

9.1 Limits on Direct Stau Production

The statistical methods described in the appendix are used to interpret the combined 2016 and 2017 observed results [App. B.5].

No significant deviation from the background only hypothesis is observed. The analysis proceeds to set 95% confidence level upper limits on the cross section for direct stau production. In the limit setting procedure, the analysis of this note is combined with an orthogonal analysis targeting the semileptonic channel [143]. The combination tends to improve expected limits by 10-20 % from the all-hadronic only result.

The mass degenerate production scenario with a nearly massless LSP and $m(\tilde{\tau}) \in 90\text{-}150$ GeV is excluded by the combined result. No points are observed to be excluded in the more difficult left-handed scenario, despite the expected upper limit on the cross section residing below the production cross section for $m(\tilde{\tau})=125$ GeV [Fig. 9.1, 9.2].

No mass points for right-handed only production are near to the exclusion curve

and so the results have been omitted for brevity. The ratio of expected cross section upper limit to signal cross section peaks around $m(\tilde{\tau})=125\text{--}150$ GeV, where the trade-off between increased acceptance and decreased cross section is optimal.

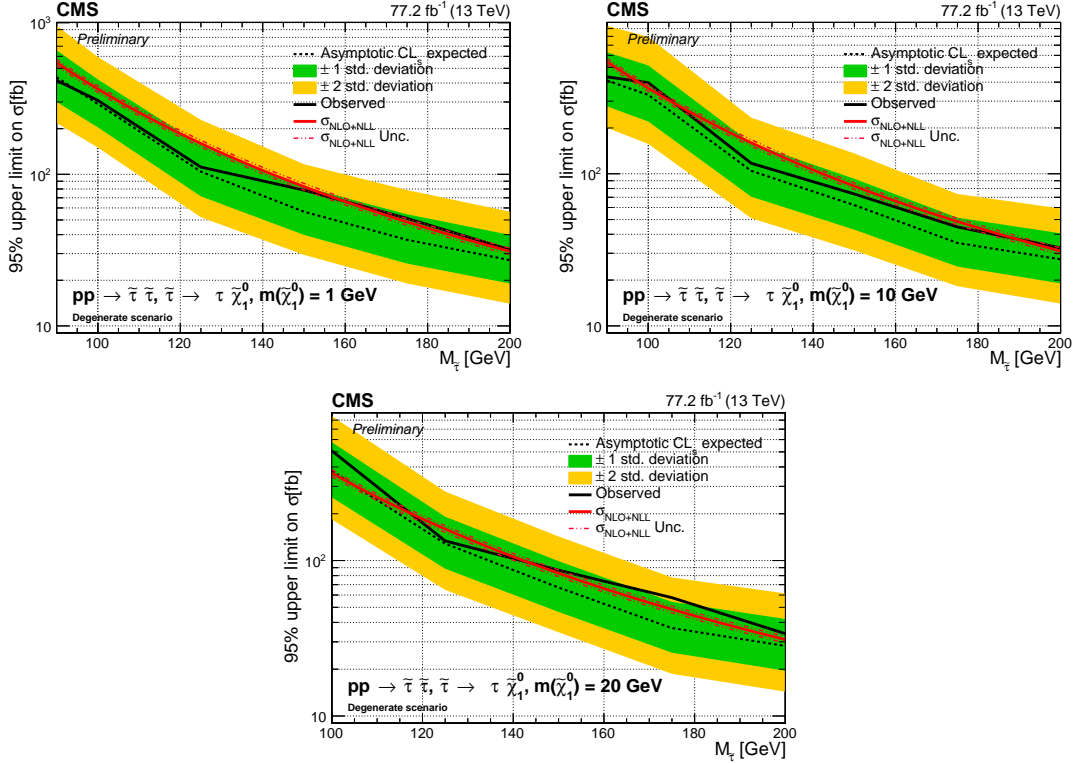


Figure 9.1: Observed and expected 95% upper limits on cross section for degenerate stau pair production. The cross section is plotted as a function of $m(\tilde{\tau})$. The top left, bottom, and top right plots correspond to $m(\tilde{\chi}_1^0)=1, 10$, and 20 GeV, respectively. Expected limits are calculated after fitting to the data with the background only hypothesis. The results are made after performing a statistical combination of 2016 and 2017. The calculated signal cross section and the associated uncertainty is plotted in red. The regions containing 68 % and 95 % of the expected upper limits are plotted in green and yellow, respectively. Lastly, the observed exclusion is plotted as a single black line.

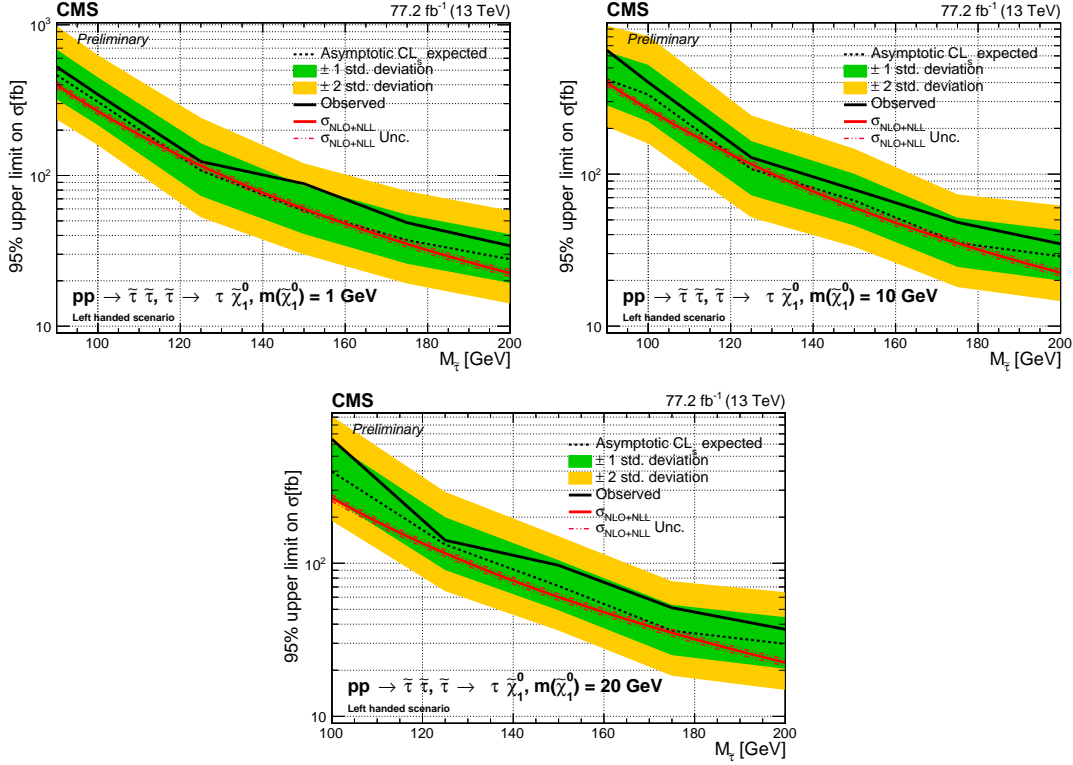


Figure 9.2: Observed and expected 95% upper limits on cross section for left-handed stau pair production. The cross section is plotted as a function of $m(\tilde{\tau})$. The top left, bottom, and top right plots correspond to $m(\tilde{\chi}_1^0)=1,10$, and 20 GeV, respectively. Expected limits are calculated after fitting to the data with the background only hypothesis. The results are made after performing a statistical combination of 2016 and 2017. The calculated signal cross section and the associated uncertainty is plotted in red. The regions containing 68 % and 95 % of the expected upper limits are plotted in green and yellow, respectively. Lastly, the observed exclusion is plotted as a single black line.

Chapter 10

CMS Future New Physics Search : Staus at the HL-LHC

10.1 The High-Luminosity LHC

The ultimate goal of any particle accelerator is to further extend the boundaries of mankind's understanding of the universe. With this in mind, the LHC initially planned to collect a total integrated luminosity of $\int \mathcal{L} dt = 300 \text{ fb}^{-1}$. As was previously discussed, the a priori goal of the LHC was to discover or rule out the existence of the Higgs boson across as wide a mass range as possible [Sec. 3.1.3]. Now, the Higgs boson has been discovered at a mass of approximately 125 GeV and with a verified spin-parity 0^+ . Combining all the recent results from CSM and ATLAS gives successful observation of the following Higgs boson decay modes : $H \rightarrow \tau\tau$, $H \rightarrow b\bar{b}$, $H \rightarrow \gamma\gamma$, $H \rightarrow WW/ZZ$ [144].

Moreover, Higgs boson production with an associated vector boson, $V + H$, and with a pair of top quarks, $t\bar{t}H$, have both been observed – a feat that was not expected to be reached with the amount of data that has been collected [145, 146]. Still, there remains a great deal about the Higgs boson and the Standard Model that is not yet grasped. Coupling of the Higgs to second generation leptons and quarks, i.e., $H \rightarrow c\bar{c}$ and $H \rightarrow \mu\mu$, has not been observed, nor has the exceedingly rare di-Higgs boson production [147, 148]. Moreover, as mentioned in the introduction, the Standard Model is an incomplete and contradictory theory. Beyond the Standard Model physics appears necessary to rectify outstanding issues, but similar null results to the analysis considered in this thesis have been uncovered by every search for new physics produced by CMS and ATLAS. These outstanding questions motivate further accelerator experiments to be carried out, but this is made quite challenging by real-world constraints.

The *High-Luminosity LHC* (HL-LHC) is a proposal to extend the original design specifications of the LHC to collect a total integrated luminosity of $\int \mathcal{L} dt = 3000 \text{ fb}^{-1}$ at the originally anticipated LHC design energy of $\sqrt{s} = 14 \text{ TeV}$ [149]. Increased data

collection will be achieved by increasing the total run-time and the instantaneous luminosity such that an average of 200 pile-up collisions take place per bunch-crossing

The current CMS detector will not withstand these new conditions and so a large part of the detector requires retrofitting in the *CMS Phase-II Upgrade* [150]. Studies of the anticipated radiation dose illustrate that the tracking system and end-cap will require complete replacement during the Phase-II upgrade. The Phase-II systems will need to be radiation hard and capable of mitigating effects from the increased pile-up. Silicon detector systems are well motivated because the intrinsic radiation hardness and well understood properties of silicon. In light of this, the *High-Granularity Calorimeter* will replace the current end-cap system with a novel and highly performant silicon and tungsten, copper, and brass sampling calorimeter. Lastly, an entirely new system called the *MIP Timing Detector* (MTD) is introduced to allow 4-D reconstruction [151]. Together with the new upgrades CMS detector is expected to operate successfully in this harsher environment.

10.2 Searching for Staus at the HL-LHC

The limited sensitivity of the analysis previously introduced in this thesis motivated an upgrade study in the context of the HL-LHC. The analysis is largely limited by the small production cross section and so this study which considers a search for staus at the HL-LHC ("the upgrade study") benefits greatly from the more than one order of magnitude increase in integrated luminosity.

10.2.1 Event simulation and reconstruction

The simulated events for the upgrade study are generated with a computationally efficient simulation called Delphes [Sec.5.2]. Rather than performing a complete simula-

tion of physics, Delphes forms a collection of reconstructed PFCands by assigning user provided resolutions to generator level particles.

Then, after clustering the reconstructed particles into jets, user provided reconstruction and identification rates probabilistically identify muons, electrons, taus and b -jets.

The values provided to Delphes for the upgrade study are derived using a *Phase-II Full Simulation* (Phase-II FS) based on the Run-II CMS Full Simulation (Run-II FS) workflow with the upgraded detector in a $\langle N_{PU} \rangle = 200$ environment.

A detailed list of the Monte Carlo simulation samples, the total number of simulated events, and the cross section used in the upgrade study are given [Tab. 10.1].

Table 10.1: Monte Carlo simulation samples for Phase II (“YR samples”) together with the corresponding cross sections.

Type	Sample name	N_{Events}	Cross section [pb]
DY+jets	DYJetsToLL_M-50_TuneCUETP8M1_14TeV-madgraphMLM-pythia8	400M	5765.4
W+Jets	W0JetsToLNu_TuneCUETP8M1_14TeV-madgraphMLM-pythia8_200PU/	80M	47380
W+Jets	W1JetsToLNu_TuneCUETP8M1_14TeV-madgraphMLM-pythia8_200PU/	80M	10370
W+Jets	W2JetsToLNu_TuneCUETP8M1_14TeV-madgraphMLM-pythia8_200PU/	NA	2965
W+Jets	W3JetsToLNu_TuneCUETP8M1_14TeV-madgraphMLM-pythia8_200PU/	40M	43
QCD	QCD_Pt-170to300_TuneCUETP8M1_14TeV_pythia8_200PU	30M	137100
QCD	QCD_Pt-300to470_TuneCUETP8M1_14TeV_pythia8_200PU/	40M	9325
QCD	QCD_Pt-470to600_TuneCUETP8M1_14TeV_pythia8_200PU/	40M	809.7
QCD	QCD_Pt-800to1000_TuneCUETP8M1_14TeV_pythia8_200PU/	80M	42.51
QCD	QCD_Pt-1000toInf_TuneCUETP8M1_14TeV_pythia8_200PU/	10M	14.08
Top	TT_TuneCUETP8M2T4_14TeV-powheg-pythia8_200PU	220M	864
Top	ST_tW_antitop_5f_NoFullyHadronicDecays_14TeV-powheg-pythia8_TuneCUETP8M1_200PU	12M	45
Top	ST_tW_top_5f_NoFullyHadronicDecays_14TeV-powheg-pythia8_TuneCUETP8M1_200PU	12M	45
Other SM	Triboson, VVto2l2nu		
Stau	mStau-100_mLSP-[1,25,50,75]_TuneCUETP8M1_14TeV-madgraphMLM-pythia8	2M	0.11358
Stau	mStau-200_mLSP-[1,100,150]_TuneCUETP8M1_14TeV	200k	0.01017
Stau	mStau-300_mLSP-[1,100,200,250]_TuneCUETP8M1_14TeV	100k	0.00216
Stau	mStau-400_mLSP-[1,100,200,300]_TuneCUETP8M1_14TeV	100k	0.00066
Stau	mStau-500_mLSP-[1,100,200,300]_TuneCUETP8M1_14TeV	100k	0.00022
Stau	mStau-600_mLSP-[1,100,200,300]_TuneCUETP8M1_14TeV	100k	0.0001
Stau	mStau-700_mLSP-[1,100,200,300]_TuneCUETP8M1_14TeV	100k	0.00005
Stau	mStau-800_mLSP-[1,100,200,300]_TuneCUETP8M1_14TeV	100k	0.000023

10.2.2 Object selection

Object selection thresholds are chosen to closely mirror the efficiencies of those introduced in Chapters 7-9.

One major difference in jet and therefore lepton reconstruction is extended η coverage provided by the upgraded detector. For the upgrade study the reconstruction range of jets and leptons are extended to $|\eta| < 2.7$.

Selected jets

Pileup Per Particle Identification (PUPPI) jets replace the standard jet collection from Run-II FS. PUPPI jets are also clustered via anti- k_T with a distance parameter of $D = .4$, but the 4-vector contribution of each PFCand is scaled according to a weight assigned by the PUPPI algorithm [152]. Utilizing the PUPPI algorithm enhances the jet energy resolution and greatly reduces the likelihood of reconstructing clusters of pile-up as jets.

Veto leptons

Leptons are chosen according to reconstruction efficiency maps which are applied to selected jets. Selected veto leptons must pass an isolation cut of $I_{\delta\beta} < .3$.

It should be noted Delphes does not introduce fake lepton objects and only makes attempts to identify generator matched jets as leptons.

Identifying b -jets

b -jets are identified from the selected jets according to a loose working point that is approximately 65% efficient for genuine b -jet candidates.

Identifying hadronic taus decays

Hadronic taus are identified from the two leading selected jets, ordered by p_T , with a restriction to $|\eta| < 2.3$ to avoid jets originating from pile-up.

The reconstructed p_T threshold is increased to $p_T(\tau_h) \geq 50$ GeV because of anticipated changes in trigger thresholds. A tighter working is necessary in the upgrade study because tau isolation performance is significantly degraded by increased pile-up. This working point corresponds to a hadronic tau reconstruction efficiency of roughly 30% efficiency for genuine τ_h candidates and approximately .1% for fake candidates.

In order to reduce the statistical error stemming from the limited size of the simulated samples, a technique was developed to dynamically weight each event. Rather than probabilistically selecting hadronic taus from the reconstructed jets, as is the default in Delphes, the product of the leading two jets efficiencies to be reconstructed as hadronic taus creates an additional event weight. Application of such events increases the statistical significance of the sample without changing the method for object selection. For events with two genuine hadronic taus the event weight is decreased by roughly ten, whereas event weights for events with two fake tau candidates are decreased by roughly $1e6$.

10.2.3 Transverse momentum calculation

The p_T^{miss} is defined as the negative vectorial sum of all PF candidates transverse momenta weighted through the PUPPI method.

10.2.4 Upgrade study design

The baseline selection requires two opposite-sign reconstructed tau candidates satisfying $|\Delta\Phi(\tau_h, \tau_h)| > 1.5$ and $p_T(\tau_h, \tau_h) > 50$ GeV.

The search regions are defined as a function of Σm_T , m_{T2} , and number of reconstructed jets, the same three quantities used in the first analysis shown in this thesis. However, the binning structure of the upgrade study has been expanded to 24 bins and

altered to adjust for the new detector environment and increased luminosity [Tab. 10.2]. Moreover, background considerations are grouped as previously defined, with the only exception being that W+Jets and QCD are introduced as dedicated backgrounds. Previously, QCD and W+Jets were estimated with the fake-rate method, but without a dataset to draw from these backgrounds must now be estimated in simulation. A plot showing the distribution of search region variables is produced after applying the baseline selection [Fig. 10.1].

Table 10.2: Definition of the SRs used in the upgrade study. Signal depleted bins (low Σm_T , high m_{T2}) are omitted from the combination. The full list of bins and background yields is presented in Table 10.4.

Variable	Bin 0	Bin 1	Bin 2	Bin 3
m_{T2}	$50 < m_{T2} < 100$ GeV	$100 < m_{T2} < 150$ GeV	$150 < m_{T2} < 200$ GeV	$m_{T2} > 200$ GeV
Σm_T	$400 < \Sigma m_T < 500$ GeV	$500 < \Sigma m_T < 600$ GeV	$\Sigma m_T > 600$ GeV	-
N_{jets}	= 0	> 0	-	-

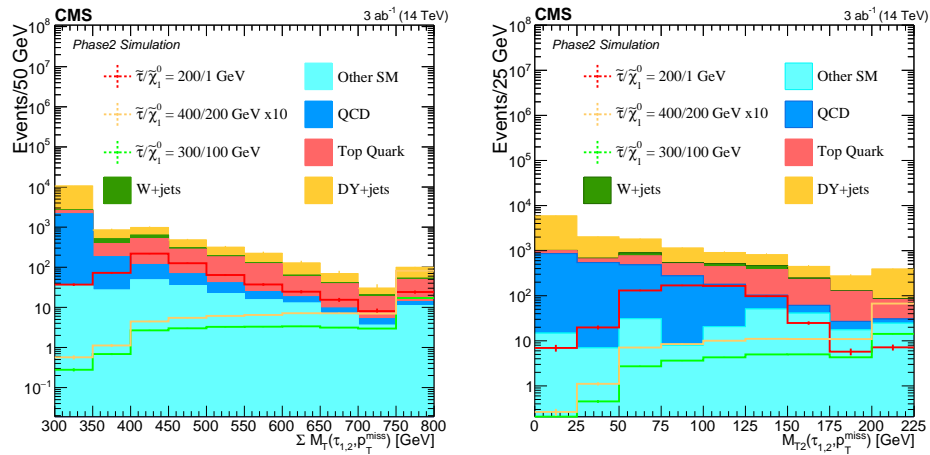


Figure 10.1: Plotted on the Left: Σm_T , and on the Right: m_{T2} , each is shown after applying the baseline selection. Scaled signal yields for mass degenerate stau production with three different $m(\tilde{\tau})$ and $m(\tilde{\chi}_1^0)$ scenarios are shown. Background definitions are aligned with those introduced in the Run-II analysis.

10.3 Adjusting Delphes Simulation

10.3.1 Jet corrections and validation

The resulting jet resolution in Delphes does not agree with that measured in Phase-II FS. Thus, corrections are applied in order to bring Delphes into agreement with Phase II FS. If a reconstructed jet (RecoJet) in Delphes has a corresponding generator-level jet (GenJet) within $\Delta R < .2$, then a jet-by-jet correction is implemented after following the steps below:

- Jet resolution distribution $\sigma_{\text{jet}} = [(\text{RecoJet}) - p_T(\text{GenJet})]/p_T(\text{GenJet})$ is calculated in bins over GenJet $p_T \in [25, 50, \dots, 500]$ GeV and $\eta \in [0, 1.44, 2.7]$ for Phase II FS and Phase II Delphes.
- Two functions are precomputed, $Q_D(\sigma_D)$, which maps a given resolution onto its corresponding quantile in Delphes, and Q_{FS}^{-1} , which takes an input quantile and returns the corresponding Phase-II FS resolution.
- The reconstructed jet p_T in Delphes, $p_T(\text{Reco}_D)$, is recomputed by mapping the reconstructed jets resolution quantile in Delphes onto the corresponding quantile in Phase-II FS, as shown below

$$p_T(\text{Reco}_D) = (\sigma_D + 1) * p_T(\text{Gen}), \quad (10.1)$$

$$p_T(\text{Reco}_D) \rightarrow (\sigma_{FS}|_{Q_{FS}(\sigma_{FS})=Q_D(\sigma_D)} + 1) * p_T(\text{Gen}), \quad (10.2)$$

$$= (Q_{FS}^{-1}(Q_D(\sigma_D)) + 1) * p_T(\text{Gen}). \quad (10.3)$$

Comparisons between the uncorrected and corrected jet p_T are made using a QCD sample with a flat \hat{p}_T distribution, after selecting 100 GeV $\leq p_T(j_1) \leq 500$ GeV and

$p_T(j_2) > 50$ GeV to mirror the upgrade studies phase space [Fig. 10.2]. The agreement between Delphes and Phase-II FS is noticeably improved for high p_T jets – objects which are typical in the final states of the upgrade study. Furthermore, inclusive jet p_T , H_T and H_T^{miss} distributions are compared in a similar manner.

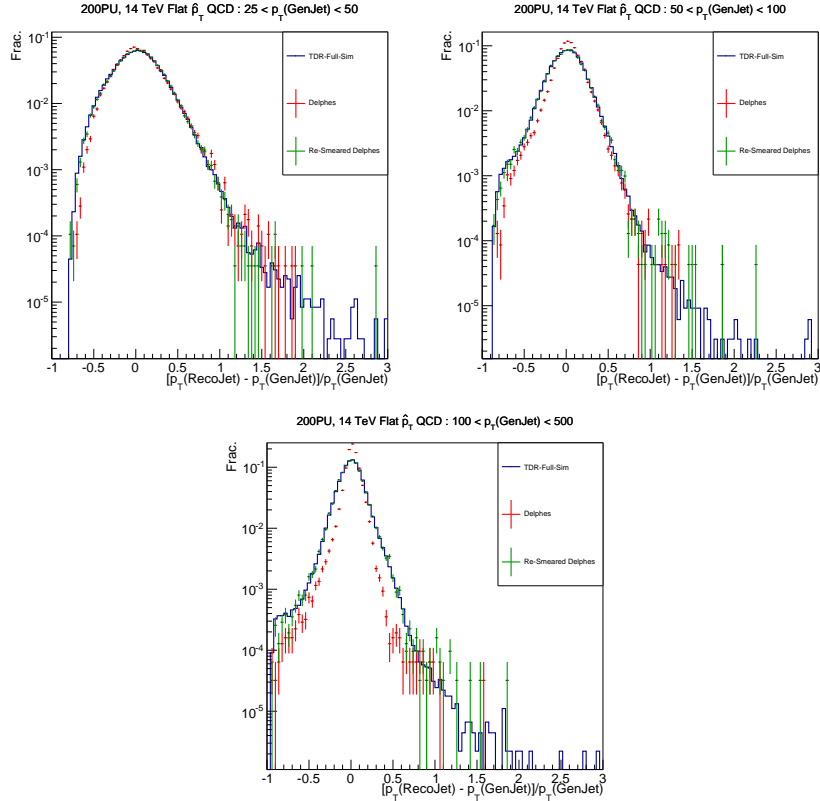


Figure 10.2: Comparison of jet resolution between corrected (uncorrected) Delphes in red (green) and Phase-II FS in blue for three bins of generator jet p_T . The corrections grow more substantial at higher energies.

The greatest improvement in agreement comes in the tails of H_T^{miss} [Fig. 10.3]. Note that all modifications of jet p_T are propagated to the p_T^{miss} according to the prescription described in earlier chapters.

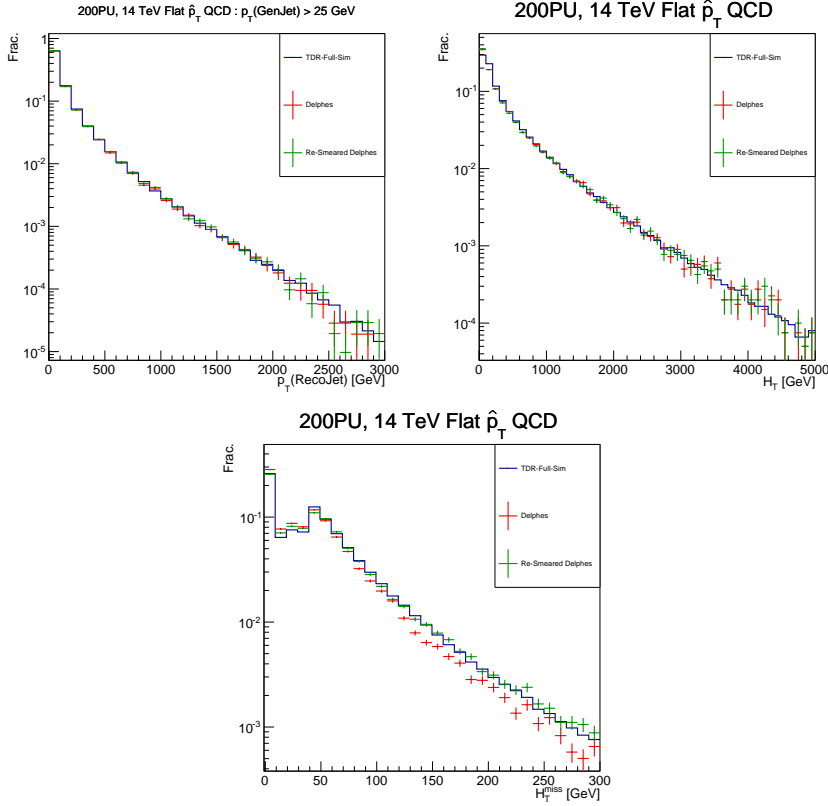


Figure 10.3: Comparison of inclusive jet p_T , H_T and H_T^{miss} between corrected (uncorrected) Delphes in red (green) and Phase-II FS in blue on the upper left, upper right and bottom, respectively.

10.3.2 Muon and electron reconstruction validation

Validation of muons and electrons is carried by comparing simulated Drell-Yan, $Z \rightarrow \ell\ell$, in Delphes and Phase-II/Run-II FS. After selecting events consistent with Z production the p_T distribution for the leading and subleading electrons or muons are compared [Fig. 10.4]. Good agreement between Delphes and Phase-II FS is observed in the muon final state and so no corrections are applied. While small differences in yields exist for electron identification, the impact was shown to have a relatively negligible impact on the veto applied in this upgrade study.

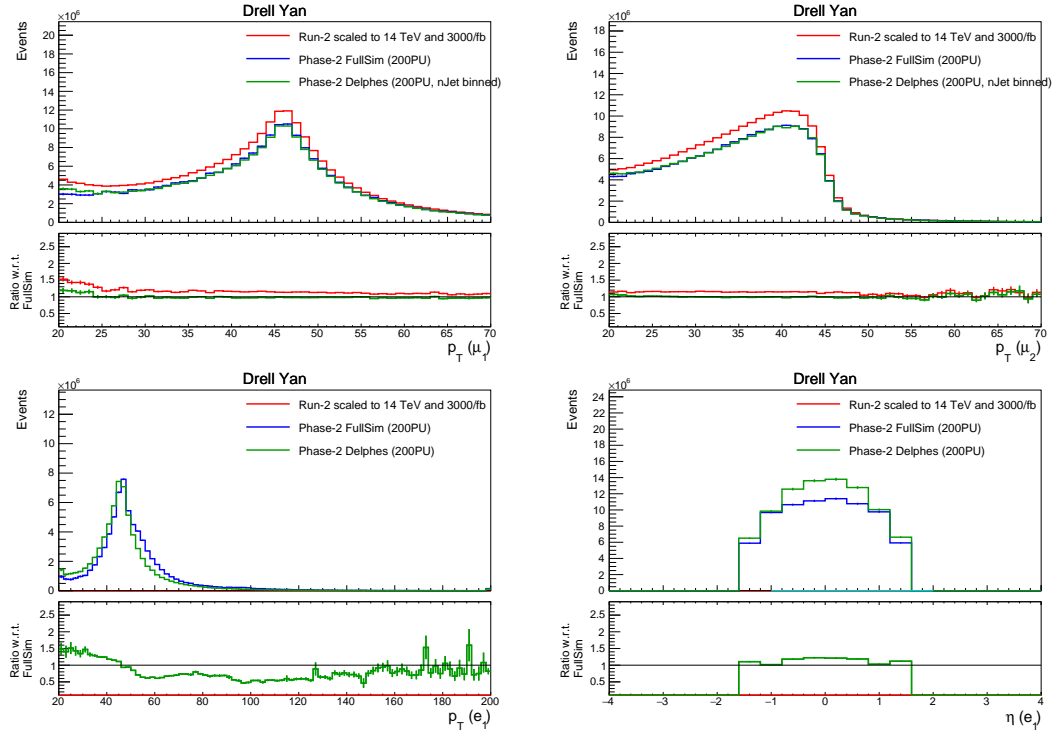


Figure 10.4: Selecting two hard leptons in DY events. Top Panel: Leading muon p_T and the sub-leading muon p_T are shown, on the left and right, respectively. Top Panel: The leading electron p_T and η are shown, on the left and right, respectively. The different distributions are Run-2 events scaled to 14 TeV and 3000 fb⁻¹ (red), Phase-2 FullSim (blue), Phase-2 Delphes (green).

10.4 Systematic Uncertainties

The experimental uncertainties are expected to be dominated by τ_h reconstruction efficiency and fake rate uncertainties. Additional uncertainties stem from jet energy scale and resolution, b -tagging efficiency, and integrated luminosity.

The values for systematic uncertainties were derived by scaling uncertainties to their expected value after collecting a total integrated luminosity of 3000 fb^{-1} and then propagating the values through the upgrade study [Tab. 10.3].

Table 10.3: Summary of the experimental systematic uncertainties.

Systematic source of uncertainty	Value
τ_h efficiency	2.5%
τ_h fake rate	15%
Jet energy scale	1-3.5%
Jet energy resolution	3-5%
b -tagging	1%
Integrated luminosity	1%

10.5 Results

The expected yields after the baseline selection are shown for each SR with an expected contribution from signal [Tab. 10.4].

10.6 Interpretation

While the di- τ_h upgrade study presented here has been found to drive the sensitivity, an additional the semileptonic channel has been included which extends the exclusion bounds by about 60–80 GeV[153].

Table 10.4: Signal region yields for degenerate scenario. The three rightmost columns show the signals, with masses given in the form of $m(\tilde{\tau})/m(\tilde{\chi}_1^0)$

Bin	DY+jets	+jets		QCD	Other	Sum	(200/100)	(500/200)	(700/300)
$m_{T2,0}m_{T,0}N_j,0$	101.79 ± 24.97	58.93 ± 43.95	18.63 ± 4.56	28.78 ± 0.44	3.98 ± 2.86	212.10 ± 50.83	91.35 ± 4.31	1.21 ± 0.05	0.21 ± 0.01
$m_{T2,0}m_{T,0}N_j,1$	76.59 ± 17.49	4.96 ± 0.31	123.23 ± 12.14	75.69 ± 0.66	9.84 ± 3.33	290.29 ± 21.56	49.43 ± 3.17	0.86 ± 0.04	0.17 ± 0.01
$m_{T2,0}m_{T,1}N_j,0$	21.06 ± 9.44	4.23 ± 0.29	4.89 ± 2.39	12.05 ± 0.30	2.61 ± 1.54	44.83 ± 9.87	29.77 ± 2.46	0.76 ± 0.04	0.18 ± 0.01
$m_{T2,0}m_{T,1}N_j,1$	13.52 ± 6.77	1.39 ± 0.13	46.04 ± 7.35	24.25 ± 0.37	-0.67 ± 1.78	85.20 ± 10.00	22.45 ± 2.14	0.61 ± 0.04	0.15 ± 0.01
$m_{T2,0}m_{T,2}N_j,0$	12.95 ± 6.77	3.23 ± 0.26	2.62 ± 1.79	4.87 ± 0.18	-0.33 ± 1.15	23.67 ± 7.01	17.54 ± 1.89	1.31 ± 0.05	0.40 ± 0.02
$m_{T2,0}m_{T,2}N_j,1$	15.85 ± 7.90	1.51 ± 0.45	36.72 ± 6.57	10.34 ± 0.21	3.84 ± 1.70	68.27 ± 10.43	13.89 ± 1.68	1.11 ± 0.05	0.35 ± 0.02
$m_{T2,1}m_{T,0}N_j,0$	142.96 ± 28.82	9.56 ± 0.64	22.99 ± 5.17	19.44 ± 0.49	9.63 ± 2.41	204.57 ± 29.39	84.33 ± 4.14	1.20 ± 0.05	0.20 ± 0.01
$m_{T2,1}m_{T,0}N_j,1$	102.16 ± 20.01	2.06 ± 0.29	121.69 ± 11.91	62.76 ± 0.88	5.65 ± 2.18	294.32 ± 23.41	43.05 ± 2.95	0.77 ± 0.04	0.14 ± 0.01
$m_{T2,1}m_{T,1}N_j,0$	34.34 ± 11.45	1.39 ± 0.21	6.22 ± 2.71	17.17 ± 0.39	0.59 ± 0.89	59.71 ± 11.81	28.38 ± 2.40	1.30 ± 0.05	0.25 ± 0.01
$m_{T2,1}m_{T,1}N_j,1$	19.42 ± 8.29	1.09 ± 0.62	27.56 ± 5.64	31.27 ± 0.46	1.24 ± 1.45	80.58 ± 10.16	16.20 ± 1.81	0.91 ± 0.05	0.17 ± 0.01
$m_{T2,1}m_{T,2}N_j,0$	24.93 ± 10.43	0.57 ± 0.11	2.61 ± 1.79	7.90 ± 0.25	2.09 ± 1.03	38.10 ± 10.64	11.23 ± 1.51	2.10 ± 0.07	0.57 ± 0.02
$m_{T2,1}m_{T,2}N_j,1$	4.78 ± 4.44	0.15 ± 0.03	15.68 ± 4.30	13.41 ± 0.26	1.21 ± 1.03	35.22 ± 6.28	8.01 ± 1.27	1.81 ± 0.06	0.58 ± 0.02
$m_{T2,2}m_{T,0}N_j,0$	0.04 ± 0.01	0.09 ± 0.05	0.01 ± 0.01	0.44 ± 0.07	0.00 ± 0.00	0.59 ± 0.08	0.41 ± 0.29	0.04 ± 0.01	0.01 ± 0.00
$m_{T2,2}m_{T,0}N_j,1$	0.08 ± 0.02	0.01 ± 0.00	2.36 ± 1.59	1.81 ± 0.17	0.00 ± 0.00	4.27 ± 1.60	0.01 ± 0.00	0.02 ± 0.01	0.00 ± 0.00
$m_{T2,2}m_{T,1}N_j,0$	13.63 ± 7.70	0.57 ± 0.12	3.54 ± 2.02	5.98 ± 0.22	0.53 ± 0.51	24.25 ± 7.98	2.07 ± 0.64	0.57 ± 0.04	0.12 ± 0.01
$m_{T2,2}m_{T,1}N_j,1$	3.88 ± 2.51	0.20 ± 0.07	15.52 ± 4.31	13.80 ± 0.35	1.05 ± 0.73	34.44 ± 5.05	2.11 ± 0.64	0.38 ± 0.03	0.08 ± 0.01
$m_{T2,2}m_{T,2}N_j,0$	0.18 ± 0.03	0.39 ± 0.10	0.07 ± 0.01	8.50 ± 0.24	1.09 ± 1.03	10.22 ± 1.06	3.50 ± 0.84	2.91 ± 0.08	0.76 ± 0.02
$m_{T2,2}m_{T,2}N_j,1$	2.03 ± 1.78	0.08 ± 0.03	9.58 ± 3.35	15.30 ± 0.29	-0.44 ± 0.51	26.99 ± 3.80	1.73 ± 0.58	2.19 ± 0.07	0.63 ± 0.02
$m_{T2,3}m_{T,2}N_j,0$	22.49 ± 18.48	0.09 ± 0.04	0.02 ± 0.00	2.25 ± 0.09	-0.48 ± 0.51	24.85 ± 18.49	0.23 ± 0.20	3.57 ± 0.09	1.74 ± 0.04
$m_{T2,3}m_{T,2}N_j,1$	0.12 ± 0.02	0.03 ± 0.01	5.15 ± 2.39	5.13 ± 0.12	0.55 ± 0.51	10.98 ± 2.45	1.10 ± 0.46	3.15 ± 0.09	1.72 ± 0.04

The expected upper limits at the 95% confidence level are calculated using the asymptotic formula, as described [App. B.5], and are plotted along with the 5σ discovery potential [Fig. 10.5].

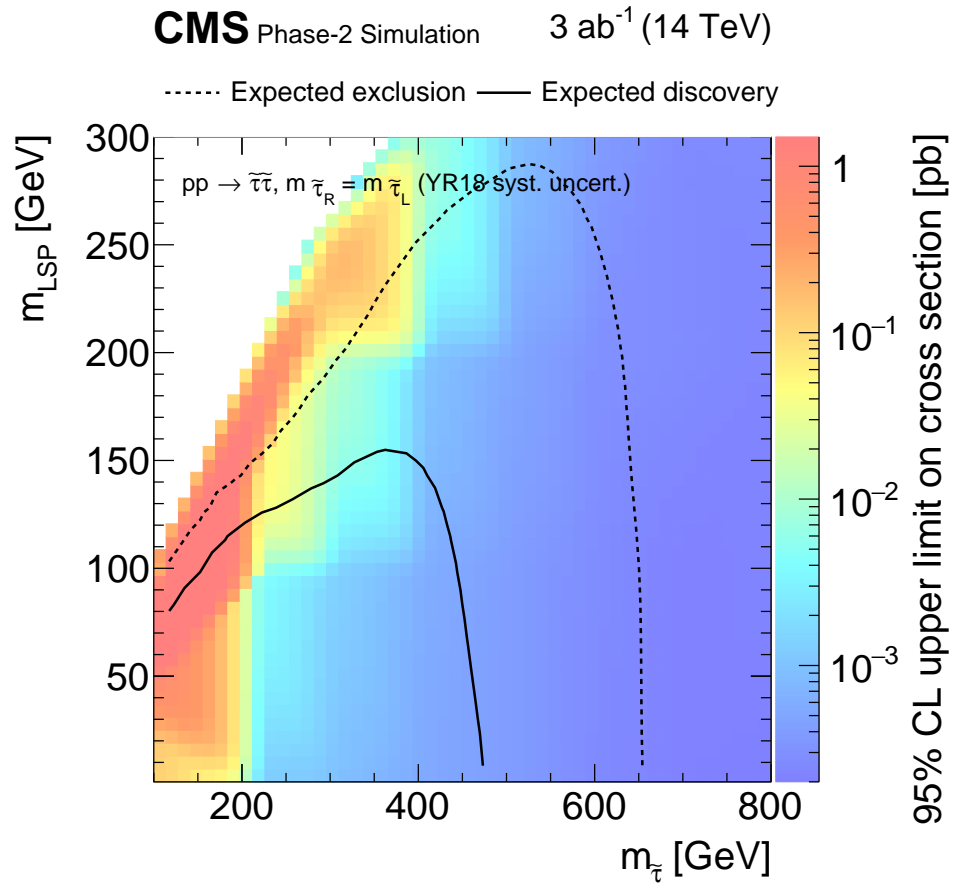


Figure 10.5: The expected upper limits at the 95% confidence level and the 5σ discovery potential for degenerate direct stau production after combining the results from the di- τ_h and semileptonic channels.

Chapter 11

Summary

11.1 Summary and Conclusions

The main analysis presented in this thesis was a search for supersymmetry in final states with two hadronically decaying taus and missing transverse momentum in 13 TeV proton-proton collisions with 77.2 fb^{-1} of data collected by the CMS Detector.

The latest analysis improves upon the first result produced by the CMS experiment by including additional data and by enhancing the analysis techniques employed. The most novel improvement is the application of a new Deep Neural Network architecture to reduce the misidentification rate of hadronically decaying taus. Additional changes were introduced to restructure the search region binning and improve the background validation. These new techniques reduce the expected upper limit on the direct stau production cross section by as much as 50%.

No significant deviation from Standard Model expectations are observed in the data and accordingly a 95% confidence level upper limit on the direct stau pair production cross section is set. Mass degenerate stau pair production is excluded for minimally supersymmetric models (MSSM) with $m(\tilde{\tau}) \in 90\text{-}150 \text{ GeV}$. Similarly, exclusion is expected for left-handed only pair production with $m(\tilde{\tau}_L)=125 \text{ GeV}$. However, no such exclusion is observed in the data.

The currently presented analysis is close to the required sensitivity to rule out much of the phase space for left handed stau pair production with $m(\tilde{\tau}_L) \in 90\text{-}175 \text{ GeV}$. These results suggest including the data collected in 2018 will provide this additional sensitivity.

Moreover, a study was presented using simulation of the High-Luminosity LHC (HL-LHC) environment with the CMS Phase-2 detector. This scenario corresponds 3000 fb^{-1} of data taken at a center-of-mass energy of 14 TeV. The study shows sufficient sensitivity to formally expect discovery of mass degenerate direct stau pair production for $m(\tilde{\tau}) \in$

[100, 650 GeV].

Appendix A

Appendix B

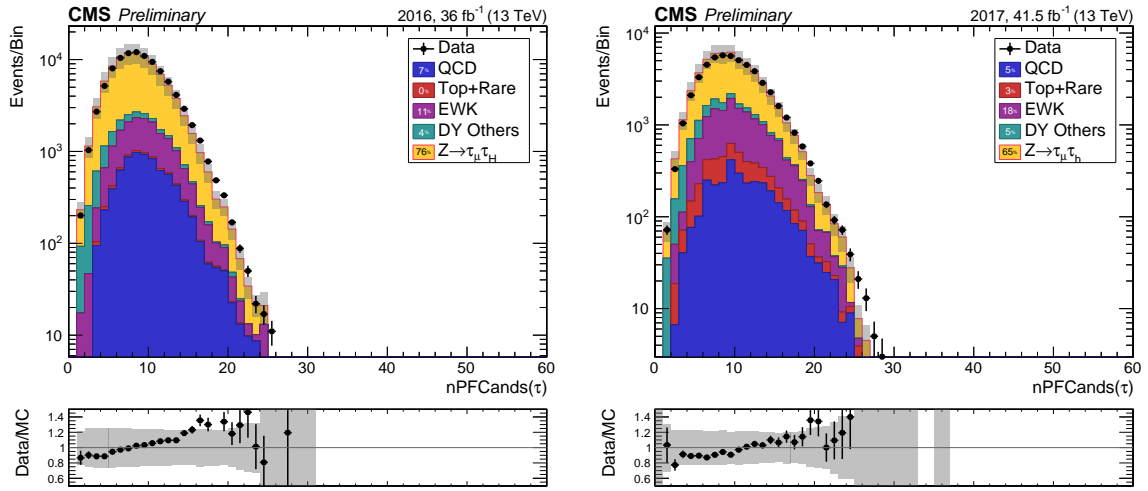
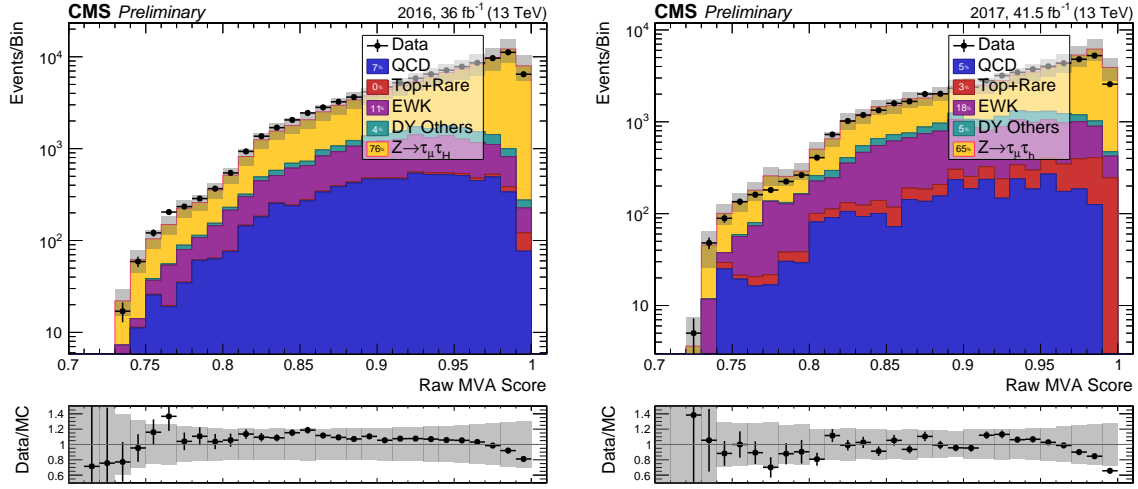
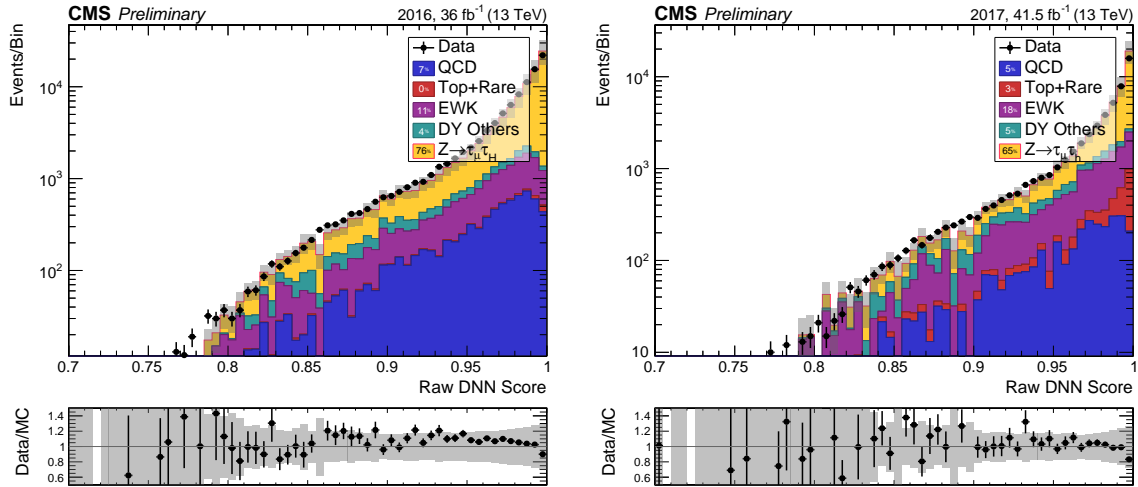
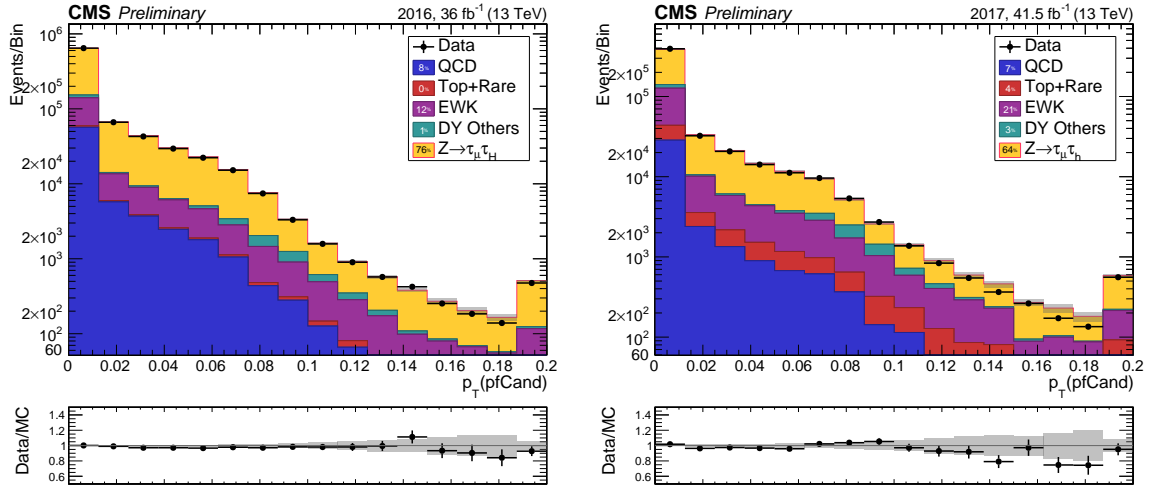
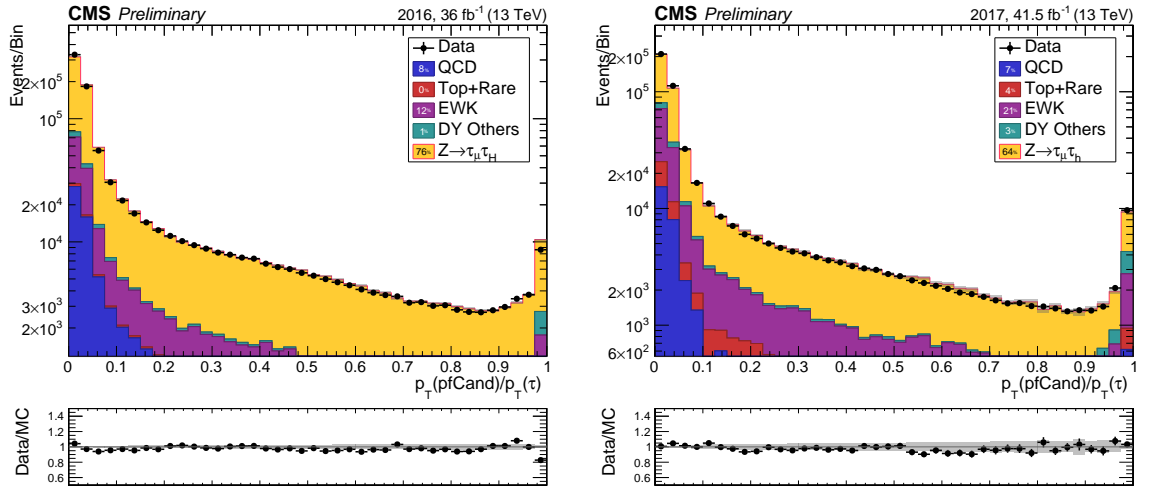
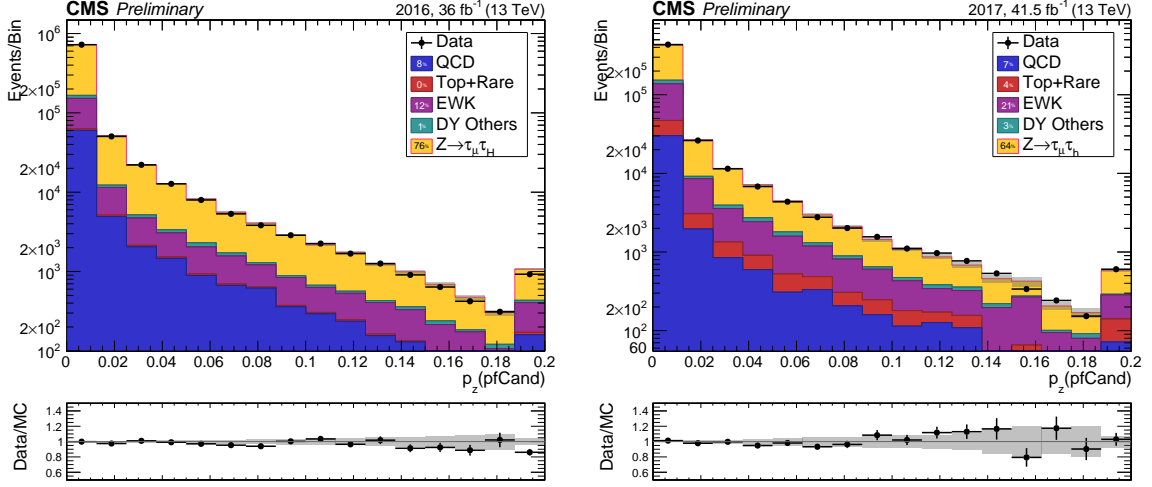
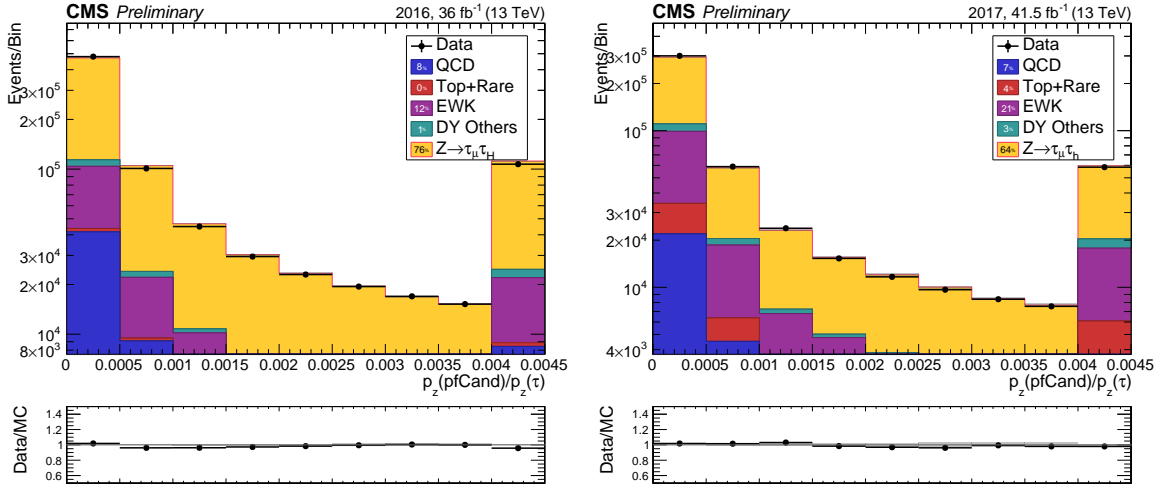
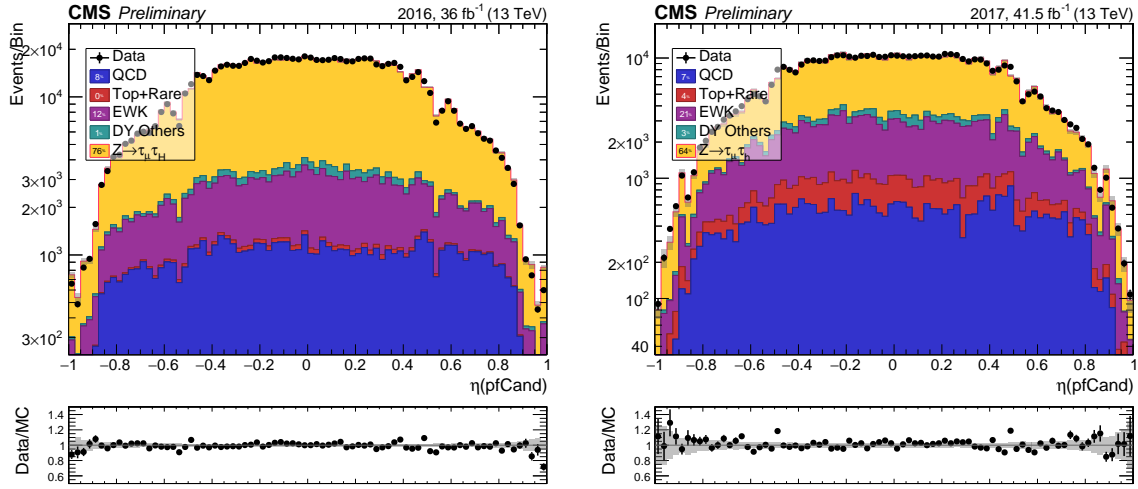
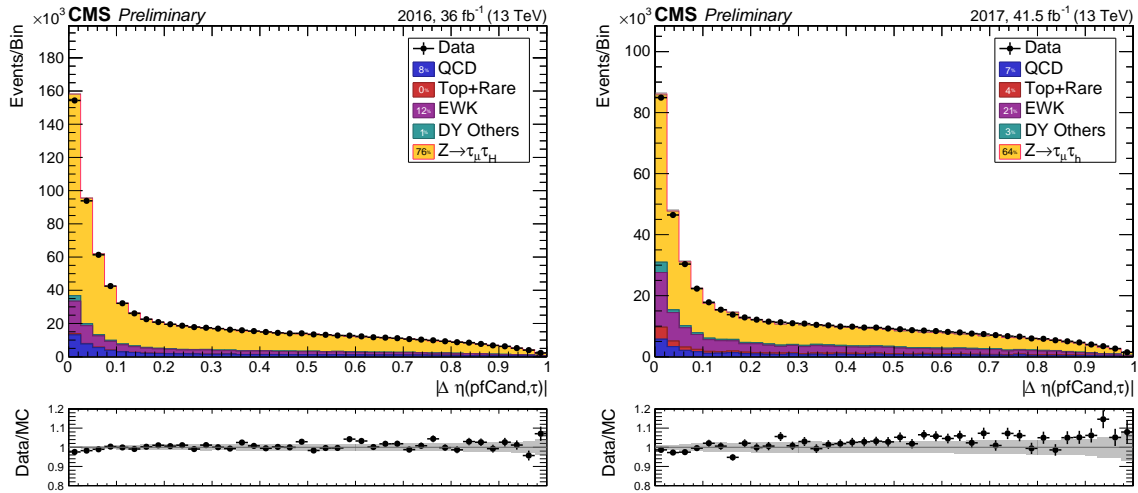


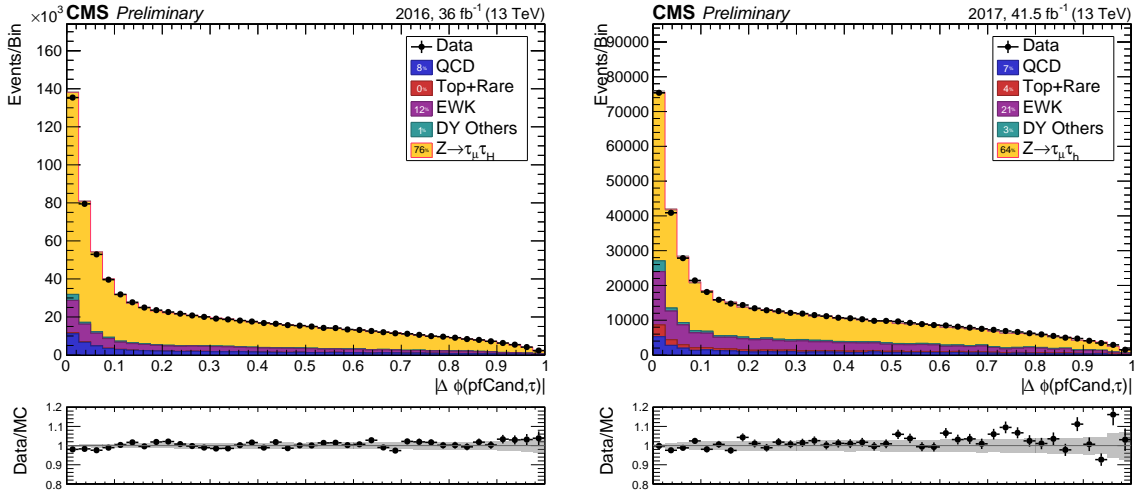
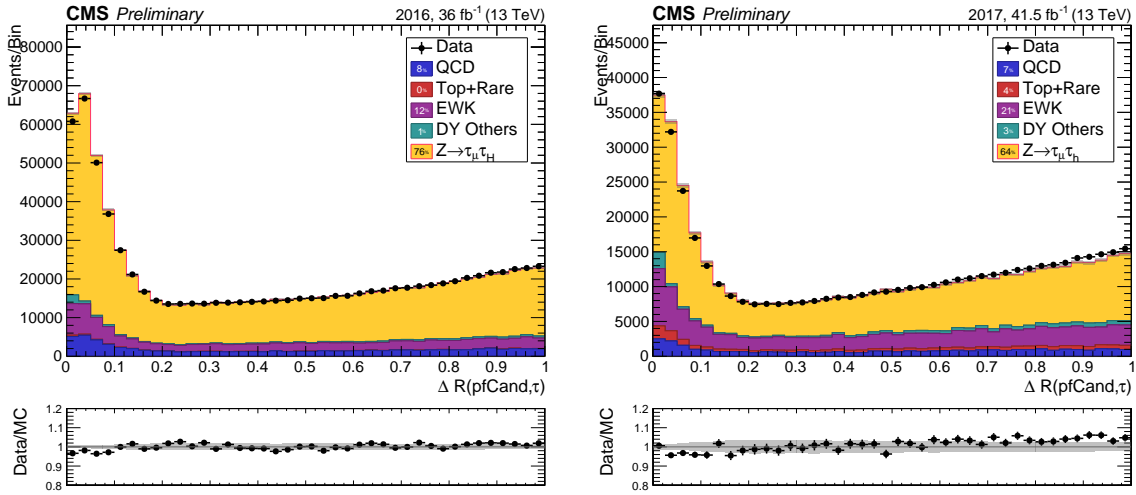
Figure A.1: Probe τ number of particle flow candidates

Figure A.2: Probe τ MVA isolationFigure A.3: Probe τ DNN Isolation, this raw value is averaged with the MVA score above to form DeepPF isolation

Figure A.4: p_T of PFCandidates associated to the probe τ Figure A.5: Relative p_T of PFCandidates associated to the probe τ

Figure A.6: p_z of PFCandidates associated to the probe τ Figure A.7: Relative p_z of PFCandidates associated to the probe τ

Figure A.8: Reconstructed $|\eta|$ of PFCandidates associated to the probe τ Figure A.9: $\Delta\eta$ between the probe τ and associated particle flow candidates

Figure A.10: $\Delta\phi$ between the probe τ and associated particle flow candidatesFigure A.11: ΔR between the probe τ and associated particle flow candidates

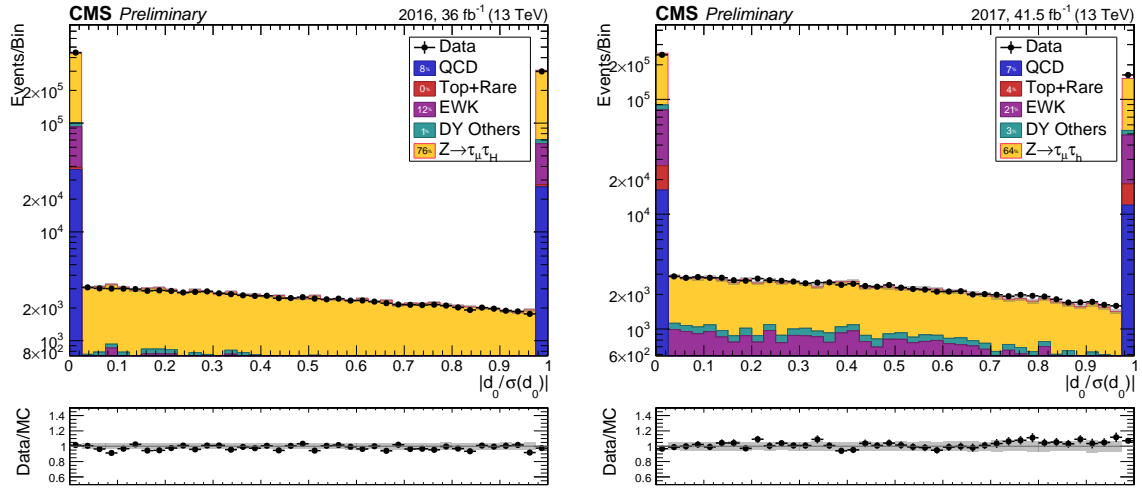
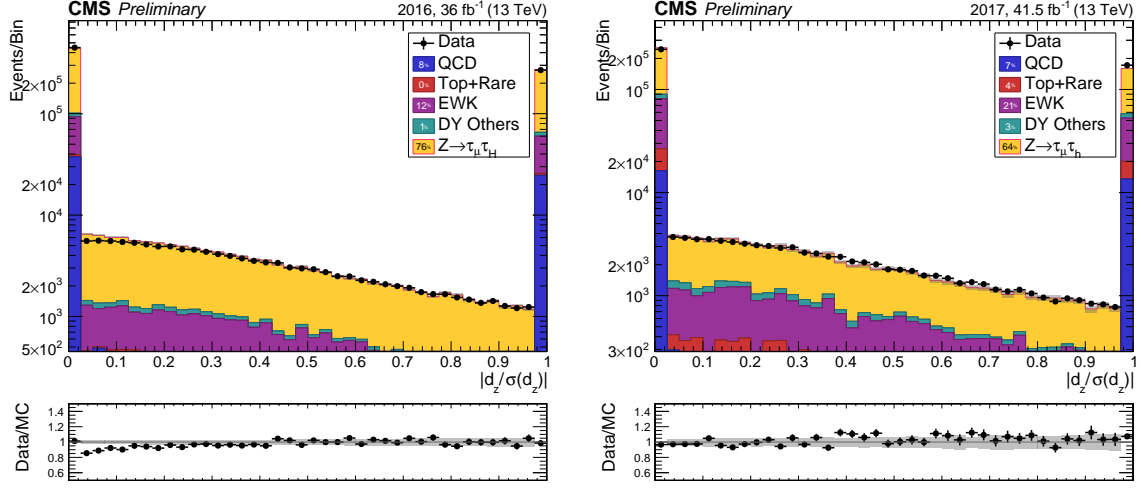
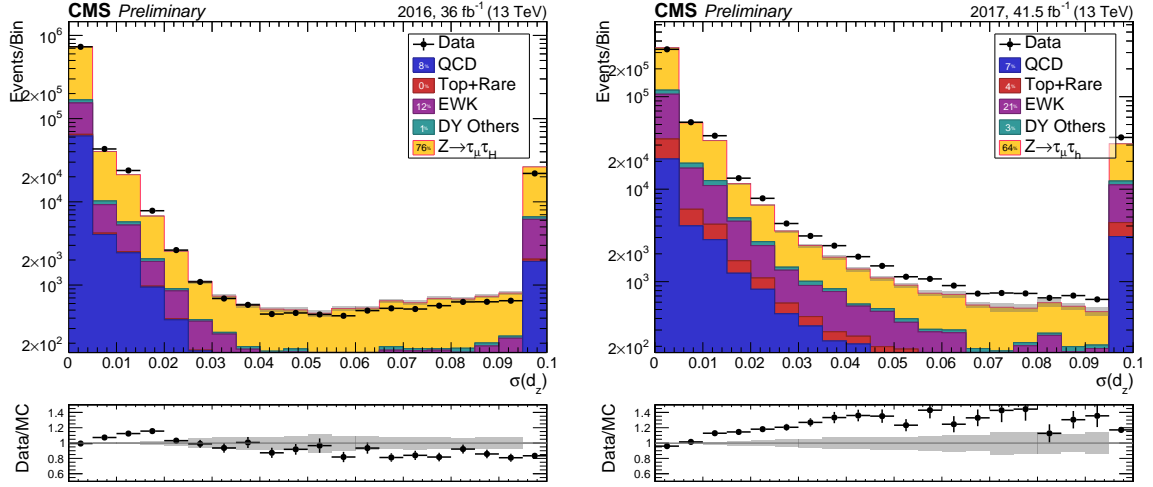
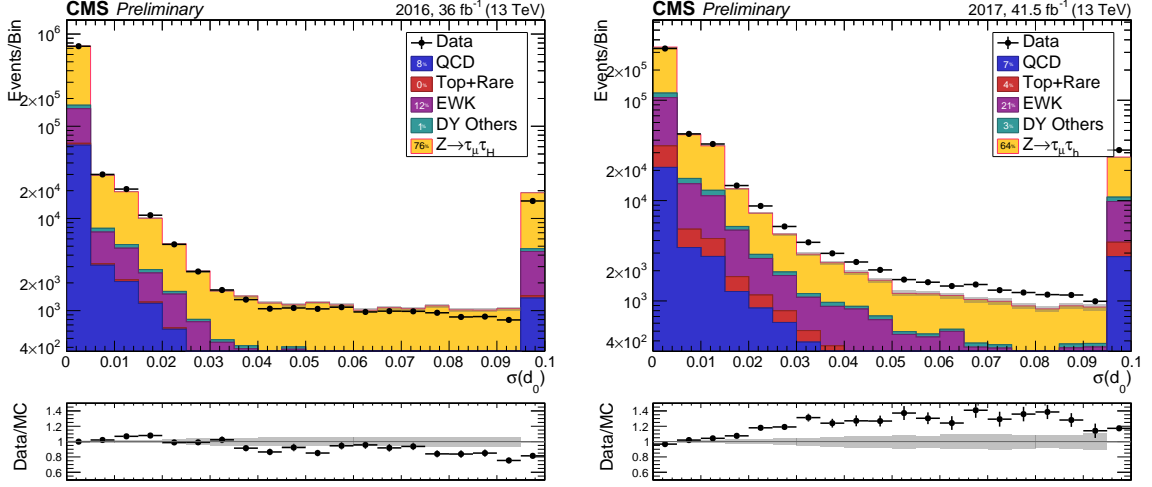
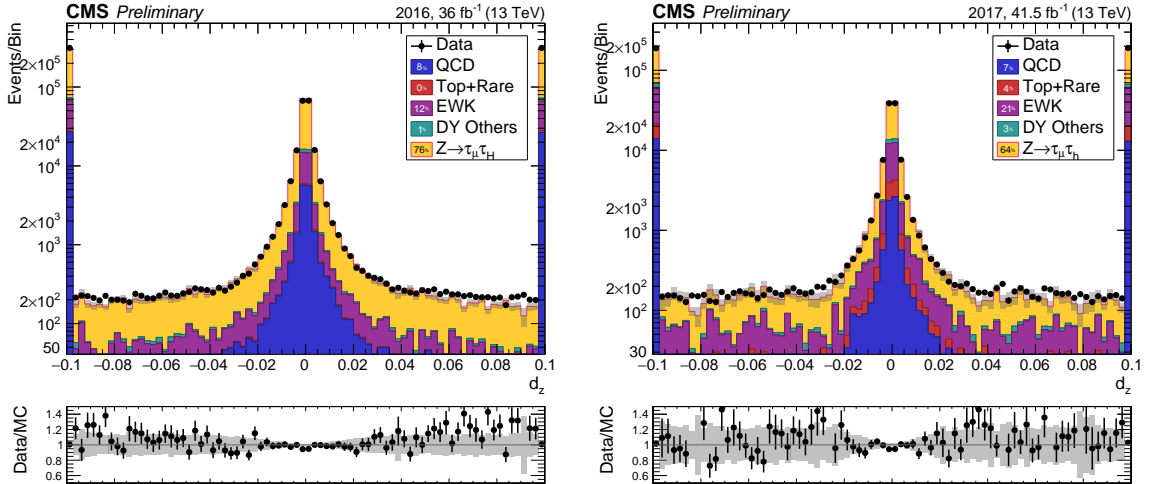
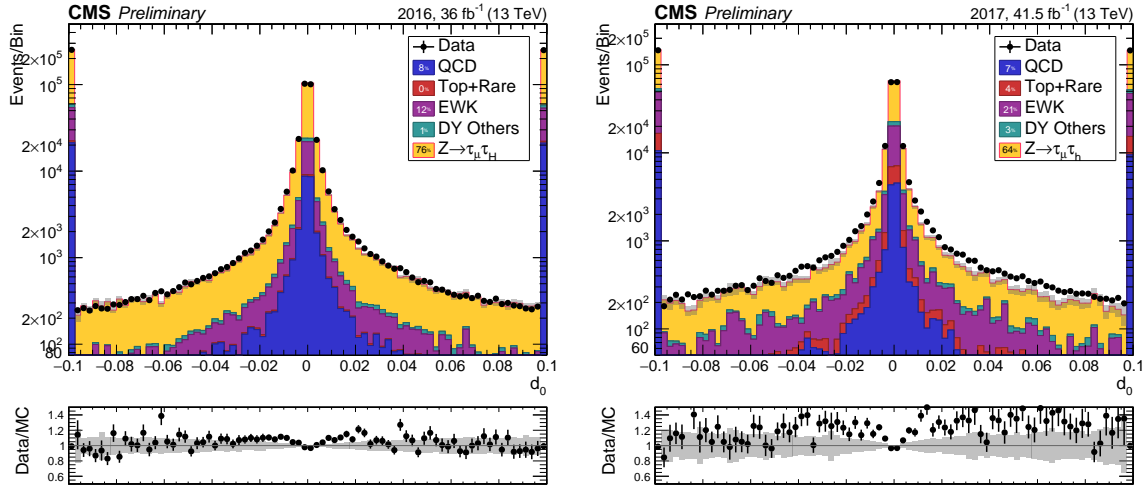
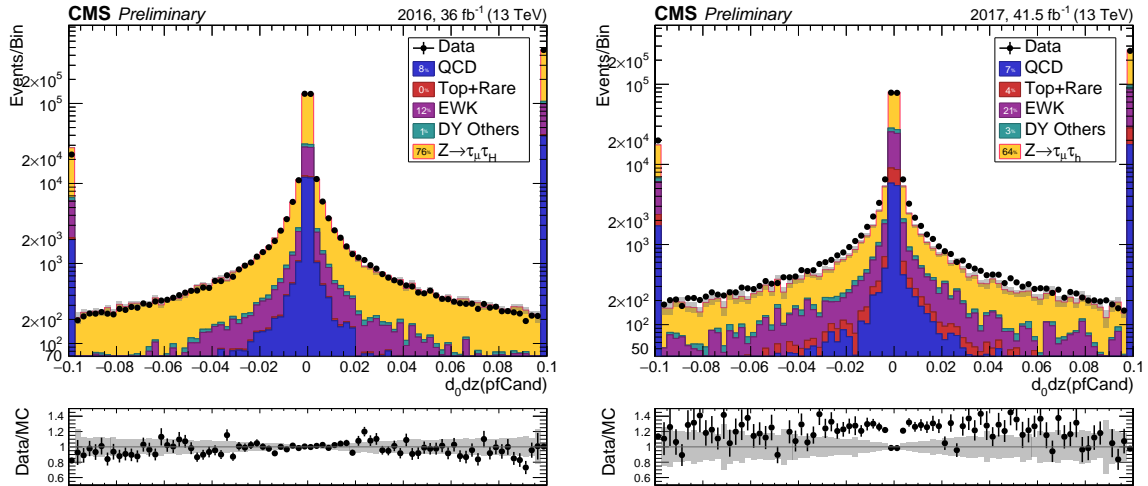
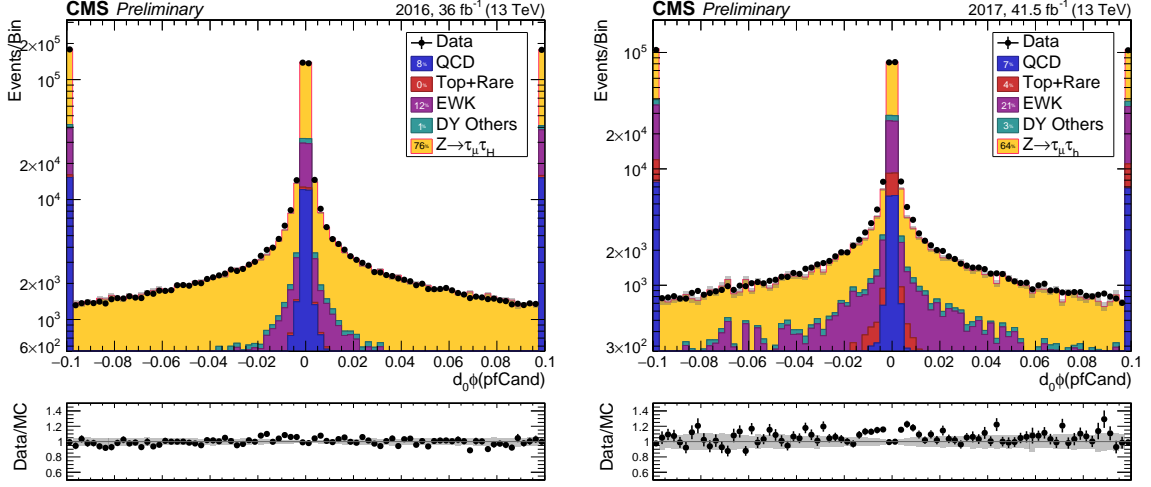
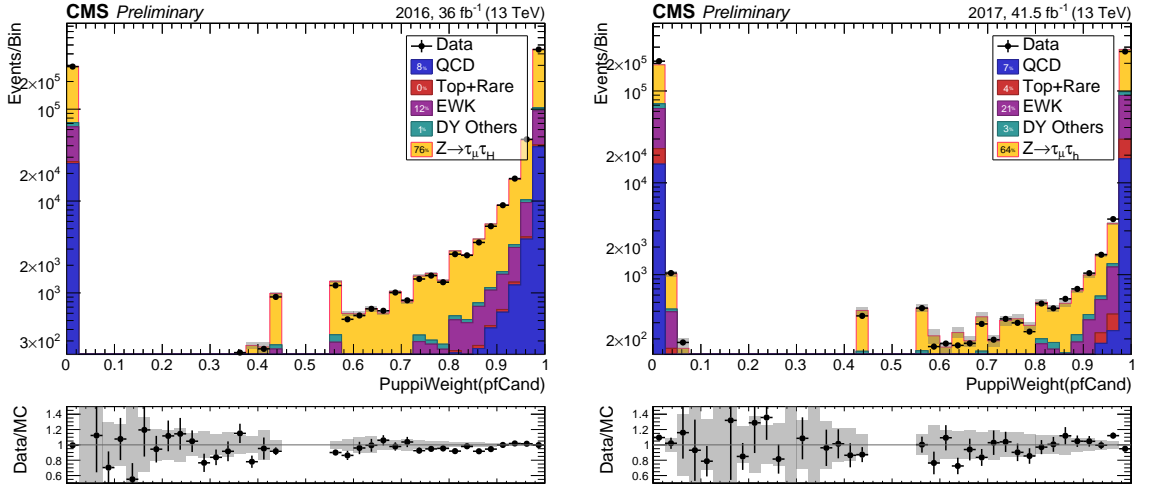


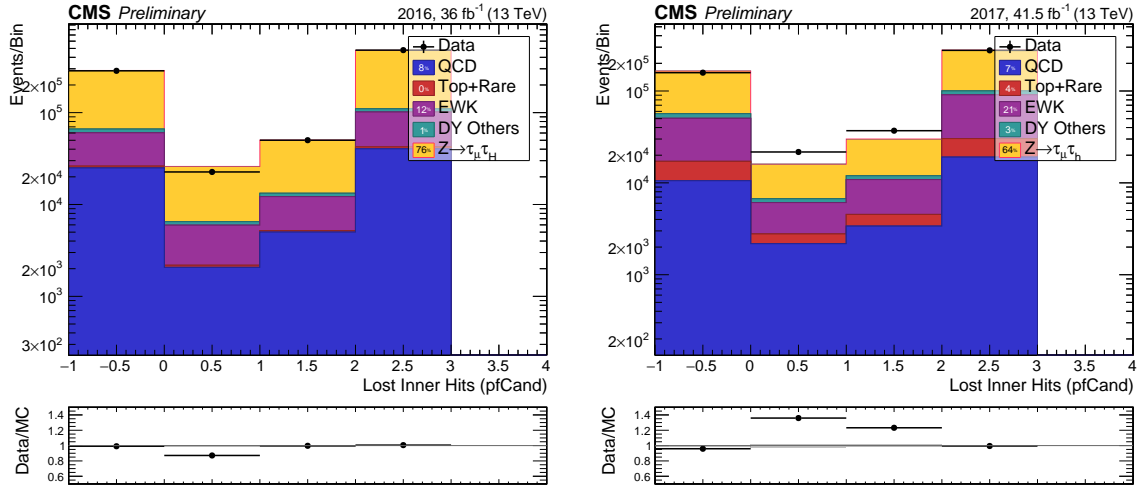
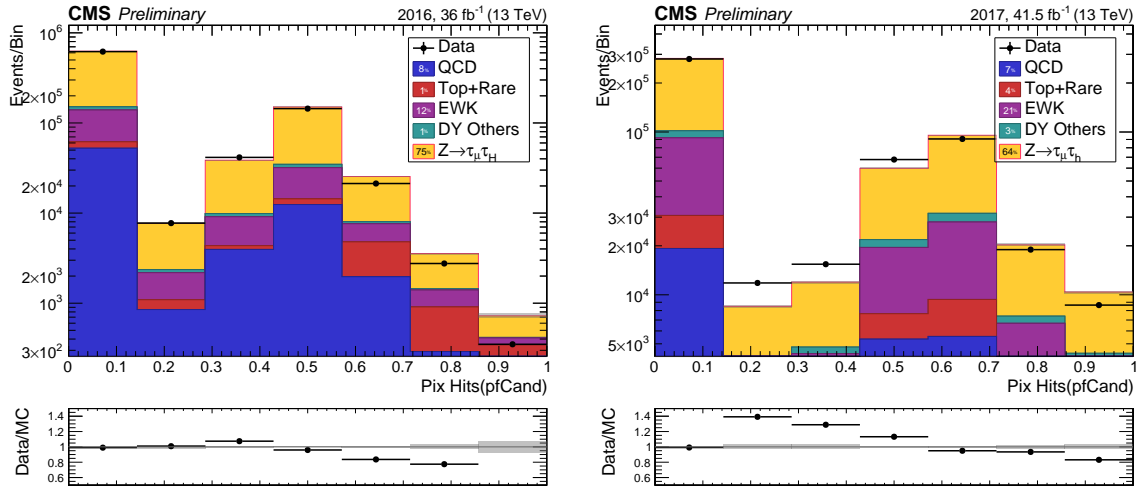
Figure A.12: Significance of d_0 for the particle flow candidates associated to the probe τ

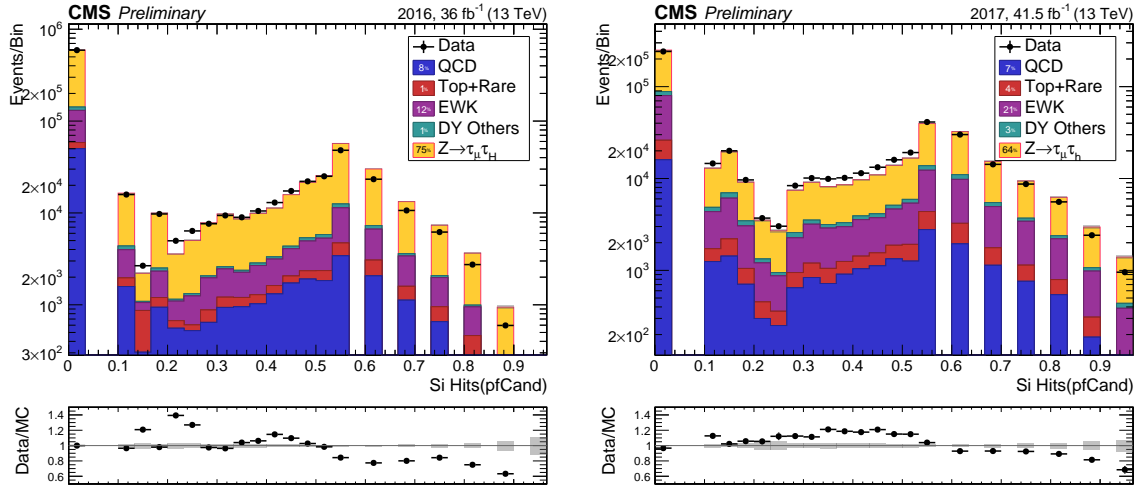
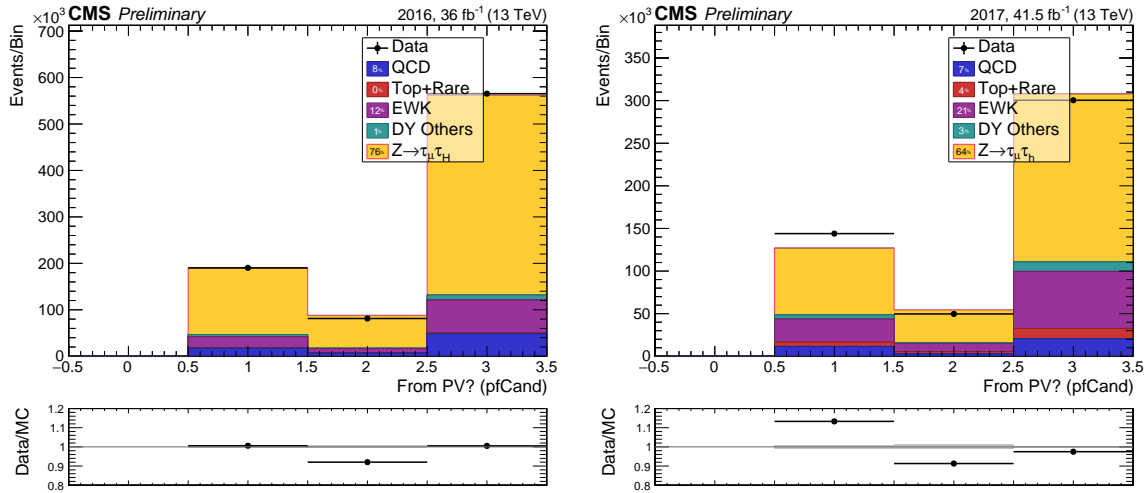
Figure A.13: Significance of d_z for the particle flow candidates associated to the probe τ Figure A.14: Error of measured d_z for the particle flow candidates associated to the probe τ

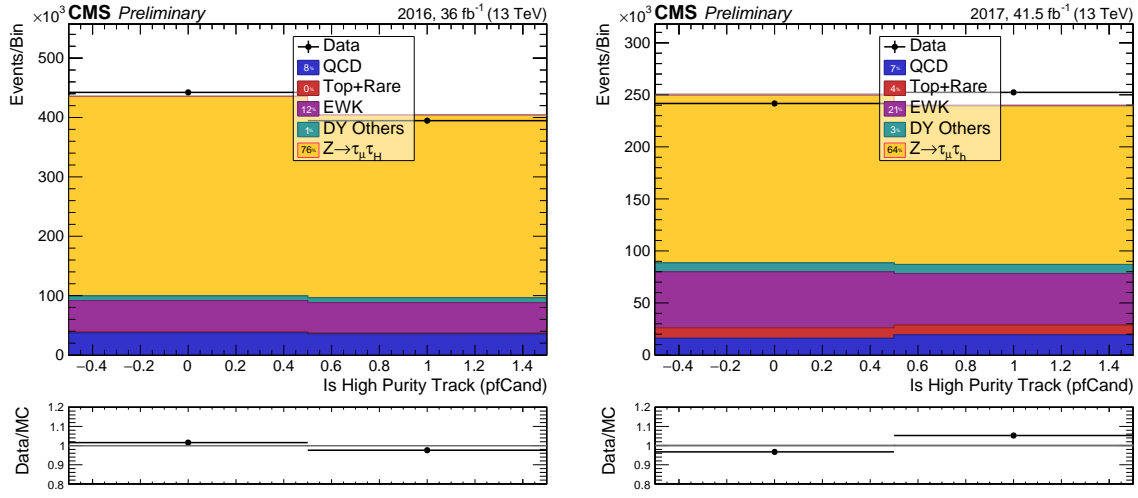
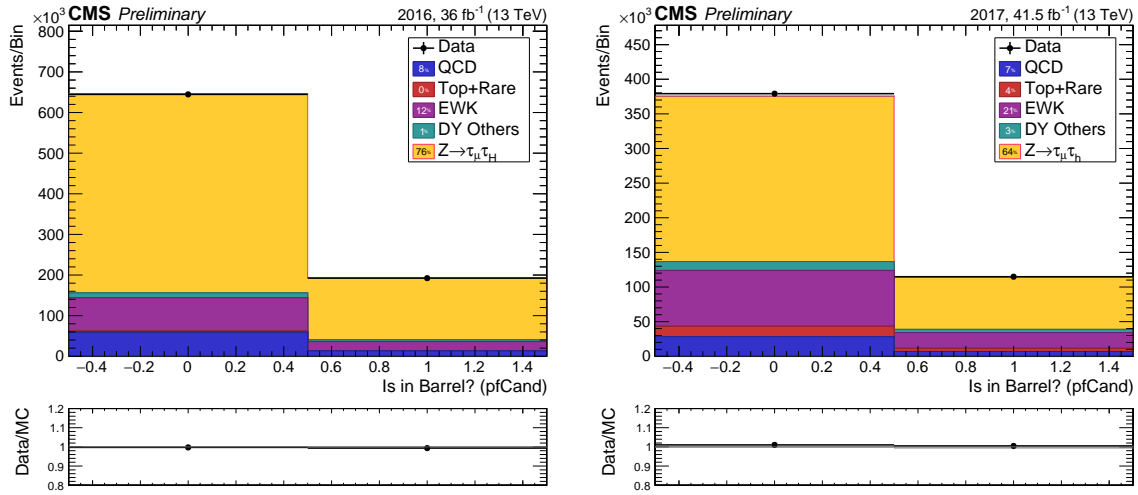
Figure A.15: Error of measured d_0 for the particle flow candidates associated to the probe τ Figure A.16: Measured d_z for the particle flow candidates associated to the probe τ

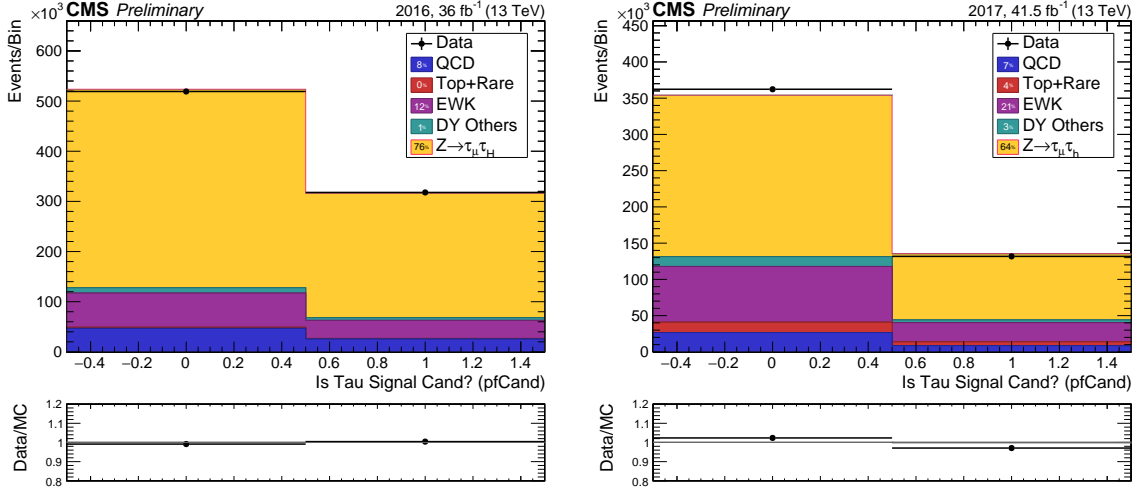
Figure A.17: Measured d_0 for the particle flow candidates associated to the probe τ Figure A.18: $d_0 d_z$ for the particle flow candidates associated to the probe τ

Figure A.19: $d_0 \Delta\phi$ for the particle flow candidates associated to the probe τ Figure A.20: Puppi weight for the particle flow candidates associated to the probe τ

Figure A.21: Lost Inner Hits for the particle flow candidates associated to the probe τ Figure A.22: Pixel Hits for the particle flow candidates associated to the probe τ

Figure A.23: Strip Hits for the particle flow candidates associated to the probe τ Figure A.24: FromPV flag for the particle flow candidates associated to the probe τ

Figure A.25: High Purity flag for the particle flow candidates associated to the probe τ Figure A.26: IsBarrel flag for the particle flow candidates associated to the probe τ



[Signal Candidate Flag for PFCands associated with Probe τ]n Signal Candidate flag
for the particle flow candidates associated to the probe τ

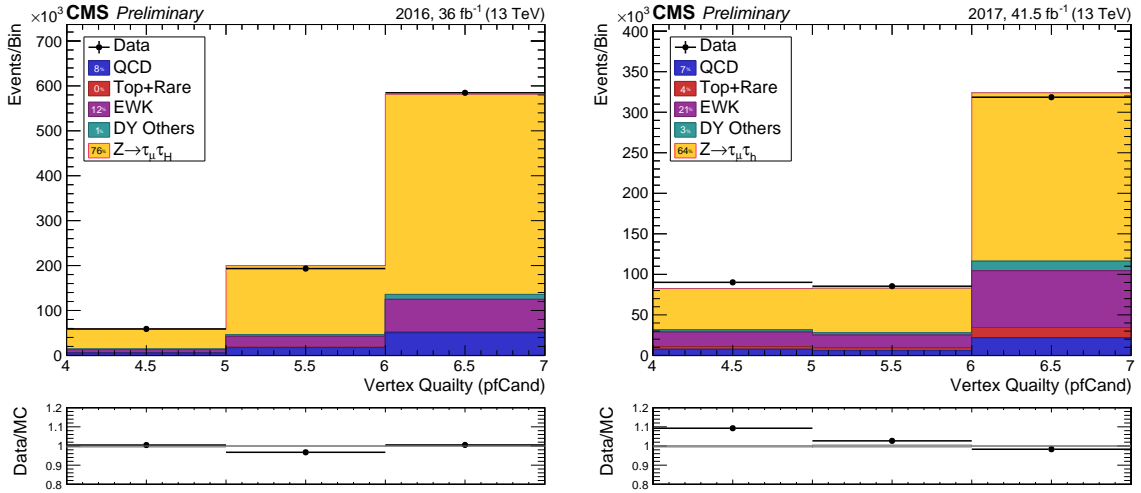


Figure A.27: Vertex Quality flag for the particle flow candidates associated to the probe τ

Appendix B

Appendix A

B.1 The di- τ_h Trigger

The current di- τ_h trigger was developed after CMS Run-I to maintain acceptable efficiency in the high activity Run-II environment, without increasing rates beyond allowable thresholds. This trigger begins by clusterizing the hits in the E/HCAL around local maxima into 3 by 3 sections in the $\eta - \phi$ plane. The energy from the decay lies inside this initial cluster for the majority of one prong and one prong plus neutral pion decays. A second maximum outside of this initial cluster exists for 20 % of all three-prong tau decays, and so additional merging is required. The scaled sum of the energy deposited in the ECAL and HCAL gives the L1T reconstructed of the tau energy CMS-DP-2016-037:

$$E_\tau = a \times E_{ECAL} + b \times E_{HCAL} + c \quad (\text{B.1})$$

The reconstruction algorithm yields fairly accurate energy and angular resolution at the L1. Next, pattern recognition is employed to verify that the cluster distribution is consistent with tau decays. After passing this criterion, the isolation of the tau is calculated as the residual energy in a 5 by 9 area in $\eta - \phi$ surrounding the primary cluster. If a jet successfully passes all these listed selections, then it continues onto the HLT trigger where a more refined choice based further on particle-flow is applied.

The final result is an efficiency of around 40 % for a tau with $p_T = 40$ GeV [Fig B.1]. The trigger has a threshold of $p_T(\tau) \geq 35$ GeV per-leg.

Measurement of the di- τ_h trigger efficiencies are made in data by the CMS τ_h Physics Object Group (POG) using a tag-and-probe method in the $\mu\tau_h$ final state. The tag is a reconstructed and isolated muon matched to a single muon trigger object, while the probe is a τ_h passing the a tight MVA selection and matched with the τ_h leg of a $\mu\tau_h$ cross-trigger. The cross-trigger is identical to that used in the hadronic di- τ_h trigger.

The corresponding simulation to data *scale factors* ($\epsilon_{\text{DATA}}/\epsilon_{\text{MC}} = \text{SF}$) for a very tight isolation selection are applied to correct each τ_h leg of the di- τ_h triggers. Analogously the offline isolation selection has a corresponding simulation to data scale factor measured in the $\mu\tau_h$ final state.

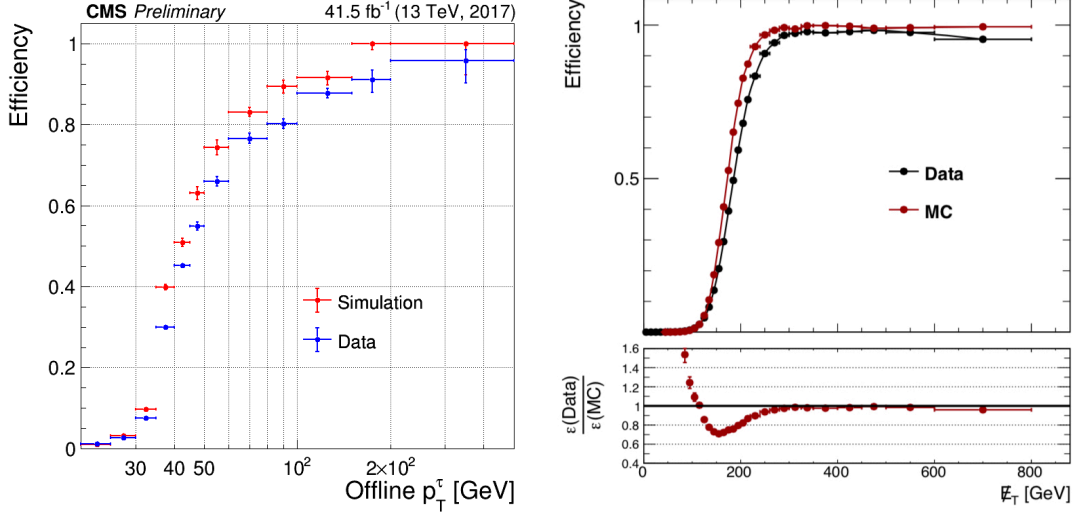


Figure B.1: Plotted on the left above is the performance per tau leg for the di- τ_h trigger CMS-DP-2018-009. The y-axis gives the efficiency to reconstruct a genuine tau decay. On the right, a similar efficiency curve is plotted for p_T^{miss} in 2017. The ratio of efficiencies yields the scale factor ($\epsilon_{\text{DATA}}/\epsilon_{\text{MC}} = \text{SF}$).

B.2 p_T^{miss} Trigger

Addition of the p_T^{miss} trigger was made as it can increase the stau signal efficiency by as much as 7 %. The p_T^{miss} trigger is much more sensitive to pile-up and calibration effects than the di- τ_h trigger, and so a more careful approach is necessary for the L1T.

At L1 *CaloJets* are found using a sliding 3 by 3 window with cells of size 4 by 4 in the H/ECAL. Windows containing central 4 by 4 regions with energy in excess of all surrounding neighbors, and above a minimum threshold, are selected as jets. The CaloJets are pile-up subtracted and calibrated. Next, the p_T^{miss} is constructed using the CaloJets. Thresholds are chosen according to trigger rate limitations. Continuing onto the HLT, PF is implemented to compute p_T^{miss} with better resolution.

The p_T^{miss} trigger efficiency is measured in data by V. Dutta with the help of an additional single electron trigger (HLT_Ele27_WPTight_Gsf in 2016, HLT_Ele32_WPTight_Gsf OR HLT_Ele32_WPTight_Gsf.L1DoubleEG in 2017). The number of events passing the single electron trigger and the following additional selection criteria defines the denominator of the efficiency ratio:

- Events must have an electron with $p_T > 35$ GeV, passing tight selection criteria, that is within $\Delta R < 0.1$ of the trigger object that fired the electron trigger.
- To match the event topology of the analysis the presence of at least two jets is required. Counting is made on jet objects that are at least $\Delta R = 0.4$ away from the electron trigger object.

- The p_T^{miss} filters are also applied [Sec. 7.4.5].

Dividing the number of events that pass the selection above and the p_T^{miss} trigger by the number of events that pass only the selection above gives the efficiency to pass the p_T^{miss} trigger. Taking the ratio of efficiencies measured in data and simulation yields the p_T^{miss} trigger scale factor [Fig. B.1].

Lastly, a trigger used to select single isolated muons is applied to construct an unbiased region to study tau performance from $Z \rightarrow \tau\tau \rightarrow \mu\nu_\tau\nu_\tau\tau_h$ and to collect events in the $Z \rightarrow \mu\mu$ channel used to correct the mass and p_T spectrum.

A summary of the selected HLT paths is shown below [Tab. B.3].

The turn-on for the di- τ_h trigger is quite slow and does not achieve full efficiency at the plateau. Therefore, utilizing the p_T^{miss} trigger recovers some signal efficiency. The OR between these two triggers is very complicated to correctly model, and so offline selections are made to orthogonalize between their use. In the region of $p_T^{miss} < 200$ GeV the di- τ_h trigger is used, whereas in the region $p_T^{miss} \geq 200$ GeV events are selected from the p_T^{miss} trigger. The relatively high offline selection value of $p_T^{miss} \geq 200$ GeV is selected to avoid modeling the complicated slope of the trigger turn-on.

B.3 Datasets Used

Data-taking period	HLT path
2016	HLT_DoubleMediumIsoPFTau35_Trk1_eta2p1_Reg
	HLT_DoubleMediumCombinedIsoPFTau32_Trk1_eta2p1_Reg
	HLT_PFMET120_PFMHT120_IDTight
	HLT_IsoMu22 or HLT_IsoMu24
2017	HLT_DoubleTightChargedIsoPFTau35_Trk1_TightID_eta2p1_Reg
	HLT_DoubleTightChargedIsoPFTau40_Trk1_eta2p1_Reg
	HLT_DoubleMediumChargedIsoPFTau40_Trk1_TightID_eta2p1_Reg
	HLT_PFMET120_PFMHT120_IDTight_PFHT60
	HLT_PFMETNoMu120_PFMHTNoMu120_IDTight_PFHT60
	HLT_PFMETTypeOne120_PFMHT120_IDTight_PFHT60
	HLT_PFMET140_PFMHT140_IDTight
	HLT_PFMETNoMu140_PFMHTNoMu140_IDTight
	HLT_PFMETTypeOne140_PFMHT140_IDTight
	HLT_IsoMu27 or HLT_IsoMu29

Table B.1: HLT paths corresponding used for data collection in 2016 and 2017. Not all trigger paths were available for the full data-taking period.

The datasets used in the combined 2016 and 2017 analysis result in 77.2 fb^{-1} [Tab. B.2], [Tab. B.3]. Separate Monte Carlos samples have been produced to replicate the separate detector conditions and to introduce improved tunes over the two years [Tab. B.4],

Dataset
/Tau/Run2016B-03Feb2017-ver1-v2/MINIAOD
/Tau/Run2016B-03Feb2017-ver2-v2/MINIAOD
/Tau/Run2016C-03Feb2017-v1/MINIAOD
/Tau/Run2016D-03Feb2017-v1/MINIAOD
/Tau/Run2016E-03Feb2017-v1/MINIAOD
/Tau/Run2016F-03Feb2017-v1/MINIAOD
/Tau/Run2016G-03Feb2017-v1/MINIAOD
/Tau/Run2016H-03Feb2017-ver2-v1/MINIAOD
/Tau/Run2016H-03Feb2017-ver3-v1/MINIAOD
/MET/Run2016B-03Feb2017_ver1-v1/MINIAOD
/MET/Run2016B-03Feb2017_ver2-v2/MINIAOD
/MET/Run2016C-03Feb2017-v1/MINIAOD
/MET/Run2016D-03Feb2017-v1/MINIAOD
/MET/Run2016E-03Feb2017-v1/MINIAOD
/MET/Run2016F-03Feb2017-v1/MINIAOD
/MET/Run2016G-03Feb2017-v1/MINIAOD
/MET/Run2016H-03Feb2017_ver2-v1/MINIAOD
/MET/Run2016H-03Feb2017_ver3-v1/MINIAOD
/SingleMuon/Run2016B-03Feb2017_ver1-v1/MINIAOD
/SingleMuon/Run2016B-03Feb2017_ver2-v2/MINIAOD
/SingleMuon/Run2016C-03Feb2017-v1/MINIAOD
/SingleMuon/Run2016D-03Feb2017-v1/MINIAOD
/SingleMuon/Run2016E-03Feb2017-v1/MINIAOD
/SingleMuon/Run2016F-03Feb2017-v1/MINIAOD
/SingleMuon/Run2016G-03Feb2017-v1/MINIAOD
/SingleMuon/Run2016H-03Feb2017_ver2-v1/MINIAOD
/SingleMuon/Run2016H-03Feb2017_ver3-v1/MINIAOD

Table B.2: Datasets used in the 2016 analysis.

[Tab. B.5]. Because of the large cross section DY+jets is generated at LO, whereas rarer events such as top quark, di-boson, and Higgs boson related processes are generated at NLO. Background processes are then rescaled to the most precisely calculated cross section available, typically that of NNLO.

Dataset
/Tau/Run2017B-31Mar2018-v1/MINIAOD
/Tau/Run2017C-31Mar2018-v1/MINIAOD
/Tau/Run2017D-31Mar2018-v1/MINIAOD
/Tau/Run2017E-31Mar2018-v1/MINIAOD
/Tau/Run2017F-31Mar2018-v1/MINIAOD
/MET/Run2017B-31Mar2018-v1/MINIAOD
/MET/Run2017C-31Mar2018-v1/MINIAOD
/MET/Run2017D-31Mar2018-v1/MINIAOD
/MET/Run2017E-31Mar2018-v1/MINIAOD
/MET/Run2017F-31Mar2018-v1/MINIAOD
/SingleMuon/Run2017B-31Mar2018-v1/MINIAOD
/SingleMuon/Run2017C-31Mar2018-v1/MINIAOD
/SingleMuon/Run2017D-31Mar2018-v1/MINIAOD
/SingleMuon/Run2017E-31Mar2018-v1/MINIAOD
/SingleMuon/Run2017F-31Mar2018-v1/MINIAOD

Table B.3: Datasets used in the 2017 analysis.

Category	Sample name	Cross section [pb]
DY+jets	DYJetsToLL_M-50_TuneCUETP8M1_13TeV-madgraphMLM-pythia8	5765.4
DY+jets	DY1JetsToLL_M-50_TuneCUETP8M1_13TeV-madgraphMLM-pythia8	1231.20
DY+jets	DY2JetsToLL_M-50_TuneCUETP8M1_13TeV-madgraphMLM-pythia8	404.685
DY+jets	DY3JetsToLL_M-50_TuneCUETP8M1_13TeV-madgraphMLM-pythia8	123.789
DY+jets	DY4JetsToLL_M-50_TuneCUETP8M1_13TeV-madgraphMLM-pythia8	66.6368
DY+jets	DYJetsToLL_M-10to50_TuneCUETP8M1_13TeV-madgraphMLM-pythia8	18610
Top	TTTo2L2Nu_TuneCUETP8M2_ttHtranche3_13TeV-powheg-pythia8	87.315
Top	ST_tW_antitop_5f_NoFullyHadronicDecays_13TeV-powheg-pythia8_TuneCUETP8M1	19.6
Top	ST_tW_top_5f_NoFullyHadronicDecays_13TeV-powheg-pythia8_TuneCUETP8M1	19.6
Top	TTWJetsToLL_Nu_TuneCUETP8M1_13TeV-amcatnloFXFX-madspin-pythia8	0.204
Top	TTZToLLNuNu_M-10_TuneCUETP8M1_13TeV-amcatnlo-pythia8	0.253
Other SM	ZZTo2L2Nu_13TeV-powheg-pythia8	0.564
Other SM	ZZTo2L2Q_13TeV-amcatnloFXFX-madspin-pythia8	3.22
Other SM	ZZTo4L_13TeV-amcatnloFXFX-pythia8	1.212
Other SM	WZTo2L2Q_13TeV-amcatnloFXFX-madspin-pythia8	5.6
Other SM	WZTo3LNu_TuneCUETP8M1_13TeV-powheg-pythia8	4.43
Other SM	WWTo2L2Nu_13TeV-powheg	10.481
Other SM	WWW_4F_TuneCUETP8M1_13TeV-amcatnlo-pythia8	0.209
Other SM	WWZ_TuneCUETP8M1_13TeV-amcatnlo-pythia8	0.165
Other SM	WZZ_TuneCUETP8M1_13TeV-amcatnlo-pythia8	0.056
Other SM	ZZZ_TuneCUETP8M1_13TeV-amcatnlo-pythia8	0.014
Other SM	GluGluHTToTauTau_M125_13TeV-powheg-pythia8	2.78
Other SM	ZHTToTauTau_M125_13TeV-powheg-pythia8	0.0532144
Other SM	WplusHTToTauTau_M125_13TeV-powheg-pythia8	0.0340648
Other SM	WminusHTToTauTau_M125_13TeV-powheg-pythia8	0.0549587

Table B.4: Simulated samples used for the background prediction in the analysis of 2016 data. The Moriond17 datasets are used. Note that first the Standard Model process is listed, next the specific topology of that process, e.g., number of additional jets. Lastly the PYTHIA tune (*_Tune**) and the matrix element generator (*13TeV**) are listed.

Category	Sample name	Cross section [pb]
DY+jets	DYJetsToLL_M-50_TuneCP5_13TeV-madgraphMLM-pythia8	5765.4
DY+jets	DY1JetsToLL_M-50_TuneCP5_13TeV-madgraphMLM-pythia8	1070.5
DY+jets	DY2JetsToLL_M-50_TuneCP5_13TeV-madgraphMLM-pythia8	375.03
DY+jets	DY3JetsToLL_M-50_TuneCP5_13TeV-madgraphMLM-pythia8	147.11
DY+jets	DY4JetsToLL_M-50_TuneCP5_13TeV-madgraphMLM-pythia8	49.741
Top	TTTo2L2Nu_TuneCP5_13TeV-powheg-pythia8	87.31
Top	TTToSemiLeptonic_TuneCP5_PSweights_13TeV-powheg-pythia8	364.36
Top	ST_tW_antitop_5f_NoFullyHadronicDecays_TuneCP5_13TeV-powheg-pythia8	19.56
Top	ST_tW_antitop_5f_NoFullyHadronicDecays_TuneCP5_13TeV-powheg-pythia8	19.56
Top	ST_tW_top_5f_inclusiveDecays_TuneCP5_13TeV-powheg-pythia8	19.56
Top	TTWJetsToLNu_TuneCP5_13TeV-amcatnloFXFX-madspin-pythia8	0.2125
Top	TTZToLLNuNu_M-10_TuneCP5_13TeV-amcatnlo-pythia8	0.2432
Other SM	ZZTo2L2Nu_13TeV-powheg-pythia8	0.60
Other SM	ZZTo2L2Q_13TeV-amcatnloFXFX-madspin-pythia8	5.07
Other SM	ZZTo4L_13TeV-amcatnloFXFX-pythia8	1.325
Other SM	WZTo2L2Q_13TeV-amcatnloFXFX-madspin-pythia8	9.24
Other SM	WZTo3LNu_TuneCUETP8M1_13TeV-powheg-pythia8	4.43
Other SM	WWTo2L2Nu_13TeV-powheg	4.9
Other SM	WWW_4F_TuneCUETP8M1_13TeV-amcatnlo-pythia8	0.209
Other SM	WWZ_TuneCUETP8M1_13TeV-amcatnlo-pythia8	0.165
Other SM	WZZ_TuneCUETP8M1_13TeV-amcatnlo-pythia8	0.056
Other SM	ZZZ_TuneCUETP8M1_13TeV-amcatnlo-pythia8	0.014
Other SM	GluGluHTToTauTau_M125_13TeV-powheg-pythia8	2.78
Other SM	ZHTToTauTau_M125_13TeV-powheg-pythia8	0.0532144
Other SM	WplusHTToTauTau_M125_13TeV-powheg-pythia8	0.0340648
Other SM	WminusHTToTauTau_M125_13TeV-powheg-pythia8	0.0549587

Table B.5: Simulated samples used for the background prediction in the analysis of 2017 data. The 12Apr2018 re-miniAOD datasets are used.

B.4 Simulation Corrections and Their Uncertainties

- **Tau energy scale** is corrected in the simulation according to measurements made by the CMS τ_h POG in the $\mu\tau_h$ channel. The measured shifts are -0.5 (0.7)%, 1.1 (-0.3) %, 0.6 (-1) % for one prong, one prong + π_0 , and three prong decays, respectively, in 2016 (2017). An uncertainty in this correction of 1.2 % is propagated through to the final results.
- In initial Monte Carlo simulation an anticipated **pile-up** distribution is used to *mix* in the expected pile-up events. The underlying generator distribution is later corrected to match the distribution delivered by the LHC. Uncertainties in this correction are propagated into the yields as a difference of event weights.
- There are known differences between efficiency in simulation and data for genuine and fake jets to pass the **b-jet** selection. These differences are corrected jet-by-jet and the product of these weights is used to adjust the overall event weight. Uncertainties in each scale-factor are propagated into the yields as a difference of event weights.
- There are known differences between efficiency in simulation and data for genuine and fake events to pass the **b-jet** selection. These differences are corrected jet-by-jet and the product of which is used to adjust the event weight. Uncertainties in each scale-factor are propagated into the yields as a difference of event weights.
- Differences in jet-by-jet **energy scale and resolution** are corrected for. Global variables such as p_T^{miss} and N_j are calculated with the varied collections. This results in a variation of the event yields which is propagated as a systematic.
- **Drell-Yan mass and p_T** are simultaneously corrected using binned measurements from the $Z \rightarrow \mu\mu$ channel. These corrections can be thought of an LO to highest order correction. A systematic is propagated by measuring the difference between this correction and a simulated LO to NLO correction.
- **Tau Isolation Efficiency** is corrected by using the scale factor previously described along with the previously described uncertainty [App. 7.4.3, Sec. 8.3]
- **Tau Trigger Efficiency** is corrected using the scale factor derivation previously described [App. B.1]. No systematic is propagated as this uncertainty is considered to be covered by the offline isolation systematic.
- **Muon Trigger and Reconstruction Efficiency** is measured and corrected for when using the $\mu\tau_h$ control region. No systematic is considered.

B.5 Statistical Methods at the LHC

In order to make a formal statistical claim regarding the outcome of the analysis two hypothesis must be posited, one in which the universe contains only Standard Model processes (H_0) and one in which stau production exists as described by the SMP describing direct stau production (H_1). In this case the Neyman-Pearson lemma dictates that the ratio of the likelihoods gives the most powerful hypothesis test statistic, this in turn motivates the *profile-likelihood* test statistic λ_μ defined below Gross:1099994,Cowan:2013pha,Cranmer:2015nia

$$\lambda_\mu = \frac{\mathcal{L}(\mu, \hat{\theta}(\mu))}{\mathcal{L}(\hat{\mu}, \hat{\theta})}, \quad (\text{B.2})$$

here the terms $\hat{\theta}$ and $\hat{\mu}$ in the denominator are the nuisance parameters and signal strength multiplier, $\hat{\mu} = \sigma_{\text{obs}}/\sigma_{\text{SM}}$, which maximize the likelihood estimate, \mathcal{L} , respectively. In the numerator, the signal strength μ is allowed to float and a new best fit of the nuisances $\hat{\theta}(\mu)$ is performed at each point. This test statistic along with the predicted and observed data are used to evaluate the p-value of each hypothesis. The background only hypothesis is constructed to be one-sided with respect to $\hat{\mu}$:

$$q_0 = \begin{cases} -2\log(\lambda(0)) & \hat{\mu} \geq 0 \\ 0 & \hat{\mu} < 0 \end{cases} \quad (\text{B.3})$$

B.6 Additional Validation Regions

Table B.6: Validation region yields for the 2016 analysis.

Search Region	Fake	DY	Top	Rare	Total Pred.	Obs
Low M_{T2} VR						
$300 < \Sigma M_T, N_J = 0$	$4.08 \pm 1.41 \pm 2.67$	$26.9 \pm 5.59 \pm 9.24$	$0.154 \pm 0.0755 \pm 0.0396$	$0.509 \pm 0.288 \pm 0.238$	$31.6 \pm 5.78 \pm 9.62$	25
$300 < \Sigma M_T, N_J \geq 1$	$2.88 \pm 0.991 \pm 1.86$	$6.83 \pm 1.82 \pm 3.19$	$0.941 \pm 0.199 \pm 0.475$	$1.15 \pm 0.387 \pm 0.682$	$11.8 \pm 2.12 \pm 3.78$	14
$250 < \Sigma M_T < 300, N_J = 0$	$3.55 \pm 1.38 \pm 1.78$	$21.9 \pm 4.91 \pm 6.15$	$0.788 \pm 0.195 \pm 0.347$	$1.2 \pm 0.495 \pm 0.546$	$27.4 \pm 5.13 \pm 6.44$	27
$250 < \Sigma M_T < 300, N_J \geq 1$	$4 \pm 1.23 \pm 2.02$	$11.9 \pm 2.91 \pm 3.86$	$1.25 \pm 0.224 \pm 0.599$	$0.734 \pm 0.287 \pm 0.55$	$17.8 \pm 3.18 \pm 4.43$	17
$200 < \Sigma M_T < 250, N_J = 0$	$19.4 \pm 3.14 \pm 4.46$	$50.4 \pm 7.91 \pm 17$	$1.72 \pm 0.276 \pm 0.492$	$1.26 \pm 0.475 \pm 0.741$	$72.8 \pm 8.53 \pm 17.6$	84
$200 < \Sigma M_T < 250, N_J \geq 1$	$15.8 \pm 2.35 \pm 7.36$	$22.9 \pm 3.71 \pm 6.98$	$4.05 \pm 0.403 \pm 1.51$	$2.96 \pm 0.674 \pm 1.14$	$45.7 \pm 4.46 \pm 10.3$	25
High M_{T2} Same-Sign VR						
$300 < \Sigma M_T, N_J = 0$	$0.743 \pm 0.398 \pm 0.403$	$< .7$	$< .2$	$0.0348 \pm 0.0233 \pm 0.0514$	$0.777 \pm 0.399 \pm 0.406$	1
$300 < \Sigma M_T, N_J \geq 1$	$0.702 \pm 0.478 \pm 0.25$	$< .7$	$0.0952 \pm 0.0561 \pm 0.0238$	$0.149 \pm 0.0493 \pm 0.0841$	$0.945 \pm 0.484 \pm 0.265$	0
$250 < \Sigma M_T < 300, N_J = 0$	$0.234 \pm 0.721 \pm 0.316$	$< .7$	$< .2$	$0.0524 \pm 0.0263 \pm 0.0512$	$0.287 \pm 0.722 \pm 0.32$	4
$250 < \Sigma M_T < 300, N_J \geq 1$	$2.28 \pm 1.05 \pm 0.372$	$< .7$	$0.082 \pm 0.0519 \pm 0.0796$	$0.062 \pm 0.0283 \pm 0.0755$	$2.43 \pm 1.06 \pm 0.388$	2
$200 < \Sigma M_T < 250, N_J = 0$	$5.57 \pm 1.75 \pm 1.17$	$< .7$	$0.0365 \pm 0.0365 \pm 0.0131$	$0.0389 \pm 0.0219 \pm 0.0285$	$5.65 \pm 1.75 \pm 1.17$	7
$200 < \Sigma M_T < 250, N_J \geq 1$	$11.8 \pm 2.44 \pm 0.784$	$< .7$	$0.132 \pm 0.0888 \pm 0.0929$	$0.151 \pm 0.0445 \pm 0.0735$	$12.1 \pm 2.44 \pm 0.793$	9
Low M_{T2} Same-Sign VR						
$300 < \Sigma M_T, N_J = 0$	$1.24 \pm 0.644 \pm 0.382$	$< .7$	$< .2$	$0.106 \pm 0.0368 \pm 0.0482$	$1.34 \pm 0.645 \pm 0.385$	2
$300 < \Sigma M_T, N_J \geq 1$	$3.33 \pm 0.916 \pm 1.8$	$< .7$	$0.0245 \pm 0.00595 \pm 0.0565$	$0.421 \pm 0.077 \pm 0.197$	$3.77 \pm 0.919 \pm 1.81$	3
$250 < \Sigma M_T < 300, N_J = 0$	$2.97 \pm 0.963 \pm 0.78$	$1.95 \pm 1.53 \pm 0.482$	$< .7$	$0.129 \pm 0.0409 \pm 0.0658$	$5.05 \pm 1.8 \pm 0.919$	2
$250 < \Sigma M_T < 300, N_J \geq 1$	$3.3 \pm 1.2 \pm 0.467$	$0.375 \pm 0.375 \pm 0.181$	$0.296 \pm 0.113 \pm 0.14$	$0.441 \pm 0.079 \pm 0.179$	$4.41 \pm 1.27 \pm 0.55$	3
$200 < \Sigma M_T < 250, N_J = 0$	$18.9 \pm 2.92 \pm 1.28$	$1.51 \pm 0.878 \pm 1.68$	$0.152 \pm 0.0902 \pm 0.107$	$0.257 \pm 0.0596 \pm 0.187$	$20.8 \pm 3.06 \pm 2.13$	14
$200 < \Sigma M_T < 250, N_J \geq 1$	$19.7 \pm 2.9 \pm 4.04$	$< .7$	$0.787 \pm 0.177 \pm 0.401$	$0.97 \pm 0.223 \pm 0.3$	$21.4 \pm 2.91 \pm 4.07$	18
High M_{T2} B-Enriched VR						
$300 < \Sigma M_T, N_J \geq 1$	$2.52 \pm 0.989 \pm 1.72$	$< .7$	$4.66 \pm 0.467 \pm 1.92$	$0.0962 \pm 0.0357 \pm 0.0449$	$7.27 \pm 1.09 \pm 2.58$	12
$250 < \Sigma M_T < 300, N_J \geq 1$	$4.31 \pm 1.31 \pm 2.5$	$0.37 \pm 0.37 \pm 0.232$	$8.14 \pm 0.625 \pm 3.22$	$0.0511 \pm 0.0255 \pm 0.0438$	$12.9 \pm 1.5 \pm 4.09$	11
$200 < \Sigma M_T < 250, N_J \geq 1$	$6.33 \pm 1.97 \pm 1.94$	$1.97 \pm 1.06 \pm 2.84$	$11.1 \pm 0.723 \pm 3.57$	$0.341 \pm 0.122 \pm 0.188$	$19.7 \pm 2.36 \pm 4.96$	20
Low M_{T2} B-Enriched VR						
$300 < \Sigma M_T, N_J \geq 1$	$3.82 \pm 1.07 \pm 2.75$	$0.777 \pm 0.55 \pm 1.52$	$14.2 \pm 0.823 \pm 4.27$	$0.726 \pm 0.321 \pm 0.269$	$19.6 \pm 1.49 \pm 5.31$	12
$250 < \Sigma M_T < 300, N_J \geq 1$	$2.89 \pm 1.67 \pm 1.44$	$2.45 \pm 1.11 \pm 1.88$	$20.3 \pm 0.971 \pm 5.58$	$0.15 \pm 0.0373 \pm 0.228$	$25.8 \pm 2.22 \pm 6.07$	29
$200 < \Sigma M_T < 250, N_J \geq 1$	$17.6 \pm 2.91 \pm 10.3$	$5.85 \pm 1.69 \pm 3.59$	$55.2 \pm 1.62 \pm 14.3$	$1.5 \pm 0.483 \pm 0.658$	$80.2 \pm 3.77 \pm 18$	59
High M_{T2} , Small $\Delta\phi$ VR						
$300 < \Sigma M_T, N_J = 0$	$0 \pm 0.416 \pm 0.336$	$< .7$	$< .2$	$1.92 \pm 0.122 \pm 0.441$	$1.82 \pm 0.433 \pm 0.554$	3
$300 < \Sigma M_T, N_J \geq 1$	$0.714 \pm 0.898 \pm 0.0551$	$1.58 \pm 0.918 \pm 1.32$	$0.106 \pm 0.0596 \pm 0.0531$	$2.23 \pm 0.271 \pm 0.557$	$4.63 \pm 1.31 \pm 1.44$	9
$250 < \Sigma M_T < 300, N_J = 0$	$2.12 \pm 0.78 \pm 1.27$	$0.658 \pm 0.658 \pm 0.17$	$0.0859 \pm 0.0859 \pm 0.0629$	$0.621 \pm 0.072 \pm 0.137$	$3.49 \pm 1.03 \pm 1.29$	0
$250 < \Sigma M_T < 300, N_J \geq 1$	$2.23 \pm 1.26 \pm 1.01$	$9.18 \pm 2.31 \pm 6.19$	$0.0781 \pm 0.0531 \pm 0.145$	$0.926 \pm 0.116 \pm 0.275$	$12.4 \pm 2.64 \pm 6.28$	5
$200 < \Sigma M_T < 250, N_J = 0$	$5.1 \pm 1.87 \pm 2.01$	$1.18 \pm 0.836 \pm 1.71$	$0.0753 \pm 0.0753 \pm 0.0898$	$0.422 \pm 0.0609 \pm 0.12$	$6.78 \pm 2.05 \pm 2.64$	12
$200 < \Sigma M_T < 250, N_J \geq 1$	$19.3 \pm 3.49 \pm 4.82$	$22 \pm 3.58 \pm 24.2$	$0.723 \pm 0.189 \pm 0.238$	$1.72 \pm 0.315 \pm 0.425$	$43.8 \pm 5.02 \pm 24.7$	41

Table B.7: Validation regions yields for the 2017 analysis.

Search Region	Fake	DY	Top	Rare	Total Pred.	Obs
Low M_{T2} VR						
$300 < \Sigma M_T, N_J = 0$	$0.942 \pm 1.31 \pm 0.22$	$16.9 \pm 4.95 \pm 7.39$	$0.413 \pm 0.298 \pm 0.137$	$0.67 \pm 0.361 \pm 0.631$	$18.9 \pm 5.14 \pm 7.42$	29
$300 < \Sigma M_T, N_J \geq 1$	$3.32 \pm 1.34 \pm 2.47$	$4.22 \pm 1.25 \pm 3.28$	$0.443 \pm 0.377 \pm 0.186$	$4.24 \pm 1.04 \pm 1.33$	$12.2 \pm 2.15 \pm 4.32$	16
$250 < \Sigma M_T < 300, N_J = 0$	$2.93 \pm 1.47 \pm 0.965$	$13.8 \pm 4.05 \pm 8.51$	$0.0582 \pm 0.0582 \pm 0.2$	$0.644 \pm 0.359 \pm 0.274$	$17.4 \pm 4.32 \pm 8.57$	21
$250 < \Sigma M_T < 300, N_J \geq 1$	$1.49 \pm 1.03 \pm 0.319$	$12 \pm 3.15 \pm 3.31$	$0.00149 \pm 0.00111 \pm 0.00701$	$2.18 \pm 0.696 \pm 1.01$	$15.7 \pm 3.38 \pm 3.48$	16
$200 < \Sigma M_T < 250, N_J = 0$	$12.9 \pm 3.1 \pm 3.53$	$43.2 \pm 7.56 \pm 18.6$	$0.546 \pm 0.37 \pm 0.732$	$1.49 \pm 0.575 \pm 0.902$	$58.2 \pm 8.2 \pm 19$	56
$200 < \Sigma M_T < 250, N_J \geq 1$	$11.3 \pm 2.37 \pm 4.27$	$15.4 \pm 2.62 \pm 4.46$	$1.94 \pm 0.808 \pm 1.41$	$2.54 \pm 0.708 \pm 1.42$	$31.2 \pm 3.69 \pm 6.49$	26
High M_{T2} Same-Sign VR						
$300 < \Sigma M_T, N_J = 0$	$0.679 \pm 0.404 \pm 0.413$	< 1	$< .2$	$0.0101 \pm 0.00224 \pm 0.00388$	$0.689 \pm 0.404 \pm 0.413$	1
$300 < \Sigma M_T, N_J \geq 1$	$1.42 \pm 0.782 \pm 0.214$	< 1	$0.0125 \pm 0.0046 \pm 0.0082$	$0.0362 \pm 0.0209 \pm 0.00878$	$1.47 \pm 0.782 \pm 0.214$	0
$250 < \Sigma M_T < 300, N_J = 0$	$0.858 \pm 0.906 \pm 0.668$	< 1	$< .2$	$0.0117 \pm 0.00223 \pm 0.00417$	$0.869 \pm 0.906 \pm 0.668$	5
$250 < \Sigma M_T < 300, N_J \geq 1$	$2.7 \pm 1.12 \pm 0.0236$	< 1	$0.00382 \pm 0.00237 \pm 0.00563$	$0.0123 \pm 0.00245 \pm 0.00588$	$2.71 \pm 1.12 \pm 0.0249$	0
$200 < \Sigma M_T < 250, N_J = 0$	$2.01 \pm 1.36 \pm 1.81$	< 1	$< .2$	$0.0146 \pm 0.00257 \pm 0.00651$	$2.03 \pm 1.36 \pm 1.81$	4
$200 < \Sigma M_T < 250, N_J \geq 1$	$7.64 \pm 2.05 \pm 0.46$	< 1	$0.000815 \pm 0.000815 \pm 0.000751$	$0.0163 \pm 0.00283 \pm 0.0156$	$7.65 \pm 2.05 \pm 0.46$	4
Low M_{T2} Same-Sign VR						
$300 < \Sigma M_T, N_J = 0$	$1.11 \pm 0.573 \pm 0.457$	< 1	$< .2$	$0.0232 \pm 0.0032 \pm 0.00761$	$1.13 \pm 0.573 \pm 0.457$	1
$300 < \Sigma M_T, N_J \geq 1$	$2.51 \pm 0.846 \pm 1.37$	< 1	$0.0315 \pm 0.007 \pm 0.0734$	$0.241 \pm 0.161 \pm 0.0603$	$2.78 \pm 0.861 \pm 1.37$	2
$250 < \Sigma M_T < 300, N_J = 0$	$0.0864 \pm 0.769 \pm 2.2$	< 1	$< .2$	$0.0178 \pm 0.00291 \pm 0.00455$	$0.104 \pm 0.769 \pm 2.2$	2
$250 < \Sigma M_T < 300, N_J \geq 1$	$3.06 \pm 1.13 \pm 0.798$	< 1	$0.343 \pm 0.226 \pm 0.413$	$0.0418 \pm 0.00446 \pm 0.011$	$3.45 \pm 1.15 \pm 0.899$	3
$200 < \Sigma M_T < 250, N_J = 0$	$17.5 \pm 3.14 \pm 3.68$	< 1	$0.000345 \pm 0.000345 \pm 0.000848$	$0.0495 \pm 0.0048 \pm 0.0135$	$17.6 \pm 3.14 \pm 3.68$	17
$200 < \Sigma M_T < 250, N_J \geq 1$	$11.3 \pm 2.52 \pm 2.43$	< 1	$0.0379 \pm 0.00778 \pm 0.0201$	$0.956 \pm 0.439 \pm 0.267$	$12.3 \pm 2.56 \pm 2.44$	12
High M_{T2} B-Enriched VR						
$300 < \Sigma M_T, N_J \geq 1$	$0.535 \pm 0.743 \pm 0.134$	< 1	$4.25 \pm 1.37 \pm 0.9$	$0.237 \pm 0.185 \pm 0.182$	$5.03 \pm 1.57 \pm 0.928$	7
$250 < \Sigma M_T < 300, N_J \geq 1$	$3.02 \pm 1.16 \pm 1.46$	$0.471 \pm 0.471 \pm 0.416$	$6.57 \pm 1.63 \pm 4.35$	$0.449 \pm 0.394 \pm 0.628$	$10.5 \pm 2.09 \pm 4.65$	8
$200 < \Sigma M_T < 250, N_J \geq 1$	$6.07 \pm 1.54 \pm 3.13$	$0.974 \pm 0.691 \pm 1.6$	$6.06 \pm 1.61 \pm 2.31$	$0.294 \pm 0.205 \pm 0.534$	$13.4 \pm 2.34 \pm 4.24$	8
Low M_{T2} B-Enriched VR						
$300 < \Sigma M_T, N_J \geq 1$	$1.82 \pm 0.894 \pm 1.09$	$1.2 \pm 0.949 \pm 1.46$	$9.85 \pm 1.81 \pm 4.41$	$2.1 \pm 0.915 \pm 0.759$	$15 \pm 2.41 \pm 4.83$	9
$250 < \Sigma M_T < 300, N_J \geq 1$	$4.54 \pm 1.33 \pm 3.19$	$2.07 \pm 1 \pm 2.42$	$17.8 \pm 2.6 \pm 6.85$	$0.692 \pm 0.385 \pm 0.929$	$25.1 \pm 3.12 \pm 7.99$	17
$200 < \Sigma M_T < 250, N_J \geq 1$	$10.4 \pm 2.54 \pm 5.48$	$6.17 \pm 2.01 \pm 4.01$	$32.5 \pm 3.34 \pm 7.44$	$2.1 \pm 0.804 \pm 1.39$	$51.1 \pm 4.72 \pm 10.2$	46
High M_{T2} , Small $\Delta\phi$ VR						
$300 < \Sigma M_T, N_J = 0$	$0.949 \pm 0.521 \pm 0.488$	$1e-07 \pm 0 \pm 2e-07$	$0.000895 \pm 0.000895 \pm 0.000192$	$1.81 \pm 0.405 \pm 0.388$	$2.75 \pm 0.66 \pm 0.623$	0
$300 < \Sigma M_T, N_J \geq 1$	$1.04 \pm 1.02 \pm 0.359$	$6.98 \pm 2.07 \pm 3.91$	$0.00474 \pm 0.0022 \pm 0.00127$	$1.87 \pm 0.455 \pm 0.42$	$9.9 \pm 2.36 \pm 3.95$	11
$250 < \Sigma M_T < 300, N_J = 0$	$0.91 \pm 0.692 \pm 0.0505$	$3.11 \pm 1.95 \pm 4.28$	$0.00202 \pm 0.00202 \pm 0.00121$	$0.354 \pm 0.21 \pm 0.16$	$4.38 \pm 2.08 \pm 4.28$	2
$250 < \Sigma M_T < 300, N_J \geq 1$	$3.36 \pm 1.61 \pm 0.0821$	$9.1 \pm 2.5 \pm 6.48$	$0.00101 \pm 0.00101 \pm 0.00114$	$0.751 \pm 0.302 \pm 1.07$	$13.2 \pm 2.99 \pm 6.57$	17
$200 < \Sigma M_T < 250, N_J = 0$	$1.59 \pm 1.02 \pm 0.466$	$1.26 \pm 0.936 \pm 3.79$	$1e-07 \pm 0 \pm 0$	$0.106 \pm 0.0238 \pm 0.0502$	$2.95 \pm 1.38 \pm 3.81$	5
$200 < \Sigma M_T < 250, N_J \geq 1$	$4.07 \pm 2.45 \pm 2.92$	$22 \pm 3.86 \pm 9.69$	$0.492 \pm 0.491 \pm 0.116$	$1.13 \pm 0.425 \pm 0.906$	$27.7 \pm 4.62 \pm 10.2$	43

To ensure the test statistic is not penalized when fluctuations bring the background below predictions a lower bound is introduced. This statistic is valuable for rejecting the hypothesis H_0 which is equivalent to affirming H_1 , i.e., claiming a discovery. When rejecting the latter hypothesis the one-sided test statistic for a hypothesis of H_1 with signal strength μ becomes

$$q_\mu = \begin{cases} -2 \log(\lambda(\mu)) & \hat{\mu} \leq \mu \\ 0 & \hat{\mu} > \mu \end{cases} \quad (\text{B.4})$$

The p-value test statistic of q_0 is calculated by integrating over the corresponding probability distribution function of the background only hypothesis $f(q_0|b)dq_0$ from the observed $q_{0,obs}$ to infinity, i.e.

$$p_b = \int_{q_{0,obs}}^{\infty} f(q_0|\mu = 0, \hat{\theta}(\mu = 0)) dq_0. \quad (\text{B.5})$$

Similarly, such a p-value also exists for the hypothesis of background with signal and

corresponding multiplier μ , q_μ ,

$$p_{s+b} = \int_{q_{\mu,obs}}^{\infty} f(q_\mu|\mu, \hat{\theta}(\mu)) dq_\mu. \quad (\text{B.6})$$

A Z-score can then be computed assuming that the distribution of p-values is Gaussian distributed:

$$Z = \Phi^{-1}(1 - p), \quad (\text{B.7})$$

where Φ is the cumulative distribution function of the Gaussian. The typical threshold for claiming the discovery of a new process is 5 sigma, whereas exclusion takes place at 1.64 sigma (95 %).

When setting upper limits on signal cross sections the standard prescription is to create a more robust estimate by adjusting the p-value p_{s+b} as follows:

$$p'_{s+b} = \frac{p_{s+b}}{1 - p_b}. \quad (\text{B.8})$$

This can be statistically interpreted as the ratio of the probability to produce a false-negative signal rejection normalized by background only true-positive probability. The convention is to *exclude* a signal production scenario when $p'_{s+b} < .05$.

In the most general case, these probability distributions cannot be calculated exactly and must be sampled explicitly by *throwing toys*, i.e., by varying the nuisance parameters and sampling the resulting event counts. Often explicit generation of toys can be avoided by making use of the asymptotic form of the test statistic from which it can be shown that Gross:1099994:

$$p_{\mu s+b}(\text{Asymptotic}) = 1 - \Phi(\sqrt{q_\mu}) \longrightarrow p'_{\mu s+b}(\text{Asymptotic}) = \frac{1 - \Phi(\sqrt{q_\mu})}{\Phi(\sqrt{q_0} - \sqrt{q_\mu})}. \quad (\text{B.9})$$

Stress tests carried out for the analysis showed that the 95% confidence level expected upper limit was decreased by roughly 10 % when using the asymptotic formulas in the analysis – for computational convenience, it was decided to use the asymptotic formulation.

Bibliography

- [1] K. Hentschel, *Atomic Models, J.J. Thomson's "Plum Pudding" Model*, pp. 18–21. Springer Berlin Heidelberg, Berlin, Heidelberg, 2009.
- [2] J. R. Garbarino and M. A. Wartell, *The rutherford scattering experiment: Cai in the laboratory*, *Journal of Chemical Education* **50** (1973), no. 11 792, [<https://doi.org/10.1021/ed050p792>].
- [3] C. Gearhart, *Black-Body Radiation*, pp. 39–42. Springer Berlin Heidelberg, Berlin, Heidelberg, 2009.
- [4] M. K. Gaillard, P. D. Grannis, and F. J. Sciulli, *The standard model of particle physics*, *Rev. Mod. Phys.* **71** (Mar, 1999) S96–S111.
- [5] A. S. Kronfeld and C. Quigg, *Resource letter qcd-1: Quantum chromodynamics*, *American Journal of Physics* **78** (2010), no. 11 1081–1116, [<https://doi.org/10.1119/1.3454865>].
- [6] K. Kumericki, *Feynman Diagrams for Beginners*, *arXiv e-prints* (Feb, 2016) arXiv:1602.04182, [arXiv:1602.0418].
- [7] M. E. Peskin and D. V. Schroeder, *An Introduction to Quantum Field Theory*. Westview Press, 1995. Reading, USA: Addison-Wesley (1995) 842 p.
- [8] E. R. Jones, R. A. Bach, and H. Batelaan, *Path integrals, matter waves, and the double slit*, *European Journal of Physics* **36** (oct, 2015) 065048.
- [9] A. Zee, *Quantum Field Theory in a Nutshell*. Nutshell handbook. Princeton Univ. Press, Princeton, NJ, 2003.
- [10] S. Willenbrock, *Symmetries of the standard model*, in *Physics in D $\hat{=}$ 4. Proceedings, Theoretical Advanced Study Institute in elementary particle physics, TASI 2004, Boulder, USA, June 6-July 2, 2004*, pp. 3–38, 2004. hep-ph/0410370.
- [11] J. M. Dudley and A. M. Kwan, *Richard Feynman's popular lectures on quantum electrodynamics: The 1979 Robb lectures at Auckland University*, *American Journal of Physics* **64** (June, 1996) 694–698.

- [12] S. Bilenky and J. Hošek, *Glashow-weinberg-salam theory of electroweak interactions and the neutral currents*, *Physics Reports* **90** (1982), no. 2 73 – 157.
- [13] **Particle Data Group** Collaboration, C. Patrignani *et. al.*, *Review of Particle Physics*, *Chin. Phys.* **C40** (2016), no. 10 100001.
- [14] A. Pich, *The Standard model of electroweak interactions*, in *2004 European School of High-Energy Physics, Sant Feliu de Guixols, Spain, 30 May - 12 June 2004*, pp. 1–48, 2005. hep-ph/0502010.
- [15] G. Altarelli, *A QCD primer*, *AIP Conf. Proc.* **631** (2002), no. 1 70, [hep-ph/0204179].
- [16] J. Ellis, *The Discovery of the Gluon*, *Int. J. Mod. Phys.* **A29** (2014), no. 31 1430072, [arXiv:1409.4232]. [,189(2015)].
- [17] D. J. Gross and F. Wilczek, *Ultraviolet Behavior of Non-Abelian Gauge Theories*, *Physical Review Letters* **30** (June, 1973) 1343–1346.
- [18] C. Ratti, *Lattice QCD and heavy ion collisions: a review of recent progress*, *Rept. Prog. Phys.* **81** (2018), no. 8 084301, [arXiv:1804.0781].
- [19] ATLAS, *Measurement of inclusive jet and dijet cross-sections in proton-proton collisions at $s=\sqrt{13}$ with the atlas detector*, *Journal of High Energy Physics* **2018** (May, 2018).
- [20] M. Rauch, *Vector-Boson Fusion and Vector-Boson Scattering*, arXiv:1610.0842.
- [21] M. S. Chanowitz, *Electroweak Symmetry Breaking: Unitarity, Dynamics, Experimental Prospects*, *Ann. Rev. Nucl. Part. Sci.* **38** (1988) 323–420.
- [22] S. Dawson, *Introduction to electroweak symmetry breaking*, in *Proceedings, Summer School in High-energy physics and cosmology: Trieste, Italy, June 29-July 17, 1998*, pp. 1–83, 1998. hep-ph/9901280.
- [23] CMS, *Observation of a new boson at a mass of 125 gev with the cms experiment at the lhc*, *Physics Letters B* **716** (2012), no. 1 30 – 61.
- [24] U. Dore and L. Zanello, *Bruno Pontecorvo and neutrino physics*, arXiv:0910.1657.
- [25] C. Giganti, S. Lavignac, and M. Zito, *Neutrino oscillations: the rise of the PMNS paradigm*, *Prog. Part. Nucl. Phys.* **98** (2018) 1–54, [arXiv:1710.0071].
- [26] M. Thomson, *Modern particle physics*. Cambridge University Press, New York, 2013.
- [27] S. F. King, *Neutrino Mass Models*, *Rep. Prog. Phys.* **67** (Oct, 2003) 107–158. 61 p.

- [28] **MINOS** Collaboration, P. Adamson *et. al.*, *Measurement of the Neutrino Mass Splitting and Flavor Mixing by MINOS*, *Phys. Rev. Lett.* **106** (2011) 181801, [arXiv:1103.0340].
- [29] A. Samanta and A. Yu. Smirnov, *The 2-3 mixing and mass split: atmospheric neutrinos and magnetized spectrometers*, *JHEP* **07** (2011) 048, [arXiv:1012.0360].
- [30] **Particle Data Group** Collaboration, K. A. Olive *et. al.*, *Review of Particle Physics*, *Chin. Phys.* **C38** (2014) 090001.
- [31] A. Pich, *Precision tests of the standard model*, in *Fundamental physics: Selected topics on high-energy and astroparticle physics. Proceedings, 25th International Winter Meeting, Formigal, Spain, March 3-7, 1997*, pp. 1–30, 1997. hep-ph/9711279.
- [32] P. Langacker, *Precision tests of the Standard Model*, in *Frontiers of neutrino astrophysics. Proceedings, International Symposium, Takayama, Japan, October 19-22, 1992*, 1993. hep-ph/9303304.
- [33] J. R. Ellis, *Limits of the standard model*, in *PSI Zuoz Summer School on Exploring the Limits of the Standard Model Zuoz, Engadin, Switzerland, August 18-24, 2002*, 2002. hep-ph/0211168.
- [34] K. Garrett and G. Duda, *Dark Matter: A Primer*, *Adv. Astron.* **2011** (2011) 968283, [arXiv:1006.2483].
- [35] G. P. Efstathiou, R. S. Ellis, J. E. Gunn, D. York, A. N. Lasenby, A. W. Jones, and Y. Dabrowski, *Observations of the cosmic microwave background and implications for cosmology and large-scale structure*, *Philosophical Transactions of the Royal Society of London. Series A: Mathematical, Physical and Engineering Sciences* **357** (1999), no. 1750 35–56.
- [36] S. Joudaki, *Beyond the Standard Model of Cosmology: Dark Energy, Massive Neutrinos, and Primordial Non-Gaussianity*. PhD thesis, UC, Irvine, 2012.
- [37] N. Arkani-Hamed, S. Dimopoulos, and G. R. Dvali, *The Hierarchy problem and new dimensions at a millimeter*, *Phys. Lett.* **B429** (1998) 263–272, [hep-ph/9803315].
- [38] I. Antoniadis, *The Physics of extra dimensions*, *Lect. Notes Phys.* **720** (2007) 293–321, [hep-ph/0512182].
- [39] W. Buchmuller and C. Ludeling, *Field Theory and Standard Model*, in *High-energy physics. Proceedings, European School, Kitzbuehel, Austria, August 21-September, 2005*, 2006. hep-ph/0609174.

- [40] W. Ahmed, X.-J. Bi, T. Li, J.-S. Niu, S. Raza, Q.-F. Xiang, and P.-F. Yin, *Status of natural supersymmetry from the generalized minimal supergravity in light of the current lhc run-2 and lux data*, *Phys. Rev. D* **98** (Jul, 2018) 015040.
- [41] A. Bilal, *Introduction to supersymmetry*, hep-th/0101055.
- [42] F. Quevedo, S. Krippendorff, and O. Schlotterer, *Cambridge Lectures on Supersymmetry and Extra Dimensions*, arXiv:1011.1491.
- [43] S. K. Vempati, *Introduction to MSSM*, arXiv:1201.0334.
- [44] N. Pietsch, *Search for Supersymmetry in Final States with a Single Lepton, B-Quark Jets, and Missing Transverse Energy at the CMS Experiment.*, PhD thesis, Dept. Phys., 2014.
- [45] M. Drees, *An Introduction to supersymmetry*, in *Current topics in physics. Proceedings, Inauguration Conference of the Asia-Pacific Center for Theoretical Physics (APCTP), Seoul, Korea, June 4-10, 1996. Vol. 1, 2, 1996.* hep-ph/9611409.
- [46] R. N. Mohapatra, *Supersymmetric grand unification*, in *Supersymmetry, supergravity and supercolliders. Proceedings, Theoretical Advanced Study Institute in elementary particle physics, TASI'97, Boulder, USA, June 2-27, 1997*, pp. 601–657, 1997. hep-ph/9801235.
- [47] S. A. Raby, *Grand unified theories 1 15 . grand unified theories, .*
- [48] W. Beenakker, M. Krämer, T. Plehn, M. Spira, and P. M. Zerwas, *Stop Production at Hadron Colliders*, *Nucl. Phys. B* **515** (Oct, 1997) 3–14. 15 p.
- [49] J. Cao, C. Han, L. Wu, J. M. Yang, and Y. Zhang, *Probing Natural SUSY from Stop Pair Production at the LHC*, *JHEP* **11** (2012) 039, [arXiv:1206.3865].
- [50] M. R. and, *Susy searches: Recent results from atlas and cms*, *Journal of Physics: Conference Series* **631** (jul, 2015) 012072.
- [51] J. Fiaschi and M. Klasen, *Neutralino-chargino pair production at NLO+NLL with resummation-improved parton density functions for LHC Run II*, *Phys. Rev.* **D98** (2018), no. 5 055014, [arXiv:1805.1132].
- [52] A. Alloul, M. Frank, B. Fuks, and M. Rausch de Traubenberg, *Chargino and neutralino production at the Large Hadron Collider in left-right supersymmetric models*, *JHEP* **10** (2013) 033, [arXiv:1307.5073].
- [53] **CMS** Collaboration, A. M. Sirunyan *et. al.*, *Combined search for electroweak production of charginos and neutralinos in proton-proton collisions at $\sqrt{s} = 13$ TeV*, *JHEP* **03** (2018) 160, [arXiv:1801.0395].

- [54] **ATLAS** Collaboration, M. Aaboud *et. al.*, *Search for electroweak production of supersymmetric states in scenarios with compressed mass spectra at $\sqrt{s} = 13$ TeV with the ATLAS detector*, *Phys. Rev.* **D97** (2018), no. 5 052010, [arXiv:1712.0811].
- [55] **CMS** Collaboration, A. M. Sirunyan *et. al.*, *Search for supersymmetric partners of electrons and muons in proton-proton collisions at $\sqrt{s} = 13$ TeV*, *Phys. Lett.* **B790** (2019) 140–166, [arXiv:1806.0526].
- [56] S. Ask, *A Review of the supersymmetry searches at LEP*, in *38th Rencontres de Moriond on Electroweak Interactions and Unified Theories Les Arcs, France, March 15-22, 2003*, 2003. hep-ex/0305007.
- [57] J. M. Lindert, F. D. Steffen, and M. K. Trenkel, *Direct stau production at hadron colliders in cosmologically motivated scenarios*, *JHEP* **08** (2011) 151, [arXiv:1106.4005].
- [58] J. R. Ellis, T. Falk, K. A. Olive, and M. Srednicki, *Calculations of neutralino-stau coannihilation channels and the cosmologically relevant region of MSSM parameter space*, *Astropart. Phys.* **13** (2000) 181–213, [hep-ph/9905481]. [Erratum: *Astropart. Phys.*15,413(2001)].
- [59] G. H. Duan, C. Han, B. Peng, L. Wu, and J. M. Yang, *Vacuum stability in stau-neutralino coannihilation in MSSM*, *Phys. Lett.* **B788** (2019) 475–479, [arXiv:1809.1006].
- [60] **ATLAS** Collaboration, G. Aad *et. al.*, *Search for the direct production of charginos, neutralinos and staus in final states with at least two hadronically decaying taus and missing transverse momentum in pp collisions at $\sqrt{s} = 8$ TeV with the ATLAS detector*, *JHEP* **10** (2014) 96, [arXiv:1407.0350].
- [61] *Search for supersymmetry in events with a τ lepton pair and missing transverse momentum in proton-proton collisions at $\sqrt{s}=13$, Journal of High Energy Physics* **2018** (Nov, 2018) 151.
- [62] Wikipedia contributors, *List of largest machines — Wikipedia, the free encyclopedia*, 2019. [Online; accessed 10-April-2019].
- [63] **ALICE** Collaboration, K. Aamodt *et. al.*, *The ALICE experiment at the CERN LHC*, *JINST* **3** (2008) S08002.
- [64] **ATLAS** Collaboration, G. Aad *et. al.*, *The ATLAS Experiment at the CERN Large Hadron Collider*, *JINST* **3** (2008) S08003.
- [65] **CMS** Collaboration, S. Chatrchyan *et. al.*, *The CMS Experiment at the CERN LHC*, *JINST* **3** (2008) S08004.

- [66] **LHCb** Collaboration, A. A. Alves, Jr. *et. al.*, *The LHCb Detector at the LHC*, *JINST* **3** (2008) S08005.
- [67] **CMS** Collaboration, S. Chatrchyan *et. al.*, *Observation and studies of jet quenching in PbPb collisions at nucleon-nucleon center-of-mass energy = 2.76 TeV*, *Phys. Rev.* **C84** (2011) 024906, [arXiv:1102.1957].
- [68] H. Wiedemann, *Introduction to Accelerator Physics*, pp. 3–41. Springer International Publishing, Cham, 2015.
- [69] H. Schopper, *LEP: The lord of the collider rings at CERN 1980-2000: The making, operation and legacy of the world’s largest scientific instrument*. 2009.
- [70] L. Evans, *The large hadron collider*, *New Journal of Physics* **9** (sep, 2007) 335–335.
- [71] **ATLAS** Collaboration, M. Aaboud *et. al.*, *Luminosity determination in pp collisions at $\sqrt{s} = 8$ TeV using the ATLAS detector at the LHC*, *Eur. Phys. J.* **C76** (2016), no. 12 653, [arXiv:1608.0395].
- [72] *Expected pileup values at the HL-LHC*, Tech. Rep. ATL-UPGRADE-PUB-2013-014, CERN, Geneva, Sep, 2013.
- [73] Z. M. and, *Simulation of pile-up in the ATLAS experiment*, *Journal of Physics: Conference Series* **513** (jun, 2014) 022024.
- [74] T.-M. Yan and S. D. Drell, *The Parton Model and its Applications*, *Int. J. Mod. Phys.* **A29** (2014) 0071, [arXiv:1409.0051].
- [75] H. Abramowicz and A. Caldwell, *HERA collider physics*, *Rev. Mod. Phys.* **71** (1999) 1275–1410, [hep-ex/9903037].
- [76] The ZEUS Collaboration, *An nlo qcd analysis of inclusive cross-section and jet-production data from the zeus experiment*, *The European Physical Journal C - Particles and Fields* **42** (Jul, 2005) 1–16.
- [77] **NNPDF** Collaboration, R. D. Ball *et. al.*, *Parton distributions for the LHC Run II*, *JHEP* **04** (2015) 040, [arXiv:1410.8849].
- [78] R. Placakyte, *Parton Distribution Functions*, in *Proceedings, 31st International Conference on Physics in collisions (PIC 2011): Vancouver, Canada, August 28-September 1, 2011*, 2011. arXiv:1111.5452.
- [79] A. Denner, S. Heinemeyer, I. Puljak, D. Rebuszi, and M. Spira, *Standard Model Higgs-Boson Branching Ratios with Uncertainties*, *Eur. Phys. J.* **C71** (2011) 1753, [arXiv:1107.5909].

- [80] **CMS** Collaboration, D. Dobur, *Jets and Missing Transverse Energy Reconstruction with CMS*, *PoS 2008LHC* (2014) 039, [arXiv:0904.0391].
- [81] **CMS** Collaboration, S. Chatrchyan *et. al.*, *Alignment of the CMS tracker with LHC and cosmic ray data*, *JINST* **9** (2014) P06009, [arXiv:1403.2286].
- [82] **ATLAS** Collaboration, G. Aad *et. al.*, *Charged-particle multiplicities in pp interactions measured with the ATLAS detector at the LHC*, *New J. Phys.* **13** (2011) 053033, [arXiv:1012.5104].
- [83] C. Heidegger.
- [84] A. Dominguez, D. Abbaneo, K. Arndt, N. Bacchetta, A. Ball, E. Bartz, W. Bertl, G. M. Bilei, G. Bolla, H. W. K. Cheung, M. Chertok, S. Costa, N. Demaria, D. D. Vazquez, K. Ecklund, W. Erdmann, K. Gill, G. Hall, K. Harder, F. Hartmann, R. Horisberger, W. Johns, H. C. Kaestli, K. Klein, D. Kotlinski, S. Kwan, M. Pesaresi, H. Postema, T. Rohe, C. Schäfer, A. Starodumov, S. Streuli, A. Tricomi, P. Tropea, J. Troska, F. Vasey, and W. Zeuner, *CMS Technical Design Report for the Pixel Detector Upgrade*, Tech. Rep. CERN-LHCC-2012-016. CMS-TDR-11, Sep, 2012. Additional contacts: Jeffrey Spalding, Fermilab, Jeffrey.Spalding@cern.ch Didier Contardo, Universite Claude Bernard-Lyon I, didier.claude.contardo@cern.ch.
- [85] **CMS Collaboration** Collaboration, G. L. Bayatian and Chatrchyan, *CMS Physics: Technical Design Report Volume 1: Detector Performance and Software*. Technical Design Report CMS. CERN, Geneva, 2006. There is an error on cover due to a technical problem for some items.
- [86] **CMS Collaboration** Collaboration, R. M. Hadjiiska, *The performance of the CMS Muon system with data at $\sqrt{s} = 13$ TeV*, Tech. Rep. CMS-CR-2018-167, CERN, Geneva, Aug, 2018.
- [87] G. Bauer, B. Beccati, U. Behrens, K. Biery, O. Bouffet, J. Branson, S. Bukowiec, E. Cano, H. Cheung, M. Ciganek, S. Cittolin, J. A. Coarasa, C. Deldicque, A. Dupont, S. Erhan, D. Gigi, F. Glege, R. Gomez-Reino, D. Hatton, A. Holzner, Y. L. Hwong, L. Masetti, F. Meijers, E. Meschi, R. K. Mommsen, R. Moser, V. ODell, L. Orsini, C. Paus, A. Petrucci, M. Pieri, A. Racz, O. Raginel, H. Sakulin, M. Sani, P. Schieferdecker, C. Schwick, D. Shpakov, M. Simon, and K. Sumorok, *The data-acquisition system of the CMS experiment at the LHC*, *Journal of Physics: Conference Series* **331** (dec, 2011) 022021.
- [88] F. Bechtel and P. Schleper, *The underlying event in proton-proton collisions*, .
- [89] **CMS** Collaboration, A. M. Sirunyan *et. al.*, “Particle-flow reconstruction and global event description with the CMS detector.” Submitted to *JINST*, 2017.

- [90] S. Cucciarelli, M. Konecki, D. Kotlinski, and T. Todorov, *Track reconstruction, primary vertex finding and seed generation with the Pixel Detector*, Tech. Rep. CMS-NOTE-2006-026, CERN, Geneva, Jan, 2006.
- [91] R. Frühwirth, W. Waltenberger, and P. Vanlaer, *Adaptive Vertex Fitting*, Tech. Rep. CMS-NOTE-2007-008, CERN, Geneva, Mar, 2007.
- [92] **CMS** Collaboration, S. Chatrchyan *et. al.*, *Description and performance of track and primary-vertex reconstruction with the CMS tracker*, *JINST* **9** (2014), no. 10 P10009, [arXiv:1405.6569].
- [93] **CMS** Collaboration, A. M. Sirunyan *et. al.*, *Performance of the CMS muon detector and muon reconstruction with proton-proton collisions at $\sqrt{s} = 13$ TeV*, *JINST* **13** (2018), no. 06 P06015, [arXiv:1804.0452].
- [94] “Pat exercise 07: Pf2pat tutorial.” <https://twiki.cern.ch/twiki/bin/view/CMSPublic/SWGuidePATPF2PATExercise>.
- [95] **CMS** Collaboration, V. Khachatryan *et. al.*, *Performance of electron reconstruction and selection with the CMS detector in proton-proton collisions at $\sqrt{s} = 8$ TeV*, *JINST* **10** (2015) P06005, [arXiv:1502.0270].
- [96] M. Cacciari, G. P. Salam, and G. Soyez, *FastJet user manual*, *Eur. Phys. J. C* **72** (2012) 1896, [arXiv:1111.6097].
- [97] “Cms data analysis school 2015: Jet analysis.”
- [98] **CMS** Collaboration, V. Khachatryan *et. al.*, *Jet energy scale and resolution in the CMS experiment in pp collisions at 8 TeV*, *JINST* **12** (2017), no. 02 P02014, [arXiv:1607.0366].
- [99] “Jet energy corrections: Official software tools for applying jec corrections and uncertainties..”
- [100] **CMS** Collaboration, *Plans for Jet Energy Corrections at CMS*, .
- [101] T. C. collaboration, *Identification of b-quark jets with the CMS experiment*, *Journal of Instrumentation* **8** (apr, 2013) P04013–P04013.
- [102] **CMS** Collaboration, M. Stoye, *Deep learning in jet reconstruction at CMS*, *J. Phys. Conf. Ser.* **1085** (2018), no. 4 042029.
- [103] C. Collaboration, *Performance of q-lepton reconstruction and identification in CMS*, *Journal of Instrumentation* **7** (jan, 2012) P01001–P01001.
- [104] **CMS** Collaboration, A. M. Sirunyan *et. al.*, *Performance of reconstruction and identification of τ leptons decaying to hadrons and ν_τ in pp collisions at $\sqrt{s} = 13$ TeV*, *JINST* **13** (2018), no. 10 P10005, [arXiv:1809.0281].

- [105] **CMS** Collaboration, V. Khachatryan *et. al.*, *Reconstruction and identification of τ lepton decays to hadrons and ν_τ at CMS*, *JINST* **11** (2016) P01019, [arXiv:1510.0748].
- [106] **CMS** Collaboration, *Performance of reconstruction and identification of tau leptons in their decays to hadrons and tau neutrino in LHC Run-2*, CMS Physics Analysis Summary CMS-PAS-TAU-16-002, 2016.
- [107] **CMS** Collaboration, A. M. Sirunyan *et. al.*, *Performance of missing transverse momentum reconstruction in proton-proton collisions at $\sqrt{s} = 13$ TeV using the CMS detector*, arXiv:1903.0607.
- [108] T. Gleisberg, S. Hoeche, F. Krauss, M. Schonherr, S. Schumann, F. Siegert, and J. Winter, *Event generation with SHERPA 1.1*, *JHEP* **02** (2009) 007, [arXiv:0811.4622].
- [109] J. M. Butterworth, G. Dissertori, and G. P. Salam, *Hard Processes in Proton-Proton Collisions at the Large Hadron Collider*, *Ann. Rev. Nucl. Part. Sci.* **62** (2012) 387–405, [arXiv:1202.0583].
- [110] D. Kotlorz and A. Kotlorz, *Evolution equations for truncated moments of the parton distributions*, *Phys. Lett.* **B644** (2007) 284–287, [hep-ph/0610282].
- [111] N. Fischer and T. Sjöstrand, *Thermodynamical String Fragmentation*, *JHEP* **01** (2017) 140, [arXiv:1610.0981].
- [112] T. Sjostrand, S. Mrenna, and P. Z. Skands, *A Brief Introduction to PYTHIA 8.1*, *Comput. Phys. Commun.* **178** (2008) 852–867, [arXiv:0710.3820].
- [113] J. Alwall, M. Herquet, F. Maltoni, O. Mattelaer, and T. Stelzer, *MadGraph 5 : Going Beyond*, *JHEP* **06** (2011) 128, [arXiv:1106.0522].
- [114] C. Oleari, *The POWHEG-BOX*, *Nucl. Phys. Proc. Suppl.* **205-206** (2010) 36–41, [arXiv:1007.3893].
- [115] **NNPDF** Collaboration, R. D. Ball *et. al.*, *Parton distributions from high-precision collider data*, *Eur. Phys. J.* **C77** (2017), no. 10 663, [arXiv:1706.0042].
- [116] A. Kalogeropoulos and J. Alwall, *The SysCalc code: A tool to derive theoretical systematic uncertainties*, arXiv:1801.0840.
- [117] **GEANT4** Collaboration, S. Agostinelli *et. al.*, *GEANT4: A Simulation toolkit*, *Nucl. Instrum. Meth.* **A506** (2003) 250–303.

- [118] **DELPHES 3** Collaboration, J. de Favereau, C. Delaere, P. Demin, A. Giammanco, V. Lemaître, A. Mertens, and M. Selvaggi, *DELPHES 3, A modular framework for fast simulation of a generic collider experiment*, *JHEP* **02** (2014) 057, [arXiv:1307.6346].
- [119] B. Mehlig, *Artificial Neural Networks*, *arXiv e-prints* (Jan, 2019) arXiv:1901.05639, [arXiv:1901.0563].
- [120] M. Kaiser, C. C. Hilgetag, and A. van Ooyen, *A simple rule for axon outgrowth and synaptic competition generates realistic connection lengths and filling fractions*, *arXiv e-prints* (Jun, 2009) arXiv:0906.0685, [arXiv:0906.0685].
- [121] U. Güçlü and M. A. J. van Gerven, *Modeling the dynamics of human brain activity with recurrent neural networks*, *arXiv e-prints* (Jun, 2016) arXiv:1606.03071, [arXiv:1606.0307].
- [122] Z. Zhang and M. R. Sabuncu, *Generalized Cross Entropy Loss for Training Deep Neural Networks with Noisy Labels*, *arXiv e-prints* (May, 2018) arXiv:1805.07836, [arXiv:1805.0783].
- [123] D. P. Kingma and J. Ba, *Adam: A method for stochastic optimization*, in *ICLR*, 2015.
- [124] Y. Lecun, *A theoretical framework for back-propagation*, in *Proceedings of the 1988 Connectionist Models Summer School, CMU, Pittsburg, PA* (D. Touretzky, G. Hinton, and T. Sejnowski, eds.), pp. 21–28, Morgan Kaufmann, 1988.
- [125] J. Koushik, *Understanding Convolutional Neural Networks*, *arXiv e-prints* (May, 2016) arXiv:1605.09081, [arXiv:1605.0908].
- [126] “Convolutional neural networks tutorial in tensorflow.” <https://adventuresinmachinelearning.com/convolutional-neural-networks-tutorial-tensorflow/>, 2015.
- [127] F. Chollet, “keras.” <https://github.com/fchollet/keras>, 2015.
- [128] M. Abadi, A. Agarwal, P. Barham, E. Brevdo, Z. Chen, C. Citro, G. S. Corrado, A. Davis, J. Dean, M. Devin, S. Ghemawat, I. Goodfellow, A. Harp, G. Irving, M. Isard, Y. Jia, R. Jozefowicz, L. Kaiser, M. Kudlur, J. Levenberg, D. Mane, R. Monga, S. Moore, D. Murray, C. Olah, M. Schuster, J. Shlens, B. Steiner, I. Sutskever, K. Talwar, P. Tucker, V. Vanhoucke, V. Vasudevan, F. Viegas, O. Vinyals, P. Warden, M. Wattenberg, M. Wicke, Y. Yu, and X. Zheng, *TensorFlow: Large-Scale Machine Learning on Heterogeneous Distributed Systems*, *arXiv e-prints* (Mar, 2016) arXiv:1603.04467, [arXiv:1603.0446].

- [129] J. Alwall, P. Schuster, and N. Toro, *Simplified models for a first characterization of new physics at the LHC*, *Phys. Rev. D* **79** (2009) 075020, [arXiv:0810.3921].
- [130] D. Alves, N. Arkani-Hamed, S. Arora, Y. Bai, M. Baumgart, J. Berger, M. Buckley, B. Butler, S. Chang, H.-C. Cheng, C. Cheung, R. S. Chivukula, W. S. Cho, R. Cotta, M. D'Alfonso, S. E. Hedri, R. Essig, J. A. Evans, L. Fitzpatrick, P. Fox, R. Franceschini, A. Freitas, J. S. Gainer, Y. Gershtein, R. Gray, T. Gregoire, B. Gripaios, J. Gunion, T. Han, A. Haas, P. Hansson, J. Hewett, D. Hits, J. Hubisz, E. Izaguirre, J. Kaplan, E. Katz, C. Kilic, H.-D. Kim, R. Kitano, S. A. Koay, P. Ko, D. Krohn, E. Kuflik, I. Lewis, M. Lisanti, T. Liu, Z. Liu, R. Lu, M. Luty, P. Meade, D. Morrissey, S. Mrenna, M. Nojiri, T. Okui, S. Padhi, M. Papucci, M. Park, M. Park, M. Perelstein, M. Peskin, D. Phalen, K. Rehermann, V. Rential, T. Roy, J. T. Ruderman, V. Sanz, M. Schmaltz, S. Schnetzer, P. Schuster, P. Schwaller, M. D. Schwartz, A. Schwartzman, J. Shao, J. Shelton, D. Shih, J. Shu, D. Silverstein, E. Simmons, S. Somalwar, M. Spannowsky, C. Spethmann, M. Strassler, S. Su, T. Tait, B. Thomas, S. Thomas, N. Toro, T. Volansky, J. Wacker, W. Waltenberger, I. Yavin, F. Yu, Y. Zhao, and K. Z. and, *Simplified models for LHC new physics searches*, *Journal of Physics G: Nuclear and Particle Physics* **39** (sep, 2012) 105005.
- [131] B. Fuks, M. Klasen, D. R. Lamprea, and M. Rothering, *Revisiting slepton pair production at the Large Hadron Collider*, *JHEP* **01** (2014) 168, [arXiv:1310.2621].
- [132] W. Beenakker, M. Klasen, M. Kramer, T. Plehn, M. Spira, and P. M. Zerwas, *Production of Charginos, Neutralinos, and Stopped at Hadron Colliders*, *Phys. Rev. Lett.* **83** (1999) 3780, [hep-ph/9906298]. [Erratum: *Phys. Rev. Lett.* **100** (2008) 029901, 10.1103/PhysRevLett.100.029901].
- [133] L. Cadamuro, *The CMS level-1 trigger system for LHC run II*, *Journal of Instrumentation* **12** (mar, 2017) C03021–C03021.
- [134] T. C. Collaboration, *The CMS trigger system*, *Journal of Instrumentation* **12** (jan, 2017) P01020–P01020.
- [135] “Tau id for 13 tev run.”
<https://twiki.cern.ch/twiki/bin/view/CMS/TauIDRecommendation13TeV>.
- [136] **CMS Collaboration** Collaboration, *Muon Identification and Isolation efficiency on full 2016 dataset*, .
- [137] **CMS Collaboration** Collaboration, *Muon identification and isolation efficiencies with 2017 and 2018 data*, .
- [138] “ p_T performance and recommendations for run ii.”
<https://twiki.cern.ch/twiki/bin/view/CMS/MissingET>.

- [139] C. G. Lester and D. J. Summers, *Measuring masses of semiinvisibly decaying particles pair produced at hadron colliders*, *Phys. Lett. B* **463** (1999) 99, [hep-ph/9906349].
- [140] A. Barr, C. Lester, and P. Stephens, *m(T2): The truth behind the glamour*, *J. Phys. G* **29** (2003) 2343, [hep-ph/0304226].
- [141] H. Bakhshian *et. al.*, *Computing the contamination from fakes in leptonic final states*, CMS Analysis Note 2010/261, 2010.
- [142] K. Cranmer, *Practical Statistics for the LHC*, in *Proceedings, 2011 European School of High-Energy Physics (ESHEP 2011): Cheile Gradistei, Romania, September 7-20, 2011*, pp. 267–308, 2015. arXiv:1503.0762. [247(2015)].
- [143] **CMS Collaboration** Collaboration, *Search for direct τ slepton pair production in proton-proton collisions at $\sqrt{s} = 13$ TeV*, Tech. Rep. CMS-PAS-SUS-18-006, CERN, Geneva, 2019.
- [144] Particle Data Group, K. A. Olive, *et. al.* *Phys. Rev. D* **98** (Aug, 2018) 030001.
- [145] **ATLAS** Collaboration, M. Aaboud *et. al.*, *Observation of $H \rightarrow b\bar{b}$ decays and VH production with the ATLAS detector*, *Phys. Lett. B* **786** (2018) 59–86, [arXiv:1808.0823].
- [146] **CMS** Collaboration, A. M. Sirunyan *et. al.*, *Observation of $t\bar{t}H$ production*, *Phys. Rev. Lett.* **120** (2018), no. 23 231801, [arXiv:1804.0261].
- [147] J. Zurita, *Di-Higgs production at the LHC and beyond*, in *5th Large Hadron Collider Physics Conference (LHCP 2017) Shanghai, China, May 15-20, 2017*, 2017. arXiv:1708.0089.
- [148] G. Perez, Y. Soreq, E. Stamou, and K. Tobioka, *Prospects for measuring the Higgs boson coupling to light quarks*, *Phys. Rev. D* **93** (2016), no. 1 013001, [arXiv:1505.0668].
- [149] G. Arduini, J. Barranco, A. Bertarelli, N. Biancacci, R. Bruce, O. Brüning, X. Buffat, Y. Cai, L. R. Carver, S. Fartoukh, M. Giovannozzi, G. Iadarola, K. Li, A. Lechner, L. M. Medrano, E. Métral, Y. Nosochkov, Y. Papaphilippou, D. Pellegrini, T. Pieloni, J. Qiang, S. Redaelli, A. Romano, L. Rossi, G. Rumolo, B. Salvant, M. Schenk, C. Tambasco, R. Tomás, S. Valishev, and F. F. V. d. Veken, *High Luminosity LHC: challenges and plans*, *JINST* **11** (2016), no. CERN-ACC-2016-0344. FERMILAB-CONF-16-621-AD-APC. 12 C12081.
- [150] **CMS Collaboration** Collaboration, J. Butler, D. Contardo, M. Klute, J. Mans, L. Silvestris, and C. on behalf of the CMS, *CMS Phase II Upgrade Scope Document*, Tech. Rep. CERN-LHCC-2015-019. LHCC-G-165, CERN, Geneva, Sep, 2015.

- [151] C. Collaboration, *TECHNICAL PROPOSAL FOR A MIP TIMING DETECTOR IN THE CMS EXPERIMENT PHASE 2 UPGRADE*, Tech. Rep. CERN-LHCC-2017-027. LHCC-P-009, CERN, Geneva, Dec, 2017. This document describes a MIP timing detector for the Phase-2 upgrade of the CMS experiment, in view of HL-LHC running.
- [152] D. Bertolini, P. Harris, M. Low, and N. Tran, *Pileup Per Particle Identification*, *JHEP* **10** (2014) 059, [arXiv:1407.6013].
- [153] **CMS Collaboration** Collaboration, *Search for supersymmetry with direct stau production at the HL-LHC with the CMS Phase-2 detector*, Tech. Rep. CMS-PAS-FTR-18-010, CERN, Geneva, 2019.